

Proton conducting electrolytes for ceramic fuel cells

Von der Fakultät Chemie der Universität Stuttgart
zur Erlangung der Würde eines Doktors der
Naturwissenschaften (Dr. rer. nat.) genehmigte Abhandlung

Vorgelegt von
Yuanye Huang
aus Beijing, China

Hauptberichter: Prof. Dr. Joachim Maier
Mitberichter: Prof. Dr. Thomas Schleid
Prüfungsvorsitzender: Prof. Dr. Frank Gießelmann
Tag der mündlichen Prüfung: 16.09.2020

Max-Planck-Institut für Festkörperforschung
2020

Erklärung über die Eigenständigkeit der Dissertation

Ich versichere, dass ich die vorliegende Arbeit mit dem Titel *Proton conducting electrolytes for ceramic fuel cells* selbständig verfasst und keine anderen als die angegebenen Quellen und Hilfsmittel benutzt habe; aus fremden Quellen entnommene Passagen und Gedanken sind als solche kenntlich gemacht.

Declaration of Authorship

I hereby certify that the dissertation entitled *Proton conducting electrolytes for ceramic fuel cells* is entirely my own work except where otherwise indicated. Passages and ideas from other sources have been clearly indicated.

Name/Name: _____Yuanye Huang_____

Unterschrift/Signed: _____

Datum/Date: _____

Contents

Contents	5
Zusammenfassung.....	7
Abstract.....	11
Abbreviations and symbols.....	15
Chapter 1 Introduction	19
1.1 Protonic ceramic fuel and electrolysis cells	19
1.2 Protonic defect formation and transport.....	21
1.3 Blocking grain boundaries and space charge model	22
1.4 Possible improvements for proton conductivity of BaZrO ₃ ceramics.....	25
1.4.1 Improving the specific GB conductivity	25
1.4.2 Improving the sintering process	26
1.5 Approaches taken in the present thesis	27
Chapter 2 Experimental	29
2.1 Sample preparation.....	29
2.1.1 Abbreviation for BZCY sample composition.....	29
2.1.2 Powder preparation by solid state reaction.....	30
2.1.3 Spark plasma sintering.....	30
2.1.4 GB-decorated ceramics.....	31
2.1.5 Ceramics with phosphate phase at GBs.....	31
2.1.6 Solid state reactive sintering.....	32
2.2 Sample characterizations.....	33
2.2.1 Measurements of relative density	33
2.2.2 X-ray diffraction (XRD).....	33
2.2.3 ICP-OES	34
2.2.4 Thermogravimetry	34
2.2.5 BET.....	35
2.2.6 Scanning electron microscopy	35
2.2.7 Transmission electron microscopy	36
2.2.8 Raman spectroscopy	38

2.2.9 Electrochemical impedance spectroscopy	38
Chapter 3 Results and discussion.....	45
3.1 Discussion of composition of Ba(Zr,Ce,Y)O _{3-δ}	45
3.1.1 XRD patterns and lattice parameter.....	45
3.1.2 Chemical composition	47
3.1.3 Hydration behavior	48
3.1.4 Proton conductivity and other electrochemical properties	48
3.1.5 Instability of the pellets related to Ce content	57
3.2 Solid state reactive sintering	58
3.2.1 Perovskite formation and sintering.....	58
3.2.2 Grain growth kinetics	84
3.2.3 Discussion of sintering mechanism	87
3.2.4 Proton uptake.....	95
3.3 Transport properties of SSRS ceramics	100
3.3.1 Electrochemical impedance spectroscopy	100
3.3.2 Comparison to literature	108
3.3.3 Discussion in terms of space charge.....	111
3.3.4 Long time stability.....	114
3.3.5 Discussion on GB conductivity scattering.....	114
3.3.6 Relation to TEM-EELS results on Ce valence	123
3.4 Transport properties of SSRS tape-cast membranes	125
3.4.1 Sequential tape-casting, choice of anode composition.....	125
3.4.2 Phases and morphology of the membranes	128
3.4.3 Electrochemical properties of the membranes.....	131
3.5 GB-decoration Method, amorphous phosphate at GB	136
Chapter 4 Conclusions	139
References.....	143
Acknowledgements.....	153
Curriculum Vitae	155

Zusammenfassung

Protonenleitende keramische Brennstoffzellen nutzen protonenleitende Oxide als Elektrolyte und wandeln chemische Energie bei mittleren Temperaturen mit hohem Wirkungsgrad in Elektrizität um. Innerhalb der protonenleitenden Keramiken weist Y-dotiertes BaZrO_3 bei 400 – 700 °C die höchste Bulk-Protonenleitfähigkeit auf. Die hohe Temperatur und die lange Haltezeit, die beim konventionellen Sintern erforderlich sind, können jedoch zu großen BaO-Verlusten führen, die die Leistungsfähigkeit beeinträchtigen. Daher müssen geeignete Methoden entwickelt werden, um großflächige Keramikmembranen mit guter Protonenleitfähigkeit und mechanischer Festigkeit herzustellen.

In Y-dotiertem BaZrO_3 kompensieren Sauerstoffleerstellen die negativ geladenen Y'_{Zr} Akzeptoren. Durch Wassereinbau bilden sich für jede Sauerstoffleerstelle zwei protonische Defekte OH_O . Protonen in Y-dotiertem BaZrO_3 haben aufgrund der niedrigen Migrationsbarriere eine hohe Beweglichkeit. Korngrenzen die den Protonentransport stark blockieren (v.a. durch eine Raumladungszone mit einem positiv geladenen Korngrenzen-Kern), mechanische Sprödigkeit, notorisch schlechte Sinterbarkeit und daraus resultierende kleine Korngrößen, hemmen jedoch den Einsatz dieses Materials als Elektrolyt für protonische keramische Brennstoffzellen.

Im ersten Teil der vorliegenden Arbeit wird die Zusammensetzung von $\text{Ba}(\text{Zr,Ce,Y})\text{O}_{3-\delta}$ diskutiert. Mit steigendem Ce-Anteil nimmt die Löslichkeit von Y zu, da Ce das Gittervolumen vergrößert. Die Protonenleitfähigkeit nimmt mit steigendem Y-Gehalt zu. Dies gilt insbesondere für die gemittelte wie auch für die spezifische Korngrenzenleitfähigkeit, da das Raumladungspotential abnimmt. Ce wirkt sich nur geringfügig auf die Leitfähigkeit aus,

verbessert aber die Sinterbarkeit. Die chemische Stabilität gegenüber H_2O und CO_2 bleibt erhalten, solange der Ce-Anteil 20 at.% nicht überschreitet. Höhere Ce-Gehalte und mehr als 24 at.% Y führen zur Zersetzung der Probe und Zerfall in kleine Stücke, was für die praktische Anwendung sehr nachteilig ist. Daher konzentriert sich der Hauptteil dieser Arbeit auf die Zusammensetzung $\text{Ba}_{1,015}\text{Zr}_{0,664}\text{Ce}_{0,20}\text{Y}_{0,136}\text{O}_{3-\delta}$ (BZCY, 1,5 at.% überschüssiges Ba wird zur Kompensation der BaO-Verdampfung während des Sinterns verwendet).

Die vorliegende Arbeit befasst sich mit Festkörper-Reaktivsintern (Solid State Reactive Sintering, SSRS) mit 0,125 – 1,0 Gew.-% NiO als Sinterhilfe zur Verbesserung der Sinterfähigkeit und des Kornwachstums. Festkörper-Reaktivsintern bedeutet, dass die Perowskitbildung und das Sintern in einem Schritt erfolgen. In der Literatur ist nicht wirklich klar, ob beim Festkörper-Reaktivsintern von BaZrO_3 -Keramiken eine flüssige Phase beteiligt ist. In der vorliegenden Arbeit werden mehrere Aspekte des reaktiven Festkörpersinterns untersucht:

(i) Bildung der Perowskit-Phase. Laut XRD beginnt mit NiO-Zugabe die Bildung von Perowskitphasen (undotiertes BaZrO_3 , und ein zweiter Ce,Y-reicher $\text{Ba}(\text{Zr,CeY})\text{O}_{3-\delta}$ Perowskit) bei 1050 – 1100 °C. Mit zunehmender Temperatur verschwindet die undotierte Phase und es existiert nur noch eine BZCY-Perowskit-Phase. Ein höherer NiO-Zusatz senkt die Temperatur, die zum Erreichen der Einphasigkeit erforderlich ist.

(ii) Sinterverhalten. Bei einer NiO-Zugabe von $\leq 0,25$ Gew.-% sind hohe Temperaturen ≥ 1550 °C und lange Haltezeiten notwendig, um die Keramik vollständig zu verdichten, wobei die Korngröße $\sim 1 \mu\text{m}$ nicht übersteigt. Wenn der NiO-Gehalt $\geq 0,375$ Gew.-% beträgt, ermöglicht die transiente $(\text{Ba,Y,Ni})\text{O}_x$ -Flüssigphase ein Kornwachstum parallel zur Verdichtung. Die maximalen Korngrößen bei 0,5 und 1,0 Gew.-% NiO-Gehalt betragen $\sim 4 \mu\text{m}$ bzw. $\sim 6 \mu\text{m}$.

(iii) Kinetik des Kornwachstums. Bei einem NiO-Gehalt über 0,25 Gew.-% folgt das Kornwachstum einem parabolischen Gesetz. Es kann gefolgert werden, dass das Kornwachstum durch das Lösen bzw. Ausfällen an der Fest-Flüssig-Grenzfläche bestimmt wird. Die Aktivierungsenergie des Kornwachstums wird durch NiO-Zugabe erhöht. Dies könnte durch eine Temperaturabhängigkeit der Zr/Ce-Löslichkeit in der transienten Flüssigphase verursacht sein.

(iv) Sintermechanismus. Der Sintermechanismus wurde mit Hilfe von abgeschreckten Proben untersucht. Obwohl die $(\text{Ba,Y,Ni})\text{O}_x$ -Phase nicht direkt durch XRD nachgewiesen werden konnte, deuten mehrere indirekte Hinweise stark darauf hin, dass sie während des Sinterns

transient gebildet wird. Diese flüssige Phase löst Zr^{4+}/Ce^{4+} auf und beschleunigt den Ionentransport, der für die Bildung der Perowskitphase, das Kornwachstum und die Verdichtung erforderlich ist. Bei ausreichender NiO-Zugabe ($\geq 0,375$ Gew.-%) erreichen die Körner eine hexagonale Form, wie durch die Wulff-Konstruktion vorhergesagt.

(v) Nachteilige Auswirkungen auf die Protonenaufnahme. Die maximale Protonenaufnahme (durch Thermogravimetrie bestimmt) nimmt mit dem NiO-Gehalt ab, insbesondere bei Erhöhung von 0,5 auf 1,0 Gew.-%. Die effektive Konzentration der Akzeptordotierung nimmt mit NiO-Zusatz näherungsweise linear ab, während die Standard-Enthalpie und -Entropie der Hydratation nicht beeinflusst werden. Der Vergleich mit TG-Daten von Proben mit Ni auf dem B-Platz, sowie das Verhalten der Gitterkonstanten und die TEM-EDX-Ergebnissen zeigen, dass sich Ba und Ni an den Korngrenzen anreichern. Daraus lässt sich schließen, dass Ba durch Ni aus dem Perowskitgitter extrahiert wird, um die transiente $(Ba,Y,Ni)O_x$ -Flüssigphase zu bilden. Die Bildung von niedrigschmelzendem $BaNiO_2$ (belegt durch TEM-EDX) und/oder BaY_2NiO_5 (unterstützt durch die Beobachtung einer geringen Verdichtung ohne Akzeptordotierung trotz NiO-Zugabe) führt somit zu einer verminderten Protonenaufnahme.

(vi) Elektrochemische Eigenschaften. Die elektrochemischen Eigenschaften wurden mittels Impedanzspektroskopie untersucht. Bei niedriger Temperatur können Volumen- und Korngrenz-Halbkreise unterschieden werden. Die Volumenleitfähigkeit nimmt systematisch mit NiO-Zugabe ab, was durch verminderte Protonenaufnahme und verminderte Protonenbeweglichkeit verursacht wird. Die gemittelte Korngrenzenleitfähigkeit nimmt mit NiO-Zugabe signifikant zu, hauptsächlich durch die stark erhöhte Korngröße. Die spezifische Korngrenzenleitfähigkeit ist leicht erhöht. Mögliche Gründe für die große Streuung der gemittelten Korngrenzenleitfähigkeit wurden untersucht, die Ursache konnte aber nicht vollständig aufgeklärt werden. Sie könnte mit der Komplexität des transienten Flüssigphasensinterprozesses zusammenhängen.

(vii) Bestimmung des optimalen NiO-Gehalts. 0,5 Gew.-% NiO wird als guter Kompromiss zwischen verbesserter Sinterbarkeit und Kornwachstum (das die gemittelte Korngrenzenleitfähigkeit erhöht) und verringerter Protonenaufnahme (die die Volumenleitfähigkeit verringert) identifiziert. Bei 600 °C erreicht die Protonenleitfähigkeit in feuchter Atmosphäre $1 \times 10^{-3} \text{ Scm}^{-1}$.

(viii) Foliengießen von großflächigen anodengestützten Membranen. Die Membranen wurden durch sequenzielles Foliengießen am IEK-1 des Forschungszentrums Jülich hergestellt. Zuerst

wird der Elektrolyt ($\text{Ba}_{1,015}\text{Zr}_{0,625}\text{Ce}_{0,20}\text{Y}_{0,175}\text{O}_{3-\delta}$ mit 0,5 Gew.-% NiO-Zusatz) gegossen, gefolgt von der Anodenschicht (einem Verbund aus dem Elektrolytmaterial plus 60 Gew.-% NiO). Nach dem Trocknen werden die Folien bei ähnlichen Temperaturen wie die keramische Pellets gesintert. Nach der Reduktion von NiO zu Ni wurde die Leitfähigkeit mittels Impedanzspektroskopie (mit Pseudo-Vierpunkt-Kontaktierung) gemessen. Einige Proben wiesen Kurzschlüsse auf, die durch kleine Löcher oder Risse in der Membran entstehen können. Die Volumenleitfähigkeit ist vergleichbar mit keramischen Pellet-Proben, während die gemittelte Korngrenzenleitfähigkeit fast eine Größenordnung niedriger ist. Nichtsdestotrotz nähert sich die Gesamtleitfähigkeit bei 600 °C dem Volumenwert an und ist mit der von keramischen Pellets vergleichbar. Die Leitfähigkeit der Membran liegt im Vergleich zu Literaturdaten keramischer Proben im oberen Drittel. Während eine weitere Verbesserung des Sinterprozesses erforderlich ist, reicht die Leitfähigkeit der Membran für den Einsatz in großflächigen protonischen keramischen Brennstoffzellen aus.

Abstract

Protonic ceramic fuel cells use proton conducting oxides as electrolytes and convert chemical energy to electricity at intermediate temperature with high efficiencies. Y-doped BaZrO₃ shows highest bulk proton conductivity in proton conducting ceramics at 400 – 700 °C, but the high temperature and long soaking time required for conventional sintering induces large BaO loss, which compromises its performance. Therefore, appropriate methods need to be developed to fabricate large-area ceramic membranes with good proton conductivity and mechanical strength.

In Y-doped BaZrO₃, oxygen vacancies compensate the negatively charged Y'_{Zr} acceptors. When water is incorporated, two protonic defects OH_O are formed for each oxygen vacancy. Protons in Y-doped BaZrO₃ have a high mobility due to the low migration barrier. However, the presence of highly proton blocking grain boundaries (GBs) (mainly from the space charge zone with a positively charged GB core), mechanical brittleness, notoriously bad sinteribility and resulting small grain sizes severely inhibit the practical utilization of this material as electrolytes for protonic ceramic fuel cells.

The first part of the present thesis discusses the composition of Ba(Zr,Ce,Y)O_{3-δ}. With increasing Ce content, the solubility of Y increases because Ce enlarges the lattice volume. The proton conductivity increases with Y content, especially the apparent as well as specific GB conductivity, due to the decreased space charge potential. Ce has only a mild impact on the conductivity but improves the sinteribility while keeping chemical stability versus H₂O and CO₂ as long as the Ce content remains ≤ 20 at.%. Higher Ce content and more than 24 at.% Y lead to sample decomposition and disintegration into small pieces, which is very detrimental

for practical use. Therefore, the main part of this work focuses on the composition of $\text{Ba}_{1.015}\text{Zr}_{0.664}\text{Ce}_{0.20}\text{Y}_{0.136}\text{O}_{3-\delta}$ (BZCY, 1.5 at.% excess Ba is used to compensate BaO evaporation during sintering).

The present thesis uses solid state reactive sintering (SSRS) with 0.125 – 1.0 wt.% NiO as sintering aid to improve sinterability and grain growth. SSRS means that the perovskite formation and sintering are achieved in the same step. From literature, it is not really clear if a liquid phase is involved in SSRS of BaZrO_3 ceramics. Several aspects of SSRS were investigated in this thesis:

(i) Perovskite phase formation. According to XRD, the formation of perovskite phases (\approx undoped BaZrO_3 and a second Ce, Y-rich $\text{Ba}(\text{Zr,CeY})\text{O}_{3-\delta}$ perovskite) starts at 1050 – 1100 °C with NiO addition. With increasing temperature, the undoped phase vanishes and only one BZCY perovskite phase exists. Higher NiO addition lowers the temperature needed to reach phase homogeneity.

(ii) Sintering behavior. For NiO addition ≤ 0.25 wt.%, a high temperature above 1550 °C and a long soaking time are necessary to fully densify the ceramic, but the grain size remains small ($\sim 1 \mu\text{m}$). For NiO ≥ 0.375 wt.%, the transient $(\text{Ba,Y,Ni})\text{O}_x$ liquid phase suffices for grain growth in parallel with densification. The maximum grain sizes for 0.5 and 1.0 wt.% NiO addition are $\sim 4 \mu\text{m}$ and $\sim 6 \mu\text{m}$, respectively.

(iii) Grain growth kinetics. For NiO > 0.25 wt.% the grain size follows a parabolic law, indicating the grain growth to be limited by the solution/precipitation at the solid/liquid interface. The activation energy of grain growth is increased with NiO addition. This might be caused by the temperature dependence of the solubility of Zr/Ce in the transient liquid phase.

(iv) Sintering mechanism. The sintering mechanism is investigated with the help of quenching experiments. Albeit the $(\text{Ba,Y,Ni})\text{O}_x$ phase was not directly detected by XRD, several indirect evidences strongly indicate that it is transiently formed during sintering. This liquid phase dissolves $\text{Zr}^{4+}/\text{Ce}^{4+}$ and accelerates the ion transport, which is required for perovskite phase formation, grain growth and densification. With sufficient NiO addition (≥ 0.375 wt.%), the final shape of the grains is hexagonal as predicted by the Wulff construction.

(v) Detrimental effects on proton uptake. The maximum proton uptake (measured by thermogravimetry) decreases with NiO content, particularly when the NiO addition increases from 0.5 to 1.0 wt.%. The effective acceptor dopant concentration decreases with NiO addition approximately linearly, while the standard enthalpy and entropy of hydration are not affected.

Comparisons of TG data from samples with substitutional Ni on the B site, lattice parameters, and TEM-EDX results indicate that Ba and Ni accumulate at the GBs. One can conclude that Ba is extracted by Ni from the perovskite lattice to form the transient (Ba,Y,Ni)O_x liquid phase. Formation of low-melting BaNiO₂ (supported by TEM-EDX) and/or BaY₂NiO₅ (supported by the observation of low densification without acceptor dopant even with NiO addition) thus lead to decreased proton uptake.

(vi) Electrochemical properties. The electrochemical properties were examined by impedance spectroscopy. At low temperature, bulk and GB semicircles can be distinguished. The bulk conductivity decreases systematically with NiO addition, which is caused by decreased proton uptake and decreased proton mobility. The apparent GB conductivity increases significantly with NiO addition, mainly from the largely improved grain growth. The specific GB conductivity is increased slightly. Reasons of the large scatter of apparent GB conductivity were investigated, but could not fully be resolved. It could be related to the complexity of the transient liquid phase sintering process.

(vii) Discussion of optimum NiO content. 0.5 wt.% NiO is identified as a good compromise between improved sinterability and grain growth which increases apparent GB conductivity, and decreased proton uptake which lowers the bulk conductivity. At 600 °C, the proton conductivity in humid atmosphere reaches $1 \times 10^{-3} \text{ Scm}^{-1}$.

(viii) Tape-casting of anode-supported large-area membranes. The membranes were prepared by sequential tape-casting by IEK-1 at the Research Center Jülich. The electrolyte (Ba_{1.015}Zr_{0.625}Ce_{0.20}Y_{0.175}O_{3-δ} with 0.5 wt.% NiO addition) is tape-cast first, followed by the anode layer (a composite of the electrolyte material plus 60 wt.% NiO). After drying, the tapes are sintered at similar temperatures as the ceramic pellets. After reduction of NiO to Ni, the conductivity was measured by impedance spectroscopy using pseudo-four-point contacts. Some samples exhibited short circuits which may arise from pinholes or cracks in the membrane. The bulk conductivity is comparable with pellet samples, while the apparent GB conductivity is almost one order of magnitude lower. Nevertheless, the total conductivity at 600 °C approaches the bulk value and is comparable to that of the pellet. This conductivity of the membrane lies in the upper third range compared to literature data on ceramic samples. While a further improvement of sintering protocol is needed, the membrane conductivity is in the range suitable for large-area protonic ceramic fuel cells.

Abbreviations and symbols

Abbreviations

AC	Alternating current
ADF	Annular dark-field
BET	Brunauer-Emmett-Teller
BF	Bright-field
BZCY	Ba(Zr,Ce,Y)O _{3-δ}
CS	Conventional sintering
DC	Direct current
EDX	Energy dispersive x-ray spectroscopy
EELS	Electron energy-loss spectroscopy
EIS	Electrochemical impedance spectroscopy
FIB	Focused ion beam
GBs	Grain boundaries
HAADF	High-angle annular dark-field
ICP-OES	Inductively coupled plasma-optical emission spectrometry
PCFC	Protonic conducting fuel cell
PLD	Pulsed laser deposition
SEM	Scanning electron microscopy
SOFC	Solid oxide fuel cell

SPS	Spark plasma sintering
SSRS	Solid state reactive sintering
TEM	Transmission electron microscopy
TG	Thermogravimetry
W-H	Williamson-Hall
XRD	X-ray diffraction

Symbols

C	Capacitance
C_b	Bulk capacitance
C_{GB}	GB capacitance
d_G	Grain size
δ_{GB}	Grain boundary thickness
ϵ_0	Dielectric constant of vacuum
ϵ_b	Bulk relative dielectric constant
ϵ_{GB}^{app}	Apparent GB relative dielectric constant
ϵ_{GB}^{spec}	Specific GB relative dielectric constant
$E_{a,b}$	Bulk activation energy
$E_{a,GB}$	GB activation energy
Φ_0	Space charge potential
λ	Debye length
λ^*	Space charge zone thickness
n	Depression parameter
Q	CPE value
R	Resistance
R_b	Bulk resistance
R_{GB}	GB resistance
R_{Total}	Total resistance of bulk and GB
σ	Conductivity
σ_b	Bulk proton conductivity

$\sigma_{\text{GB}}^{\text{app}}$	Apparent GB proton conductivity
$\sigma_{\text{GB}}^{\text{spec}}$	Specific GB proton conductivity
σ_{Total}	Total proton conductivity

Chapter 1 Introduction

1.1 Protonic ceramic fuel and electrolysis cells

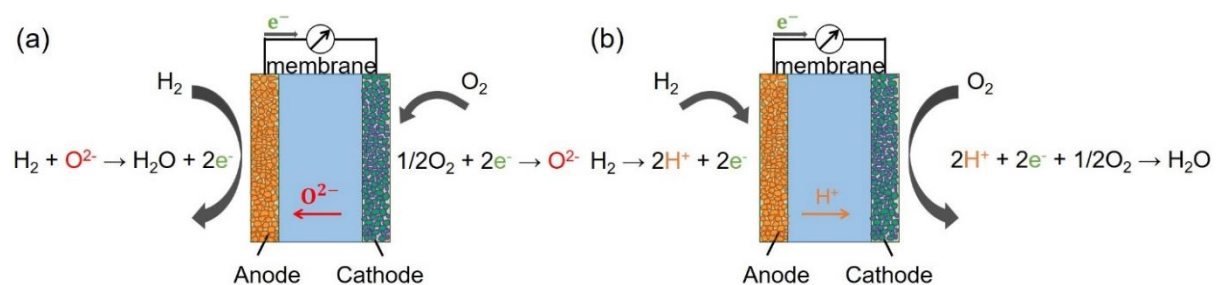


Figure 1: Schematic diagrams of (a) conventional SOFC and (b) PCFC.

Solid oxide fuel cells (SOFCs) convert chemical energy to electricity at high temperature (800 – 1000 °C) without polluting the environment ^[1]. The high efficiency without limitation by Carnot's efficiency ^[2–5], and the fuel flexibility ^[2,6–9] are key advantages of conventional SOFCs based on oxide ion conducting electrolytes. They have already been commercialized ^[10–13]. As shown in **Figure 1-(a)**, oxygen is reduced to O^{2-} at the cathode side, migrates through the oxygen ion-conducting electrolyte (for example Y-doped ZrO_2) and reacts with hydrogen at the anode side forming H_2O . Due to the high migration barrier of oxide ions (typically 0.7 – 1 eV), elevated operating temperatures are required for sufficient ion conductivity in the electrolyte ($\sim 10^{-3} - 10^{-2} \text{ Scm}^{-1}$). This may lead to long time material degradation. Water formed

at the anode side of SOFCs dilutes the fuel, decreasing the Nernst voltage, and making high fuel utilization difficult.

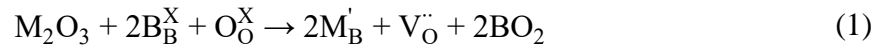
Protonic ceramic fuel cells (PCFCs) use proton conducting oxides as electrolyte, in which protons have a lower migration barrier than oxygen ions in SOFCs [14,15]. This allows for a lower operating temperature (400 – 600 °C). H. Iwahara first reported applications of perovskite proton conductors in fuel and electrolysis cells in the 1980s [16,17]. In a typical PCFC, protons generated from oxidation of hydrogen at the anode side are transported through the proton conducting electrolyte. They react with oxygen to form water at the cathode side (**Figure 1-(b)**), which avoids the problem of fuel dilution. The fuel choice for PCFCs is pure H₂ [18]. However, there are several efforts to extend the fuel possibilities. W. G. Coors [19] reported a PCFC using methane as fuel which is internally reformed at the anode with steam. Apart from CH₄ [20], other fuels such as C₂H₆ [21], NH₃ [18], and CH₃OH [18] etc. were also investigated.

Oxides with various structures exhibit proton conduction, including ABO₃ simple perovskites [16,22–29], A₂BB'O_{6-δ}/A₃BB₂'O_{9-δ} layered perovskites [30–35], A₂B₂O₅ brownmillerites [36–41], APO₄ ortho-phosphates [42–44], ANbO₄ ortho-niobates [45], and ATaO₄ ortho-tantalates [45]. Among them, acceptor doped perovskite ACeO₃ (A = Ba, Sr) [16,22,25] and AZrO₃ (A = Ba, Sr, Ca) [23–25] have been considered the most promising candidate for PCFC electrolytes.

Apart from use as electrolytes in high performance PCFCs [18,20,21,46–51], proton conducting ceramics are also utilized in protonic ceramic electrolysis cells (PCECs) [52,53]. PCECs efficiently convert electricity to chemical energy at same operation temperature as PCFCs, and directly produce dry H₂. They were also suggest by H. Iwahara *et al.* [16] in 1981. In recent years, reversible protonic ceramic electrochemical cells (RePCECs) are of interest for energy conversion and storage, e.g. from fluctuating renewable solar or wind power. A RePCEC generates hydrogen and/or hydrocarbon fuels when excess electricity is available, and works in fuel cell mode on the same device. In 2019, S. Choi *et al.* [54] and C. Duan *et al.* [55] reported RePCECs using Ba(Zr,Ce,Y,Yb)O_{3-δ} as electrolyte operating with high Faraday efficiency. S. H. Morejudo *et al.* [56] fabricated protonic ceramic electrochemical reactors (PCERs) for methane dehydroaromatization. For more details about recent progress on proton conductor research and applications, please refer to ref. [57].

1.2 Protonic defect formation and transport

For $A^{2+}B^{4+}O_3$ perovskites, acceptor dopants M^{3+} substituting on the B site introduce electrically negative M'_B defects, which are charge compensated by positively charged oxygen vacancies $V_{\text{O}}^{\cdot\cdot}$ according to



expressed in Kröger-Vink notation^[58]. In Kröger-Vink notation, taking $V_{\text{O}}^{\cdot\cdot}$ as an example, the subscript O indicates that the defect is on the oxygen site. The superscript gives the charge relative to the perfect lattice, here $\cdot\cdot$ for a doubly positively charged oxygen vacancy. If the defect is negatively charged, this is notified by a prime as in the case of M'_B .

Water can incorporate into the lattice by dissociating into a proton (H^+) and a hydroxide ion (OH^-). As shown in **Figure 2**, the proton binds to one lattice oxygen ion, and the hydroxide occupies an oxygen vacancy. Therefore, two protonic defects OH_{O}^{\cdot} (hydroxide ions on oxide ion sites) are formed as described in **Eq. (2)**.

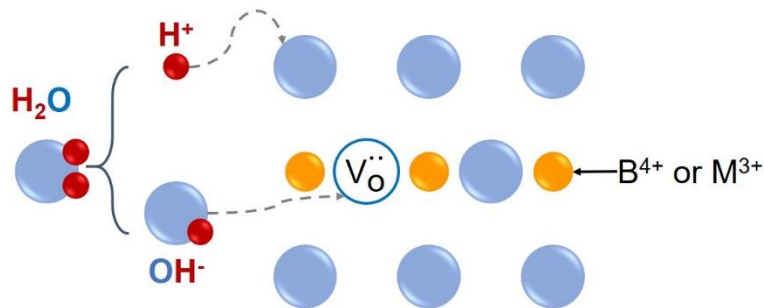
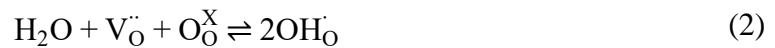


Figure 2: Formation of protonic defects from dissociative water incorporation into $A^{2+}B^{4+}O_3$ perovskites.



The reaction is described by the mass action constant of the hydration reaction K_{hydrat} (**Eq. (3)**) under the assumption that all the defects are dilute so that their activity coefficients are unity.

$$K_{\text{hydrat}} = \frac{[OH_{\text{O}}^{\cdot}]^2}{p_{H_2O}[V_{\text{O}}^{\cdot\cdot}][O_{\text{O}}^X]} \quad (3)$$

Both standard hydration enthalpy (ΔH°) and entropy (ΔS°) are negative. At sufficiently low temperature, the negative enthalpy dominates over $-\Delta S^\circ T$, and $\Delta G^\circ = \Delta H^\circ - \Delta S^\circ T$ is in favor of

proton formation ($K_{\text{hydrat}} \geq 0$). With increasing temperature, K_{hydrat} and the degree of hydration decrease. The thermogravimetric analysis of acceptor-doped $A^{2+}B^{4+}O_3$ perovskites shows that full hydration ($\geq 90\%$) is achieved for Y-doped $BaZrO_3$ and $BaCeO_3$ at temperature below 450°C due to the high basicity of the oxide ions in these two materials, whereas it is difficult to reach for other perovskites such as $SrTiO_3$ even at lower temperature ^[59,60].

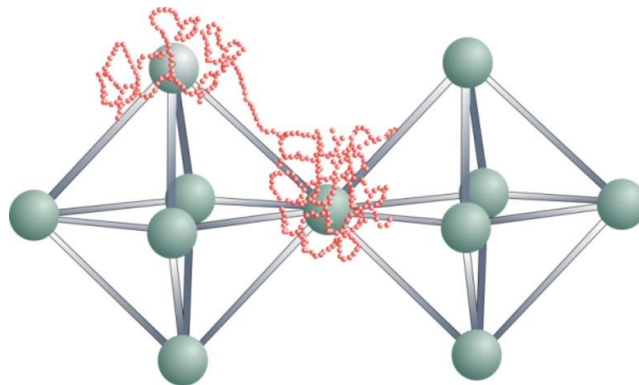


Figure 3: Proton transport in $BaCeO_3$ (blue spheres = oxide ions, red trace = trajectory of one proton). The rotational motion and proton transfer to the neighboring O is obtained by quantum-molecular dynamics simulation ^[61].

In perovskite oxides, protons shows rotational motion around the oxygen ion to which they are bound. This rotation has low activation barriers. In addition to the short covalent O-H bond, the proton interacts with a neighboring O by a longer and weaker hydrogen bond. In the equilibrium geometry, the two O are too far apart for fast proton transfer. This is facilitated by lattice vibrations which bring the two O's closer together. Elongation of the covalent bond and contraction of the hydrogen bond eventually lead to the proton hopping to the neighboring oxygen ^[60,62,63]. The migration barrier is typically $0.4 - 0.5$ eV compared to $0.8 - 1$ eV of oxygen vacancies in perovskites ^[64]. The proton mobility depends on the type of chosen dopant, dopant concentration, and symmetry of the perovskite ^[60].

1.3 Blocking grain boundaries and space charge model

In acceptor-doped $Ba(Zr,Ce)O_3$ GBs are blocking for proton, oxygen vacancy, and hole transport, especially with low dopant content, which jeopardizes the total proton conductivity

even though it has high bulk proton conductivity [60,65–68]. There is no obvious correlation between grain orientation (usually randomly distributed) and the GB conductivity [66,69]. According to the DFT calculations by B. J. Nyman *et al.* [70] and E. E. Helgee *et al.* [71], oxygen vacancies and protons have a strong tendency to segregate to the structurally distorted GB core and form a positive GB core charge. Due to the electrostatic repulsion, oxygen vacancies and protons are strongly depleted in the space charge zone adjacent to the GB core, which results in a decreased GB conductivity. The electrically blocking GB region (several nm) is wider than the visibly distorted GB core (≈ 0.5 nm), especially when the acceptor dopant concentration is low [72,73].

Space charge zones as the origin of decreased GB conductivity in oxides have been confirmed by electrochemical measurements in several oxides with large band gap, e.g. pure and acceptor doped ceria [74–77], zirconia [77–79], titanates [80–83]. For Y-doped BaZrO₃, the existence of the space charge zone with a positive GB core charge is evidenced by several experiments:

- (i) DC-bias dependence of GB impedance spectra. When a sufficiently large DC voltage is applied (either a large bias is applied on a sample with several GBs [84], or using microelectrodes to directly apply the bias on individual GB [85] such that it is comparable to the space charge potential), the GB semicircle decreases significantly together with a moderate decrease of GB capacitance, while the bulk semicircle does not change.
- (ii) Under reducing conditions, the bulk conductivity does not differ from that in high oxygen partial pressure and remains purely ionic, but the GB conductivity shows a slight increase originating from n-type conductivity caused by electron accumulation adjacent to the positive GB core [73,86].
- (iii) Y³⁺ or Sc³⁺ accumulation at GBs is observed by TEM-EDX when the samples are annealed or sintered at sufficiently high temperature which allows the acceptor dopants to diffuse to the space charge zone to compensate the positive core charge [69,73,87–89].

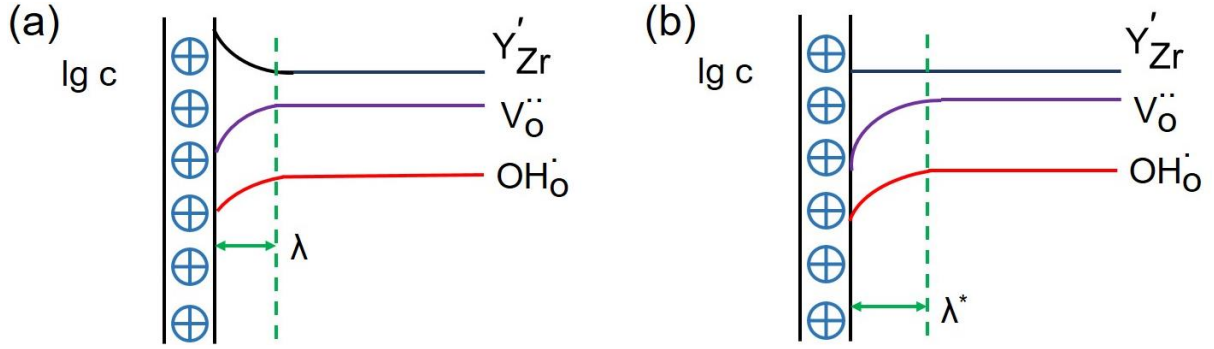


Figure 4: Space charge models based on (a) Gouy-Chapman and (b) Mott-Schottky cases.

The electrical potential and the charge distribution in the space charge zone are coupled by the Poisson-Boltzmann equation

$$\frac{\partial^2 \Phi(x)}{\partial x^2} = -\frac{F}{\epsilon_b \epsilon_0} \sum_j c_{j,b} \exp\left(-\frac{ez_j \Phi(x)}{kT}\right) \quad (4)$$

where ϵ_b and ϵ_0 are the bulk relative dielectric constant and the dielectric constant of vacuum, respectively. e is the elementary charge. k is the Boltzmann constant and F is the Faraday constant.

Regarding the distribution of dopants two limiting cases are distinguished:

(i) In the Gouy-Chapman case (**Figure 4-(a)**), the dopant cations are mobile and accumulate in the GB region to partially compensate the positive core charge. The dopant cations have an equilibrium concentration profile

$$\frac{c_d(x)}{c_{d,b}} = \exp\left(\frac{-z_d e \Phi(x)}{kT}\right) \quad (5)$$

where $c_d(x)$ and $c_{d,b}$ are dopant concentration at position x ($x = 0$ at the GB core) and in the bulk ($x = \infty$). z_d is the charge of the dopant (1 for Y in $\text{Ba}(\text{Zr,Ce})\text{O}_3$). T is the temperature at which the acceptor is mobile.

The width of the space charge zone in the Gouy-Chapman case is the Debye length

$$\lambda = \sqrt{\frac{\epsilon_b \epsilon_0 kT}{2z_d^2 e^2 c_{d,b}}} \quad (6)$$

According to **Eq. (6)**, a higher dopant concentration results in a smaller Debye length.

(ii) In the Mott-Schottky case (**Figure 4-(b)**), the dopant cations are assumed immobile (frozen-in) and the dopant concentration is constant through the whole sample ($c_d(x) = c_{d,b}$). The space charge zone thickness is

$$\lambda^* = \sqrt{\frac{2\varepsilon_b \varepsilon_0 \Phi_0}{ez_d c_{d,b}}} = \lambda \sqrt{\frac{4e\Phi_0}{kT}} \quad (7)$$

which is wider than the Debye length. The mobile defect concentration in the space charge zone and the core charge density Q are calculated as ^[90,91]

$$c_{j,GB}(x) = c_{j,b} \exp\left(-\frac{ez_j \Phi(x)}{kT}\right) \quad (8)$$

$$\Phi(x) = \Phi_0 \left(\frac{x}{\lambda^*} - 1\right)^2 \text{ for } x \leq \lambda^* \quad (9)$$

$$Q = \sqrt{8\varepsilon_b \varepsilon_0 e c_{d,b} \Phi_0} \quad (10)$$

where $c_{j,GB}$ and $c_{j,b}$ are concentrations of defect j at GB and in bulk, respectively. z_j is the charge of the mobile carrier and $z_j = 1$ when j is proton.

The space charge potential $\Phi_0 = \Phi(x = 0)$ is related to the peak frequency ratio of bulk and GB semicircles in impedance spectra (ω_b/ω_{GB}) according to

$$\frac{\omega_b}{\omega_{GB}} = \frac{R_{GB} C_{GB}}{R_b C_b} = \frac{\exp(z_d e \Phi_0 / kT)}{2z_d e \Phi_0 / kT} \quad (11)$$

In both scenarios, oxygen vacancies, protons, and electron holes are depleted compared to bulk. However, for identical dopant concentration and GB core charge density, the Gouy-Chapman model yields lower space charge potential and thus less severe proton depletion compared to the Mott-Schottky case. For both cases, the drastic decrease of proton concentration leads to the decreased specific GB conductivity. The proton mobility in the GB core and space charge zone is assumed – in first approximation – to have the bulk value.

1.4 Possible improvements for proton conductivity of BaZrO₃ ceramics

BaZrO₃ ceramics are difficult to sinter and have a high density of blocking GBs, limiting its utilization as electrolyte material for PCFCs. Several attempts have been undertaken in the recent years to decrease the total GB resistance by either improving the specific GB conductivity, and/or reducing the number of blocking GBs through increase of the grain size.

1.4.1 Improving the specific GB conductivity

M. Shirpour *et al.* [87] annealed 6 at.% Y doped BaZrO₃ prepared by SPS at elevated temperature. The high temperature transforms the space charge situation from Mott-Schottky towards Gouy-Chapman by allowing the Y dopants to accumulate in the GB region and partially compensate the positive core charge. In the present work (section 3.3.3), it will be shown that using a B-site ion such as Ce which has multiple valence states can decrease the core charge and partially change the space charge zone from a Mott-Schottky to a Gouy-Chapman situation as Ce is partially reduced from +4 to +3 in the GB region becoming an additional acceptor dopant.

1.4.2 Improving the sintering process

Conventional Sintering Conventional sintering (CS) of Y-doped BaZrO₃ requires extremely high temperature (≥ 1600 °C) and long soaking time (≥ 20 h) [59,65,66,69,89,92,93]. Nevertheless, this extreme condition only leads to a small grain size of $0.5 - 1 \mu\text{m}$ [66,69,89,92], which deteriorates the apparent GB conductivity due to the high density of GBs. Besides, because BaO has a high vapor pressure, BaO loss is significant at the required CS temperatures even when the samples are covered with sacrificial powder. This A-site cation non-stoichiometry lowers the conductivity of Y-doped BaZrO₃, more pronounced for GB than bulk conductivity [66,94,95]. Using a nominal excess of Ba can potentially prevent this issue but results in lower chemical stability [92,96]. Apparently, CS is not suitable for large-area electrolyte membrane fabrication with a large ratio of surface to bulk. In 2005 and 2006, P. Babilo *et al.* [97] and S. Tao *et al.* [98] reported by using ZnO as sintering aid the sintering temperature can be significantly decreased, together with larger grain size. However, the total proton conductivity was not improved.

Spark plasma sintering Spark plasma sintering (SPS) [99] is a sintering technique using uniaxial hot-pressing in a graphite die which is directly heated by passing a DC current. For materials with low electronic conductivity such as BZCY, the fraction of current passing through the sample is minor. The applied pressure are in the range of 50 MPa. SPS provides the possibility of a lower sintering temperature (1500 – 1600 °C) and a much shorter soaking time (~ 5 min), reducing Ba loss during sintering [100,101]. However, post-annealing treatment is necessary to eliminate the inner strain generated during SPS sintering. The high temperature annealing treatment does not promote grain growth, but increases the specific GB conductivity

by allowing mobile Y ions to move and accumulate at GBs [87]. This method is used in the present thesis to investigate BZCY composition, but it is not practical for membrane fabrication.

Solid state reactive sintering Solid state reactive sintering (SSRS) combines perovskite phase formation, ceramic densification, and grain growth in one single step at 1400 – 1500 °C. Interestingly, this approach is able to decrease the sintering temperature while increasing the grain growth. S. Nikodemski *et al.* [102] investigated various transition metal oxides for SSRS. SSRS has been proven very effective by using transition-metal oxide sintering aids such as NiO [18,49,50,100,102–110], ZnO [97,102,106,111], CoO [102,105], and CuO [50,102,106,111]. The sintering aid is either added deliberately in the electrolyte or diffuses from the anode BZCY/NiO mixture [49,103,106]. It is hypothesized that the formation of a low melting compound of $\text{BaY}_2\text{M}^{2+}\text{O}_5$ is the key of SSRS. For example, BaY_2NiO_5 starts to form at a temperature above 700 °C [112] with a low melting point of 1450 – 1500 °C [107]. This enables liquid phase sintering at a temperature much lower than CS. The ion transport is largely promoted in the liquid phase and leads to improved densification and grain growth. It was observed that residues of the BaY_2NiO_5 phase are preferentially located at GBs. BaY_2NiO_5 decomposes at later stage of SSRS at temperature higher than 1200 °C. The Ni either enters into the B-site in the perovskite lattice [107], or the compound decomposes into Y_2O_3 , BaO (gas) and NiO [113].

Although SSRS promotes densification and grain growth, shortens fuel cell fabrication, and decreases costs [50], it faces some challenges. They include: (i) possible crack formation and short-circuits under reducing conditions particularly for high sintering aid addition; (ii) degraded electrical conductivity [104,106,114]; (iii) increased electronic (hole) conductivity [106]; (iv) decreased proton conductivity [105,106]; and (v) strongly increased gas evolution and volume shrinkage owing to the direct use of BaCO_3 in the sintering step which may be detrimental in particular for large-area membranes. There have been attempts to alleviate the problems [104,114,115]. Nevertheless, the details of the sintering mechanism remain to be elucidated, as well as the balance between improved sinteribility and decreased proton conductivity.

1.5 Approaches taken in the present thesis

BaZrO_3 shows the highest proton conductivity among various oxides and is chemically stable against H_2O and CO_2 [60,116]. However, its poor sinteribility, mechanical brittleness and blocking GBs largely hamper its utilization in PCFCs [65,68,116]. BaCeO_3 has a rather high proton

conductivity, less blocking GBs and better sinterability than BaZrO₃ but decomposes into CeO₂ and BaCO₃ or Ba(OH)₂ under CO₂ or H₂O due to the high basicity of O ions [60,68,117,118]. Therefore, in the present thesis, a solid solution of BaZrO₃-BaCeO₃ is used. With the help of SPS, the chemical composition of BZCY is explored in section 3.1.

Y³⁺ is chosen as the dopant because protons in BaZrO₃ show highest mobility for this dopant. Even though the ion radius of Y³⁺ (0.9 Å) is much larger than Zr⁴⁺ (0.72 Å), it does not change the basicity of O ions, and the crystal structure remains cubic [59]. Up to 20 at.%, with increasing Y content in BaZrO₃, the bulk conductivity increases due to higher proton concentration (cf. **Eq. (1)** and **Eq. (2)**). Y³⁺ more than 20 at.% will result in Y³⁺ partial occupation on the A site as a donor dopant (Y_{Ba}[']) decreasing proton uptake, and lattice distortion reducing proton mobility. The GBs become less blocking (the GB activation energy and the Debye length decrease) with increasing Y content.

For SSRS, NiO is chosen as the sintering aid because it is present on the anode side anyway. 1.0 wt.% NiO corresponds to 3 – 6 vol.% liquid phase when NiO is fully converted to BaNiO₂ and/or BaY₂NiO₅. As a result, NiO addition ≥ 0.4 wt.% can improve the sinterability and grain growth at temperature of 1450 – 1600 °C. The large grain size results in significantly enhanced apparent GB conductivity, while the specific GB conductivity increases slightly with NiO addition. However, NiO is detrimental for proton uptake because it leads to a decreased effective dopant concentration. The bulk conductivity therefore decreases. 0.5 wt.% NiO is recommended for large-area membrane fabrication. In order to reduce the large volume shrinkage during SSRS, pre-calcined powders were used for membrane sintering. The resulting membranes show comparable bulk conductivity and about 1 order of magnitude lower apparent GB conductivity than pellet samples. Although further sintering protocol improvement is recommended, the obtained conductivity at 600 °C ($\geq 2 \times 10^{-3}$ Scm⁻¹) suffices for applications such as PCFC.

Chapter 2 Experimental

2.1 Sample preparation

2.1.1 Abbreviation for BZCY sample composition

Table 1: Abbreviations of samples in this thesis

Category	Nominal Composition	Abbreviation
Single phase powders	$\text{Ba}_{1.015}\text{Zr}_{1-x-y}\text{Ce}_x\text{Y}_y\text{O}_{3-\delta}$	BZC100xY100y
	$\text{BaZr}_{1-x-y}\text{Ce}_x\text{Y}_y\text{O}_{3-\delta}$	B100ZC100xY100y
	$\text{Ba}_{1.03}\text{Zr}_{1-x-y}\text{Ce}_x\text{Y}_y\text{O}_{3-\delta}$	Ba103ZC100xY100y
Pellets from SPS	$\text{Ba}_{1.015}\text{Zr}_{1-x-y}\text{Ce}_x\text{Y}_y\text{O}_{3-\delta}$	BZC100xY100y-SPS
	$\text{BaZr}_{1-x-y}\text{Ce}_x\text{Y}_y\text{O}_{3-\delta}$	B100ZC100xY100y-SPS
	$\text{Ba}_{1.03}\text{Zr}_{1-x-y}\text{Ce}_x\text{Y}_y\text{O}_{3-\delta}$	B103ZC100xY100y-SPS
GB-decorated ceramics	$\text{Ba}_{1.015}\text{Zr}_{0.664}\text{Ce}_{0.20}\text{Y}_{0.136}\text{O}_{3-\delta} + z \text{ at.}\% \text{ K/Rb}$	BZC20Y13.6-zK/Rb
Phosphate-decorated ceramics	LaP_3O_9	LPO
	$\text{Ba}_3\text{La}(\text{PO}_4)_3$	BLPO
	$\text{Zn}_3(\text{PO}_4)_2$	ZPO
	$\text{La}_{5.5}\text{WO}_\alpha$	LWO

	$\text{Ba}_{1.015}\text{Zr}_{0.664}\text{Ce}_{0.20}\text{Y}_{0.136}\text{O}_{3-\delta}$ + 1 at.% LPO/BLPO/ZPO/LWO	BZC20Y13.6- LPO/BLPO/ZPO/LWO
“full” SSRS	$\text{Ba}_{1.015}\text{Zr}_{0.8-y}\text{Ce}_{0.20}\text{Y}_y\text{O}_{3-\delta}$ + n wt.% NiO	BZC20Y100 $y-n$ Ni
SSRS with pre-calcined powder	$\text{Ba}_{1.015}\text{Zr}_{0.8-y}\text{Ce}_{0.20}\text{Y}_y\text{O}_{3-\delta}$ + n wt.% NiO	pre-BZC20Y100 $y-n$ Ni
Ni on the B site by SPS	$\text{Ba}_{1.015}\text{Zr}_{0.8-y}\text{Ce}_{0.20}\text{Y}_y\text{Ni}_\beta\text{O}_{3-\delta}$	BZC20Y100 y Ni100 β -SPS
Ni on the B site by conventional sintering	$\text{Ba}_{1.015}\text{Zr}_{0.8-y}\text{Ce}_{0.20}\text{Y}_y\text{Ni}_\beta\text{O}_{3-\delta}$	BZC20Y100 y Ni100 β -CS

2.1.2 Powder preparation by solid state reaction

Ba(Zr,Ce,Y)O_{3-δ} (BZCY) single phase powders were prepared by solid state reaction. BaCO₃ (Alfa Aesar, 99.8%), CeO₂ (Sigma Aldrich, 99.8%), Y-stabilized ZrO₂ (TOSOH, TZ-0Y, TZ-10Y), Y₂O₃ (Alfa Aesar, 99.9%) were used as raw materials. The amounts of raw materials were calculated stoichiometrically. The raw materials which provide the B-site ions, i.e. CeO₂, Y-stabilized ZrO₂, and Y₂O₃ (if needed), were first mixed and dry ball milled for 30 min (ZrO₂ ball with a diameter of 5 cm in ZrO₂ jar on a vibrating mill). Then BaCO₃ was added and further dry milled for 1 h. After calcination at 1100 °C for 4 h in an Al₂O₃ crucible, the powder was milled for 1 h. The single phase perovskite powder was obtained after another 3 repeated calcinations at 1300 °C for 8 h followed by 1 h dry ball milling.

2.1.3 Spark plasma sintering

Spark plasma sintering (SPS) applies a DC current through a graphite die in which the sample is heated under uniaxial pressure. This hot-pressing technique enables densification in a few minutes and provides fast heating and cooling. In this work, 4.0 g of the calcined single phase powder was loaded in the graphite die with 20 mm diameter and sintered under a force of 16 kN at 1400 °C for 5 min (heating rate 100 K/h and furnace cooling). For samples without Ce, a sintering temperature of 1600 °C was used. The as-sintered pellets were then annealed in air at 1500 °C for 4 h (heating and cooling rate: 200 K/h) in Y-stabilized ZrO₂ crucibles with lid (GTS, Düsseldorf, Germany) to eliminate the inner stress and re-oxidize the pellets. During

annealing treatment, the samples were covered with sacrificial powder composed of 90 wt.% BaZrO₃ (Sigma Aldrich) and 10 wt.% BaCO₃ to avoid Ba loss. All the annealed SPS pellets possess a relative density $\geq 95\%$ and a grain size of about 0.5 μm .

2.1.4 GB-decorated ceramics

KNO₃ or CsNO₃ and single phase BZCY powder Ba_{1.015}Zr_{0.664}Ce_{0.20}Y_{0.136}O_{3- δ} were used to prepare GB-decorated ceramics. For a grain size of 0.5 μm , 1 monolayer of alkaline ions on the grain boundaries corresponds to 0.1 at.% decorating ions. KNO₃ (Alfa Aesar, 99.0%) and CsNO₃ (Fluka AG, 98.0%) were dissolved in distilled water. Then the solutions were mixed with BZCY powder in an agate mortar in desired amounts and dried at room temperature in the mortar. 0.1 at.%, 0.3 at.% and 1.0 at.% of K and Rb decoration samples were explored. The obtained powders were sintered by SPS and annealed as described as the section above.

2.1.5 Ceramics with phosphate phase at GBs

LaP₃O₉ (LPO), Ba₃La(PO₄)₃ (BLPO), Zn₃(PO₄)₂ (ZPO) or La_{5.5}WO_x (LWO) and BZC200Y136 were used to prepare samples with possible amorphous phosphate phase at the GBs. (NH₄)₂HPO₄ (Fisher BioReagents, $\geq 98.0\%$), La(NO₃)₃·6H₂O (Sigma Aldrich, 99.99%), Ba(NO₃)₂ (Alfa Aesar, $\geq 99\%$), Zn(NO₃)₂ (Sigma Aldrich, $\geq 99.0\%$) and (NH₄)H₂W₁₂O₄·xH₂O (Sigma Aldrich, $\geq 66.5\%$ W) were the raw materials for corresponding phosphates. The amount of phosphate nominally corresponds to a molar fraction of 1% relative to BZC20Y13.6.

In order to prepare the decorated ceramic samples, (NH₄)₂HPO₄ and corresponding cation nitrates (for the case of LWO, La(NO₃)₃·6H₂O and (NH₄)H₂W₁₂O₄·xH₂O) were dissolved in distilled water separately. The respective amount of calcined BZC20Y13.6 powder was added into the cation nitrate solution on magnetic stirrer, then the phosphate solution or tungstate solution in the case of LWO was added dropwise. Then the solution was fully dried in a rotary evaporator and the formed powder aggregate was crushed in mortar. The final decorated ceramics were prepared also by SPS and annealed afterwards.

LPO, BLPO, ZPO and LWO were also synthesized as pure compounds. After $(\text{NH}_4)_2\text{HPO}_4$ or $(\text{NH}_4)_2\text{W}_{12}\text{O}_{40} \cdot x\text{H}_2\text{O}$ and cation nitrates dissolved into distilled water separately, the phosphate solution or tungstate solution was added into the cation nitrate solution dropwise and fully dried in rotary evaporator. Except LWO, all the other compounds formed precipitates before drying. After crushing the aggregates in a mortar, the mixtures were calcined in air for 4 h at 1100 °C, 1300 °C, 850 °C and 1100 °C for LPO, BLPO, ZPO and LWO, respectively.

2.1.6 Solid state reactive sintering

In the “full” SSRS, perovskite phase formation and sintering occur in a single step. NiO was chosen as the sintering aid in SSRS and added in the amount of 0.125 – 1.0 wt.% in excess to the BZCY cation stoichiometry. The nominal composition of BZCY investigated in this work is $\text{Ba}_{1.015}\text{Zr}_{0.8-y}\text{Ce}_{0.20}\text{Y}_y\text{O}_{3-\delta}$ ($y = 0.136, 0.175, 0.20, 0.24, 0.28$ and 0.32). Stoichiometric amounts of BaCO_3 , ZrO_2 , CeO_2 , Y_2O_3 and excess NiO (Alfa Aesar, 99%) (total mass ~ 30 g) were wet milled in 35 mL iPrOH in a ZrO_2 jar with ZrO_2 balls on a planetary mill (1 big ball with a diameter of 20 mm, 10 small balls with a diameter of 10 mm, 200 rpm) for 24 h. After drying at 60 °C, the powders were further dry milled for 1 h to crush agglomerates. Green pellets were pressed isostatically under 200 MPa for 2 min. The samples were covered with sacrificial powder (90 wt.% BaZrO_3 + 10 wt.% BaCO_3) and sintered in Y-stabilized ZrO_2 crucibles with lid at 1450-1550 °C with a heating and cooling rate of 200 K/h. Later, also MgO crucibles with lid (Tateho Ozark, USA) were used.

Apart from the “full” SSRS, samples from BZCY powder pre-calcined at 1100 °C for 4 h (after dry milling of the combined raw materials) were also prepared. In this scenario, the pre-calcined BZCY powder was first obtained and then mixed with excess NiO by wet ball milling. Then, it went through the same process of pellet sintering as in the “full” SSRS.

For “fast sintering” experiment, a nominal heating and cooling rate of 600 K/h and 0.25 – 1 h soaking time were used. In the case of the “quenching” experiment, BZC200Y136 with 0.125 wt.% ($\text{BZC20Y13.6-0.125Ni}$) and 2.0 wt.% NiO (BZC20Y13.6-2Ni) green pellets were prepared as described above in the “full” SSRS procedure. The pellets were heated up to the desired temperature (1000 – 1600 °C) for 10 min – 4 h in small MgO crucibles. Instead of cooled in the oven, the crucibles were directly taken out from the oven by pulling them out with a Pt wire through the oven chimney and quenched in the air.

For comparison, samples with 1.0 or 4.0 at.% Ni nominally on the B site were prepared with compositions of $\text{Ba}_{1.015}\text{Zr}_{0.654}\text{Ce}_{0.20}\text{Y}_{0.136}\text{Ni}_{0.01}\text{O}_{3-\delta}$ (BZC20Y13.6Ni1) and $\text{Ba}_{1.015}\text{Zr}_{0.654}\text{Ce}_{0.20}\text{Y}_{0.136}\text{Ni}_{0.04}\text{O}_{3-\delta}$ (BZC20Y13.6Ni4), respectively. The perovskite powders were obtained by conventional solid state reaction from BaCO_3 , ZrO_2 , CeO_2 , Y_2O_3 and NiO by repeated dry ball milling and calcination. Then the pellets were densified by conventional sintering at 1500 °C or 1550 °C for 4 h, or SPS for 5 min at 1350 °C (BZC20Y13.6Ni1) and 1300 °C (BZC20Y13.6Ni4). These SPS samples were then embedded in sacrificial powder and post-annealed in Y-stabilized ZrO_2 crucibles for 4 h at 1400 °C with a heating and cooling rate of 200 K/h.

2.2 Sample characterizations

2.2.1 Measurements of relative density

The real density of samples with regular shape was calculated based on the weight and volume from geometry. The theoretical density was calculated from the lattice constants from X-ray diffraction (XRD) and molecular weight from the nominal composition.

2.2.2 X-ray diffraction (XRD)

X-ray diffractograms were measured at room temperature in Bragg-Brentano reflection geometry by a PANalytical diffractometer of Empyrean Series 2 using $\text{Cu K}\alpha$ radiation ($\lambda = 1.54184 \text{ \AA}$, 40 kV, 40 mA) and a PIXcel 3D detector in the range of $2\theta = 10^\circ - 90^\circ$ with 0.013° step size. The data were analyzed with PANalytical software HighScore Plus (Version 3.0e). Micro-strain and grain size were calculated from XRD by the Williamson-Hall (W-H) equation [119]

$$\beta_{\text{hkl}} \cos\theta = \frac{S\lambda}{D} + 4\varepsilon \sin\theta \quad (12)$$

where β_{hkl} is line broadening, S is the shape factor (here $S = 1.0$), D is the grain size and ε is the micro-strain induced by crystal imperfection and distortion.

2.2.3 ICP-OES

Inductively coupled plasma-optical emission spectrometry (ICP-OES) determines chemical composition by measuring the characteristic wavelengths of elements from the radiation generated when atoms are excited in the inductively coupled plasma in the ICP torch. About 50 mg of a ceramic sample was ground into powder, after which it was dissolved into a 3.0 vol.% HCl solution in a microwave autoclave. The measurements were conducted using a Spectro Ciros ICP-OES (Spectro Analytical Instruments GmbH in Germany) in the Max Planck Institute for Intelligent Systems, Stuttgart, by Samir Hammoud.

2.2.4 Thermogravimetry

Proton uptake and thermodynamics parameters were determined from thermogravimetry (TG) measurements. The thermogravimetric data were collected by a STA 449 (Netzsch, Germany) using N₂ flow. To avoid complications from water adsorption on fine powder, crushed sintered pellets were used instead. Pellets were crushed and sieved to a size < 300 μm, and 0.5 – 1.0 g sample was used in a large Al₂O₃ crucible. The powder was first heated up to 900 °C in dry N₂ flow with a heating rate of 15 K/min. After being stable at 900 °C, the gas was switched to wet N₂ with a H₂O partial pressure of 17 mbar (10 mL/min dry “protective” gas through balance + 50 mL/min saturated with water in an evaporator at 18 °C). The water uptake was measured during cooling from 900 °C to 300 °C (cooling rate: 1 K/min for 900 – 600 °C, 0.6 K/min for 600 – 400 °C and 0.3 K/min for 400 – 300 °C). In order to check reversibility, the sample was subsequently re-heated from 300 °C to 900 °C in the same atmosphere with equal heating rates. The TG curves were obtained by averaging the cooling and heating curves and corrected for buoyancy, which was obtained from an empty crucible measured with similar procedure without sample.

The proton concentration was calculated from the mass change. The mass action constant of the hydration reaction K_{hydrat} **Eq. (3)** was applied, based on the reversible hydration reaction (**Eq. (2)**). From the site balance and electron neutrality condition, $[V_{\text{O}}^{\bullet\bullet}]$ and $[O_{\text{O}}^{\times}]$ can be substituted by

$$[V_{\text{O}}^{\bullet\bullet}] = \frac{[A_{\text{eff}}] - [\text{OH}_{\text{O}}]}{2} \quad (13)$$

$$[\text{O}_\text{O}^\text{X}] = 3 - [\text{V}_\text{O}^\bullet] - [\text{OH}_\text{O}] \quad (14)$$

$[A_{\text{eff}}]$ is the effective dopant concentration, which may be lower than the nominal dopant concentration, $p_{\text{H}_2\text{O}}$ is water partial pressure. The Van't Hoff plot of $\ln K_{\text{hydrat}}$ versus $1/T$ was first plotted using the nominal dopant concentration as $[A_{\text{eff}}]$ in **Eq. (3)**. If the plot is bent, the saturated proton concentration was used as a first estimate of $[A_{\text{eff}}]$. Then $[A_{\text{eff}}]$ was fine-tuned until a straight van't Hoff plot in the range of 350 °C – 800 °C was obtained. Standard hydration enthalpy (ΔH°) and entropy (ΔS°) were calculated from the slope and intercept of the Van't Hoff plot using

$$\ln K_{\text{hydrat}} = \Delta S^\circ / R - \Delta H^\circ / RT \quad (15)$$

2.2.5 BET

Brunauer-Emmett-Teller (BET) measurements was used to measure the specific surface area of powders. The adsorption of N_2 was measured by Autosorb-1, Quantachrome from 3P Instruments GmbH & Co. KG, Germany.

2.2.6 Scanning electron microscopy

Grain size and element distribution of ceramic samples were measured by scanning electron microscopy (SEM). After polishing, ceramic samples were thermally etched at 50 °C below their sintering temperature (or annealing temperature for samples sintered by SPS), or chemically etched in 10 vol.% HCl for 20 min. The thermal etching was used for acquiring high quality images, and the chemical etching provided high efficiency for grain size measurements. The images were taken from the top-view of the etched surface at 1.50 kV in a Zeiss Merlin (ZEISS, Germany) equipped with a Schottky-Emitter field emission system using Smart SEM interface with secondary electron (SE) and backscattered electron (BSE) signals. Based on the images, the grain size was calculated by the linear intercept method and the grain size distribution was plotted.

SEM energy dispersive x-ray spectroscopy (SEM-EDX) was performed on ceramics surfaces to investigate the element homogeneity. The samples were coated with 0.2 nm iridium by EM ACE600 coater (Leica Microsystems, Germany) in vacuum (10^{-5} mbar) on the polished surface.

The SEM images were taken by a DSM 982 GEMINI with an EDX-detector silicon drift detector (ZEISS, Germany) at 10 kV. Spectra were acquired and analyzed on NSS 3.0 (Thermo Fisher Scientific, USA) using Ba-L α (4.4663 keV), Y-L α (1.9226 keV), Zr-L α (2.0424 keV) and Ce-L α (4.8403 keV). The work was done in the Stuttgart Center for Electron Microscopy (StEM, Germany) by Felicitas Predel.

SEM was also used for measuring cross section and top-view element distribution of membranes. For cross section, focused ion beam (FIB) preparation and SEM-EDX measurements were done on a FEI-Scios (Thermo Fisher Scientific, USA). The cross section was fine polished by FIB (firstly 30 kV, then 5 kV with 48 pA beam current and finally 2 kV with 27 pA). Secondary electron images (SE) and backscattered electron (BSE) images were obtained by Everhart-Thornley (ETD) and T1 detectors, respectively. The spectra were acquired and analyzed with Ba-L α (4.465 keV), Y-L α (1.922 keV), Zr-L α (2.042 keV), Ce-L α (4.839 keV), Ni-K α (7.477 keV) and O-K α (0.523 keV) using the software TEAM version 4.5-Released (EDAX, USA). The work was done in StEM by Julia Deuschle.

2.2.7 Transmission electron microscopy

Local element distribution and possible valence changes at GBs of ceramic samples were investigated by transmission electron microscopy (TEM) with energy dispersive analysis (TEM-EDX) and electron energy loss spectroscopy (TEM-EELS). TEM sample preparation was performed by Ute Salzberger and Julia Deuschle in StEM. Measurements and data extraction were done by Rana Yekani, Dan Zhou and Wilfried Sigle from StEM.

TEM sample were prepared by mechanical grinding followed by mechanical polishing using a MultiPrep wedge polisher (Allied High Tech Products, Inc., USA). A final ion-beam milling with low energy Ar ions (1 keV) was applied in a PIPS1 (Gatan, Inc., USA) at room temperature. The measurements were done in an ARM200CF TEM (JOEL, USA) with a cold field emission gun at 200 kV. The instrument integrates spherical (C_s) aberrations of the condenser lenses and provides atomic resolution. Bright-field (BF) images with a spatial resolution of 0.2 nm and high-angle annular dark-field (HAADF) with a spatial resolution < 0.1 nm (electron scattered to angles 0 – 111 mrad) images were taken to observe the structure at GBs.

TEM-EDX analysis was performed to acquire element distribution along line scans of ~ 25 nm length and $\sim 25 \times 25$ nm² area in element mapping mode (spatial resolution = 0.2 nm). The wedge-shaped specimen from the MultiPrep polisher provides a sufficiently long thin edge to measure a sufficient number of GBs which are oriented parallel to the electron beam. The distance from the edge of the TEM specimen was kept constant to avoid possible thickness variations. EELS was used to measure the thickness. The specimen thickness a is given by **Eq. (16)** ^[120]

$$a/l = \ln(I/I_0) \quad (16)$$

in which l is the total inelastic mean free path, I is the total integrated intensity in the EELS spectrum and I_0 is the integrated zero-loss energy intensity. The measured t was always in the range of 40 – 60 nm.

TEM-EDX line-scanning and element mapping were quantified using elements' energy edges, i.e., Ba-L α (4.465 keV), Zr-K α (15.744 keV), Ce-L α (4.839 keV), Y-K α (14.931 keV), Ni-K α (7.471 keV) and O-K α (0.525 keV). The atomic percentages were calculated based on the Cliff-Lorimer equation ^[121] (**Eq. (17)**) from the experimental X-ray intensity ratios using Cliff-Lorimer k -factors and Ba was set as reference.

$$\frac{c_1}{c_2} = k_{12} \frac{I_1}{I_2} \quad (17)$$

here c_i is the concentration of element i , which can be further transferred to atomic ratio, I_i is the X-ray intensity from element i and k_i is the Cliff-Lorimer sensitivity factor ($k_{\text{Ba,Ba}} = 1.00$, $k_{\text{Zr,Ba}} = 2.74$, $k_{\text{Ce,Ba}} = 0.813$, $k_{\text{Y,Ba}} = 2.36$, $k_{\text{Ni,Ba}} = 0.65$ and $k_{\text{O,Ba}} = 0.564$). The sensitivity factors were determined from a standard specimen of known composition.

All quantifications in this thesis were done with the standard method. Except for a few relatively thick samples, the thickness of the sample was not taken into account for the quantifications because the spatial resolution of the TEM-EDX measurements is not strongly sensitive to the sample thickness.

In the case of membrane samples, after cutting by ultramicrotome, Pt was deposited onto the side in FIB by electron beam deposition (2 kV, 0.8 μA , ~ 100 nm) followed by ion beam deposition (30 kV, 300 pA). Then the lamella was sliced and fine-polished in FIB with final thickness of Pt layer of ~ 0.7 μm . **Figure 5** shows how the lamella was prepared.

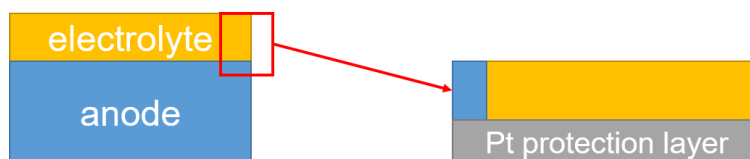


Figure 5: Schematic picture of TEM lamella preparation.

2.2.8 Raman spectroscopy

Raman spectra of ceramic samples were taken with a Jobin Yvon Typ V 010 labram single grating spectrometer (HORIBA Jobin Yvon, Japan), equipped with a double super razor edge filter and a Peltier cooled CCD camera. The spectrometer has a resolution of 1 wavenumber (cm^{-1}) (grating 1800 L/mm). Spectra were taken in quasi-backscattering geometry using the linearly polarized 632.817 nm line of a He/Ne gas laser with power less than 1 mW, focused to a $10\ \mu\text{m}$ spot through a $50\times$ microscope or a $20\ \mu\text{m}$ spot through a $20\times$ microscope objective on to the top surface of the sample. Measurements were done by Armin Schulz in the Solid State Spectroscopy group of the Max Planck Institute for Solid State Research.

2.2.9 Electrochemical impedance spectroscopy

Electrochemical impedance spectroscopy (EIS) measurement is widely used to study the electrical properties of materials. For polycrystalline ceramics, bulk, blocking GBs and electrode response can be well resolved due to their different relaxation time.

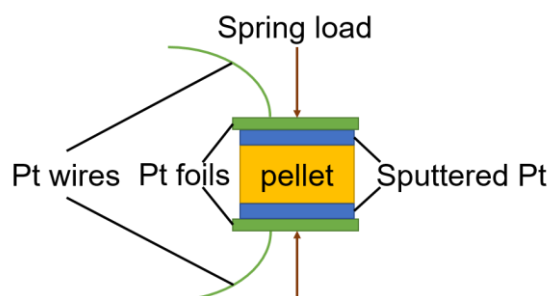


Figure 6: Schematic diagram of a two-wire EIS measurement.

Two-wire measurements were employed for ceramic samples (cf. **Figure 6**). The pellet samples usually had an area of about 50 mm² and a thickness of 1 mm. After polishing the surface, the pellet sample was sputtered with Pt (Edwards Auto 306 Turbo, UK) on both top and bottom (5.0×10^{-2} mbar Ar, 60 kV, 20 min for each side). The sample was measured in a gas tight quartz cell in a tube furnace which is electromagnetically shielded by a high-temperature resistant Cr-alloy foil. The sputtered sample was pressed in between two Pt foils connected to measurement circuit, as shown in Figure 6. Typical impedance spectra of pellets were obtained in the frequency range of 3×10^{-2} to 10^6 Hz by applying an average AC voltage of 0.1 V using a Novocontrol Alpha-A analyzer (Novocontrol Technologies, Germany). The sample was first heated up to 700 °C in dry N₂ with a slowing heating rate of 3 °C/min and then switched to N₂ with 20 mbar H₂O (controlled by the temperature of a water evaporator at 18 °C). Several spectra were measured for each temperature until equilibrium was reached (i.e. completion of water incorporation) during cooling from 700 °C to room temperature. Typical equilibrium times at 700 °C, 600 °C and 500 °C are 9 h, 12 h and 2 d, respectively. For $T < 400$ °C, the samples are fully hydrated and/or hydration too slow to further equilibrate, then samples were measured directly after temperature stabilization. For temperatures below 350 °C, 3 vol.% H₂ in Ar with 20 mbar H₂O was used to suppress the electrode semicircle for SSRS samples. The impedance spectra were analyzed using Z-View (Scribner Associates, Inc., USA) with equivalent circuits.

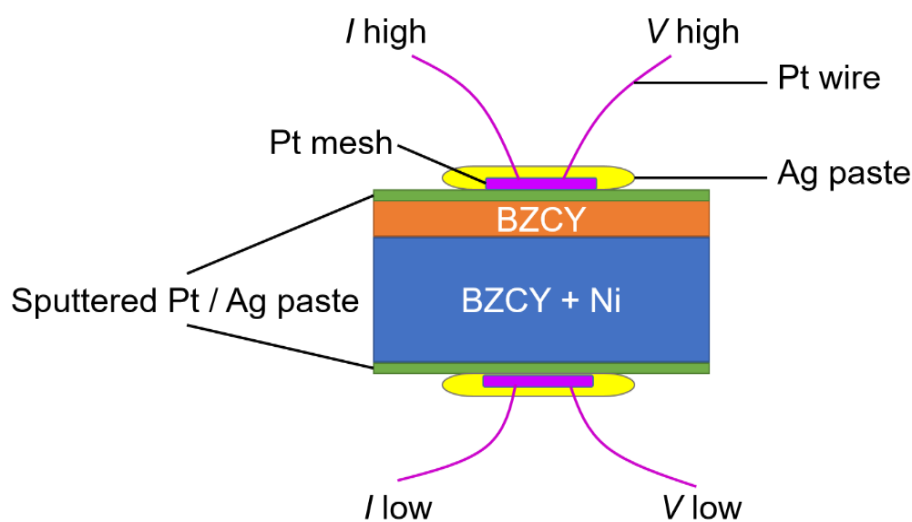


Figure 7: pseudo-four-wire EIS measurements for membranes.

When measuring membrane samples, pseudo-four-wire contacting was applied (**Figure 7**). This method eliminates the resistance from wires, which is necessary for accurate measurements of low-resistant samples. Pt was sputtered or Ag paste (Fluka Analytical, Germany) was painted and dried in air on both electrolyte and anode side of the membrane. Pt wires were fixed to Pt meshes by spot welding and then attached to the membrane surface with Ag paste (dry at 150 – 200 °C for 20 min). The measurements were done at frequencies 10^0 to 10^6 Hz by Novocontrol Alpha-A with a four-wire impedance test interface (Novocontrol Technologies, Germany) applying an average AC voltage at 0.02 V in 3 vol.% H₂ in Ar with 20 mbar H₂O from 50 – 600 °C. An additional DC voltage (0.2 – 2 V) was applied when it is difficult to distinguish electrolyte and electrode semicircles. The spectra were analyzed by equivalent circuits using Z-View.

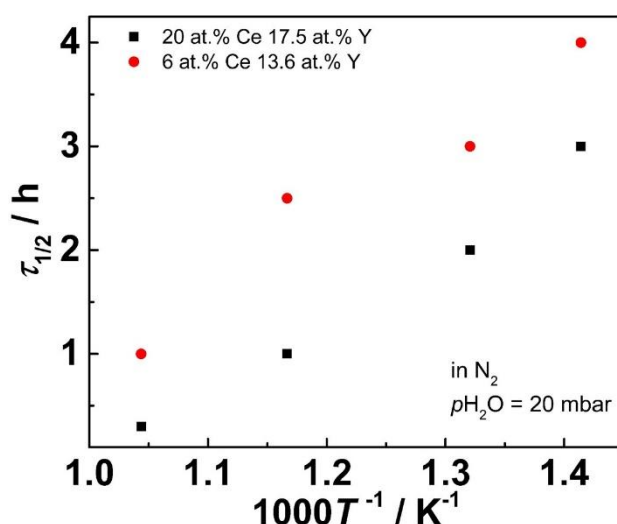


Figure 8: Time $\tau_{1/2}$ to reach 50% of final degree of hydration after a fast decrease of temperature of BZCY samples for different Ce content. The two samples measured have comparable thickness of 1 mm.

Conductivity was measured from high to low temperature, with the goal that the hydration is largely in equilibrium. Thus the equilibration kinetics after temperature decrease was exemplarily checked for some samples (**Figure 8**). The equilibration kinetics of dense ceramic pellets is determined by water chemical diffusion (the surface reaction is comparably facile and fast). For coming close to equilibrium, a time of $4 - 5 \times \tau_{1/2}$ is required. The equilibration time for hydration is lower for higher Ce content, as shown in **Figure 8**. The chemical diffusion

coefficient of water ($D_{\text{H}_2\text{O}}^\delta$) is related to the diffusion coefficients of protonic defect ($D_{\text{OH}_0^\cdot}$) and oxygen vacancies ($D_{\text{V}_0^\cdot}$), as given in **Eq. (18)** [122].

$$D_{\text{H}_2\text{O}}^\delta = \frac{(2-X)D_{\text{OH}_0^\cdot}D_{\text{V}_0^\cdot}}{XD_{\text{OH}_0^\cdot} + 2(1-X)D_{\text{V}_0^\cdot}} \quad (18)$$

where X is the degree of hydration. This yields $D_{\text{V}_0^\cdot} \leq D_{\text{H}_2\text{O}}^\delta \leq D_{\text{OH}_0^\cdot}$ with $D_{\text{H}_2\text{O}}^\delta$ approaching $D_{\text{V}_0^\cdot}$ for $X \rightarrow 1$. Thus, close to full hydration at about 400 °C, it is difficult to reach really full equilibrium due to the more sluggish diffusion of oxygen vacancies. The effect of Ce on the hydration time is related to the fact that with less Ce the individual GBs are more blocking, which impedes the water chemical diffusion.

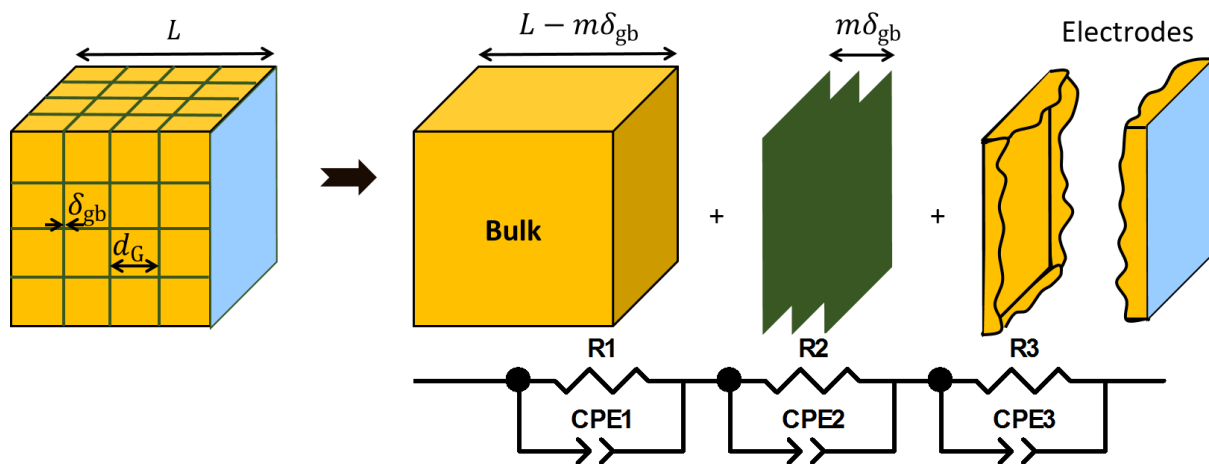


Figure 9: Equivalent circuit based on “brick layer model” [123].

In impedance spectra, the response of polycrystalline ceramics can be separated into three parts, i.e. bulk (intra grain), blocking GBs, and electrode and fitted with equivalent circuits as introduced by Bauerle [124]. The “brick layer model” [125–127] shown in **Figure 9** assuming cubic grains with equal size was used to describe each part. The “brick layer model” is composed of three parallel resistance and capacitance (RC) elements in series. Semicircles were assigned to corresponding processes based on different peak frequencies ω_p

$$\omega_p = \frac{1}{RC} \quad (19)$$

In reality, the GB semicircle is often depressed in the Nyquist plot. Therefore, instead of using ideal capacitors, the so-called constant phase element (CPE) was applied. The effective capacitance was then calculated from **Eq. (20)** ^[128]

$$C = (R^{1-n}Q)^{1/n} \quad (20)$$

where Q is the CPE value and n is the depression parameter ($0 < n \leq 1$).

Apart from non-ideality, semicircles are not always visible in Nyquist plots due to the limitation of the measured frequency range. Exemplary impedance spectra from SPS sample BZC200Y136 are shown in Figure 10. At 50 °C, high-frequency bulk and medium-frequency GB semicircles can both be recognized in the complex plane (**Figure 10-(a)**). The observation of the electrode semicircle requires rather low frequency and long term measurement. The bulk resistance decreases with increasing temperature and results in higher bulk peak frequency ($\omega_{p,b}$). As shown in **Figure 10-(b)**, the bulk semicircle disappears in the complex plane plot due to limited measurement frequency above 200 °C. Then, the bulk resistance (R_b) is obtained from the intercept of the GB semicircle with the Z_{real} axis at the high frequency side, bulk CPE and n values are fixed and C_b is the average of lower temperature C_b values. At 450 °C (see **Figure 10-(c)**), the GB semicircle also vanishes and only the total resistance ($R_{Total} = R_b + R_{GB}$) can be extracted from the intercept of the electrode semicircle with the Z_{real} axis at the high frequency side. Above 600 °C, inductance from the wires appears as shown in **Figure 10-(d)**. The apparent GB conductivity (σ_{GB}^{app}) was calculated with the sample's geometry. Assuming the bulk relative dielectric constant (ϵ_b) is also valid for the GB region, the capacitance ratio of bulk and GB ($\frac{C_b}{C_{GB}}$) can be used as $\frac{\delta_{GB}}{d_G}$ to obtain the specific GB conductivity (σ_{GB}^{spec}).

$$\frac{C_b}{C_{GB}} = \frac{\delta_{GB}}{d_G} \quad (21)$$

$$\sigma_b = \frac{1}{R_b} \times \frac{L}{A} \quad (22)$$

$$\sigma_{GB}^{app} = \frac{1}{R_{GB}} \times \frac{L}{A} \quad (23)$$

$$\sigma_{GB}^{spec} = \frac{1}{R_b} \times \frac{L}{A} \times \frac{C_b}{C_{GB}} \quad (24)$$

$$\epsilon_b = \frac{C_b}{\epsilon_0} \times \frac{L}{A} \quad (25)$$

where L and A are length and contacting area of the sample, ϵ_0 is the dielectric constant of vacuum. The bulk ($E_{a,b}$) and GB ($E_{a,GB}$) activation energies were extracted from the slopes of the Arrhenius plot based on the equations:

$$\sigma_b T = A_{0,b} e^{-E_{a,b}/RT} \quad (26)$$

$$\sigma_{GB} T = A_{0,GB} e^{-E_{a,GB}/RT} \quad (27)$$

where $A_{0,b}$ and $A_{0,GB}$ are pre-exponential factors.

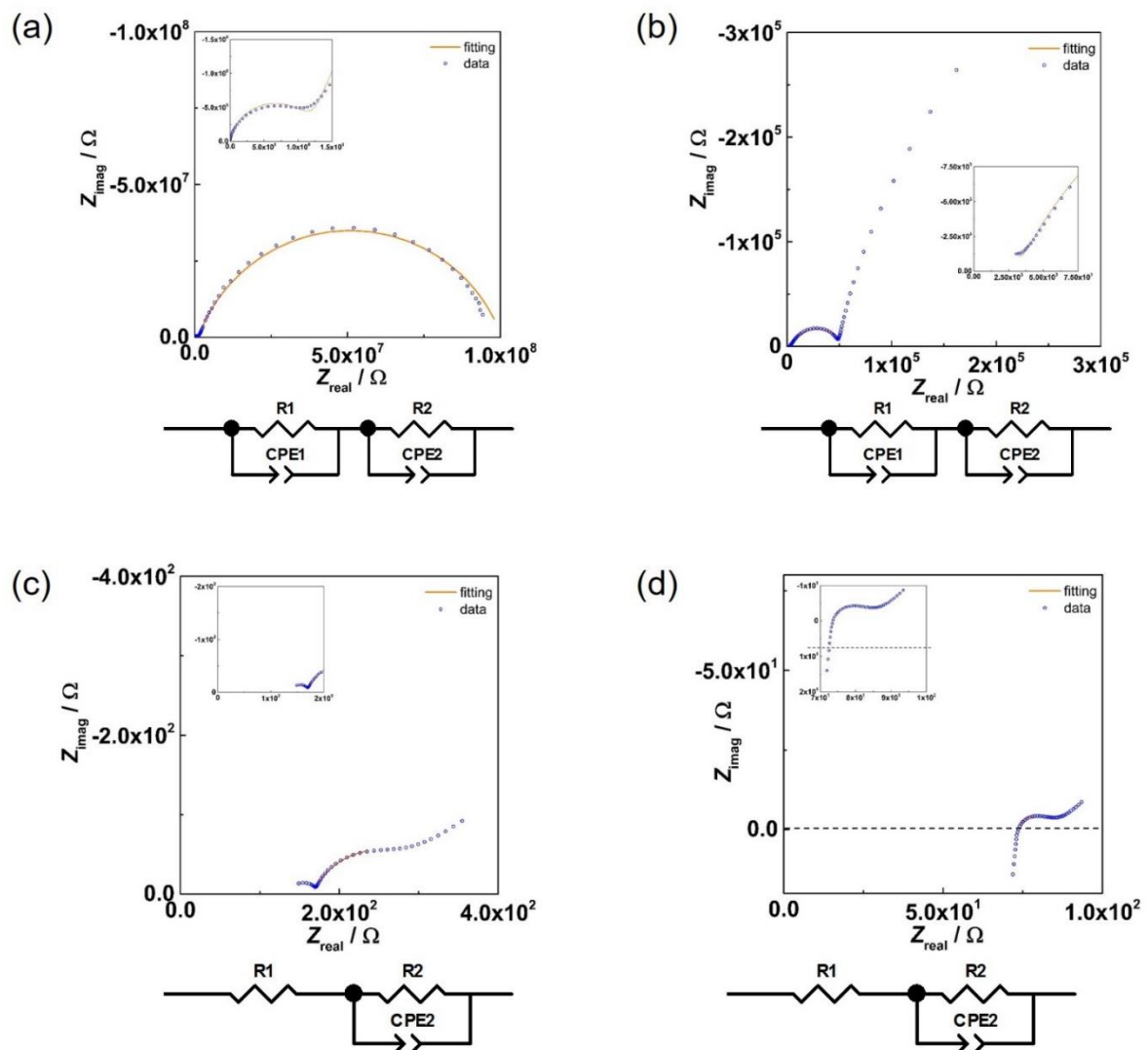


Figure 10: Typical impedance spectra (Nyquist plots) and corresponding equivalent circuits from sample BZC20Y13.6-SPS at (a) 50 °C, (b) 200 °C, (c) 450 °C and (d) 600 °C.

Chapter 3 Results and discussion

3.1 Discussion of composition of $\text{Ba}(\text{Zr,Ce,Y})\text{O}_{3-\delta}$

3.1.1 XRD patterns and lattice parameter

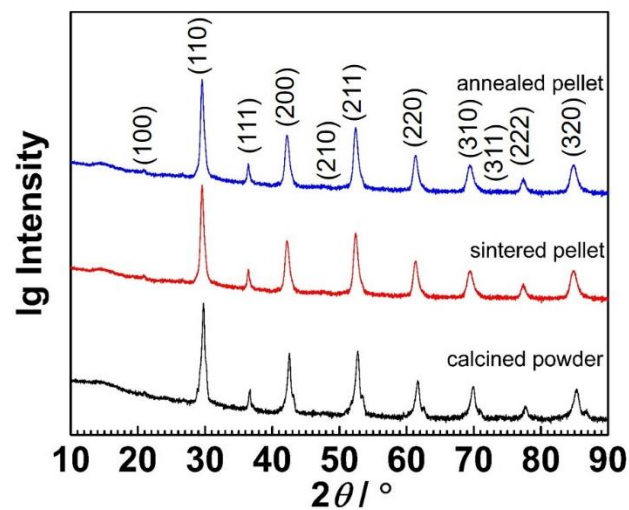


Figure 11: XRD patterns from calcined powder (after 1 calcination at 1100 °C 4 h and 3 calcinations at 1300 °C 8 h), as-sintered pellet (SPS at 1400 °C for 5 min) and annealed pellet (annealing at 1500 °C 4h) of sample BZC20Y13.6-SPS.

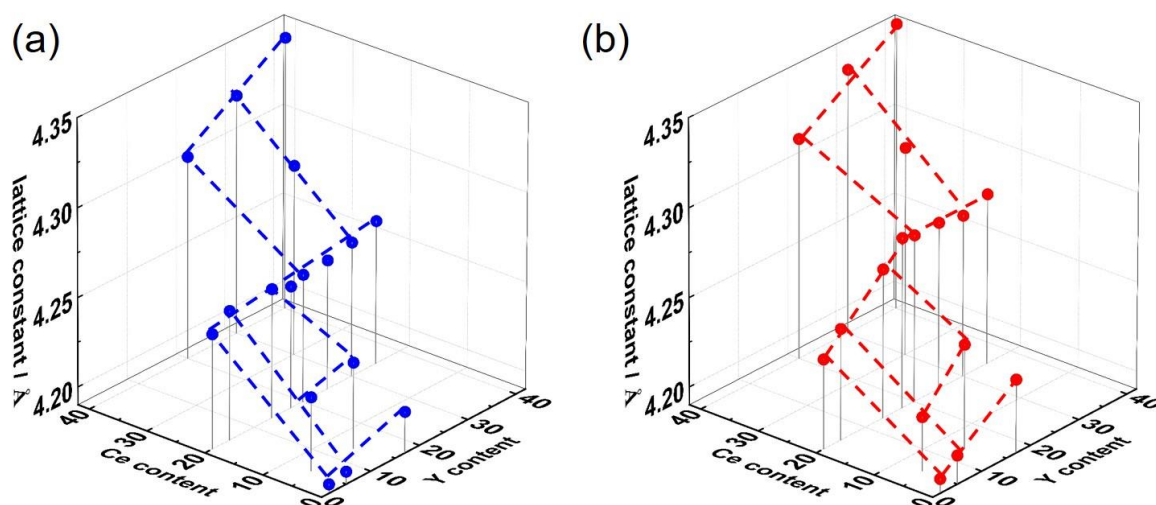


Figure 12: Lattice constant versus Y and Ce content for (a) single phase powder by solid state reaction (1 calcination at 1100 °C 4 h and 3 calcinations at 1300 °C 8 h) and (b) post-annealed SPS pellets (SPS: 1400 °C 5 min and annealing: 1500 °C 4 h). The dashed lines are only a guide for the eye.

Exemplary XRD diffraction patterns of calcined powder, as-sintered SPS pellet and annealed pellet samples with the composition of BZC20Y13.6 are shown in **Figure 11**. According to XRD, the calcined powder is single perovskite phase and does not decompose during SPS and post-annealing treatment. The lattice constants were calculated based on the $Pm\bar{3}m$ space group, and increase from 4.262 Å to 4.278 Å, and stabilized at 4.276 Å after annealing. C. Hiraiwa *et al.* ^[129] also observed enlarged lattice constants of acceptor-doped BaZrO₃ (except Sc) with higher sintering temperature by conventional sintering, while no difference was found for pure BaZrO₃. This indicates that apparently a temperature of 1300 °C does not suffice to fully incorporate the oversize Y dopant ($r_{Y^{3+}} = 0.9 \text{ \AA} > r_{Ce^{4+}} = 0.87 \text{ \AA} > r_{Zr^{4+}} = 0.72 \text{ \AA}$) as acceptor on the (Zr, Ce) site. Only for temperature > 1400 °C this is achieved.

The lattice constant of the single phase calcined powder increases with Ce and Y (cf. **Figure 12-(a)**). The increase with Y is linear up to 35 – 40 at.% Y, but with a smaller slope than for the sintered pellets. After sintering and annealing treatment, the lattice parameters expand. With 20 at.% Ce, the linear increase of the lattice constant levels off at 20 at.% Y as shown in **Figure 12-(b)**, indicating that the equilibrium Y solubility is about 20 at.%. This is consistent with data from Kreuer ^[59]. Interestingly, the lattice constants increases further with Y for higher Ce content, resulting from the unit cell expansion due to Ce which allows more Y to be incorporated.

3.1.2 Chemical composition

In order to compensate Ba loss at high temperature, 1.5 at.% extra Ba was added in the starting materials. ICP-OES results of single phase powders (**Table 2**) and annealed SPS pellets (**Table 3**) show a good agreement with the nominal composition. The Ba content is 1 within the error range. Ba addition of 3.0 at.% extra Ba could compensate more Ba loss (comparing BZC20Y13.6-SPS and B103ZC20Y13.6 in **Table 3**) but leads to bad stability of the pellets, which results from Ba accumulation at GBs, forming Ba(OH)₂ and/or BaCO₃ layers in ambient conditions and crack formation. 1% Hf from TOSOH YSZ starting powder, and about 0.1 at.% Sr from BaCO₃ were also detected. The A:B ratios of powder are comparable to the corresponding pellets within the error bar. Therefore there is no obvious Ba loss during sintering.

Table 2: Composition of powders synthesized by solid state reaction.

Nominal Composition	Measurement by ICP-OES / wt.%				Real composition	A:B ratio
	Ba	Zr	Ce	Y		
BZY17	49.9 ±0.5	26.7 ±0.3	-	5.44 ±0.06	Ba _{1.01} Zr _{0.82} Y _{0.17} Hf _{0.01} O _{3-δ}	1.01
BZC20Y13.6	47.8 ±0.5	20.3 ±0.3	9.25 ±0.15	4.23 ±0.05	Ba _{1.02} Zr _{0.66} Ce _{0.19} Y _{0.14} Hf _{0.01} O _{3-δ}	1.02
BZC20Y17.5	48.1 ±0.5	19.3 ±0.2	9.63 ±0.15	5.38 ±0.06	Ba _{1.02} Zr _{0.62} Ce _{0.20} Y _{0.18} Hf _{0.01} O _{3-δ}	1.02
BZC20Y25.0	48.2 ±0.5	17.1 ±0.2	9.65 ±0.15	7.61 ±0.08	Ba _{1.02} Zr _{0.54} Ce _{0.20} Y _{0.25} Hf _{0.01} O _{3-δ}	1.02
BZC20Y35	48.2 ±0.5	14.1 ±0.2	9.66 ±0.15	10.8 ±0.2	Ba _{1.01} Zr _{0.45} Ce _{0.20} Y _{0.35} Hf _{0.01} O _{3-δ}	1.01

Table 3: Composition of pellets sintered by SPS after annealing treatment.

Nominal Composition	Measurement by ICP-OES / wt.%				Real composition	A: B ratio
	Ba	Zr	Ce	Y		
BZY1.5-SPS	50.0 ±0.5	31.9 ±0.4	-	0.51 ±0.02	Ba _{1.00} Zr _{0.97} Y _{0.016} Hf _{0.01} O _{3-δ}	1.00
BZY17-SPS	49.8 ±0.5	26.9 ±0.3	-	5.41 ±0.06	Ba _{1.00} Zr _{0.82} Y _{0.17} Hf _{0.01} O _{3-δ}	1.00
BZC6Y5-SPS	49.5 ±0.5	28.4 ±0.3	2.93 ±0.05	1.55 ±0.03	Ba _{1.02} Zr _{0.88} Ce _{0.06} Y _{0.05} Hf _{0.01} O _{3-δ}	1.02
BZC20Y1.5-SPS	47.3 ±0.5	25.9 ±0.3	9.48 ±0.15	0.44 ±0.01	Ba _{0.95} Zr _{0.79} Ce _{0.19} Y _{0.014} Hf _{0.01} O _{3-δ}	0.95
BZC20Y5-SPS	48.0 ±0.05	23.1 ±0.3	9.71 ±0.15	1.54 ±0.03	Ba _{1.02} Zr _{0.74} Ce _{0.20} Y _{0.05} Hf _{0.01} O _{3-δ}	1.02
BZC20Y13.6-SPS	47.1 ±0.5	21.7 ±0.3	9.64 ±0.15	4.13 ±0.05	Ba _{0.96} Zr _{0.67} Ce _{0.19} Y _{0.13} Hf _{0.01} O _{3-δ}	0.96
B103ZC20Y13.6-SPS	48.0 ±0.5	20.8 ±0.3	9.47 ±0.15	4.18 ±0.05	Ba _{1.00} Zr _{0.66} Ce _{0.20} Y _{0.14} Hf _{0.01} O _{3-δ}	1.00
BZC20Y17.5-SPS	48.0 ±0.5	19.3 ±0.2	9.76 ±0.15	5.25 ±0.06	Ba _{1.02} Zr _{0.62} Ce _{0.20} Y _{0.17} Hf _{0.01} O _{3-δ}	1.02
BZC20Y25-SPS	48.3 ±0.5	16.7 ±0.2	9.69 ±0.15	7.68 ±0.08	Ba _{1.03} Zr _{0.54} Ce _{0.20} Y _{0.25} Hf _{0.01} O _{3-δ}	1.03
BZC20Y35-SPS	48.1 ±0.5	14.3 ±0.2	9.61 ±0.15	10.5 ±0.2	Ba _{1.01} Zr _{0.45} Ce _{0.20} Y _{0.34} Hf _{0.01} O _{3-δ}	1.01

3.1.3 Hydration behavior

TG measurements of crushed SPS samples show increased proton uptake with decreasing temperature, the saturation is reached at about 300 °C with a value almost matching the nominal Y content. The TG results will be discussed in more detail in section 3.2.4.

3.1.4 Proton conductivity and other electrochemical properties

Proton conductivity of annealed pellets was measured by EIS decreasing from 700 °C to room temperature in wet N₂ with a water partial pressure $p_{\text{H}_2\text{O}} = 20$ mbar. **Figure 13** shows the spectra measured at 200 °C for BZC20Y1.5-SPS and BZC20Y20-SPS. Most of the bulk semicircle can still be seen at 200 °C for a sample with low Y content (1.5 at. %, **Figure 13-**

(a)), whereas it disappears for higher Y content (20 at.%, **Figure 13-(b)**) due to its higher bulk conductivity. The GB semicircle is much more pronounced with 1.5 at.% Y compared to the bulk semicircle and shrinks significantly when Y content is increased to 20 at.%.

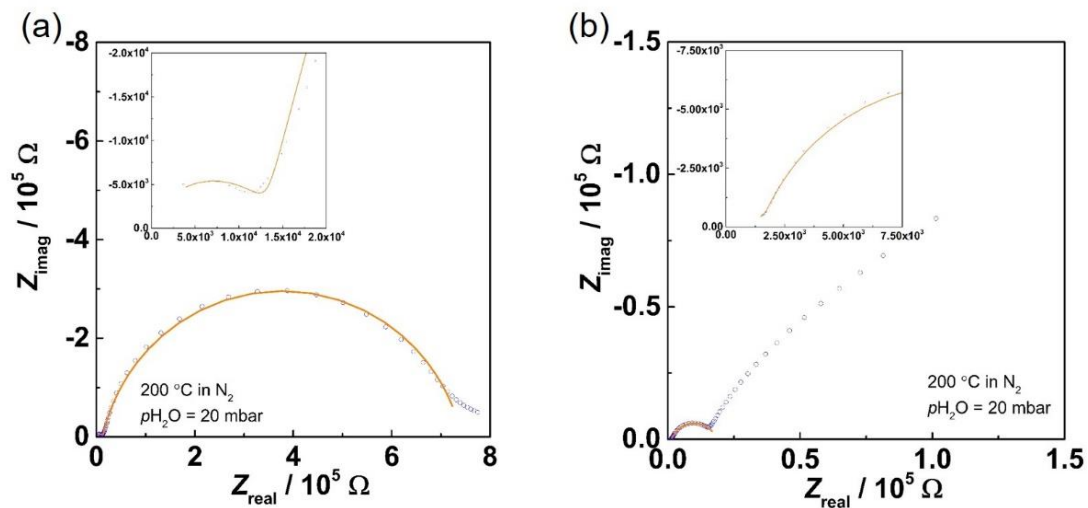


Figure 13: Impedance spectra measured at 200 °C in wet N₂ ($p_{\text{H}_2\text{O}} = 20$ mbar) from (a) BZC20Y1.5-SPS and (b) BZC20Y20-SPS. Symbols are measured data and solid lines are fitting results.

The Arrhenius plots for these two compositions are shown in **Figure 14**. The fitting was done based on the brick layer model described in section 2.2.9. At low temperature, the bulk and GB semicircle can be distinguished. Bulk, apparent GB and specific GB conductivity were then calculated from **Eq. (22)**, **Eq. (23)** and **Eq. (24)**, respectively. At high temperature, only the total conductivity can be extracted from the impedance spectra as both bulk and GB semicircles are invisible. The bulk, apparent GB, total and specific GB conductivity of 20 at.% Y sample are higher than from the 1.5 at.% Y sample. The bulk and GB activation energies were extracted from the $\log(\sigma T)$ vs. $1/T$ plot, but in order to facilitate comparison with literature data, $\log \sigma$ vs. $1/T$ was plotted instead. The bulk activation energy does not change too much while the GB activation energy decreases with higher Y content (cf. **Figure 17**) as discussed in more detail below. The relative dielectric constant was calculated from C_b (**Eq. (25)**) with a typical value of about 60. C_{GB} is about 3 orders of magnitude higher than C_b because the thickness of the blocking layer at the GB is much thinner than the bulk dimension. The conductivity curves flatten at high temperature due to water excorporation.

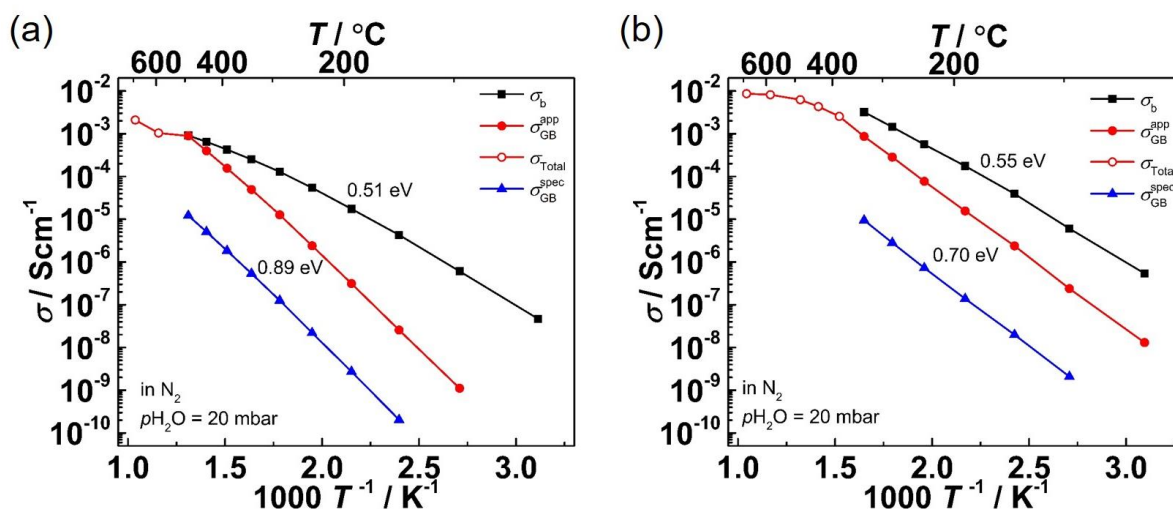


Figure 14: Arrhenius plots of (a) BZC20Y1.5-SPS and (b) BZC20Y20-SPS in wet N_2 ($p_{H_2O} = 20$ mbar).

The effects of Y and Ce content on the bulk and the apparent GB conductivity at low temperature are summarized in **Figure 15**. The bulk conductivity (**Figure 15-(a)**) increases with Y content due to higher proton concentration, and decreases slightly with Ce because $BaCeO_3$ has a lower proton mobility than $BaZrO_3$ caused by lattice distortion^[60]. The increase of the apparent GB conductivity with Y is much more pronounced, i.e. 4 – 5 order of magnitude when Y increases from 1.5 at.% to 20 at.% without Ce (**Figure 15-(b)**). A higher Ce content leads to slightly higher apparent GB conductivity; also $BaCeO_3$ has less blocking GBs than $BaZrO_3$ ^[130].

At 600 $^{\circ}C$, only the total conductivity can be extracted, and it has the same trend as the bulk conductivity at lower temperature (**Figure 16**). The total conductivity reaches $5 \times 10^{-3} Scm^{-1}$ for 20 at.% Y and 20 at.% Ce, and $1.85 \times 10^{-1} Scm^{-1}$ for 40 at.% Y and 40 at.% Ce. The bulk activation energy does not vary much with Y content, and increases a bit more strongly with Ce content. The GB activation energy slightly decreases with Y content (**Figure 17**). Thus the increase of conductivity stems mainly from the increase of acceptor dopant concentration and therefore proton uptake.

The total conductivity at 600 $^{\circ}C$ from this work is in the range of data from literature (summarized in **Table 4** and shown in **Figure 18**). According to **Figure 18-(a)**, the total conductivity of BZY increases by about 2.5 orders of magnitude when the Y content increases from 0 to 20 at.% because of higher proton uptake. After reaching a peak value, the total conductivity decreases with further increased Y content due to larger BaO loss and Y

substitution as Y_{Ba} donor on the A-site (as evidenced by the lattice parameters). Also, increased lattice distortion might reduce proton mobility [116,131]. For BZY50 sample, the total conductivity decreases to a value comparable with BZY5. Also, the total conductivity at 600 °C increases slightly with Ce content (Figure 17). This can be related to the fact that Ce-rich materials have a higher degree of hydration in the high temperature range [60].

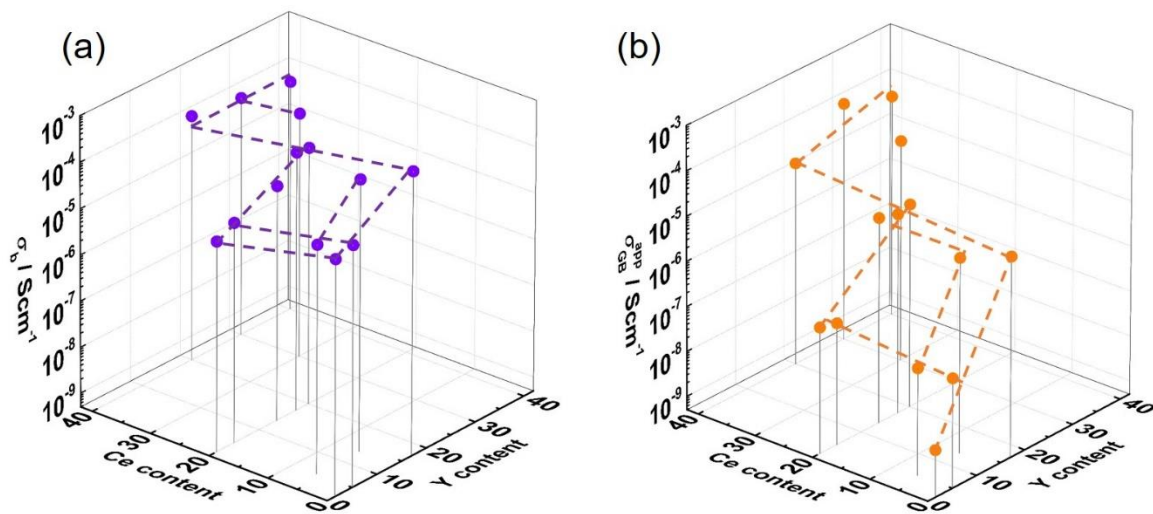


Figure 15: (a) bulk and (b) apparent GB conductivity versus Y and Ce content at 200 °C in 20 mbar H_2O partial pressure in N_2 . The dashed lines are only a guide for the eye.

Table 4: Conductivity of conventional sintering and SPS results from literature. Bulk and GB conductivity are extracted at 200 °C and the total conductivity are data from 600 °C.

Author	Composition	Sintering Conditions	Conductivity / Scm^{-1}			Measurement conditions
			σ_b	$\sigma_{\text{GB}}^{\text{app}}$	σ_{Total}	
D. Han <i>et al.</i> [132]	$\text{BaZr}_{0.98}\text{Y}_{0.02}\text{O}_{3-\delta}$	1600 °C 24 h in O_2	$\sim 8 \cdot 10^{-5}$	$\sim 1 \cdot 10^{-7}$	$\sim 1 \cdot 10^{-4}$	Wet H_2
	$\text{BaZr}_{0.95}\text{Y}_{0.05}\text{O}_{3-\delta}$		$\sim 2 \cdot 10^{-4}$	$\sim 1 \cdot 10^{-8}$	$\sim 9 \cdot 10^{-4}$	
	$\text{BaZr}_{0.9}\text{Y}_{0.1}\text{O}_{3-\delta}$		$\sim 7 \cdot 10^{-4}$	$\sim 8 \cdot 10^{-7}$	$\sim 8 \cdot 10^{-4}$	
	$\text{BaZr}_{0.85}\text{Y}_{0.15}\text{O}_{3-\delta}$		$\sim 7 \cdot 10^{-4}$	$\sim 1 \cdot 10^{-5}$	$\sim 6 \cdot 10^{-3}$	
	$\text{BaZr}_{0.8}\text{Y}_{0.2}\text{O}_{3-\delta}$		$\sim 7 \cdot 10^{-4}$	$\sim 1.5 \cdot 10^{-4}$	$\sim 1.2 \cdot 10^{-2}$	
	$\text{BaZr}_{0.75}\text{Y}_{0.25}\text{O}_{3-\delta}$		$\sim 7 \cdot 10^{-4}$	$\sim 1 \cdot 10^{-4}$	$\sim 8 \cdot 10^{-3}$	
P. Babilo <i>et al.</i> [95]	$\text{BaZr}_{0.8}\text{Y}_{0.2}\text{O}_{3-\delta}$	1600 °C 24 h in O_2			$7.9 \cdot 10^{-3}$	Wet N_2
D. Gao <i>et al.</i> [133]	$\text{BaZr}_{0.85}\text{Y}_{0.15}\text{O}_{3-\delta}$	1600 °C 4 h			$\sim 4 \cdot 10^{-3}$	Wet H_2
K. Park <i>et al.</i> [134]	$\text{BaZr}_{0.85}\text{Y}_{0.15}\text{O}_{3-\delta}$	1670 °C 24 h			$5.3 \cdot 10^{-3}$	Wet H_2/Ar
S. Le <i>et al.</i> [135]	$\text{BaZr}_{0.9}\text{Y}_{0.1}\text{O}_{3-\delta}$	1400 °C 24 h			$1.14 \cdot 10^{-3}$	Wet H_2
G. Reddy <i>et al.</i> [136]	$\text{BaZr}_{0.3}\text{Ce}_{0.4}\text{Y}_{0.2}\text{O}_{3-\delta}$	1450 °C 5 h			$9.61 \cdot 10^{-3}$	Wet air
K. D. Kreuer <i>et al.</i> [59]	$\text{BaZr}_{0.8}\text{Y}_{0.2}\text{O}_{3-\delta}$	1700 °C 10 h in O_2			$\sim 3 \cdot 10^{-2}$	Wet N_2
F. Iguchi <i>et al.</i> [69]	$\text{BaZr}_{0.95}\text{Y}_{0.05}\text{O}_{3-\delta}$	1800 °C 20 h			$\sim 5 \cdot 10^{-4}$	Wet air
	$\text{BaZr}_{0.9}\text{Y}_{0.1}\text{O}_{3-\delta}$				$\sim 9 \cdot 10^{-3}$	
	$\text{BaZr}_{0.85}\text{Y}_{0.15}\text{O}_{3-\delta}$				$\sim 2 \cdot 10^{-2}$	
F. Iguchi <i>et al.</i> [89]	$\text{BaZr}_{0.95}\text{Y}_{0.05}\text{O}_{3-\delta}$	1800 °C 24 h	$\sim 1.2 \cdot 10^{-4}$	$\sim 4 \cdot 10^{-7}$	$\sim 3 \cdot 10^{-3}$	Wet O_2/Ar
	$\text{BaZr}_{0.9}\text{Y}_{0.1}\text{O}_{3-\delta}$		$\sim 3.5 \cdot 10^{-4}$	$\sim 4.5 \cdot 10^{-5}$	$\sim 9 \cdot 10^{-3}$	
	$\text{BaZr}_{0.85}\text{Y}_{0.15}\text{O}_{3-\delta}$		$\sim 3 \cdot 10^{-3}$	$\sim 7 \cdot 10^{-4}$	$\sim 3 \cdot 10^{-2}$	
	$\text{BaZr}_{0.7}\text{Y}_{0.3}\text{O}_{3-\delta}$		$\sim 7 \cdot 10^{-4}$	$\sim 3 \cdot 10^{-5}$	$\sim 7 \cdot 10^{-3}$	
E. Fabbri <i>et al.</i> [131]	$\text{BaZr}_{0.8}\text{Y}_{0.2}\text{O}_{3-\delta}$	1600 °C 12 h	$\sim 9 \cdot 10^{-4}$	$\sim 8 \cdot 10^{-6}$	$\sim 4 \cdot 10^{-3}$	Wet H_2/Ar
	$\text{BaZr}_{0.7}\text{Y}_{0.3}\text{O}_{3-\delta}$		$\sim 6 \cdot 10^{-4}$	$\sim 3 \cdot 10^{-6}$	$\sim 1.2 \cdot 10^{-3}$	
	$\text{BaZr}_{0.6}\text{Y}_{0.4}\text{O}_{3-\delta}$		$\sim 2.5 \cdot 10^{-5}$	$\sim 1 \cdot 10^{-6}$	$\sim 7 \cdot 10^{-4}$	
	$\text{BaZr}_{0.5}\text{Y}_{0.5}\text{O}_{3-\delta}$		$\sim 8 \cdot 10^{-6}$	$\sim 9 \cdot 10^{-7}$	$\sim 4 \cdot 10^{-4}$	

Continued Table 4: Conductivity of conventional sintering and SPS results from literature. Bulk and GB conductivity are extracted at 200 °C and the total conductivity are data from 600 °C.

K. Katahira <i>et al.</i> [93]	$\text{BaCe}_{0.9}\text{Y}_{0.1}\text{O}_{3-\delta}$	1700 °C 10 h				$\sim 1.5 \cdot 10^{-2}$	Wet H ₂	
	$\text{BaZr}_{0.1}\text{Ce}_{0.8}\text{Y}_{0.1}\text{O}_{3-\delta}$					$\sim 1 \cdot 10^{-2}$		
	$\text{BaZr}_{0.2}\text{Ce}_{0.7}\text{Y}_{0.1}\text{O}_{3-\delta}$					$\sim 9 \cdot 10^{-3}$		
	$\text{BaZr}_{0.3}\text{Ce}_{0.6}\text{Y}_{0.1}\text{O}_{3-\delta}$					$\sim 6 \cdot 10^{-3}$		
	$\text{BaZr}_{0.4}\text{Ce}_{0.5}\text{Y}_{0.1}\text{O}_{3-\delta}$					$\sim 4.5 \cdot 10^{-3}$		
	$\text{BaZr}_{0.6}\text{Ce}_{0.3}\text{Y}_{0.1}\text{O}_{3-\delta}$		1750 °C 5 h					$\sim 2 \cdot 10^{-3}$
	$\text{BaZr}_{0.8}\text{Ce}_{0.1}\text{Y}_{0.1}\text{O}_{3-\delta}$							$\sim 1.5 \cdot 10^{-3}$
E. Fabbri <i>et al.</i> [137]	$\text{BaZr}_{0.9}\text{Y}_{0.1}\text{O}_{3-\delta}$	1800 °C 5 h				$\sim 1.5 \cdot 10^{-3}$	Wet H ₂	
	$\text{BaCe}_{0.8}\text{Y}_{0.2}\text{O}_{3-\delta}$	1500 °C 8 h				$\sim 1 \cdot 10^{-2}$		
	$\text{BaZr}_{0.3}\text{Ce}_{0.5}\text{Y}_{0.2}\text{O}_{3-\delta}$	1550 °C 8 h				$\sim 9 \cdot 10^{-3}$		
	$\text{BaZr}_{0.5}\text{Ce}_{0.3}\text{Y}_{0.2}\text{O}_{3-\delta}$					$\sim 3.5 \cdot 10^{-3}$		
	$\text{BaZr}_{0.8}\text{Y}_{0.2}\text{O}_{3-\delta}$	1600 °C 8 h				$\sim 2.5 \cdot 10^{-3}$		
Y. Fu <i>et al.</i> [138]	$\text{BaCe}_{0.9}\text{Y}_{0.1}\text{O}_{3-\delta}$	1400 °C 6 h				$2.4 \cdot 10^{-3}$	Wet H ₂	
C. Zuo <i>et al.</i> [139]	$\text{BaZr}_{0.1}\text{Ce}_{0.7}\text{Y}_{0.2}\text{O}_{3-\delta}$	1550 °C 10 h				$\sim 1.5 \cdot 10^{-2}$	Wet H ₂	
K. Leonard <i>et al.</i> [140]	$\text{BaZr}_{0.5}\text{Ce}_{0.4}\text{Y}_{0.1}\text{O}_{3-\delta}$	1600 °C 10 h				$\sim 6.5 \cdot 10^{-3}$	Wet H ₂	
	$\text{BaZr}_{0.45}\text{Ce}_{0.35}\text{Y}_{0.2}\text{O}_{3-\delta}$					$\sim 1.5 \cdot 10^{-2}$		
N. Nasani <i>et al.</i> [141]	$\text{BaZr}_{0.1}\text{Ce}_{0.7}\text{Y}_{0.2}\text{O}_{3-\delta}$	1500 °C 8 h				$\sim 1 \cdot 10^{-2}$	Wet N ₂	
	$\text{BaZr}_{0.4}\text{Ce}_{0.4}\text{Y}_{0.2}\text{O}_{3-\delta}$					$\sim 7 \cdot 10^{-3}$		
	$\text{BaZr}_{0.6}\text{Ce}_{0.2}\text{Y}_{0.2}\text{O}_{3-\delta}$					$\sim 1.5 \cdot 10^{-3}$		
M. Hakim <i>et al.</i> [142]	$\text{BaZr}_{0.3}\text{Ce}_{0.5}\text{Y}_{0.2}\text{O}_{3-\delta}$	1470 °C				$\sim 4 \cdot 10^{-3}$	Wet H ₂	
M. Shirpour <i>et al.</i> [87,123]	$\text{BaZr}_{0.85}\text{Y}_{0.15}\text{O}_{3-\delta}$	SPS: 1600 °C 5 min	$\sim 2 \cdot 10^{-3}$	$\sim 1 \cdot 10^{-4}$	$\sim 1 \cdot 10^{-2}$	Wet N ₂		
	$\text{BaZr}_{0.94}\text{Y}_{0.06}\text{O}_{3-\delta}$	Annealing: 1700 °C 20 h	$\sim 6.3 \cdot 10^{-4}$	$\sim 4 \cdot 10^{-6}$	$\sim 1 \cdot 10^{-3}$			
S. Ricote <i>et al.</i> [101]	$\text{BaZr}_{0.9}\text{Y}_{0.1}\text{O}_{3-\delta}$	SPS: 1700 °C 5 min	$\sim 5 \cdot 10^{-5}$	$\sim 5 \cdot 10^{-6}$	$\sim 1.5 \cdot 10^{-3}$	Wet H ₂ /N ₂		
J. Bu <i>et al.</i> [143]	$\text{BaZr}_{0.5}\text{Ce}_{0.3}\text{Y}_{0.2}\text{O}_{3-\delta}$	SPS: 1350 °C 5 min				$2.6 \cdot 10^{-3}$	Wet H ₂	

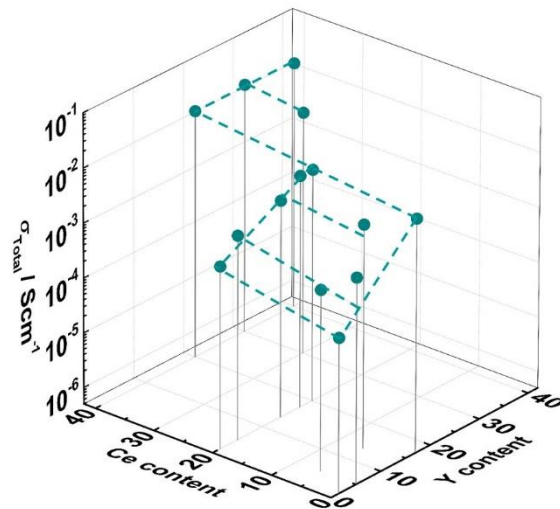


Figure 16: Total conductivity versus Y and Ce content at 600 °C in 20 mbar H_2O partial pressure in N_2 . The dashed lines are only a guide for the eye.

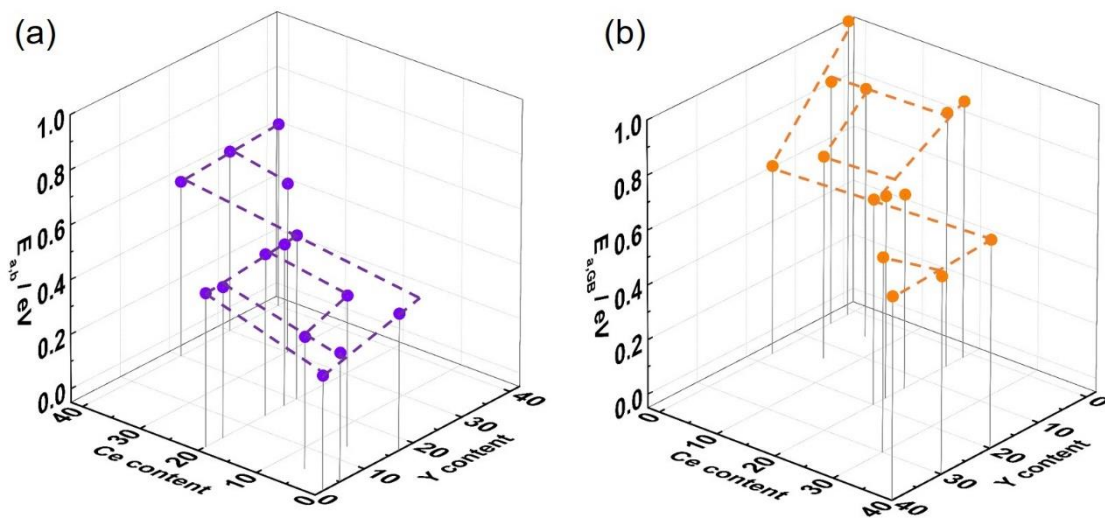


Figure 17: Bulk and GB activation energy (fitted from 100 °C to 350 °C) versus Y and Ce content from SPS samples. The Ce and Y content axes of GB activation energy plots were reversed. The dashed line are only a guide for the eye.

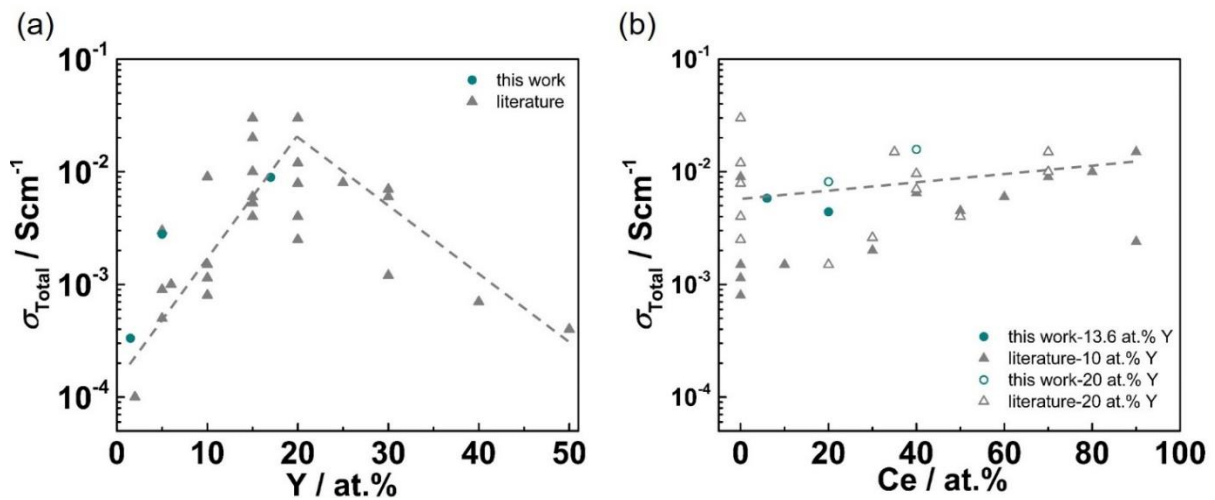


Figure 18: Comparison of total conductivity at 600 °C with data from literature. (a) versus Y content for BZY [59,69,87,89,93,95,101,123,131–137] and (b) versus Ce content for BZCY with 10/13.6 at.% Y (solid symbols) and 20 at.% Y (open symbols) [59,69,89,93,95,101,131,132,135–143]. The dashed lines are only a guide for the eye.

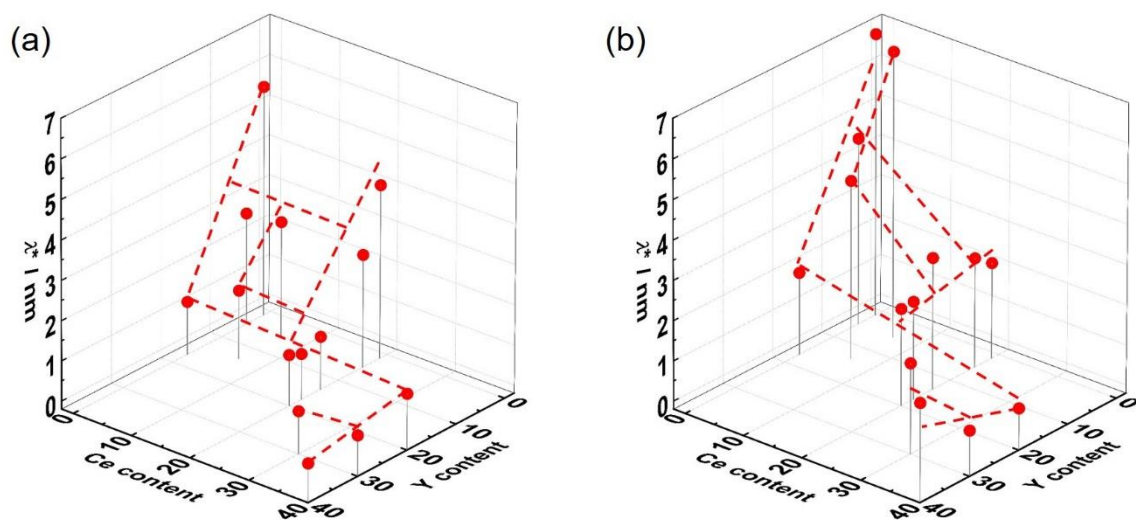


Figure 19: Space charge zone thickness extracted from (a) Debye length and space charge potential, and (b) brick layer model for SPS samples from the impedance spectra measured at 200 °C versus Y and Ce content. The Ce and Y content axis of both plots were reversed, dashed lines are only a guide for the eye.

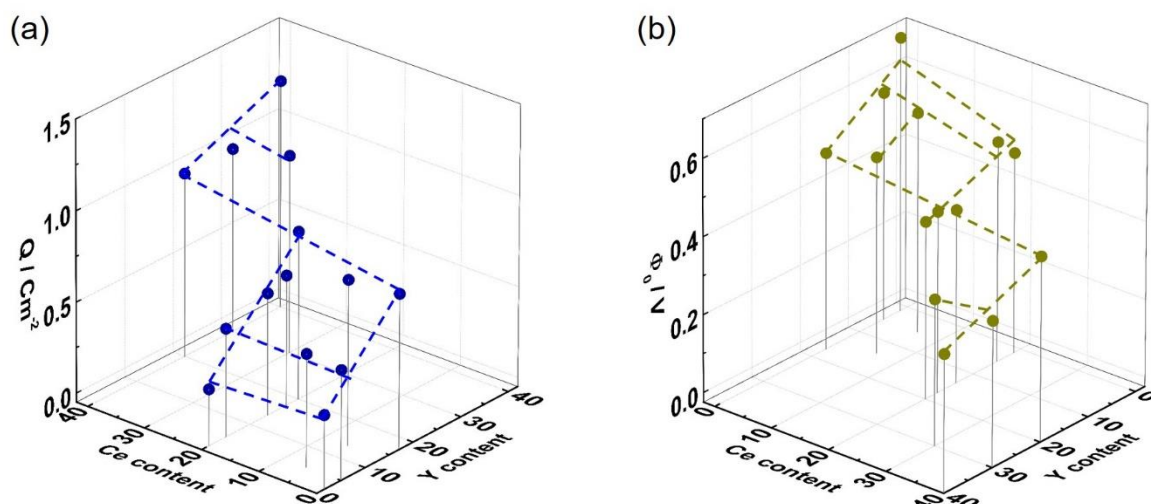


Figure 20: (a) core charge density and (b) space charge potential at 200 °C versus Y and Ce content from SPS samples. The Ce and Y content axis of the space charge potential plot were reversed. The dashed lines are only a guide for the eye. The space charge potential only slightly increases with temperature.

The space charge zone thickness and core charge density were calculated based on (i) Mott-Schottky case (i.e., assuming that the dopants are immobile, see **Eq. (7)**), and (ii) the brick layer model (C_b and C_{GB} in **Eq. (21)**). The space charge zone thickness calculated from the bulk and GB capacitance ratio is slightly larger than that obtained from the Debye length λ and space charge potential. The main factors affecting the depletion zone thickness are the space charge potential and Y content. The space charge zone thickness from the Mott-Schottky model decreases by a factor of 5 when the Y content increases from 1.5 at.% to 17 at.% (**Figure 19-(a)**), because λ decreases from 0.7 nm to 0.2 nm and Φ_0 decreases by ~ 0.2 V.

The core charge density calculated based on the Mott-Schottky model (**Eq. (10)**, **Figure 20-(a)**) increases by a factor of ~ 3.3 from BZC20Y1.5-SPS to BZC20Y20-SPS. But the apparent GB conductivity changes by about 4 orders of magnitude at 200 °C because of the decreased space charge potential (**Figure 20-(b)**). The space charge potential was extracted from the peak frequency ratio of bulk and GB (ω_b/ω_{GB}) from the impedance spectra (cf. **Eq. (11)**). The decreased space charge potential leads to a much less decreased proton concentration based on **Eq. (8)**. The space charge potential is slightly temperature dependent, e.g. typically increases by about 0.1 V from 100 °C to 300 °C.

3.1.5 Instability of the pellets related to Ce content

Even though the addition of Ce is beneficial for sinterability and provides a possibility of higher Y doping, Ce-rich samples tend to react with H₂O and/or CO₂ in air ^[144], and excessive Y induces too much lattice distortion (Y³⁺ ion is much bigger than Zr⁴⁺). As a result, the pellet decomposes and breaks into small pieces during storage, as shown in **Figure 21**. Therefore, 20 at.% Ce was chosen for this thesis. 13.6 at.% Y was used in main part of SSRS and alkaline and phosphate decoration, some higher Y contents were used for membrane fabrication.



Figure 21: Photo from sample BZC30Y30-SPS after a few weeks.

3.2 Solid state reactive sintering

3.2.1 Perovskite formation and sintering

3.2.1.1 Phase formation and micro-strain

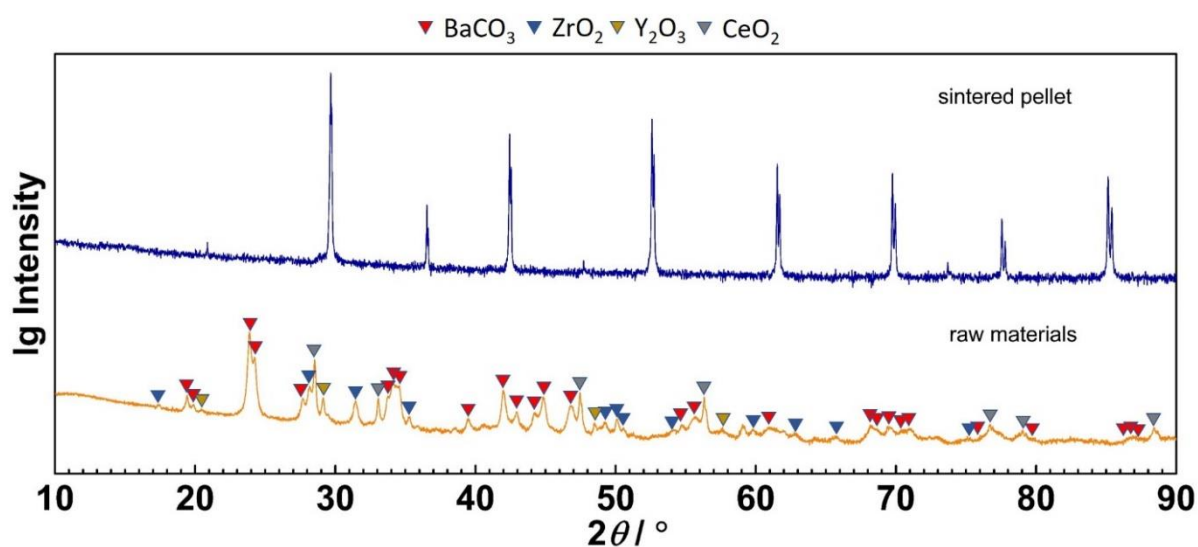


Figure 22: XRD patterns from (a) mixture of raw materials with nominal 1.0 wt.% NiO relative to BZC20Y13.6 and (b) BZC20Y13.6-1.0Ni sintered at 1550 °C 4 h.

Figure 22 shows an example of XRD patterns from the raw materials ball milled together, and the sintered ceramic. BaCO₃, ZrO₂, CeO₂ and Y₂O₃ were detected in the raw materials (no NiO due to its low content), which means that there was no phase formation or decomposition during the wet ball milling. Then without any further calcination, the green pellets were directly sintered at 1450 – 1600 °C. In the XRD pattern, no phase belonging to the raw materials was observed, and only sharp peaks ascribed to the cubic BZCY perovskite structure were observed above 1450 °C. However, the transient BaY₂NiO₅ phase indicated in literature ^[107,108,113,145] was not detected in the samples in this work because of the low NiO content used.

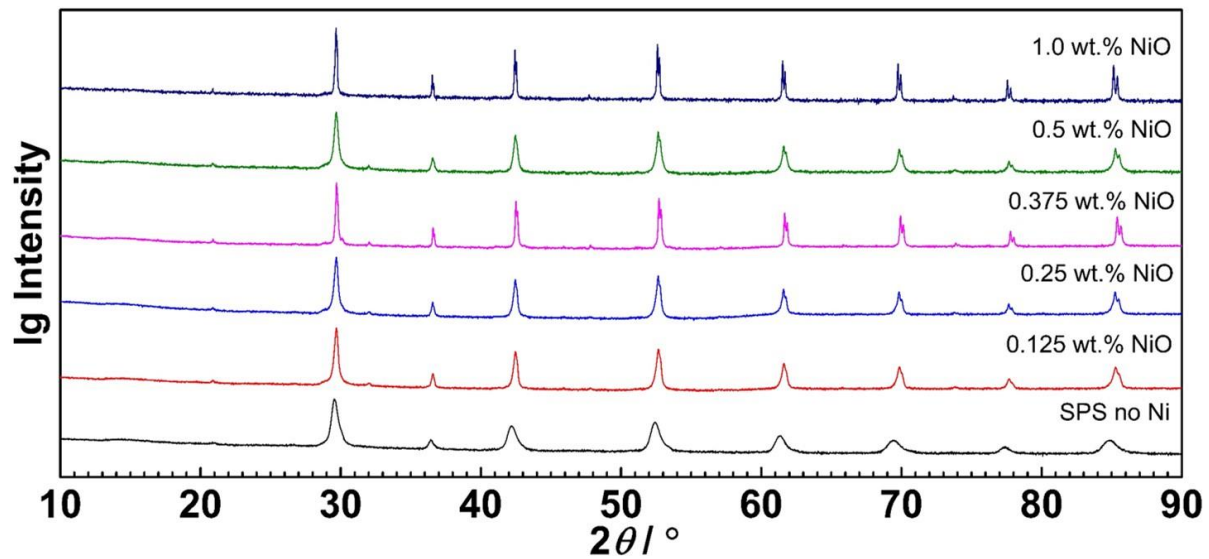


Figure 23: XRD patterns of SPS sample BZC20Y13.6-SPS without Ni (1400 °C 5 min and annealed at 1500 °C 4 h), and SSRS samples BZC20Y13.6 with varying NiO addition (sintered 4 h at 1550 °C).

Even a small amount of NiO used in SSRS can already result in a single perovskite phase (more details in section 3.2.1.6). **Figure 23** shows that the peaks become sharper with higher Ni content, indicating less internal micro-strain. Especially between 85 – 86 °, the two peaks from Cu $K_{\alpha 1}$ and $K_{\alpha 2}$ can be recognized more clearly when the NiO content increases. The micro-strain was quantified by Williamson-Hall analysis, the result is shown in **Figure 24**. Without NiO, the pellets have a high micro-strain of 0.4 %. The micro-strain decreases with NiO content, especially from 0 – 0.25 wt.% it reduces by about 80 %, and disappears when the NiO content exceeds 0.25 wt.%. Clearly, the amount of transient $(\text{Ba}, \text{Y}, \text{Ni})\text{O}_x$ liquid phase is vital to release the inner strain in the ceramics. For $\text{NiO} \leq 0.25$ wt.%, the volume of the transient liquid phase is very low (0.25 wt.% NiO corresponds to 0.75 – 1.5 vol.% transient liquid phase). Therefore, the liquid phase does not suffice to release all lattice distortion. For high NiO content, due to the higher transient liquid phase volume, the effective ion mobility is higher.

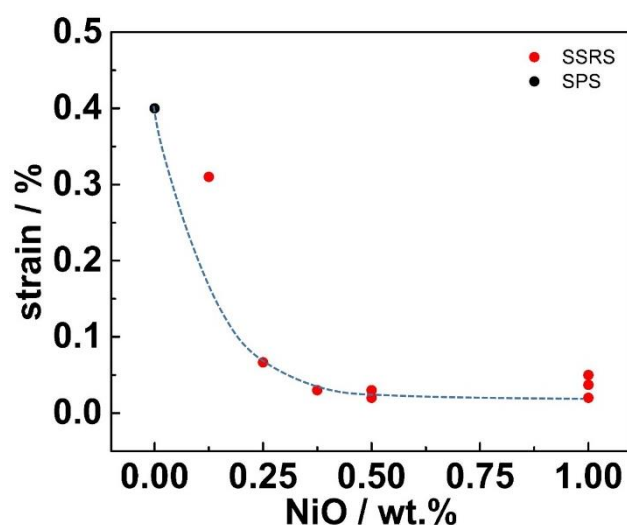


Figure 24: Micro-strain calculated by Williamson-Hall analysis versus NiO content. The Ni-free sample is BZC20Y13.6-SPS sintered at 1400 °C 5 min and annealed at 1500 °C 4 h. The SSRS samples were sintered at 1550 °C 4 h. The dashed line is only a guide for the eye.

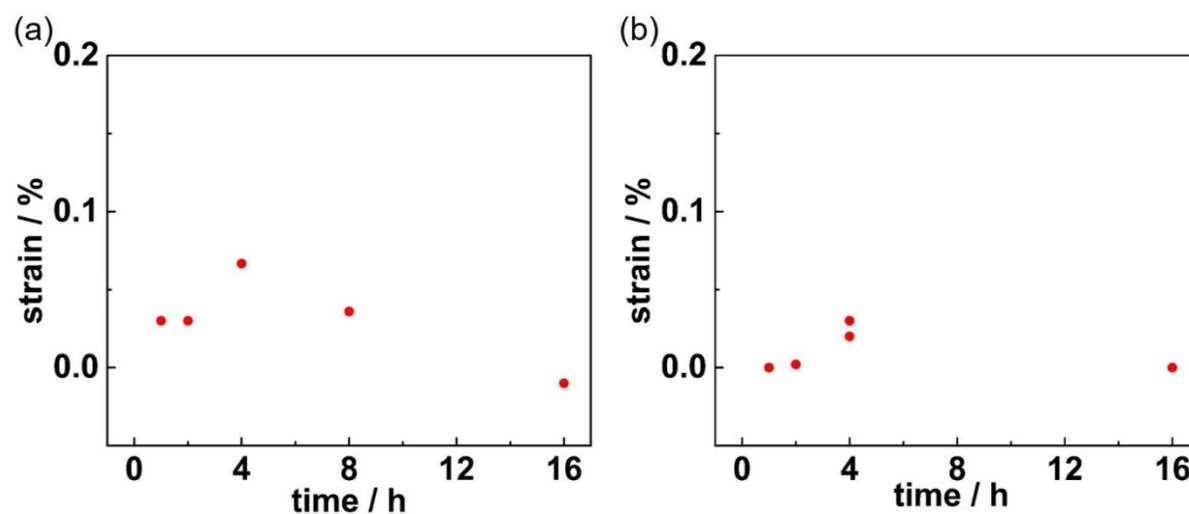


Figure 25: Micro-strain versus soaking time at 1550 °C with composition of (a) BZC20Y13.6-0.25Ni and (b) BZC20Y13.6-0.5Ni.

The soaking time dependence of the micro-strain is not very pronounced, the data in **Figure 25** rather indicate the scattering with the uncertainty range. The typical error bar of micro-strain is 0.03%.

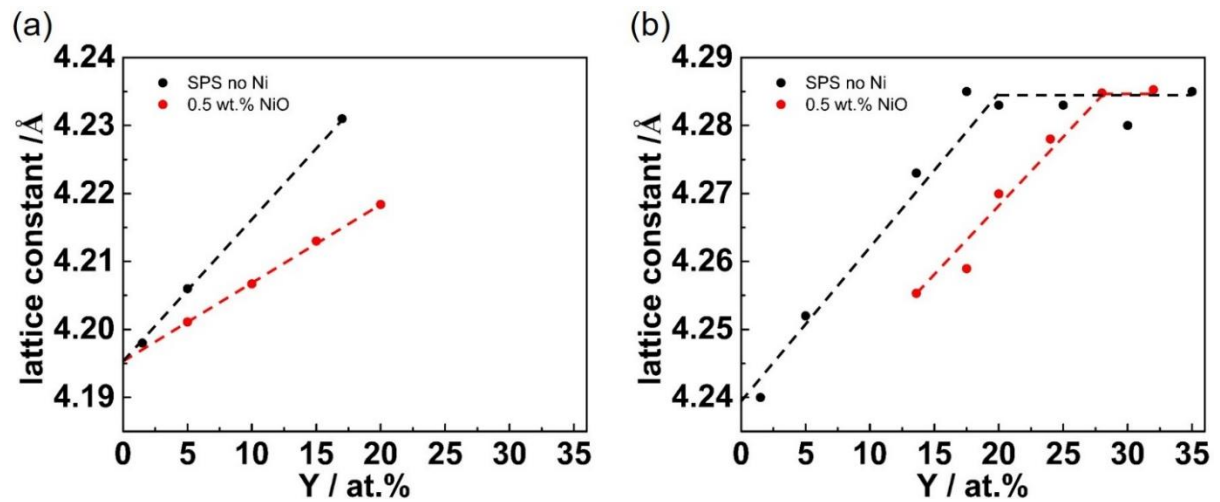


Figure 26: Lattice constant versus Y content for SSRS samples with 0.5 wt.% NiO and SPS samples without Ni from (a) BZY (the data of SSRS samples are from ref. [146], sintered at 1550 °C 16 h) and (b) BZC20Y. The BZC20Y-0.5Ni samples were sintered at 1550 C ° 4 h (13.6 at.% Y) and 8 h.

The lattice constants of BZY and BZC20Y samples with 0.5 wt.% NiO or without NiO are summarized in **Figure 26**. For both BZY and BZC20Y, the lattice constants increase linearly with the nominal Y content. For BZC20Y, high Y contents up to 35 at.% were tested. The lattice parameters level off at the same value of $\sim 4.285 \text{ \AA}$ for BZC20Y28-0.5Ni and BZC20Y20-SPS. The lattice constants from the Ni-free samples are always larger than those of SSRS samples for a given Y content, as shown also in **Figure 27**. Y. Yamazaki *et al.* [94] and K. D. Kreuer *et al.* [147] concluded that the B site acceptor dopant changes its position to become a donor on the A site when there is a Ba-deficiency, resulting in a decreased lattice constant and effective dopant concentration. In this case, $r_{\text{Ba}^{2+}} = 1.61 \text{ \AA} > r_{\text{Y}^{3+}} = 1.25 \text{ \AA}$ on the A site (coordinated by 12 O) and $r_{\text{Y}^{3+}} = 0.9 \text{ \AA} > r_{\text{Ce}^{4+}} = 0.87 \text{ \AA} > r_{\text{Zr}^{4+}} = 0.72 \text{ \AA}$ on the B site (coordinated by 6 O) [148]. The decrease of the lattice constant indicates that Ni addition drags Ba^{2+} out from the lattice and Y^{3+} moves on the A-site with a ion radius mismatch of 0.36 \AA between Ba^{2+} and Y^{3+} . The lattice constants of SPS samples with Ni on the B site show less decrease because of the smaller size difference between Ni^{2+} (0.69 \AA) and Zr^{4+} .

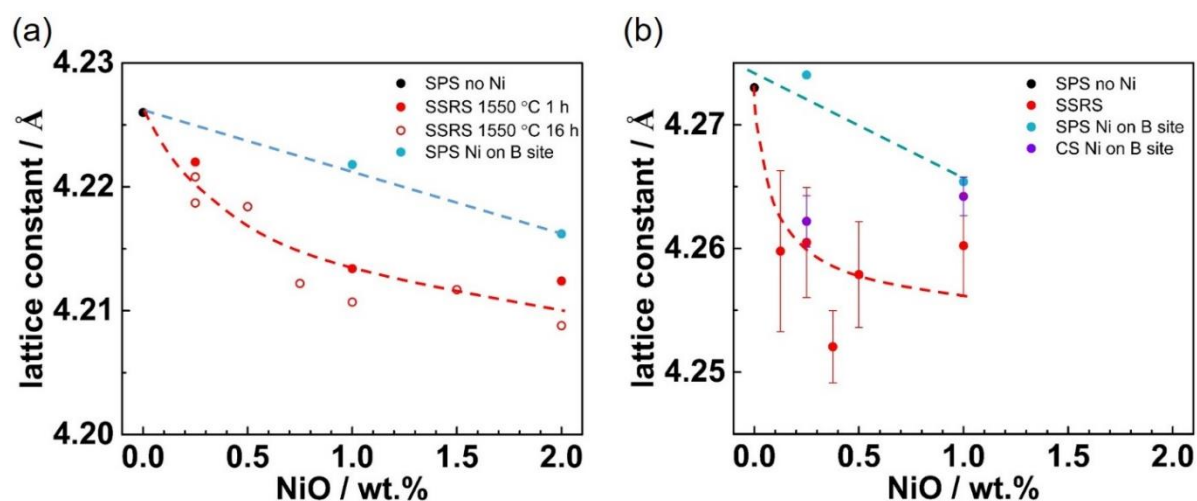


Figure 27: Lattice constant versus NiO content for (a) BZY20 (data from ref. ^[146]) and (b) BZC20Y13.6. The average lattice constants and corresponding error bars of BZC20Y13.6 SSRS, BZC20Y13.6Ni1-CS and BZC20Y13.6Ni4-CS samples were calculated from several samples obtained.

Interestingly, the lattice constants increase more sharply with Y content for Ni-free BZY than for BZY-0.5Ni (see **Figure 26-(a)**), whereas the slopes are more similar for BZC20Y-SPS and BZC20Y-0.5 wt.% (see **Figure 26-(b)**). In the case of BZC20Y, the existence of Ce^{4+} already expands the lattice, therefore, Y^{3+} is less oversized on the B site relative to (Zr, Ce) which decreases the driving force for changing to the A site. As shown in **Figure 26-(b)**, the lattice constant of SSRS samples can reach the same maximum value compared to Ni-free samples but at a higher Y content. This already gives a hint that the decreased effective dopant concentration can be compensated by a higher nominal dopant content, which will be discussed in more details in section 3.2.4.

Another interesting point is that the lattice constants of BZY20-*n*Ni smoothly decreases with NiO content, but for BZC20Y13.6 after a first strong drop from BZC20Y13.6-SPS to BZC20Y13.6-0.125Ni, it remains almost constant (0.125 wt.% NiO to 1.0 wt.% NiO) but with large scatter. It suggests that for BZCY, which contains one more B site element, it is more difficult to distribute all elements homogeneously (see next section), which could also help to explain the difficulty of reproducibility of the GB conductivity measurement (see section 3.3.1 and 3.3.5).

3.2.1.2 Chemical composition

Overall chemical compositions measured by ICP-OES are summarized in **Table 5**. BZCY pellets from SSRS and BZCY with Ni on the B site sintered by SPS show a good agreement with the nominal composition. The Ba content is 1 within the error bar, indicating no significant Ba loss during SPS sintering and post-annealing. Typically after sintering, the sacrificial powder covering the pellet turns dark, which can be ascribed to Ni diffusion from the pellet (NiO evaporation is excluded because the lid of the crucible does not change color). Therefore it is necessary to compare the remaining NiO content with the nominal one in particular for SSRS samples. As shown in **Figure 28-(a)**, the NiO content does not vary with Y content and stays at the nominal value of 0.5 wt.%. However, when comparing the remaining NiO content versus nominal NiO content (see **Figure 28-(b)**), it can be clearly seen that for NiO content \leq 0.5 wt.% the real NiO content is comparable to the nominal value, but for 1.0 wt.% NiO, it is about 0.5 wt.% lower. This can also explain why the average lattice constant of BZC20Y13.6-1.0Ni is only slightly different from BZC20Y13.6-0.5Ni (**Figure 27-(b)**). **Table 6** compares the real NiO content with soaking time at 1550 °C for nominally 1.0 wt.% NiO. Already after 1 h, about 0.4 wt.% NiO is lost, and further decreases with time, leaving 0.48 wt.% after 16 h.

Table 5: Composition of pellets sintered by SSRS and SPS with Ni on B site. SSRS samples with 13.6 at.% Y were sintered at 1550 °C 4 h and samples with higher Y content were sintered at 1550 °C 8 h. SPS samples were sintered at 1350 °C and 1300 °C for 1 at.% and 4 at.% Ni, respectively and annealed at 1400 °C 4 h.

Nominal Composition	Measurement by ICP-OES / wt.%					Real composition	A: B ratio
	Ba	Zr	Ce	Y	Ni		
BZC20Y13.6-0.125Ni	48.5 ±0.5	20.7 ±0.3	9.61 ±0.1	4.12 ±0.05	0.126 ±0.009	Ba _{1.02} Zr _{0.66} Ce _{0.20} Y _{0.13} Hf _{0.01} O _{3-δ} + 0.16 wt.% NiO	1.02
BZC20Y13.6-0.25Ni	48.4 ±0.5	20.5 ±0.3	9.69 ±0.1	4.11 ±0.05	0.163 ±0.01	Ba _{1.03} Zr _{0.66} Ce _{0.20} Y _{0.13} Hf _{0.01} O _{3-δ} + 0.21 wt.% NiO	1.03
BZC20Y13.6-0.375Ni	48.2 ±0.5	21.5 ±0.3	9.02 ±0.1	4.59 ±0.06	0.344 ±0.01	Ba _{0.99} Zr _{0.67} Ce _{0.18} Y _{0.15} Hf _{0.01} O _{3-δ} + 0.44 wt.% NiO	0.99
BZC20Y13.6-0.5Ni	48.2 ±0.5	20.6 ±0.3	9.55 ±0.1	4.01 ±0.09	0.35 ±0.03	Ba _{1.03} Zr _{0.66} Ce _{0.20} Y _{0.13} Hf _{0.01} O _{3-δ} + 0.45 wt.% NiO	1.03
BZC20Y13.6-1.0Ni	48.2 ±0.5	20.7 ±0.3	9.78 ±0.1	4.01 ±0.05	0.41 ±0.03	Ba _{1.01} Zr _{0.66} Ce _{0.20} Y _{0.13} Hf _{0.01} O _{3-δ} + 0.52 wt.% NiO	1.02
BZC20Y17.5-0.5Ni	48.1 ±0.5	19.9 ±0.2	9.67 ±0.1	5.11 ±0.06	0.323 ±0.01	Ba _{1.00} Zr _{0.63} Ce _{0.20} Y _{0.17} Hf _{0.01} O _{3-δ} + 0.41 wt.% NiO	1.01
BZC20Y20-0.5Ni	48.3 ±0.5	18.9 ±0.2	9.73 ±0.1	6.1 ±0.07	0.371 ±0.004	Ba _{1.01} Zr _{0.60} Ce _{0.20} Y _{0.20} Hf _{0.01} O _{3-δ} + 0.47 wt.% NiO	1.02
B100ZC20Y20-0.5Ni	47.9 ±0.5	18.8 ±0.2	9.72 ±0.1	6.13 ±0.07	0.367 ±0.004	Ba _{1.01} Zr _{0.59} Ce _{0.20} Y _{0.20} Hf _{0.01} O _{3-δ} + 0.47 wt.% NiO	1.01
BZC20Y24-0.5Ni	48.3 ±0.5	17 ±0.2	9.74 ±0.1	7.27 ±0.08	0.392 ±0.01	Ba _{1.04} Zr _{0.55} Ce _{0.20} Y _{0.24} Hf _{0.01} O _{3-δ} + 0.50 wt.% NiO	1.04
B100ZC20Y24-0.5Ni	48.1 ±0.5	17.6 ±0.2	9.81 ±0.1	7.36 ±0.08	0.429 ±0.01	Ba _{1.01} Zr _{0.55} Ce _{0.20} Y _{0.24} Hf _{0.01} O _{3-δ} + 0.55 wt.% NiO	1.01
BZC20Y28-0.5Ni	48.4 ±0.5	16.3 ±0.2	9.77 ±0.1	8.65 ±0.09	0.426 ±0.005	Ba _{1.01} Zr _{0.51} Ce _{0.20} Y _{0.28} Hf _{0.01} O _{3-δ} + 0.55 wt.% NiO	1.02
B100ZC20Y28-0.5Ni	48.0 ±0.5	16.4 ±0.2	9.85 ±0.1	8.69 ±0.08	0.452 ±0.005	Ba _{1.00} Zr _{0.51} Ce _{0.20} Y _{0.28} Hf _{0.01} O _{3-δ} + 0.58 wt.% NiO	1.00
BZC20Y32-0.5Ni	48.2 ±0.5	15.0 ±0.2	9.71 ±0.1	9.72 ±0.1	0.394 ±0.004	Ba _{1.02} Zr _{0.48} Ce _{0.20} Y _{0.32} Hf _{0.01} O _{3-δ} + 0.50 wt.% NiO	1.02
B100ZC20Y32-0.5Ni	48.2 ±0.5	14.9 ±0.2	9.68 ±0.1	9.82 ±0.1	0.407 ±0.005	Ba _{1.02} Zr _{0.47} Ce _{0.20} Y _{0.32} Hf _{0.01} O _{3-δ} + 0.52 wt.% NiO	1.02
BZC20Y13.6Ni1-SPS	48.0 ±0.5	20.6 ±0.3	9.85 ±0.1	4.56 ±0.09	0.25 ±0.01	Ba _{0.99} Zr _{0.64} Ce _{0.20} Y _{0.14} Ni _{0.01} Hf _{0.01} O _{3-δ}	0.99
BZC20Y13.6Ni4-SPS	47.8 ±0.5	20.1 ±0.3	9.88 ±0.1	4.47 ±0.09	0.56 ±0.04	Ba _{0.99} Zr _{0.62} Ce _{0.20} Y _{0.14} Ni _{0.03} Hf _{0.01} O _{3-δ}	0.99

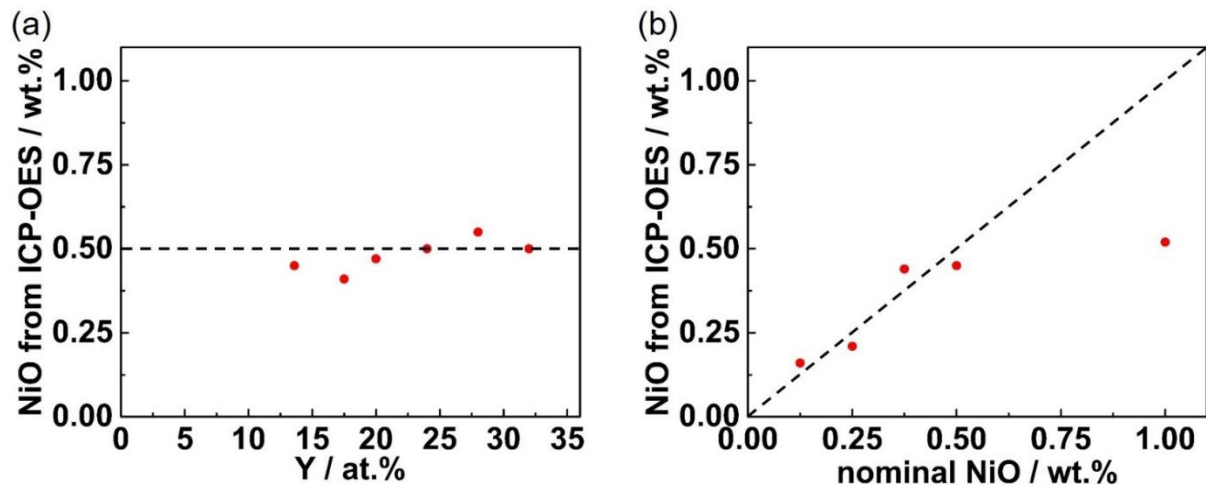


Figure 28: NiO content measured from ICP-OES versus (a) Y content and (b) nominal NiO content. BZC20Y13.6 SSRS samples were sintered at 1550 °C 4 h and others were sintered at 1550 °C 16 h. The dashed lines indicate the nominal NiO content.

Table 6: Composition of BZC20Y13.6-1.0Ni sintered at 1550 °C for different time.

Sintering time / h	Measurement by ICP-OES / wt.%					Real composition	A: B ratio
	Ba	Zr	Ce	Y	Ni		
1	48.2 ±0.5	21.6 ±0.3	9.68 ±0.1	4.19 ±0.06	0.487 ±0.005	Ba _{0.99} Zr _{0.67} Ce _{0.19} Y _{0.13} Hf _{0.01} O _{3-δ} + 0.62 wt.% NiO	0.99
4	48.2 ±0.5	20.7 ±0.3	9.78 ±0.1	4.01 ±0.05	0.41 ±0.03	Ba _{1.02} Zr _{0.66} Ce _{0.20} Y _{0.13} Hf _{0.01} O _{3-δ} + 0.52 wt.% NiO	1.02
16	48.1 ±0.5	20.8 ±0.3	9.67 ±0.1	4.19 ±0.17	0.377 ±0.007	Ba _{1.01} Zr _{0.66} Ce _{0.20} Y _{0.14} Hf _{0.01} O _{3-δ} + 0.48 wt.% NiO	1.01

3.2.1.3 Using YSZ as raw material

Y can be introduced into BZCY either from Y₂O₃ or from YSZ, where the latter is less sensitive to forming hydroxides. Thus, both sources are compared here. **Figure 29** shows comparison of the relative density versus sintering temperature when using YSZ powder (a solid solution of ZrO₂-Y₂O₃) and separate ZrO₂ and Y₂O₃. For both Zr and Y sources, the relative density increases with sintering temperature, and is slightly higher for separate ZrO₂ and Y₂O₃, especially at 1400 °C. This could be related to the fact that from YSZ, the Y first needs to be

excorporated from the YSZ solid solution to form the transient $(\text{Ba,Ni,Y})\text{O}_x$ liquid phase. Therefore, in the SSRS part, ZrO_2 and Y_2O_3 were used instead of YSZ.

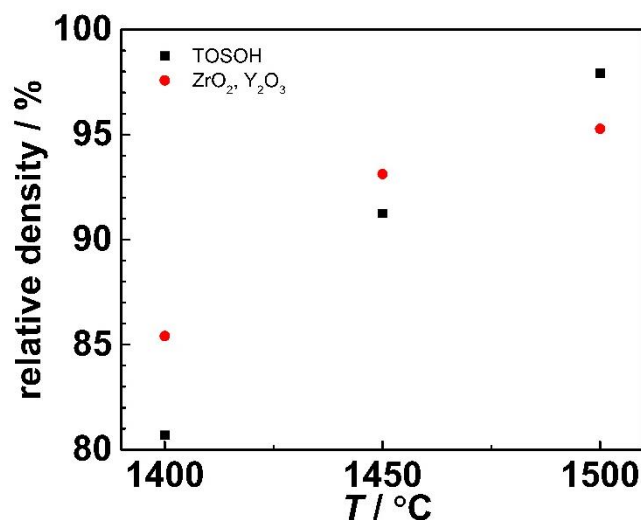


Figure 29: Relative density using TOSOH or ZrO_2 and Y_2O_3 as raw materials versus sintering temperature. The nominal composition is BZC20Y13.6-1.0Ni. All the samples were sintered for 4 h.

3.2.1.4 Other possible SSRS-related sintering procedures

A so-called “hybrid” SSRS method was also attempted. “Hybrid” SSRS means that after obtaining phase pure BZCY powder, ball milled SSRS raw materials powder with 1.0 wt.% NiO was mixed together with a mole ratio of $n(\text{BZCY}):n(\text{SSRS}) = 2:1$ or $1:2$, corresponding to ~ 0.33 and 0.66 wt.% NiO with respect to the cation stoichiometry. As shown in **Figure 30**, the sample does not fully densify even at 1550 °C, indicating that the presence of pre-formed perovskite is detrimental for successful SSRS.

In the context of membrane fabrication at IEK-1 in Jülich, another sintering procedure was tried to decrease the volume shrinkage. BZCY starting raw powders were dry ball milled for 1 h and then pre-calcined at 1100 °C for 4 h. This largely decomposes the BaCO_3 , but the perovskite is not fully formed. After wet milling with NiO this approach yields comparable densities as pure SSRS with same nominal composition (**Figure 31-(a)**). This method decreases the volume shrinkage by about 40% during sintering (**Figure 31-(b)**), which is beneficial for membrane fabrication and was used in section 3.4.

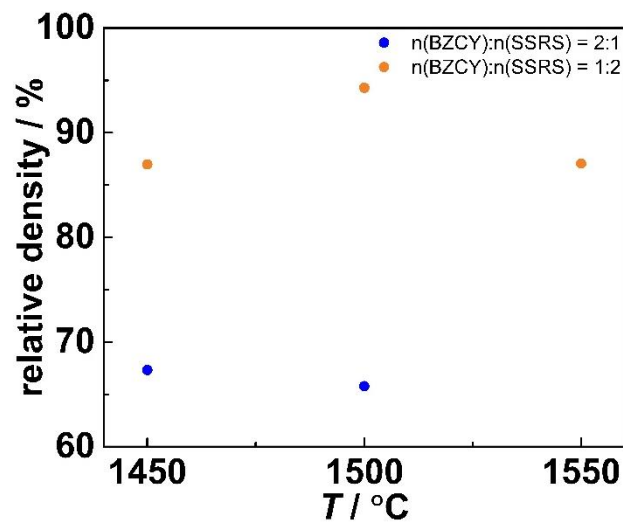


Figure 30: Relative density of samples sintered by “hybrid” SSRS versus sintering temperature. All the samples were sintered for 4 h.

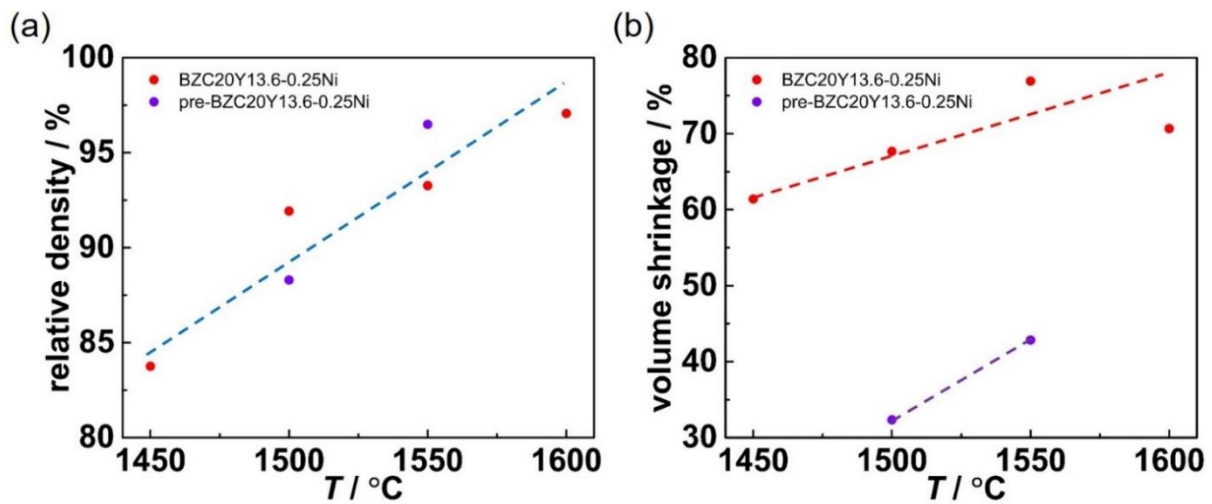


Figure 31: (a) relative density and (b) volume shrinkage comparison of BZC20Y13.6-0.25Ni and pre-BZC20Y13.6-0.25Ni versus sintering temperature. All samples were sintered for 4 h.

3.2.1.5 Sintering behavior of SSRS samples

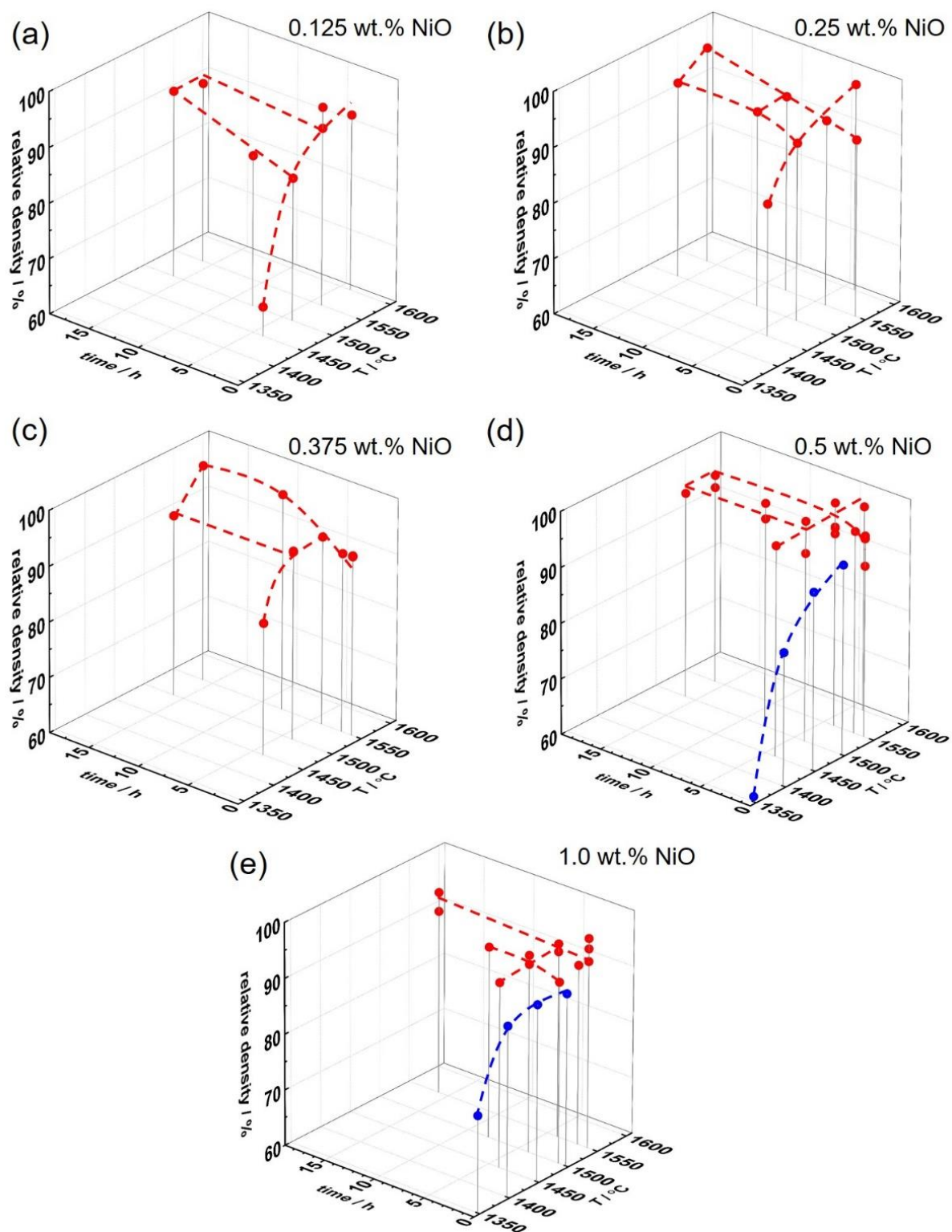


Figure 32: Relative density of SSRS samples versus sintering temperature and soaking time for BZC20Y13.6 with different NiO addition. The red and blue dots refer to the samples sintered with a heating and cooling rate of 200 °C/h and 600 °C/h, respectively. The dashed lines are only a guide for the eye.

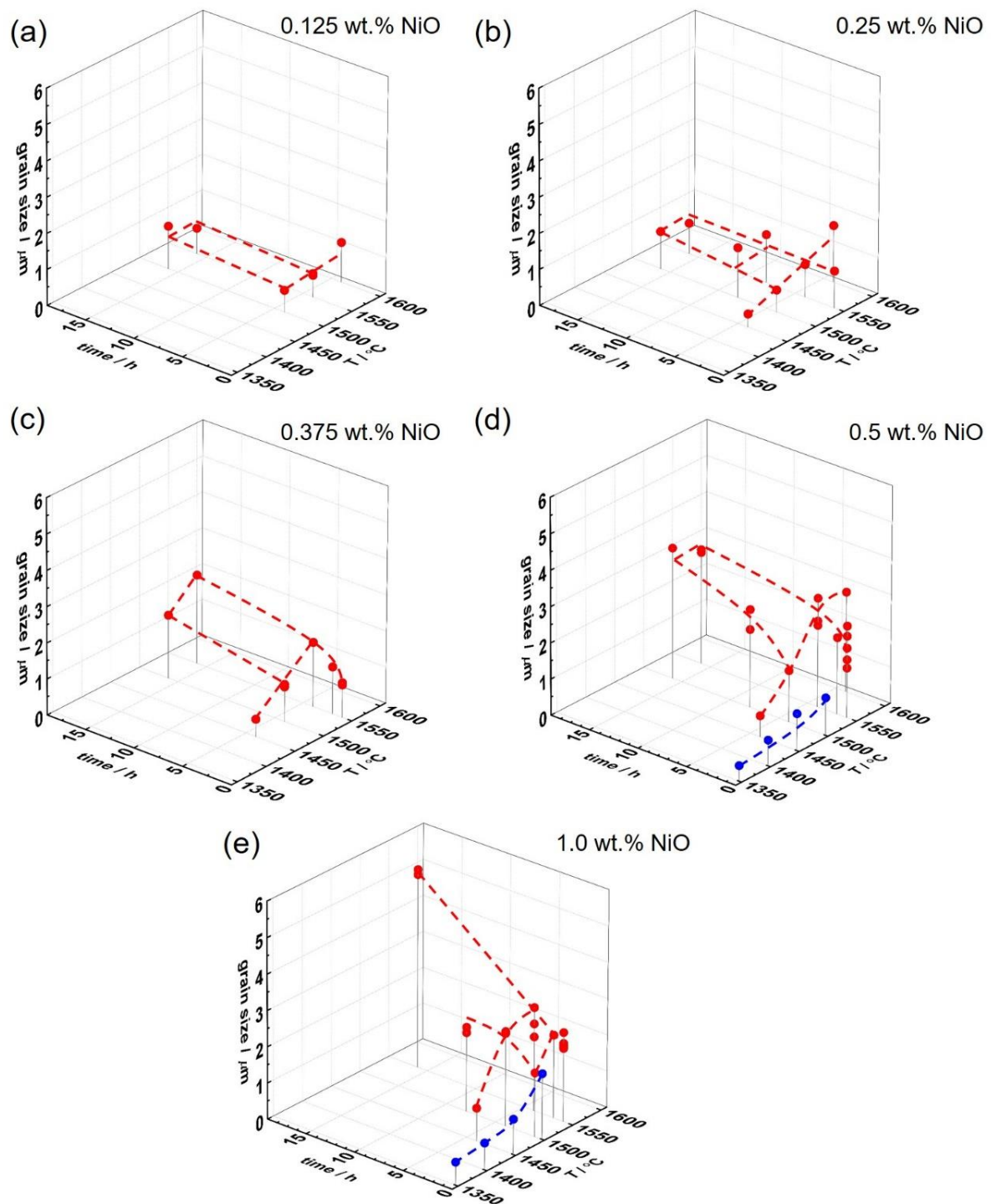


Figure 33: Grain size of SSRS samples versus sintering temperature and soaking time for BZC20Y13.6 with different NiO addition. The red and blue dots refer to the samples sintered with a heating and cooling rate of 200 $^{\circ}\text{C}/\text{h}$ and 600 $^{\circ}\text{C}/\text{h}$, respectively. The dashed lines are only a guide for the eye.

The relative density and grain size for samples with different NiO content are summarized in **Figure 32** and **Figure 33**. 1.0 wt.% NiO corresponds to 3 – 6 vol.% liquid phase when NiO is fully converted to BaNiO₂ and/or BaY₂NiO₅. As shown in **Figure 32-(a)** and **Figure 32-(b)**, with small NiO addition (≤ 0.25 wt.%) high sintering temperature and long soaking time are required to fully densify the ceramics. Because of insufficient transient liquid phase (0.125 wt.% NiO provides only 1.5 vol.% liquid phase) the grain size remains small at $\approx 1 \mu\text{m}$ even when sintered at 1600 °C (**Figure 33-(a)** and **Figure 33-(b)**). When the NiO content increases to 0.375 wt.%, a sintering temperature of at least 1500 °C is required to get $\geq 90\%$ relative density (**Figure 32-(c)**). The grains tend to grow with temperature and time and the grain size is 2.5 μm after 16 h at 1550 °C, as shown in **Figure 33-(c)**. Further increasing the NiO content to 0.5 and 1.0 wt.%, the pellets are fully densified above 1450 °C owing to sufficient liquid phase volume (**Figure 32-(d)** and **Figure 32-(e)**). As can be seen from **Figure 33-(d)** and **Figure 33-(e)**, the grains grow significantly with increasing temperature and soaking time up to about 3.5 and 6 μm . There is no doubt that the amount of NiO strongly influences the sintering behavior: the higher the NiO content, the better densification and the larger the grain size.

In order to further understand the mechanism, a fast sintering experiment for BZC20Y13.6-0.5Ni and BZC20Y13.6-1.0Ni with high nominal heating and cooling rate of 600 K/h was applied, trying to preserve the transient liquid phase. However, because it is difficult to reach the nominal cooling rate of 600 K/h in the oven, more detailed discussion about the sintering mechanism will be shown in section 3.2.1.6 from quenching experiments. As shown in **Figure 32-(d)**, the pellets sintered at 1350 °C show a rather low relative density of $\sim 60\%$. The relative density increases significantly with temperature and reaches $\sim 90\%$ at 1500 °C. In contrast, with 1.0 wt.% NiO the relative density is already $\sim 90\%$ at 1350 °C and increases smoothly to near 100% at 1500 °C. So more liquid phase is formed at a lower temperature for higher NiO content (< 1350 °C for 1.0 wt.% NiO and 1400 °C for 0.5 wt.% NiO). The lattice constants for both NiO contents reach the value of pellets sintered with a heating and cooling rate of 200 K/h ($\approx 4.26 \text{ \AA}$). Only BZC20Y13.6-0.5Ni sintered at 1350 °C has 3.2 wt.% of undoped BaZrO₃ phase (see **Figure 34-(a)**). **Figure 34-(b)** shows that, the grain size of fast sintering pellets increases slightly with temperature (from $\sim 0.5 \mu\text{m}$ to $\sim 1.5 \mu\text{m}$ from 1350 to 1500 °C) in a similar manner for samples with slower or faster heating rate.

Comparing the relative density (**Figure 32-(d)** and **Figure 32-(e)**), lattice constant (**Figure 34-(a)**) and grain size (**Figure 34-(b)**), one can conclude that the perovskite structure formation is

easier than densification and grain growth, and the pure perovskite phase can be obtained at low temperature (1350 °C) with sufficient NiO content. The grain growth is rather difficult and time-consuming even with high liquid phase volume. For ≤ 0.25 wt.% NiO, the grain growth is almost absent although at high temperature dense samples are obtained.

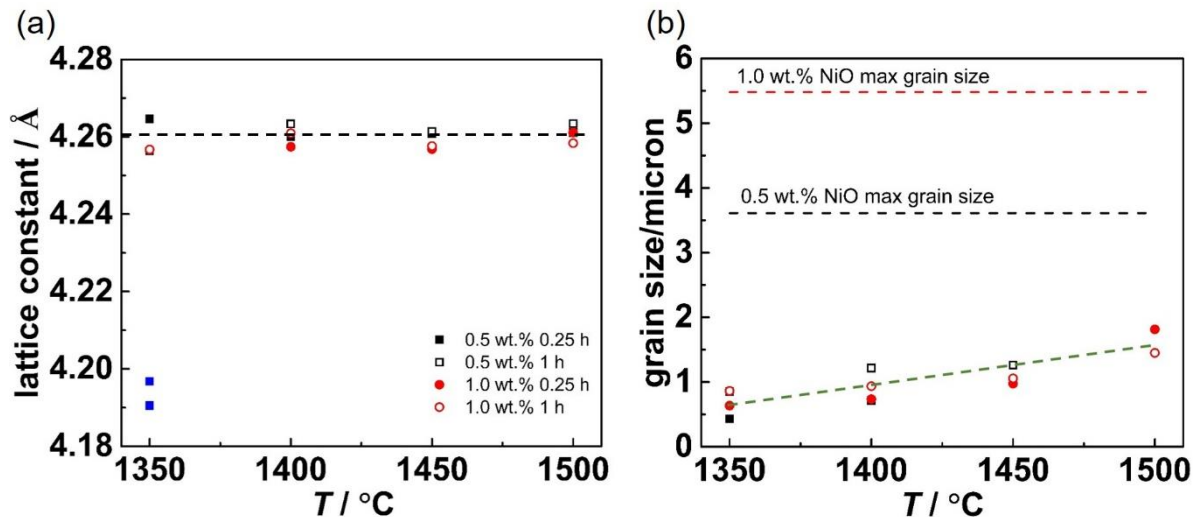


Figure 34: Lattice constant and grain size of BZC20Y13.6 with varying NiO addition versus sintering temperature for samples with 0.5 and 1.0 wt.% NiO sintered for 15 min and 1 h. The blue dots indicate a small amount of nominally undoped BaZrO₃ for 0.5 wt.% NiO.

Top-view SEM images from Ni-free SPS samples and SSRS samples with different NiO content are shown in **Figure 35**. For Ni-free samples, the grain size is small ~ 0.5 μm and shows a rather uniform grain size distribution (**Figure 35-(a)**). For a small addition of NiO (0.25 wt.%) in **Figure 35-(b)**, the grains grow slightly but show a bimodal grain size distribution. For 0.5 wt.% NiO (**Figure 35-(c)**), the grains grow strongly and approach a hexagonal shape as predicted by the Wulff construction. When the NiO content is further increased to 1.0 wt.%, the grains grow with a bimodal size distribution (**Figure 35-(d)**).

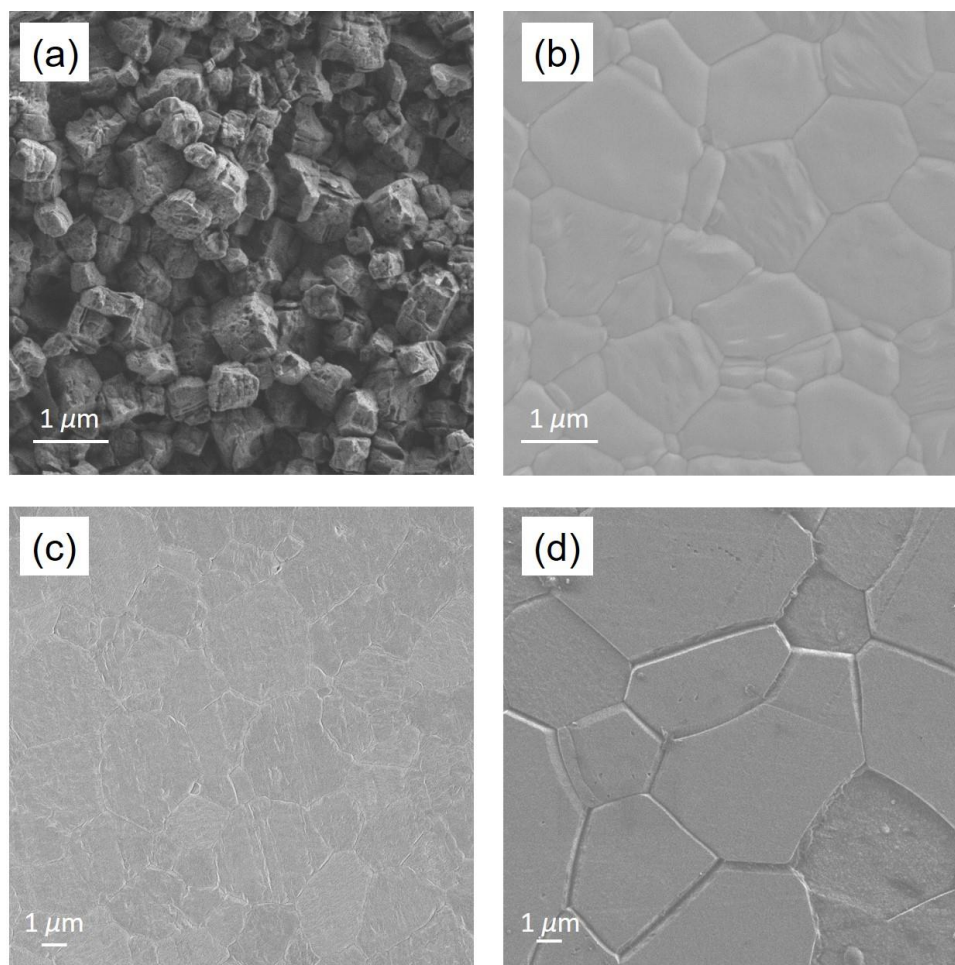


Figure 35: Top-view SEM images from (a) BZC20Y13.6-SPS, (b) BZC20Y13.6-0.25Ni, (c) BZC20Y13.6-0.5Ni and (d) BZC20Y13.6-1.0Ni. The SPS sample was sintered at 1400 °C 5 min and post-annealed at 1500 °C 4 h, the SSRS samples were all sintered at 1550 °C 16 h. The SPS sample surface was prepared by chemical etching and the SSRS samples by thermal etching.

The grain size distribution with low (0.25 wt.%) and high (1.0 wt.%) NiO addition is summarized in **Figure 36**. The average grain size in these plots is larger than the one calculated based on interception method because individual grains were counted by measuring the longest diagonals. Even though the average grain size of BZC20Y13.6-1.0Ni is much larger than BZC20Y13.6-0.25Ni, the shape and relative width of the grain size distribution is comparable. The ratios of largest grain to average grain size are 2.67 and 2.85 for 0.25 and 1.0 wt.% NiO, respectively.

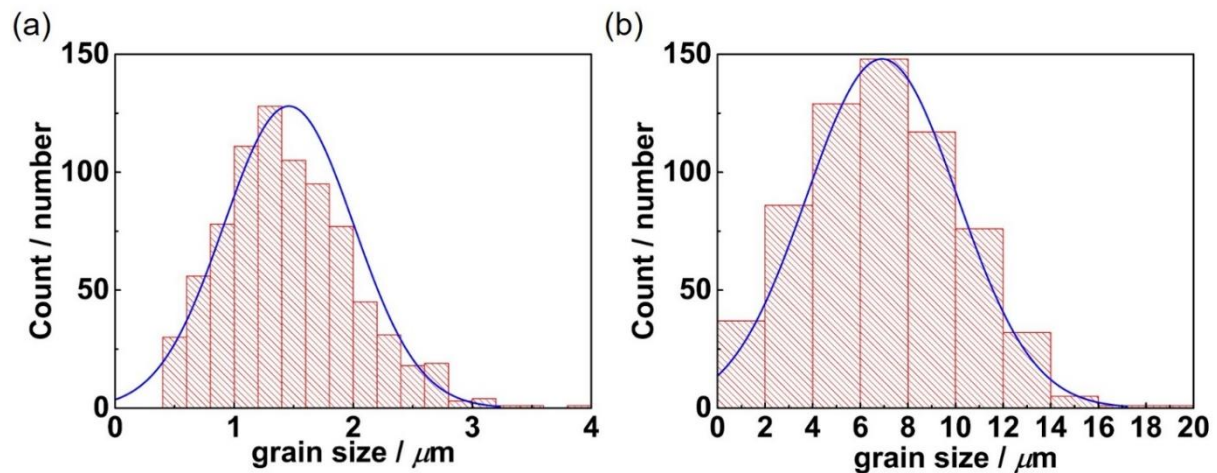


Figure 36: Grain size distribution from statistical analysis of (a) BZC20Y13.6-0.25Ni and (b) BZC20Y13.6-1.0Ni. Both samples were sintered at 1550 °C 16 h. At least 300 grains were analyzed. The blue lines were fitted Gaussian curves.

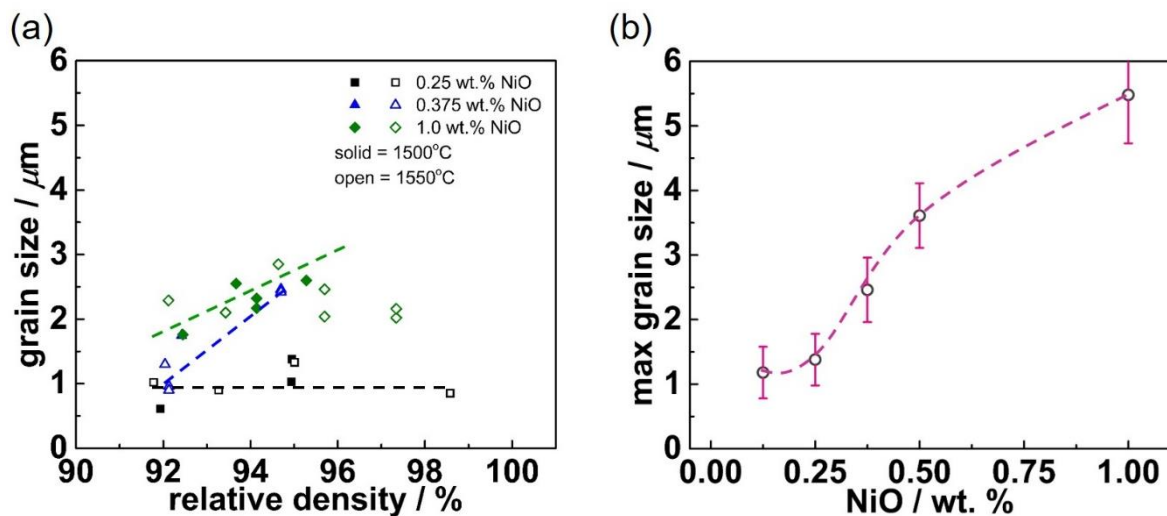


Figure 37: (a) grain size versus relative density for different NiO content and (b) maximum grain size obtained for different NiO content. The dashed line are only a guide for the eye.

The impact of NiO on the sintering behavior of BZCY can also be observed from **Figure 37**. When the NiO content is ≤ 0.25 wt.%, the grains do not grow in parallel to the densification. For NiO contents ≥ 0.375 wt.%, grain growth occurs together with densification and starts earlier for higher NiO content. The maximum grain size varies with the NiO content, (**Figure 37-(b)**). The maximum grain size remains small for 0.125 to 0.25 wt.% NiO due to the limited

liquid phase volume, increases to $\sim 2.5 \mu\text{m}$ with 0.375 wt.% NiO, and further increases to $\sim 4 \mu\text{m}$ and $\sim 6 \mu\text{m}$ when NiO increases from 0.5 to 1.0 wt.%. But from the ICP-OES result (see **Table 5** and **Figure 28-(b)**) the NiO content remaining in the sintered pellet is similar for BZC20Y13.6-0.5Ni and BZC20Y13.6-1.0Ni. Therefore, even though the Ni in BZC20Y13.6-1.0Ni sample is partially lost during the sintering it still promotes the grain growth in the early stage.

3.2.1.6 Quenching experiments

Because the “fast sintering” experiment does not have a sufficiently fast cooling rate, quenching experiments were launched in which the crucible was directly dragged out from the oven at the sintering temperature. In order to detect remainders of the liquid phase in TEM without affecting the mechanism by too much Ni, an increased NiO content of 2.0 wt.% was used. **Figure 38** shows the XRD pattern evolution with temperature for quenched BZC20Y13.6-2.0Ni. Except NiO, all other raw materials are detected in the ball-milled powder. At 1000 – 1050 °C, BaCO₃ partially decomposes and the BZCY/BZ perovskite phases start to form, with residual ZrO₂, CeO₂ and Y₂O₃. At 1050 °C, ZrO₂ and CeO₂ peaks disappear. The peaks of undoped BZ are very prominent, and a separate set of weaker Ba(Ce,Y)O_{3- δ} peaks is visible. At 1100 °C the lattice constant of this phase shifts to smaller values, indicating gradual transformation to Ba(Zr,Ce,Y)O_{3- δ} . In addition to the two perovskite phases, only Y₂O₃ are present, indicating that it is more difficult for Y to be incorporated into the lattice. When the temperature is increased above 1200 °C, no BaO, ZrO₂, CeO₂, and Y₂O₃ residues are observed. From 1050 – 1300 °C, two perovskite phases can be recognized in the XRD pattern. Comparing the lattice constants of both phases, one is a BZCY phase with high Y and Ce content, and the other is undoped BaZrO₃ (see also **Figure 43-(b)**). At low temperature the distribution of Y and Ce is still inhomogeneous, almost as it was in the binary oxide starting powder. With increasing temperature, Y and Ce ions progressively undergo dissolution in the liquid phase from which larger BZCY grains with more homogenous cation distribution grow. Longer soaking time also improves the element homogeneity. At 1300 °C, as shown in **Figure 39**, the second phase vanishes when the soaking time increases from 10 to 30 min. When the temperature is above 1350 °C, second phase is absent already after 10 min (**Figure 38**).

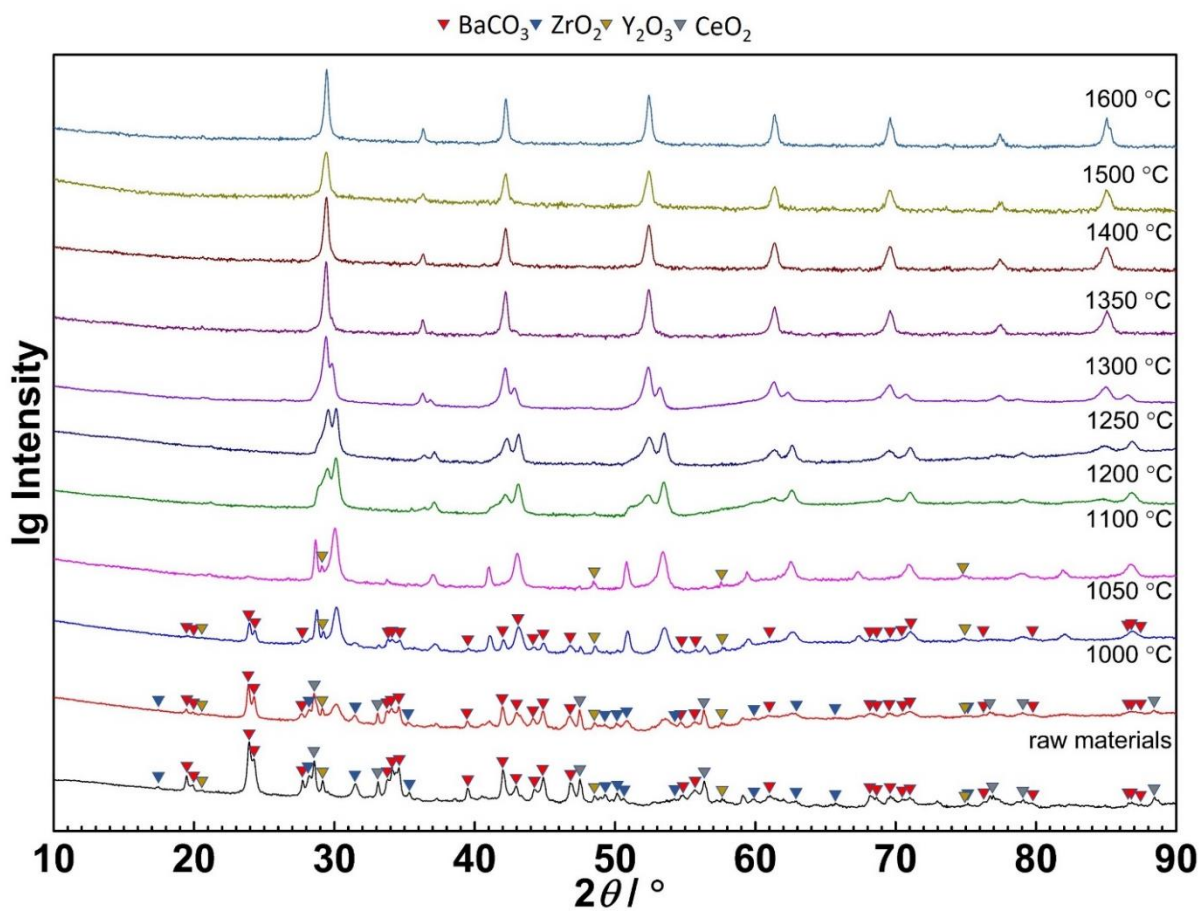


Figure 38: XRD patterns of BZC20Y13.6-2.0Ni sintered at different temperature for 10 min.

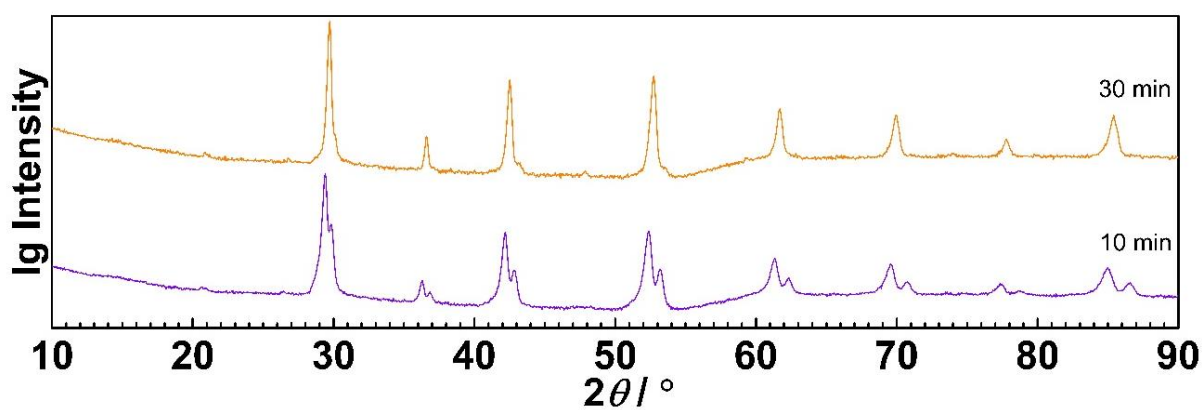


Figure 39: XRD patterns of BZC20Y13.6-2.0Ni sintered at 1300 °C for different time. The sloping of the baseline of 55 – 60 ° results from odd-shaped small sample pellets with rough surface.

As discussed in the last section, NiO content has impact on the liquid phase volume which affects the temperature of densification, therefore it is natural to also check it from quenching experiment with lower NiO content (0.125 and 0.5 wt.%). As shown in **Figure 40** and **Figure 41**, the perovskite phases also start to form at around 1100 °C, with Y₂O₃ residue. But it requires 1400 and 1500 °C to form a single BZCY phase for 0.5 wt.% and 0.125 wt.% NiO, respectively. Therefore, a higher NiO content facilitates a homogenous distribution. Another interesting phenomenon observed from the XRD patterns is that at 1300 °C, BZC20Y13.6-0.5Ni and BZC20Y13.6-0.125Ni show three perovskite phases instead of two for BZC20Y13.6-2.0Ni. **Figure 42** compares the XRD patterns with different NiO content sintered at 1300 °C for 10 min. From BZC20Y13.6-0.125Ni, three perovskite phases can be clearly distinguished. For BZC20Y13.6-0.5Ni, two perovskite phases are obvious, and the other perovskite phase can be recognized as the left shoulder of the peaks at 28.5°, 41°, 51°, 59.5°. No third perovskite phase is observed for BZC20Y13.6-2.0Ni. It confirms that with low NiO addition it is difficult to achieve the proper homogenous cation occupation of the B site.

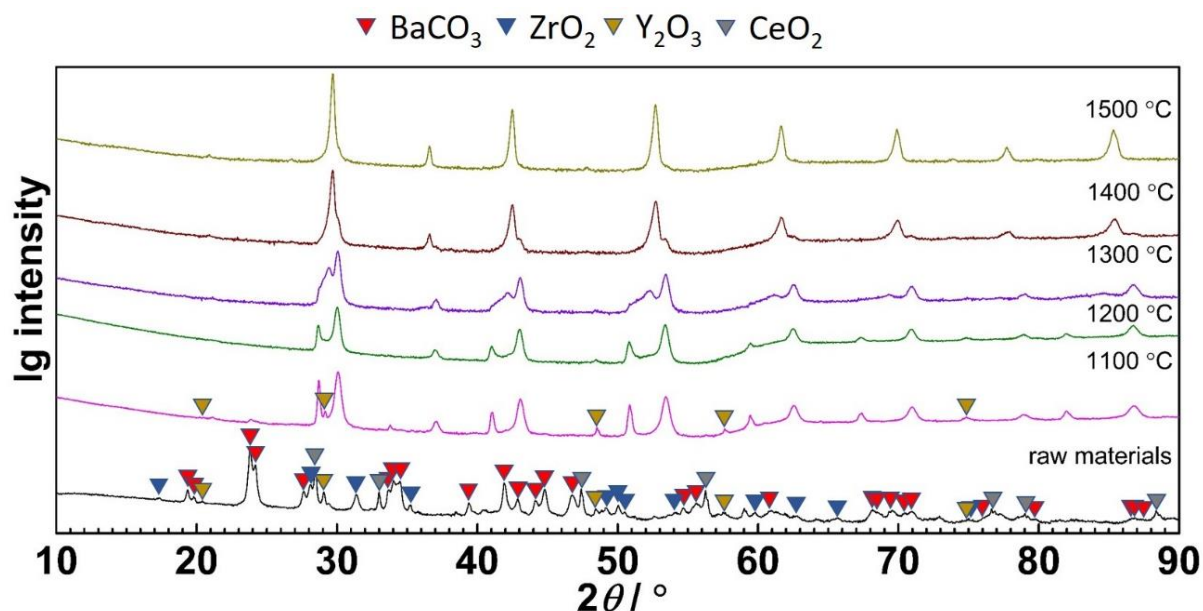


Figure 40: XRD patterns of BZC20Y13.6-0.5Ni sintered at different temperature for 10 min.

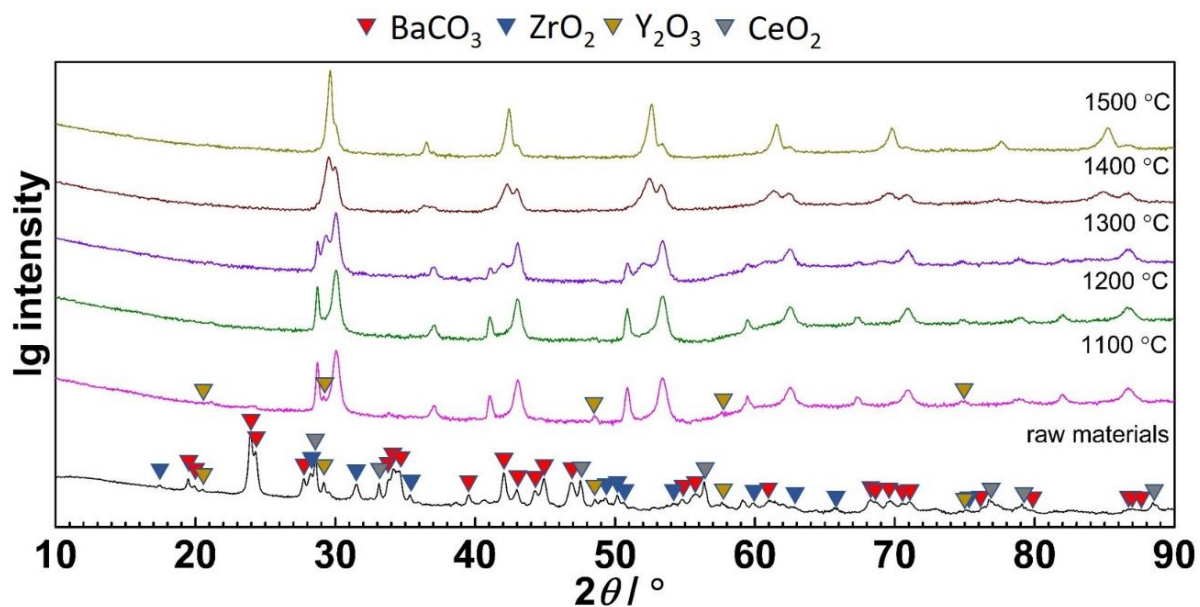


Figure 41: XRD patterns of BZC20Y13.6-0.125Ni sintered at different temperature for 10 min.

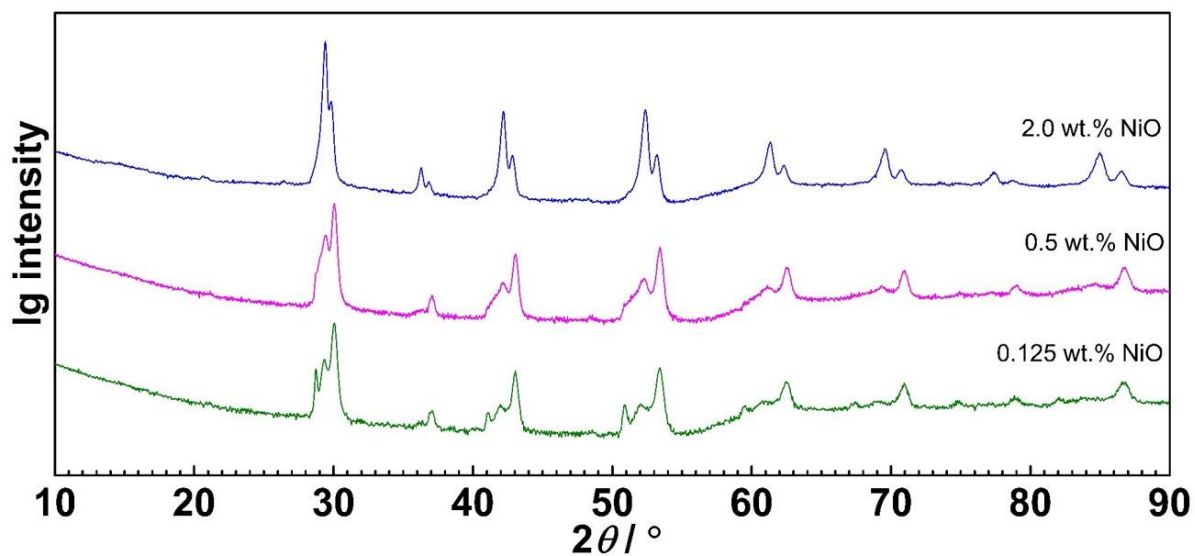


Figure 42: XRD patterns of samples sintered at 1300 °C 10 min with different NiO content.

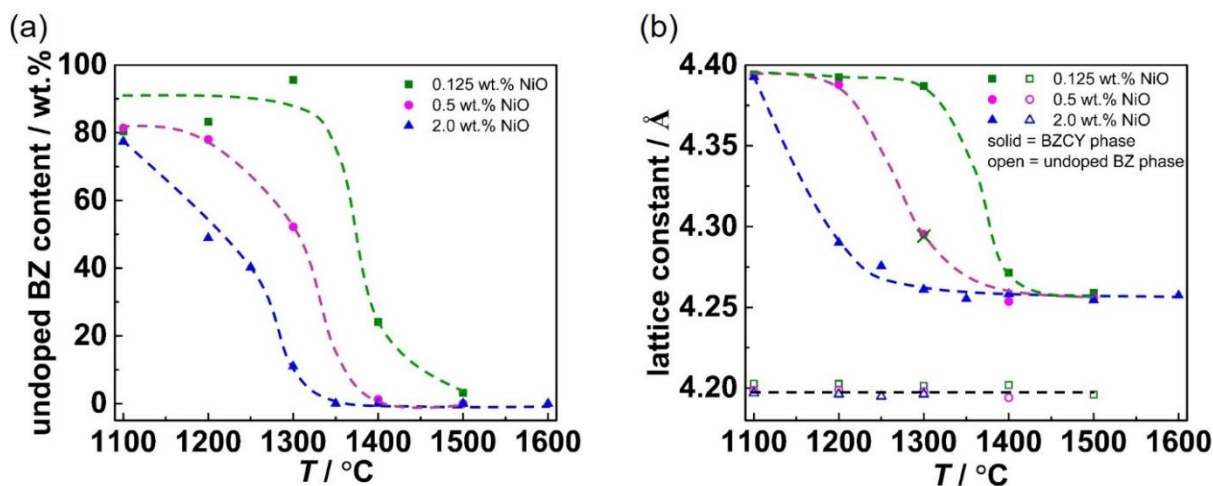


Figure 43: (a) Phase content of undoped BZ and (b) lattice constant of BZCY and BZ phase from samples with different NiO content sintered for 10 min versus sintering temperature. The dashed lines are only a guide for the eye. The \times symbol in (b) indicate the third perovskite phase in BZC20Y13.6-0.125Ni sample sintered at 1300 °C 10 min.

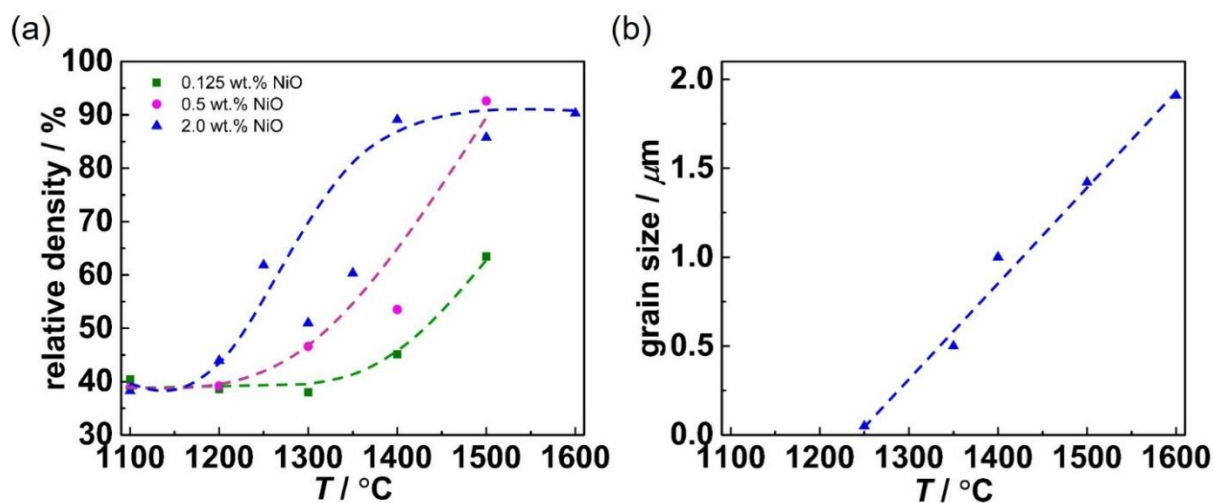


Figure 44: Relative density obtained with different NiO content sintered for 10 min versus sintering temperature. The dashed lines are only a guide for the eye.

The impacts of NiO content on the lattice constant and second perovskite phase are summarized in **Figure 43**. As can be seen in **Figure 43-(a)**, for 2.0 wt.% NiO, the second perovskite phase content is high (~80 wt.%) at 1100 °C with a lattice constant equal to the undoped BZ phase (open symbols in **Figure 43-(b)**). It decreases with increasing temperature until the second phase vanishes above 1350 °C. The main phase has a large lattice constant of 4.394 Å at 1100

°C which decreases with increasing main phase content. When the second perovskite phase has vanished, the main phase lattice constant levels off at 4.256 Å, which is equal to the value of “normal” BZC20Y13.6-*n*Ni lattice parameter (cf. also **Figure 27-(b)**). At 1300 °C, the lattice constant of the third BZCY phase for BZC20Y13.6-0.125Ni sample is comparable to the main BZCY phase lattice constant of BZC20Y13.6-0.5Ni. For BZC20Y13.6-0.5Ni and BZC20Y13.6-0.125Ni, the second phase content decreases more slowly and disappears at 1400 and 1500 °C. The lattice constant reaches the “normal” BZCY value when only one perovskite phase is left. For all three NiO contents, the main phase lattice constant at 1100 °C is ~ 4.39 Å and the second phase lattice constant is always 4.195 Å which corresponds to that of undoped BaZrO₃. Therefore, at low temperature the Y and Ce ion inhomogeneity is larger than at higher temperature or for longer soaking times.

As shown in **Figure 44-(a)**, the relative density increases with sintering temperature. For BZC20Y13.6-2.0Ni, the relative density is comparable with green body density at 1200 °C and increases significantly from 1200 to 1400 °C. The relative density is not further improved at higher temperature (1400 – 1600 °C) and stays at 90%, which is mainly due to the limited soaking time. The grains grow from 50 nm at 1250 °C up to ~ 2 μm at 1600 °C (**Figure 44-(b)**) because of larger liquid phase volume, probably higher solubility of Zr/Ce in the transient liquid phase, and faster ion transportation at higher temperature.

The change of relative density and grain size can be also clearly seen from the BF and HAADF TEM images, as shown in **Figure 45**. At 1250 °C, the sample has a high porosity (cf. **Figure 45-(a)**) and tiny particles with rough GBs. The porosity decreases with increasing temperature. At 1350 °C, the ceramic densifies and the grains grow with soaking time (**Figure 46**). At 1400 °C, it shows ~ 10% porosity (**Figure 45-(c)**). At 1500 and 1600 °C, there are only few small pores and large grains. The porosity observed from the HAADF images at 1500 and 1600 °C (see **Figure 45-(d)** and **Figure 45-(e)**) is much lower than 10% and should not result in only ~ 90% relative density as calculated in **Figure 44-(a)**. This difference can be ascribed to the irregular shape of the samples. One can also recognize that the density variation within the SSRS sample is more pronounced when the soaking time is too short.

For BZC20Y13.6-0.5Ni, the relative density increases more slowly with temperature than for BZC20Y13.6-2.0Ni due to lower transient liquid phase volume. 90% relative density is reached at 1500 °C (**Figure 44-(a)**). With 0.125 wt.% NiO, the sample does not start to densify until 1350 °C and the relative density is only ~ 60% even at 1500 °C. Compared with the XRD

pattern evolution, the BZCY phases formed at a lower temperature than ceramic densification and grain growth (cf. **Figure 38**, **Figure 39**, **Figure 40**, **Figure 41**).

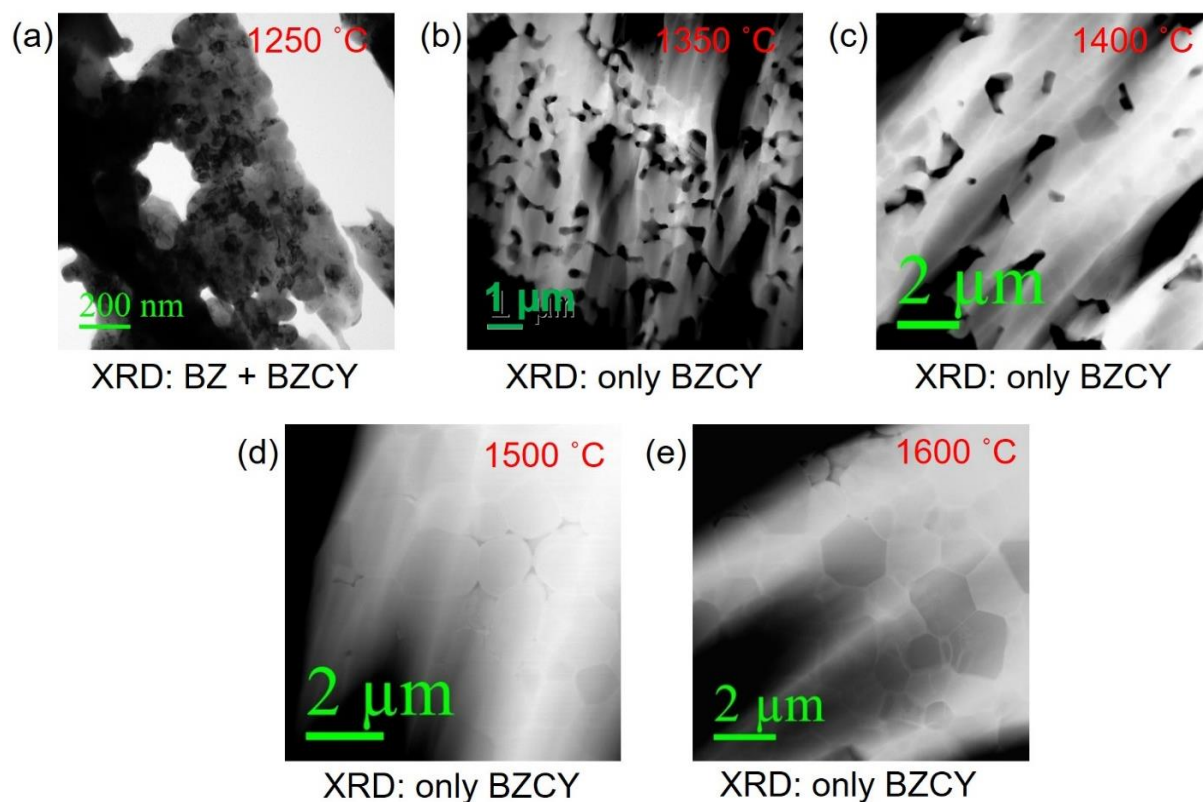


Figure 45: (a) BF image from 1250 °C and (b-e) HAADF images from quenched BZC20Y13.6-2.0Ni samples sintered for 10 min at different temperatures. TEM was done by W. Sigle.

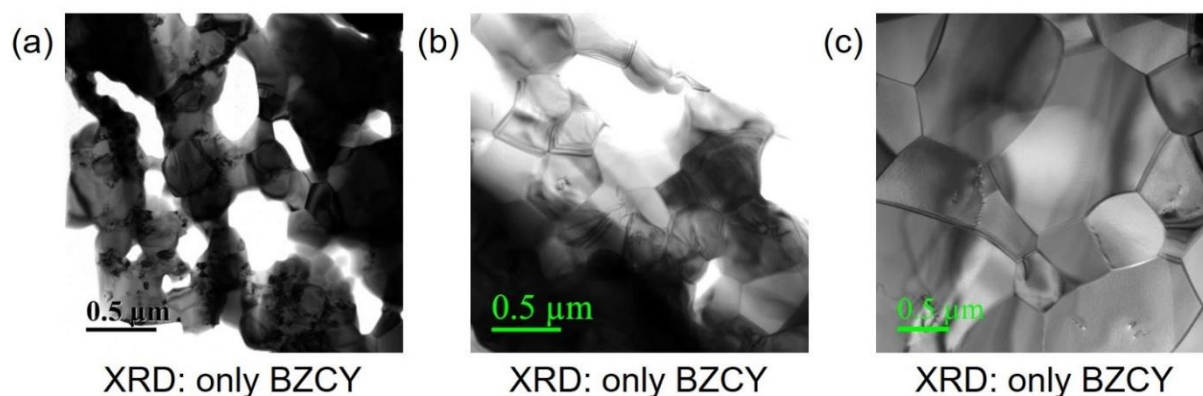


Figure 46: BF images from quenched BZC20Y13.6-2.0Ni samples sintered at 1350 °C for (a) 10 min, (b) 30 min and (c) 4 h. TEM was done by W. Sigle.

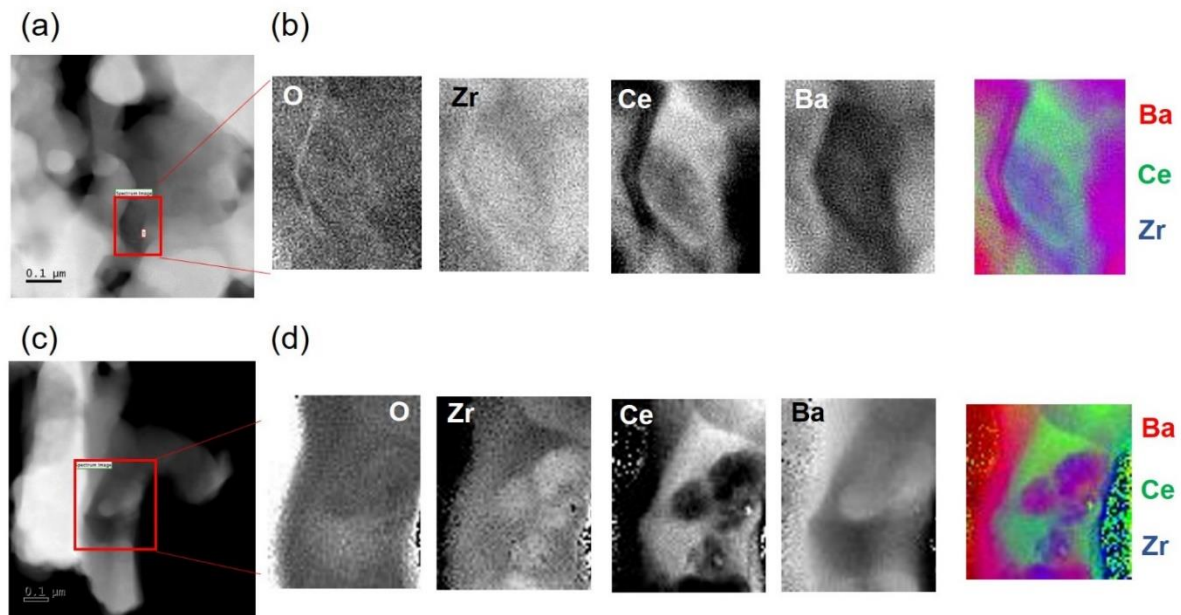


Figure 47: (a) and (c) images, (b) and (d) corresponding element mapping TEM-EELS measurement. The squares indicated in (a) and (c) are mapping area. The quenched sample BZC20Y13.6-2.0Ni was sintered at 1250 °C for 10 min, according to XRD it contains BZ and BZCY perovskite phases. The measurement was done by W. Sigle.

TEM-EELS and -EDX measurements on BZC20Y13.6-2.0Ni sintered at different temperatures (1250 – 1600 °C) were done to observe remainders of the transient liquid phase. At 1250 °C, according to the TEM-EELS mapping result (**Figure 47**), the elements show pronounced inhomogeneity on the 100 nm scale, with some grains high in Ce, and low in Ba and Zr. This is consistent with the XRD result of one Ce-rich and one undoped BZ phase (**Figure 38**). At 1350 °C, according to XRD only one BZCY phase is present. This agrees with TEM-EDX (**Figure 48**) which indicates presence of Ce, Y within perovskite grains. Two types of GBs can be observed in HAADF images. **Figure 48-(a)** shows the case of a “thick” GB. In the corresponding TEM-EDX line scan, (**Figure 48-(c)**), the Ni signal is extremely high with all other elements depleted. This could be NiO or a residue of the liquid phase. A “thin” GB structure is shown in **Figure 48-(b)** and **Figure 48-(d)**, which shows a much more moderate Ni accumulation at the GB, indicating it is a well-formed GB as in the sintered ceramics. The elements distribute evenly within the grains, agreeing with the single phase XRD pattern (**Figure 38**). Therefore, at 1350 °C, the single BZCY phase and some grains are already formed, while the remnant liquid phase can further facilitate densification and grain growth. At 1500

°C, from the HAADF image (**Figure 49**) pockets and sharp GBs can be seen. TEM-EDX mapping shows that at pocket positions, Ni is strongly enriched. At GBs, Ba, Y are enriched and Zr depleted, which might be assigned to BaNiO_2 and/or BaY_2NiO_5 phases. The TEM-EDX line scan for the pellet sintered at 1600 °C shows similar results (**Figure 50**). More detailed discussion of the sintering mechanisms will be shown in section 3.2.3.

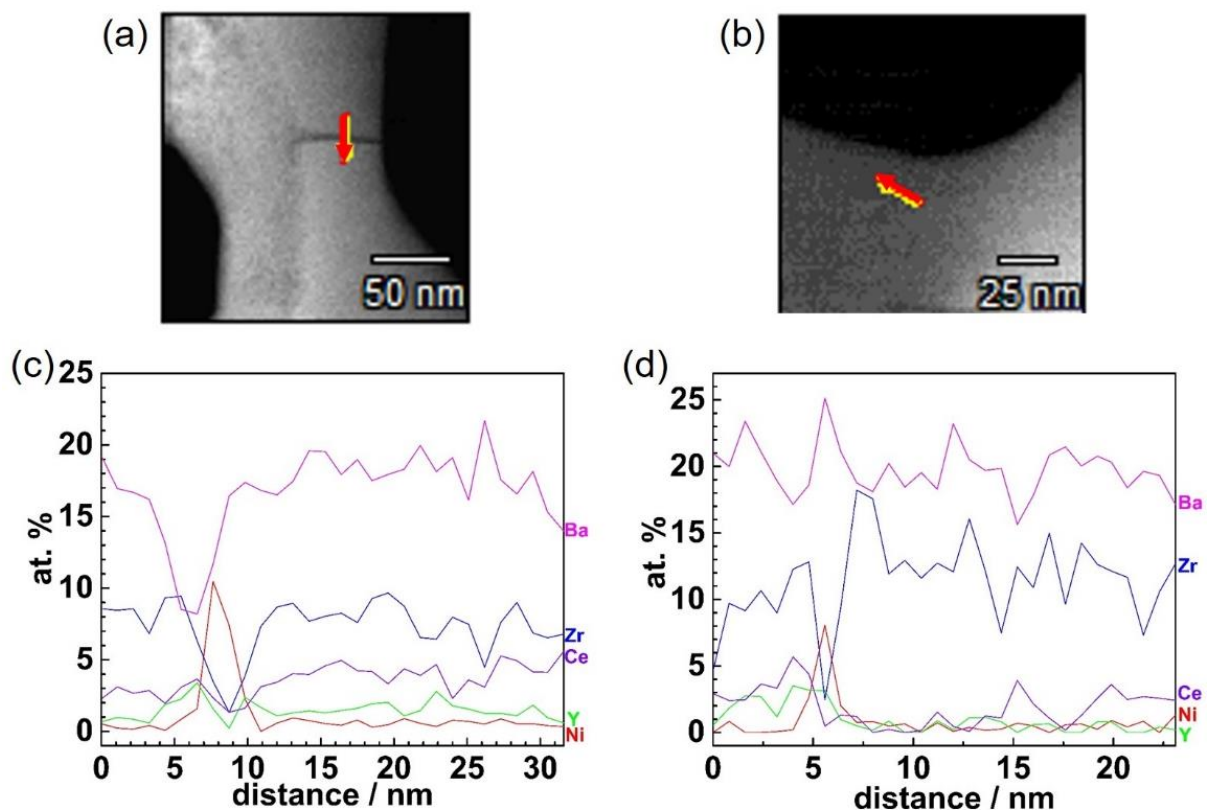


Figure 48: TEM-EDX line scan on (a) “thick” GB and (b) “thin” GB. (c) and (d) are corresponding element distributions in at.%. The arrows in (a) and (b) indicate the measurement positions and directions. The quenched sample of BZC20Y13.6-2.0Ni was sintered at 1350 °C 10 min. The measurement was done by W. Sigle.

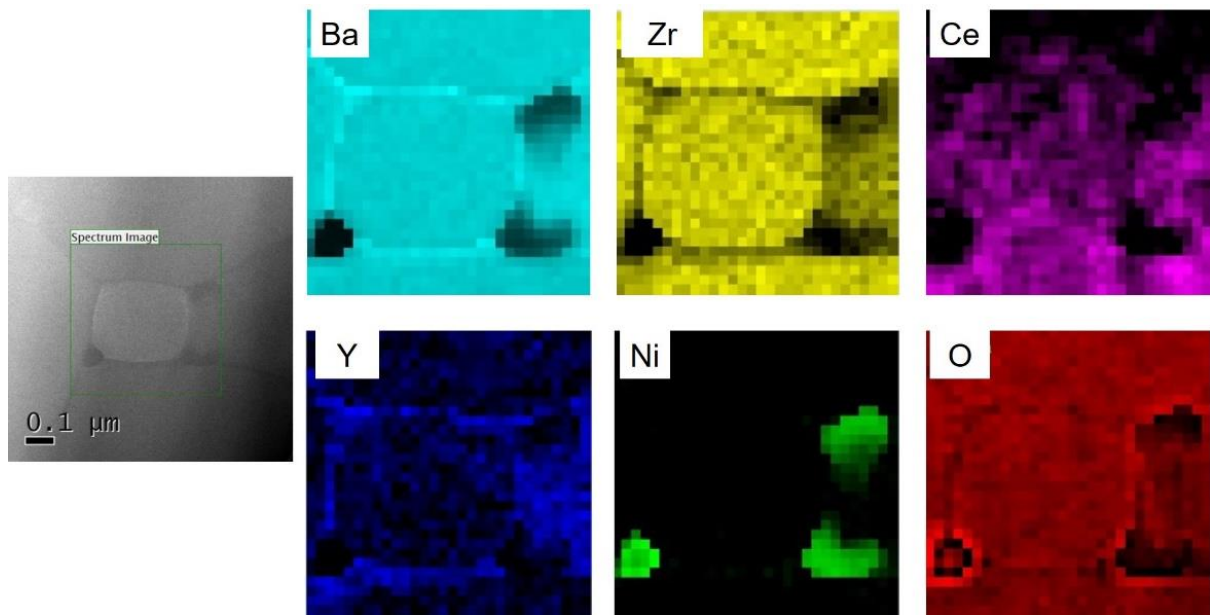


Figure 49: TEM-EDX mapping on quenched sample of BZC20Y13.6-2.0Ni sintered at 1500 °C 10 min. The square indicates the measured area. The measurement was done by W.Sigle.

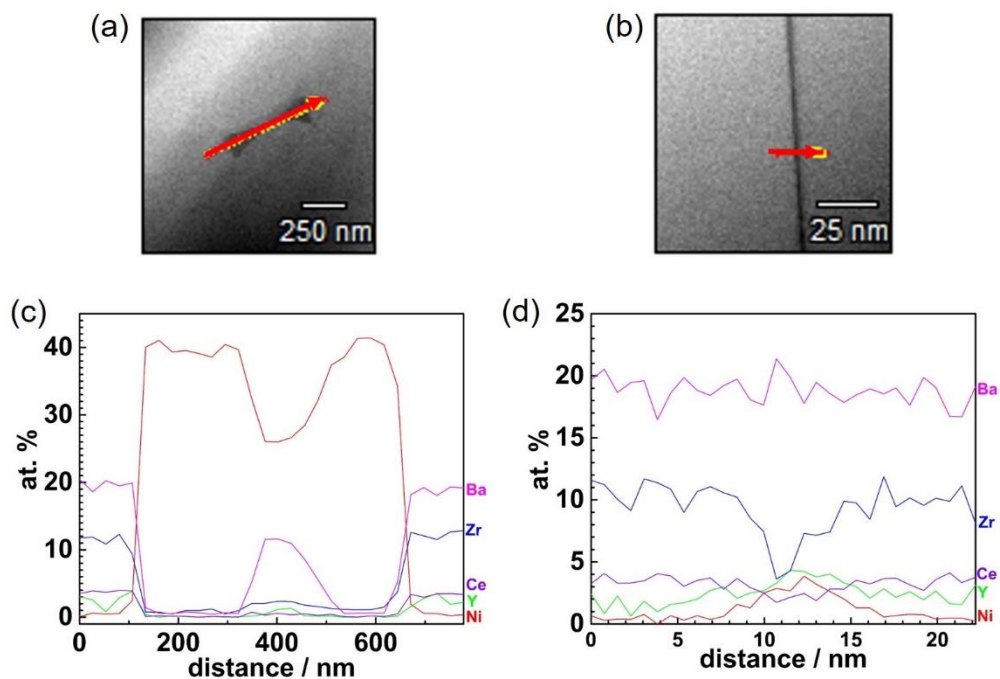


Figure 50: TEM-EDX line scan on (a) possible liquid phase and (b) GB. (c) and (d) are corresponding element distribution in at.%. The arrows in (a) and (b) indicate the measurement positions and directions. The quenched sample of BZC20Y13.6-2.0Ni was sintered at 1600 °C 10 min. The measurement was done by W. Sigle.

3.2.2 Grain growth kinetics

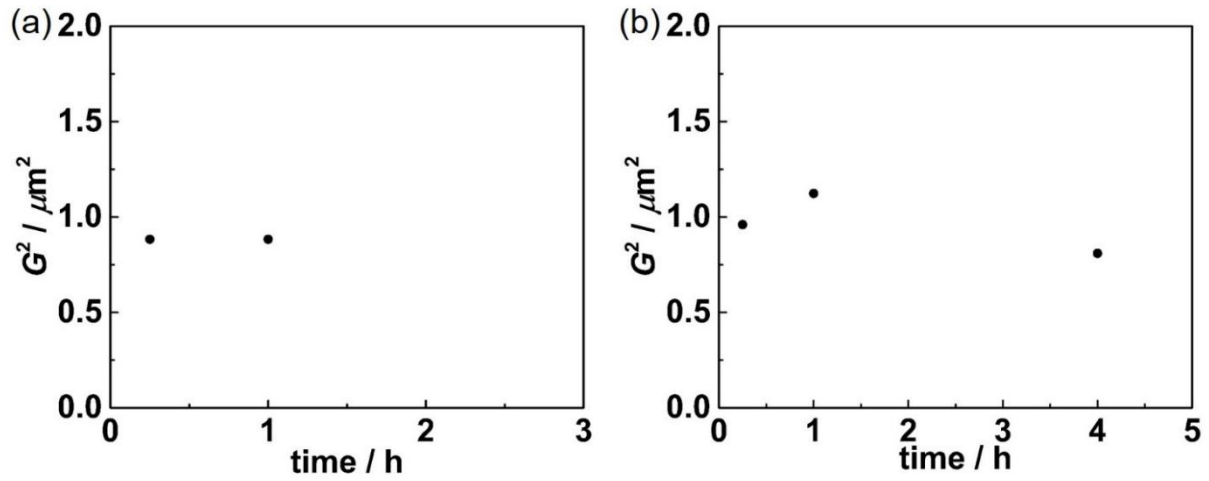


Figure 51: Grain size square versus soaking time at (a) 1400 °C and (b) 1450 °C for BZC20Y13.6-1.0Ni.

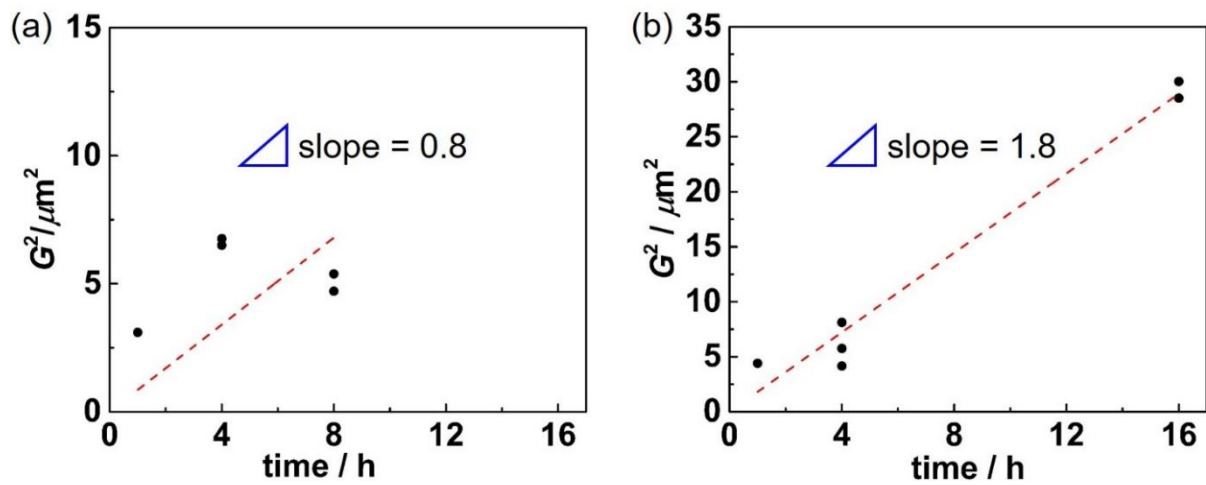


Figure 52: Grain size square versus soaking time at (a) 1500 °C and (b) 1550 °C for BZC20Y13.6-1.0Ni.

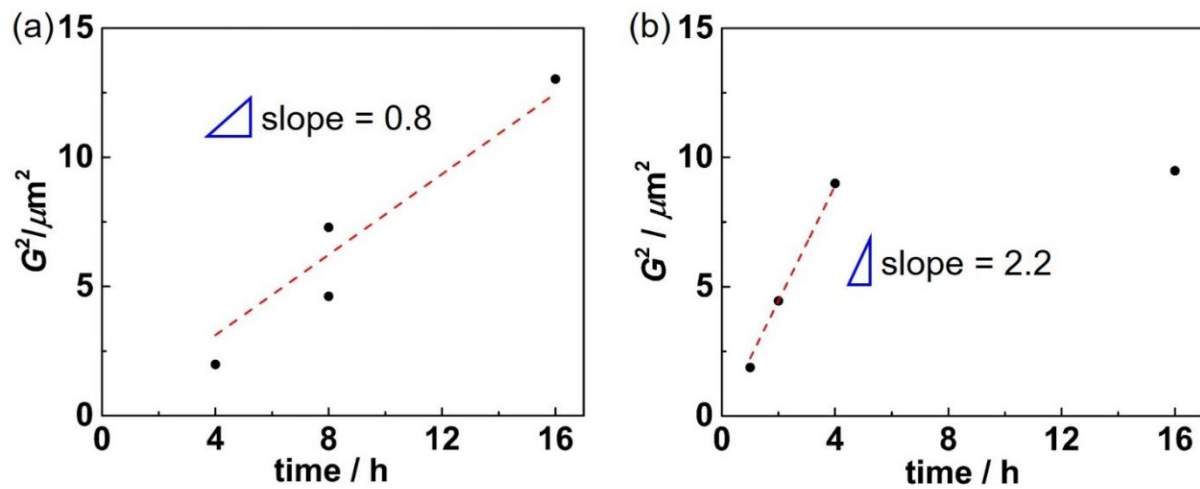


Figure 53: Grain size square versus soaking time at (a) 1500 °C and (b) 1550 °C for BZC20Y13.6-0.5Ni.

For some samples the grain growth kinetics was analyzed quantitatively. As shown in **Figure 51**, the grain size of BZC20Y13.6-1.0Ni has increased from 50 nm at 1250 °C when the sample is composed of BZ and BZCY perovskite grains, to $\sim 1 \mu\text{m}$ at 1400 – 1450 °C without further grain growth with time. Even though the liquid phase starts to form at low temperature for high NiO content, higher temperature is necessary to further promote grain growth.

For BZC20Y13.6-0.5Ni and BZC20Y13.6-1.0Ni at 1500 and 1550 °C (**Figure 52** and **Figure 53**), the grain growth follows the relationship in **Eq. (28)** ^[149] with $n = 2$

$$G^n - G_0^n = kt \quad (28)$$

where G is the grain size, G_0 is the initial grain size (here 50 nm is used from the grain size of BZC20Y13.6-2.0Ni sintered for 10 min at 1250 °C) and k is the grain growth kinetics constant. According to W. D. Kingrey ^[150], k is determined by the boundary mobility. n can be 2, 3 or 4, depending on different mechanisms and shapes of particles. The equation is applicable for many systems, such as MgO-Al₂O₃, CaO-ThO₂ and etc., and was derived for a system without liquid phase but can also be applied for liquid phase sintering ^[151]. In the solution-precipitation model with a small liquid phase volume, the diffusion length in the liquid is short. An exponent of $n = 2$ indicates that the grain growth would be limited by the solution/precipitation at the interface of solid and liquid. For $n = 3$, the grain growth is limited by diffusion of ions, especially for large liquid phase volume. In the present work, the liquid phase volume of 3 – 6 vol.% for 1.0 wt.% NiO is rather small, which fits to the model with $n = 2$.

Figure 53-(b) shows that at long time the grain growth ceases, and that this occurs earlier for lower NiO content (compare 0.5 wt.% NiO versus 1.0 wt.% NiO in **Figure 52-(b)**). So with increased NiO content, not only do the grains grow faster at 1500 °C, but the grains can also keep growing at higher temperature (1550 °C) for much longer time because of more liquid phase volume. This indicates that the transient liquid phase is consumed during SSRS. After it is fully decomposed, the grain growth stops as it transforms to solid state sintering which requires a much higher temperature (≥ 1700 °C). For BZC20Y13.6-0.25Ni, due to the limited transient liquid phase the grains remain small at ~ 1 μm at 1500 and 1550 °C even for 16 h.

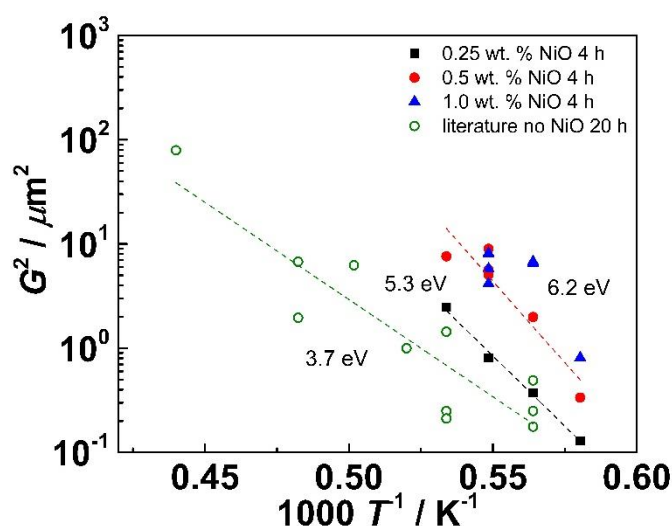


Figure 54: Arrhenius plot of squared grain size. Open symbols: conventionally sintered Ni-free BZY samples with 5 – 20 at.% Y, soaking time 20 – 24 h, data from literature [69,84,95,108,115,132,152–155]. Solid symbols: BZC20Y13.6-0.25Ni, BZC20Y13.6-0.5Ni and BZC20Y13.6-1.0Ni samples with soaking time of 4 h. The dashed lines are linear fitting of corresponding data.

Figure 54 shows the Arrhenius plot of squared grain size, open circles are data of Ni-free samples from literature. With some scatter, the activation energy fitted from the Ni-free samples amounts to 3.7 eV. This value is comparable to the GB diffusion activation energies of Zr (3.6 eV) [156] and Ba (3.0 eV) in BaZrO_3 [157], and slightly higher than Ba (2.6 eV) in BaCeO_3 [157]. For SSRS with 0.25 wt.% NiO content, the activation energy increases to 5.3 eV. The activation energy further increases to 6.2 eV when 0.5 – 1.0 wt.% NiO is used. Surprisingly, the higher grain growth rates come together with higher activation energy. This might be related to a temperature dependent solubility of Zr/Ce in the transient $\text{BaNiO}_2/\text{BaY}_2\text{NiO}_5$ phase,

as the densification and grain growth depend more on the liquid phase with increasing NiO content. Also one can notice that the activation energy does not vary from 0.5 to 1.0 wt.% NiO, indicating that rather than increasing the NiO content to more than 0.5 wt.%, increasing the sintering temperature and elongating the soaking time are more practical.

3.2.3 Discussion of sintering mechanism

3.2.3.1 Evidence of transient liquid phase formation

Although the transient liquid phase BaY_2NiO_5 detected in literature ^[107,108,113,145] is not found in SSRS samples from this work due to the low NiO content used, there are three phenomena that evidence the existence of the transient liquid phase. (i) the micro-strain decreases significantly with the NiO content, as shown in **Figure 24**, especially when the NiO content increases from 0 to 0.25 wt.%. Apart from the NiO addition, the samples have the same composition, indicating the release of lattice distortion in BZC20Y13.6 is related only to the NiO addition, i.e. the transient liquid phase volume. (ii) In the quenched samples, Zr, Ce, Y are mixed already at low temperature. Comparing with the phase pure powder obtained for SPS, which needs 3 calcinations at 1300 °C 8 h (**Figure 11**), the BZC20Y13.6-2.0Ni has already been transformed to perovskite phases without remainder of raw materials at 1200 °C 10 min. (iii) The grain growth depends on the NiO content. In **Figure 33**, the grains can grow up to ~ 6 μm for ≥ 0.375 wt.% NiO addition sintered for ≤ 16 h at 1450 – 1550 °C, which is much lower than for conventional sintering of BZY. Typically, BZY requires extremely high temperature (≥ 1700 °C) and long soaking time (≥ 24 h), and results only in small grain size ~ 0.5 μm . Therefore, there must be a low temperature (≤ 1550 °C) formed liquid phase facilitates the grain growth. All these three evidences confirm that a transient liquid phase has developed during sintering. It promotes ion transport to eliminate the inner strain, to form the perovskite phases, and to facilitate grain growth.

3.2.3.2 Discussion of composition of transient liquid phase

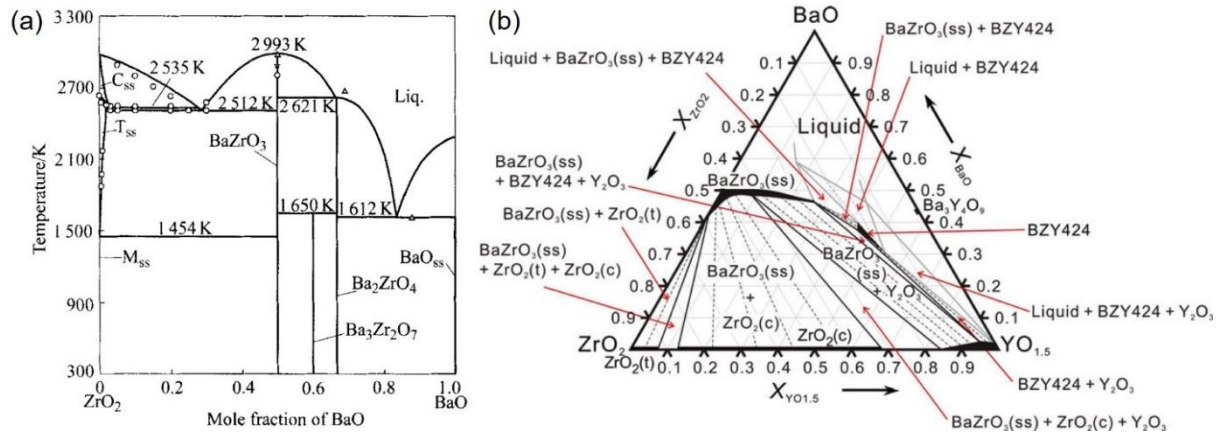


Figure 55: Phase diagrams of (a) BaO-ZrO₂, and (b) BaO-ZrO₂-YO_{1.5} at 1600 °C. (a) is from ref. [158] and (b) from ref. [159].

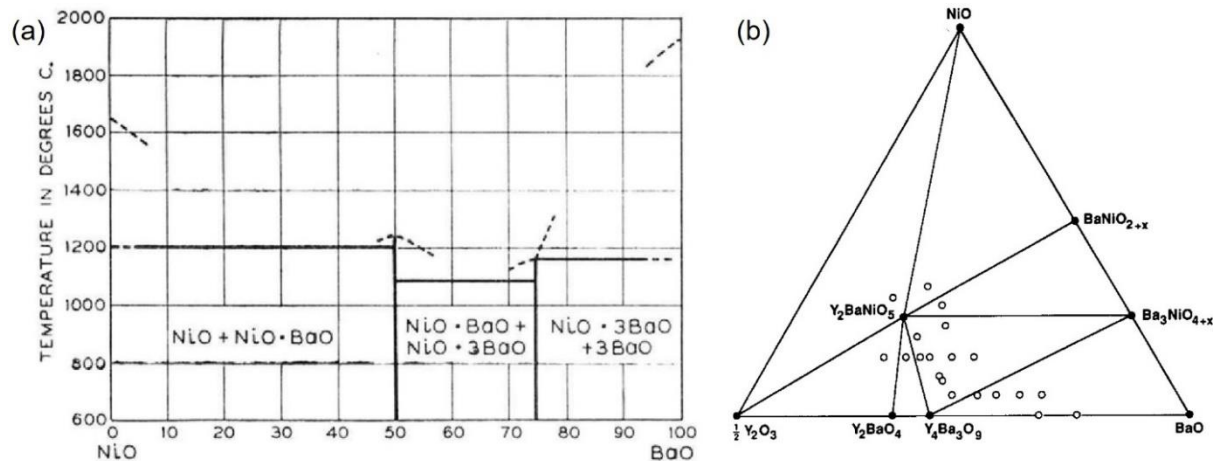


Figure 56: Phase diagrams of (a) BaO-NiO [160], and (b) BaO-NiO-YO_{1.5} [112] in the temperature range of 1000 – 1350 °C.

Pure BaZrO₃ has a melting point of 2720 °C (**Figure 55-(a)**). Also doped with Y, as shown in **Figure 55-(b)**, BaZrO₃ is still in solid phase at 1600 °C. The phase diagram of these two systems without transient liquid phase can explain why CS requires extremely high temperature. Although there are two eutectic points shown in the phase diagram **Figure 55-(a)**, the composition with too much Ba excess lowers the chemical stability, or with too much Ba deficiency lowers the proton conductivity. Even though the ceramic can be densified at high temperature, the ion transportation is limited so the grain cannot grow large. When NiO is added, it can form the BaNiO₂ phase which decreases the melting point to ~ 1200 °C and even

lower with BaO excess (**Figure 56-(a)**). BaY_2NiO_5 can also form in the temperature range of 1000 – 1350 °C (**Figure 56-(b)**) and become liquid at about 1450 – 1500 °C [107,113]. A more detailed discussion on the transient liquid phase composition will be given below.

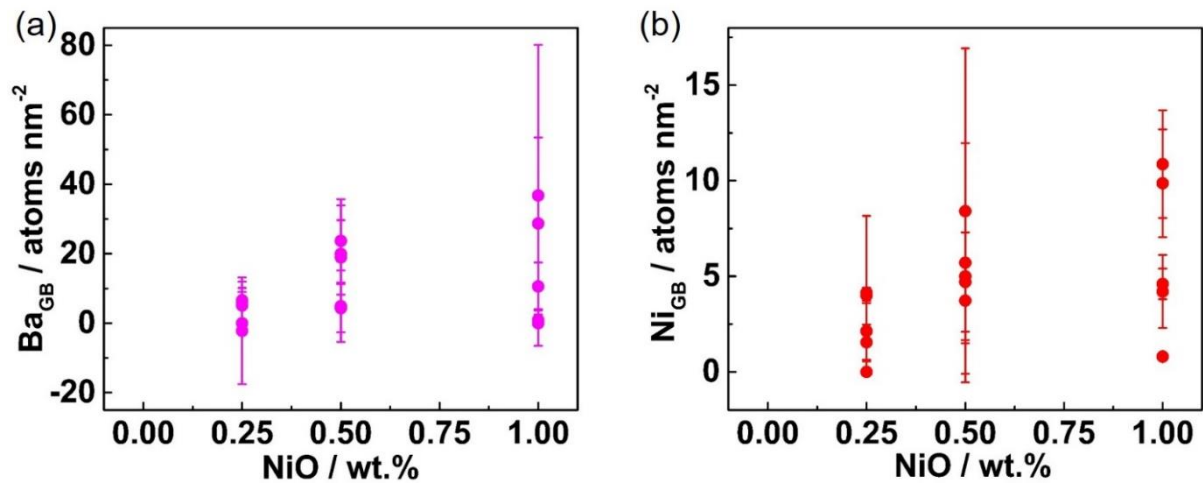


Figure 57: (a) Ba and (b) Ni element average excess/deficiency at GBs compared to the bulk calculated from TEM-EDX measurement. At least 10 GBs were measured for each sample sintered with a heating and cooling rate of 200 °C/h.

Figure 57 shows Ba and Ni element excess/deficiency at GBs compared to the bulk. Both Ba and Ni show an excess at GBs which increases with the nominal NiO content. Even though the remaining NiO contents are comparable for nominal 0.5 wt.% and 1.0 wt.% NiO samples, Ba and Ni show a higher accumulation at GBs for nominal 1.0 wt.% NiO sample. Together with the decreased proton uptake with increasing NiO content (section 3.2.4, **Figure 60-(a)**), this indicates that Ba is extracted from the perovskite lattice to form the transient $(\text{Ba,Ni,Y})\text{O}_x$ liquid phase. Two possible mechanisms have to be considered how Ni acts during the liquid phase sintering.

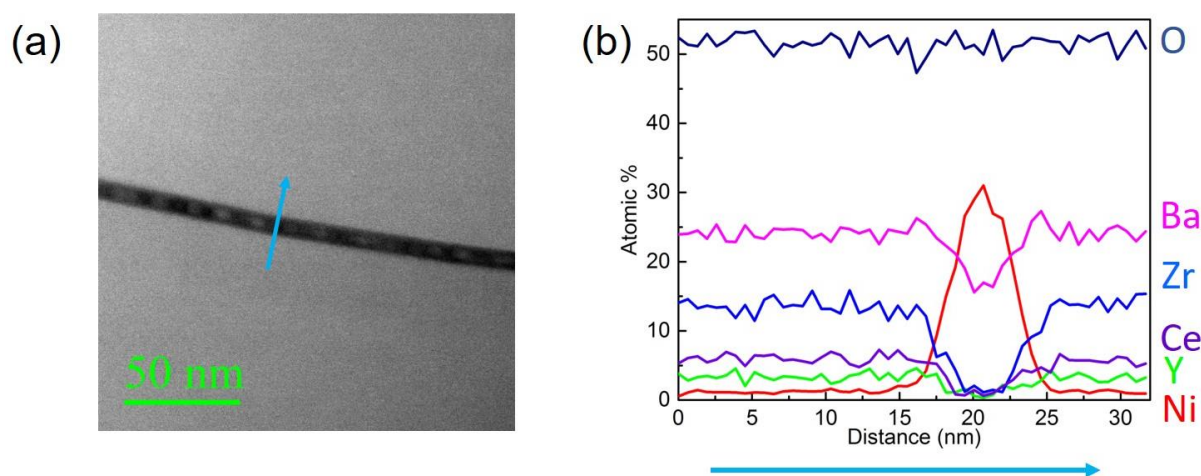


Figure 58: (a) HAADF image and (b) TEM-EDX line scan result in at.%. The arrow in (a) indicates the measurement direction and position. The BZC20Y13.6-1.0Ni was sintered at 1500 °C 1 h with a heating and cooling rate of 600 °C/h.

i) Formation of BaNiO₂

Pure BaNiO₂ can be synthesized at 900 – 950 °C, has a melting point of about 1240 °C, and a lower eutectic point with excess BaO (**Figure 56-(a)**)^[160]. At typical sintering temperature for SSRS (1400 – 1550 °C), it is liquid and can facilitate ion transport. The total defect reaction is:



which generates one Y donor dopant on the A site for each two NiO involved, and results in smaller lattice constants as $r_{\text{Ba}^{2+}} = 1.61 \text{ \AA} > r_{\text{Y}^{3+}} = 1.25 \text{ \AA}$ on the A site^[148]. Also, based on **Eq. (29)**, two Ni annihilate one oxygen vacancy and therefore 2 protons (**Eq. (2)**). The formation of BaNiO₂ is consistent with TEM-EDX results, as shown in **Figure 58** from the fast sintering sample. One can clearly see that there is a “liquid” secondary phase at the GB region from the HAADF image (**Figure 58-(a)**). The TEM-EDX line scan, as shown in **Figure 58-(b)**, shows an atom ratio of Ba:Ni:O = 1:2:3, which is close to the nominal value of BaNiO₂ (1:1:2). The lower content of Ba and O may be caused by BaO evaporation, or some liquid phase already starts to decompose so that Ba and O go back to the perovskite lattice after certain time at high temperature.

ii) Formation of BaY₂NiO₅

The other possibility is formation of BaY_2NiO_5 , as observed in literature ^[107,108]. The material of BaY_2NiO_5 phase can be obtained at 1150 – 1200 °C ^[107,112]. In this work, BaY_2NiO_5 was not detected by XRD due to the low NiO content used. The corresponding defect reaction is



In this reaction, for each two Ni, two Ba ions, two Y on the B site and one oxygen vacancy are consumed. This reaction also leads to annihilation of one proton for each Ni. Although the element distribution from TEM-EDX results (**Figure 58**) does not fully fit to the formation of BaY_2NiO_5 , samples without Y cannot be fully densified even with NiO addition ^[146]. Sc-doped BaZrO_3 with NiO can also be fully densified at 1550 °C, indicating that some acceptor dopant is necessary for SSRS.

Other hypothetical possibilities include Ni substituting on the B site forming a Ni_{Zr}'' defect, and Ni incorporating as an interstitial defect $\text{Ni}_i^{\bullet\bullet}$. However, the formation of Ni_{Zr}'' should increase the proton uptake due to an increase of $[\text{V}_{\text{O}}^{\bullet\bullet}]$. Together with the discrepancy of lattice constant, and hydration enthalpy and entropy from SSRS and Ni on B site samples as shown in **Figure 63**, this assumption can be ruled out. The interstitial defect $\text{Ni}_i^{\bullet\bullet}$ is energetically not stable based on DFT calculations ^[161], and needs to form a defect pair ($\text{V}_{\text{Ba}}''\text{Ni}_i^{\bullet\bullet}$) with a pre-existing barium vacancy which is not likely from the ICP-OES results (**Table 5**). D. Han *et al.* ^[162] claimed that Ni forms $\text{Ni}_i^{\bullet\bullet}$ on the lattice position of (1/2, 0, 0), which however has an unfavorable formation energy ^[161]. Therefore, Ni interstitials are not included in this thesis as one of the possibilities.

3.2.3.3 Decomposition of the transient liquid phase

As observed from the quenched samples sintered at 1500 and 1600 °C (**Figure 49** and **Figure 50**), Ni accumulates at GBs and adjacent areas, whereas other elements are depleted. D. Han *et al.* ^[162] also observed the same phenomenon for BZY with 5 mol.% NiO (~ 1.25 wt.%) addition sintered at 1600 °C 24 h. J. Tong *et al.* ^[107,108] detected the BaY_2NiO_5 phase from BZY20 with 2.0 wt.% NiO addition sintered at 1150 and 1250 °C but the BaY_2NiO_5 peaks disappear when sintered at 1350 °C. This implies the transient nature of the liquid phase. It is formed at low temperature and consumed during sintering with increasing temperature. The Ni finally accumulates at GB regions. According to J. J. Lander ^[160], (**Figure 56-(a)**), BaNiO_2 is rather stable even above 1800 °C. However, BaY_2NiO_5 decomposes to Y_2O_3 , BaO (gas) and

NiO at 1500 °C according to D. Han *et al.* [113], or the elements go back to their original lattice sites and Ni substitutes on the B site already at > 1200 °C according to J. Tong *et al.* [107]. The first possibility fits to the TEM-EDX results as shown in **Figure 49** and **Figure 50**, but Y₂O₃ phase was not detected at GBs in pellet samples though it was found in membrane electrolyte layers. The second possibility that the elements return to their original positions would result in Ni''_{Zr} defects, which is not consistent with the lattice constant variation (**Figure 27**), and thermodynamic parameters measured by TG (see section 3.2.4, **Figure 60**, **Figure 62**, and **Figure 63**) compared to samples with Ni on the B site. So, the real nature of the transient liquid phase which may be a mixture of BaNiO₂ and BaY₂NiO₅ still remains unclear, and the decomposition mechanism of the transient liquid phase is not really well-defined.

3.2.3.4 Possible sintering mechanism and comparison to literature

The possible sintering mechanism of SSRS with sufficient liquid phase is schematically shown in **Figure 59**, based on the discussion in former sections. Surrounding a large grain with equilibrium hexagon shape, there are small grains with pure perovskite BZCY phase, and BaO, ZrO₂, CeO₂, and Y₂O₃ raw material particles in molten (Ba,Ni,Y)O_x phase which dissolves Zr⁴⁺ and Ce⁴⁺ ions. The solubility is probably temperature dependent. During SSRS, with the aid of the transient (Ba,Ni,Y)O_x liquid phase, the ions transport much faster than in solid state reaction or sintering. This facilitates also the perovskite phase formation from the binary oxides. The porosity of the pellet decreases (densification) while in parallel some large grains grow with the consumption of small grains. Section 3.2.1.6 illustrates that the three main processes of i) perovskite formation, ii) densification and iii) grain growth are closely coupled during SSRS. There is no doubt that the transient liquid phase promotes all these three. Besides, the transient liquid phase decomposes (no remainders of the liquid phase from SSRS pellets with long soaking time) at high temperature when the three processes are ongoing, and the cations may incorporate into the lattice and/or accumulate at GBs.

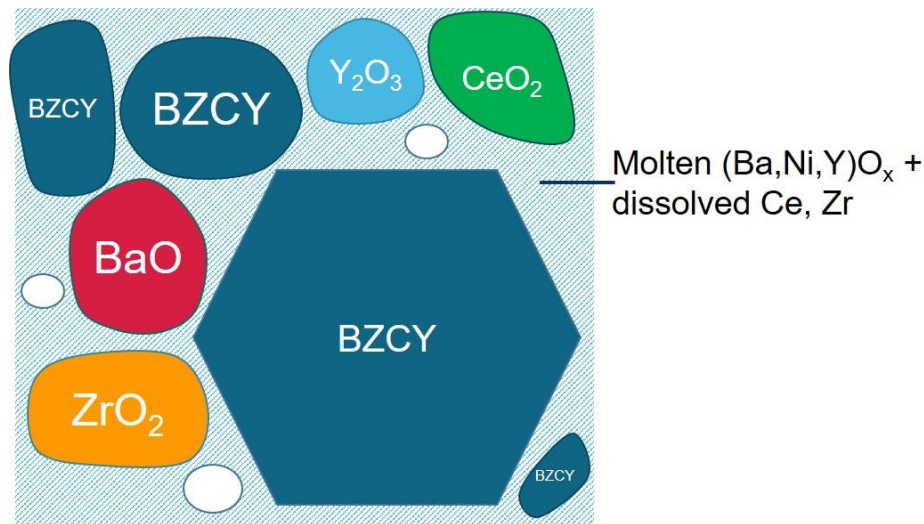


Figure 59: Schematic diagram of sintering mechanism of SSRS.

J. Tong *et al.* ^[107] investigated SSRS sintering of BZY20 by sintering the green pellets with a high NiO content of 2.0 wt.% at different temperatures for 10 h. Different from the present work, the BZY phase already starts to form at 900 – 950 °C, which can be ascribed to the higher NiO content and longer soaking time they used. A BaY_2NiO_5 liquid phase is suggested, but not finally proven. It is discussed that BaY_2NiO_5 decomposes at temperature higher than 1200 °C into V_{Ba}'' , Y_{Zr}' , V_{O}'' , and Ni enters into the lattice to form Ni_{Zr}'' or Ni_i' interstitials. However, based on the discussion in section 3.2.3.2, it is energetically not likely to form either of these two defects. The hypothesis of formation of BaNiO_2 and/or BaY_2NiO_5 is consistent with the TEM-EDX results of Ni accumulation at GBs in this work (**Figure 49**, **Figure 50**, and **Figure 58**). When applying the SSRS procedure to a mixture of BaCO_3 , NiO and Y_2O_3 , at 800 – 850 °C, J. Tong *et al.* ^[107] observed BaNiO_2 , which transforms to BaY_2NiO_5 at higher temperature. While in ref. ^[107] 2.0 wt.% was used, 0.5 – 2.0 wt.% NiO is applied in ref. ^[108], but without detailed analysis of grain sizes. In contrast to the behavior of BZCY in the present work, 0.5 wt.% NiO did not lead to full densification of BZY20 at 1500 °C. This points towards a beneficial effect of Ce in SSRS. This is further confirmed by SSRS of BCY20 in ref. ^[145] where full densification is achieved at 1400 °C with 1.0 wt.% NiO, i.e. at lower temperature compared to BZY20.

D. Fagg *et al.* ^[104] investigated effects of NiO, BaNiO_2 and BaY_2NiO_5 addition in the sintering of pre-formed BZY20 perovskite powder. All three additives help to fully densify ceramics including grain growth at a temperature much lower than CS for BZY20. BaNiO_2 shows the

largest grain size, probably due to its low eutectic point (cf. **Figure 56-(a)**). All three sintering aids yield comparable total conductivities, which are lower than in Ni-free BZY20. Thus, pre-formation of BaNiO₂ and BaY₂NiO₅ does not seem to yield an advantage over NiO addition. D. Han *et al.* ^[113] studied pre-calcined BZY20 with 70 wt.% NiO (as PCFC anode composition). Due to the high NiO content, the sintering mechanism can differ strongly from SSRS of the electrolyte with much less NiO addition (typically ≤ 2.0 wt.%). The authors claimed a different melting point and decomposition mechanism of BaY₂NiO₅ compared to ref. ^[107] by investigating pure BaY₂NiO₅. Remarkably, the BaY₂NiO₅ pellet remained solid at 1500 °C, but partially decomposed into Y₂O₃, BaO and NiO. BaY₂NiO₅ started to partially melt at 1600 °C when it partially decomposed into Y₂O₃ and a liquid phase, which further decomposed into BaNiO₂ and small precipitates during cooling. This work also discussed about the impact of BaO activity on phase appearance by using different sintering strategies (open, covered and embedded). It shows that a high BaO vapor pressure can suppress Y₂O₃ formation. A comparison of BZY20 powder with 1300 °C and 1600 °C pre-calcination temperature indicated BaY₂NiO₅ formation at lower temperature and in higher amounts for the powder prepared at 1300 °C, which had a smaller lattice parameter and lower homogeneity of the element distribution. This again emphasized the importance of BaO and Y₂O₃ availability for liquid phase formation in SSRS.

3.2.3.5 Consequences for membrane fabrication

Even without deliberately adding NiO into the electrolyte layer, it was discovered that the Ni can diffuse several micrometers ^[46,49,106,163] from the anode layer, which is usually composed of BZCY and NiO (50 – 60 wt.%). This can activate SSRS in the electrolyte layer (cf. also section 3.4.2). The diffused Ni and/or the Ni added in the electrolyte raw materials, as in this work, promote the grain growth and densification. Also, the lower sintering temperature required for SSRS is beneficial for membrane fabrication. In order to have well-defined conditions instead of uncontrolled Ni-diffusion, it is desirable to have some Ni in the electrolyte. However, due to the detrimental effect of NiO on proton uptake, which will be shown in section 3.2.4, the amount of NiO in the electrolyte layer should be carefully controlled. Also, too much Ni in the electrolyte layer after reduction may lead to short circuit of the fuel cell, and the reduction process itself may bring in too much volume change which is bad for the membrane's

mechanical strength. Therefore, a controlled amount of NiO was used in membrane fabrication in this work (cf. section 3.4.1) to have a better-defined situation. More details about the suitable amount of NiO will be shown in section 3.3.1.

3.2.3.6 Possible modifications

D. Han *et al.* ^[114] proposed a so-called high temperature reduction cleaning process which involves several reduction and oxidation procedures and results in Ni metal particles accumulating at GBs without disconnecting grains. The BZY20 with 5 mol% NiO (~ 1.34 wt.%) addition shows a higher total conductivity at 600 °C of 6.7×10^{-3} S/cm than as-sintered pellets (2.3×10^{-3} S/cm) in wet H₂. But such a repeated heating treatment is not suitable for membranes, and also the segregated Ni partials may potentially lead to short circuit problem perpendicular to the electrolyte layer. In this work a mild reduction condition (900 °C, 3 vol.% H₂) was used for anode-supported membranes to fully reduce NiO at the anode side. At the electrolyte side Ni stayed partially oxidized as BaY₂NiO₅.

3.2.4 Proton uptake

The water uptake of SSRS samples is investigated for two reasons. (i) As it will be shown, the NiO addition decreases the proton incorporation and thus affects the proton conductivity. (ii) From this decreased proton uptake, conclusion about the formation and composition of the transient liquid phase can be drawn (as in section 3.2.3).

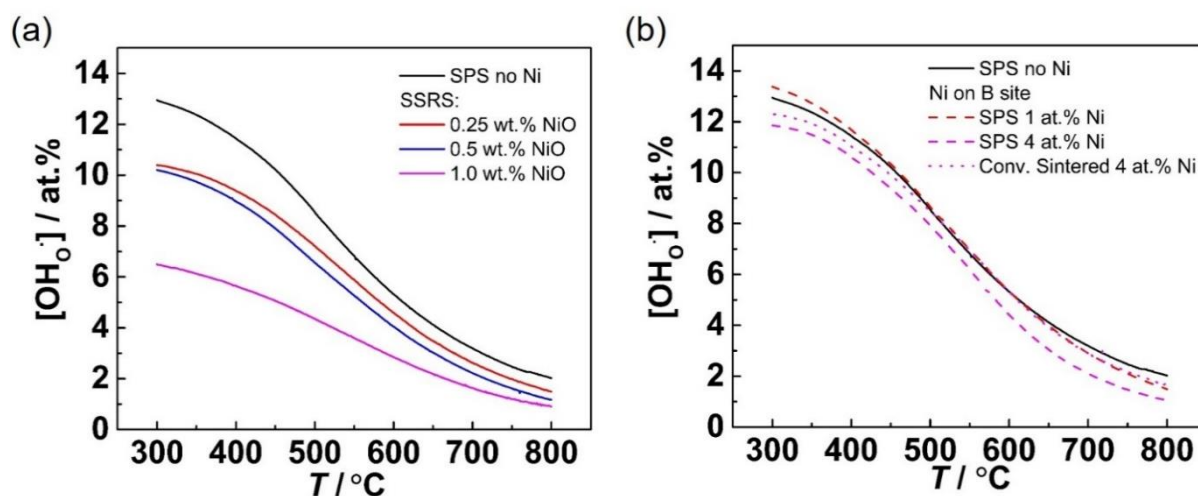


Figure 60: Proton uptake versus temperature measured by TG. (a) with different NiO content and (b) with Ni on B site. The BZC20Y13.6-SPS sample was sintered at 1400 °C 5 min and annealed at 1500 °C 4 h, BZC20Y13.600.25Ni was sintered at 1550 °C 4 h, BZC20Y13.6-0.5Ni was sintered at 1450 °C 4 h, NZC20Y13.6-1.0Ni was sintered at 1450 °C 4 h, BZC20Y13.6Ni1-SPS was sintered at 1350 °C 5 min and annealed at 1400 °C 4 h, BZC20Y13.6Ni4-SPS was sintered at 1300 °C 5 min and annealed at 1400 °C 4 h, and BZC20Y13.6Ni4-CS was sintered at 1500 °C 4 h. 1.0 wt.% NiO \approx 4 at.% Ni on B site.

Figure 60 shows the TG results of BZC20Y13.6 samples prepared by SPS without Ni, SSRS with different NiO content, Ni on B site (bulk Ni) samples by SPS, and CS. Heating and cooling measurements were both executed with rather small hysteresis for all the samples, indicating the measurements are in equilibrium. The average was calculated from heating and cooling mass change. For BZC20Y13.6-SPS without Ni, the sample shows a saturated proton uptake at 300 °C while comes close to the nominal dopant concentration (13.6 at.%). The proton uptake decreases with increasing temperature due to water excorporation. With 0.25 wt.% NiO the proton uptake at 300 °C decreases to ~ 10 %. The decreased proton uptake is more pronounced when the NiO content increases from 0.5 to 1.0 wt.%, as shown in **Figure 60-(a)**. For samples with Ni on the B site, cf. **Figure 60-(b)**, the proton uptake decreases slightly with Ni content (~ 1.5 %) and does not vary too much with preparation methods (SPS or CS). D. Han *et al.* ^[106] also reported a detrimental effect of NiO on the proton uptake of BaZr_{0.8}Y_{0.2}O_{3- δ} . CuO, ZnO have similar decreased proton concentration trends with increasing sintering aid content ^[106].

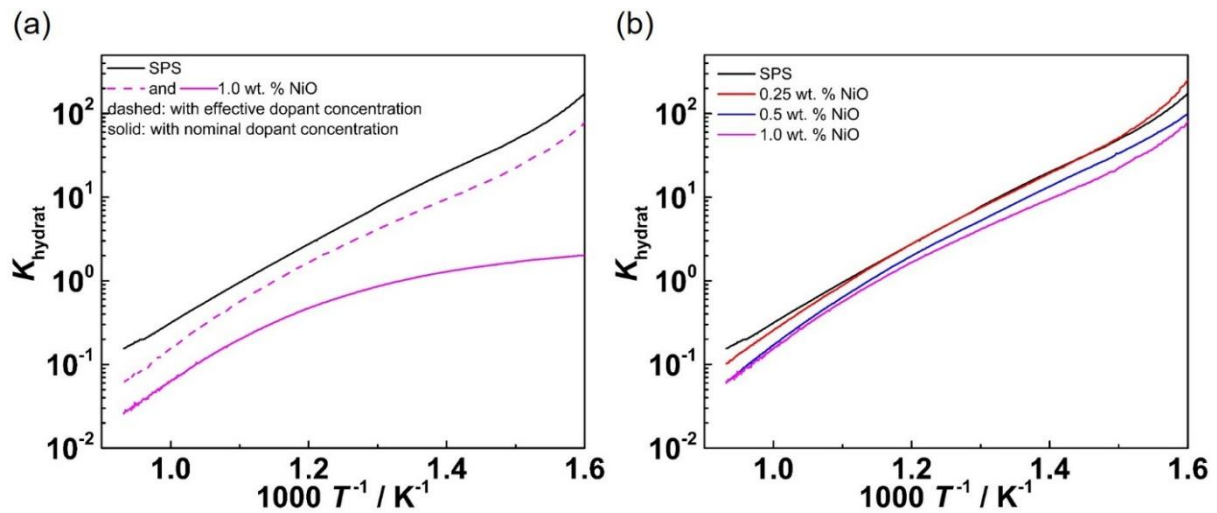


Figure 61: Van't Hoff plots of (a) BZC20Y13.6-1.0Ni compared to BZC20Y13.6-SPS, the plot of BZC20Y13.6-1.0Ni was calculated with both effective and nominal dopant concentration, and (b) different NiO content using effective dopant concentrations.

The mass action constant of the hydration reaction K_{hydrat} was calculated by **Eq. (3)**, using **Eq. (13)** to obtain $[V_{\text{O}}^{\bullet}]$. For Ni-free samples, linear van't Hoff plots were obtained with the nominal dopant concentration. However, for SSRS samples, the van't Hoff plots are depressed in the low temperature range when using the nominal dopant concentration, as shown by the pink solid line in **Figure 61-(a)**. Therefore, a decreased effective dopant concentration has to be used, where $[A_{\text{eff}}]$ corresponds to the low-temperature plateau value of $[OH_{\text{O}}^{\bullet}]$ in **Figure 60-(a)**. This yields approximately linear van't Hoff plots, as shown in **Figure 61-(b)**. The linear fitting for extraction of ΔH° and ΔS° was done in the temperature range of 350 – 800 °C.

Figure 62 shows the effective dopant concentration as function of NiO content. The samples with Ni on B site show a slightly decreased effective dopant concentration, while the effective dopant concentration decreases strongly with NiO content for the SSRS samples. For BZC20Y13.6-1.0Ni by SSRS, the effective dopant concentration is only half of the nominal value, corresponding to a halved proton uptake.

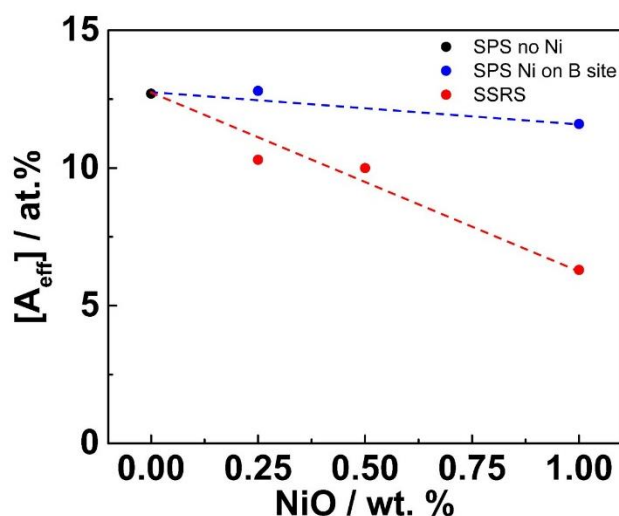


Figure 62: Effective dopant concentration of BZC20Y13.6 Ni-free sample, bulk Ni samples and SSRS samples with different NiO content. The dashed lines are only a guide for the eye.

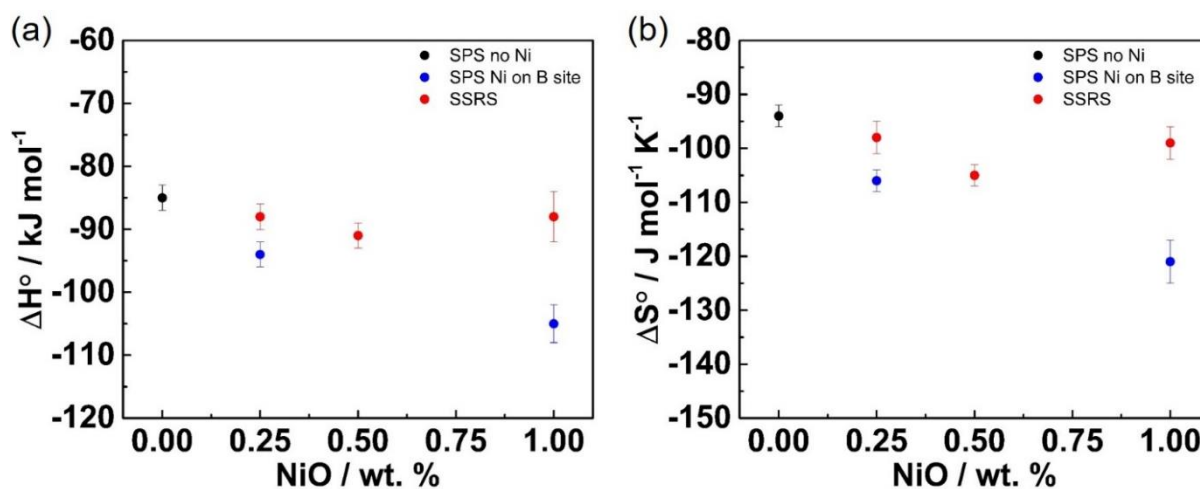


Figure 63: (a) hydration enthalpy and (b) hydration entropy of BZC20Y13.6 Ni-free sample, bulk Ni samples and SSRS samples. The enthalpy and entropy were calculated from the linear fitting of van't Hoff plots.

The hydration enthalpies and entropies are summarized in **Figure 63**. While NiO addition in BZCY does not change ΔH° and ΔS° within the error bar, the samples with Ni on the B site show a more negative hydration enthalpy and entropy, possibly resulting from the trapping effect of $\text{Ni}_{\text{Zr}}^{2+}$ for protons [146]. This difference confirms that Ni in SSRS does not or only slightly incorporate on the B site. The decreased proton uptake induced by NiO addition mainly

comes from decreased effective dopant concentration rather than changing its thermodynamic parameters.

By increasing the nominal Y dopant content the proton uptake increases due to higher effective dopant concentration, as shown in **Figure 64**. With 32 at.% Y doping, the maximum proton uptake can reach $\sim 26\%$. Samples with 1.5 at.% excess Ba on A site do not show much difference to sample without Ba excess. The effective dopant concentration increases linearly with nominal Y content but remains below the nominal value. The increased nominal Y content decreases the hydration enthalpy slightly (for BZY the hydration enthalpy does not vary with Y content ^[146]) and does not affect the hydration entropy (**Figure 65**). However, a high Y content ≥ 28 at.% leads to high sample brittleness due to the lattice distortion caused by the much larger Y^{3+} ion (0.9 Å) than Zr^{4+} (0.72 Å). Therefore, it is preferable to use 20 – 24 at.% Y in PCFC electrolyte fabrication.

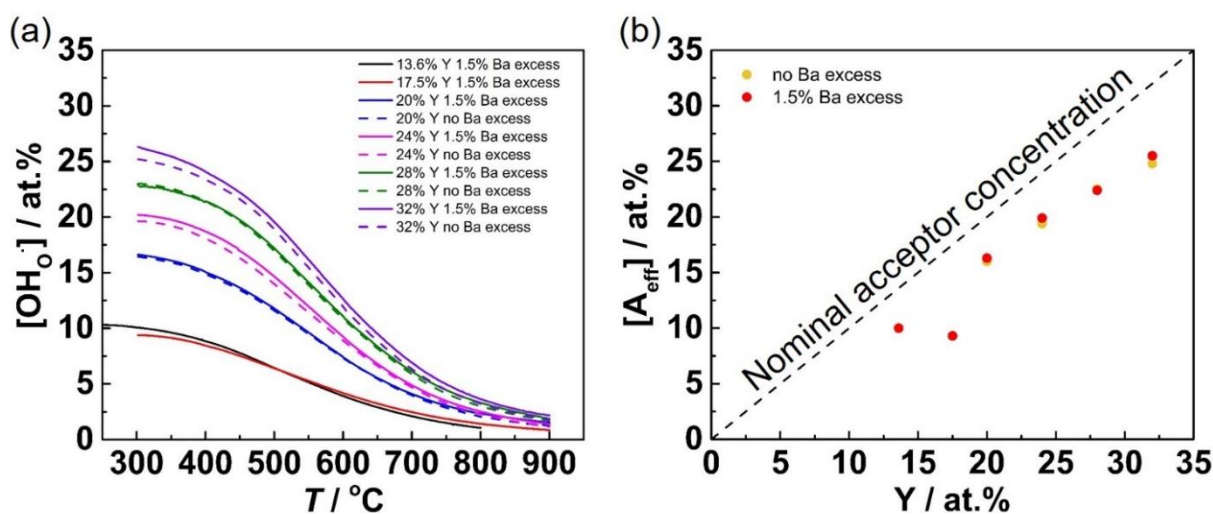


Figure 64: (a) proton uptake with different Y content, with and without 1.5 at.% Ba excess versus temperature and (b) effective dopant concentration versus different Y content. 0.5 wt.% NiO was added in all samples. BZC20Y13.6-0.5Ni was sintered at 1450 °C 4 h and other samples were sintered at 1550 °C 8 h.

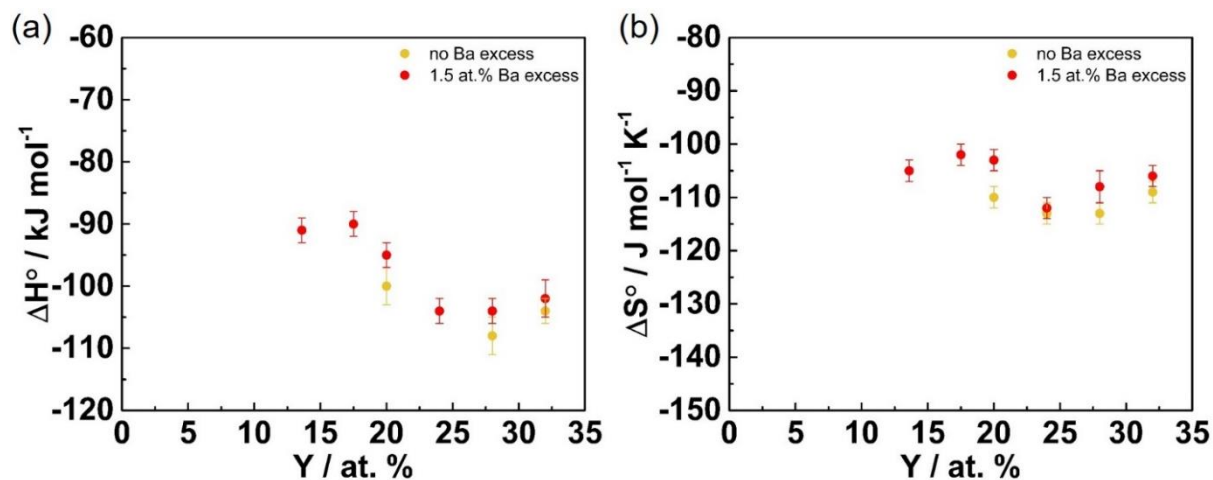


Figure 65: (a) hydration enthalpy and (b) hydration entropy of samples sintered with 0.5 wt.% NiO. The values were calculated from linear fitting of van't Hoff plots.

3.3 Transport properties of SSRS ceramics

3.3.1 Electrochemical impedance spectroscopy

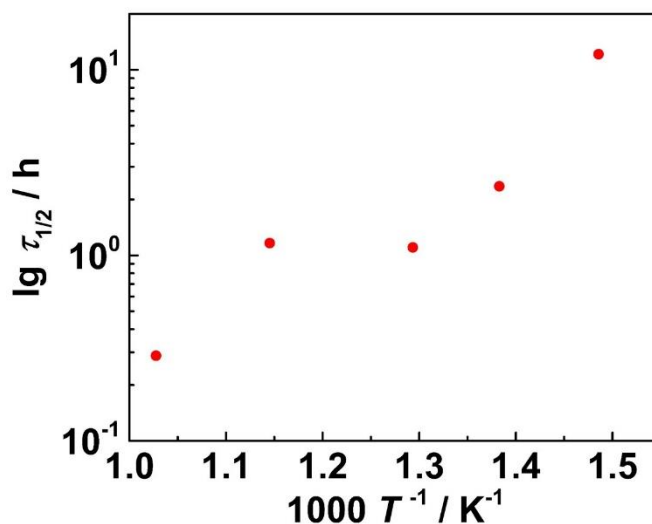


Figure 66: Time $\tau_{1/2}$ to reach 50% of the final degree of hydration of a BZC20YY13.6-1.0Ni sample sintered at 1550 °C 16 h. The measured sample has a thickness of 1 mm.

In order to investigate on the electrochemical properties of SSRS samples, EIS was applied. The sample was first heated to 700 °C in dry N_2 and then switched to humid conditions (20

mbar H_2O). With decreasing temperature, the sample becomes more and more hydrated. **Figure 66** shows as an example the half-time $\tau_{1/2}$ of this equilibration for a 1 mm thick sample. $\tau_{1/2}$ of SSRS samples is shorter than for SPS Ni-free samples (cf. **Figure 8**) due to the largely reduced number of GBs which are blocking for protons and even more for oxygen vacancies. At 400 °C, the hydration is sluggish due to the slow diffusion of oxygen vacancies which becomes limiting at high hydration (more detailed explanation in section 2.2.9 and **Eq. (18)**). For each temperature, typically about 4 – 5 times of $\tau_{1/2}$ was needed to come close to equilibrium. At temperatures ≤ 350 °C, as the hydration is largely complete, the spectra were measured as soon as the temperature stabilized.

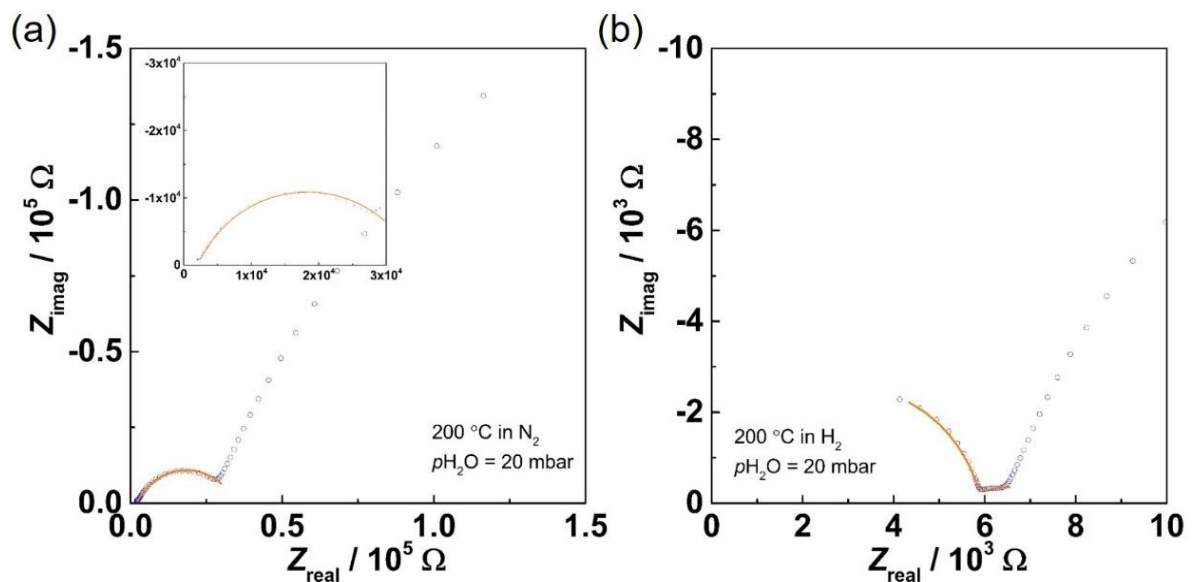


Figure 67: Impedance spectra measured at 200 °C in wet N_2/H_2 ($p_{\text{H}_2\text{O}} = 20$ mbar) from sample (a) BZC20Y13.6-SPS sintered at 1400 °C 5 min and post-annealed at 1500 °C 4 h, and (b) BZC20Y13.6-1.0Ni sintered at 1550 °C 16 h. Symbols are measured data and solid lines are fitting results.

Figure 67 compares the impedance spectra measured at 200 °C in wet atmosphere (N_2 or 3% H_2 in Ar) from BZC20Y13.6-SPS and BZC20Y13.6-1.0Ni. The measurement was done from 700 °C to room temperature after equilibration at each temperature. The spectra consist of a semicircle at high frequencies, which can be assigned to the bulk response based on the capacitance which corresponds to a dielectric constant ϵ_r in the range of 45-65. This bulk semicircle gradually moves out of the measured frequency range for $T > 150$ °C, then only the axis intercept R_b is visible. The semicircle at lower frequencies can be assigned to blocking

grain boundaries (C_{GB} in the range of $10^{-8} - 10^{-9}$). The spectra were fitted by the brick layer model described in section 2.2.9. Compared to the Ni-free sample, the GB semicircle of BZC20Y13.6-1.0Ni is much less pronounced than the bulk semicircle. But even though the GB resistance is smaller than the bulk resistance, the GB is still blocking for proton transport.

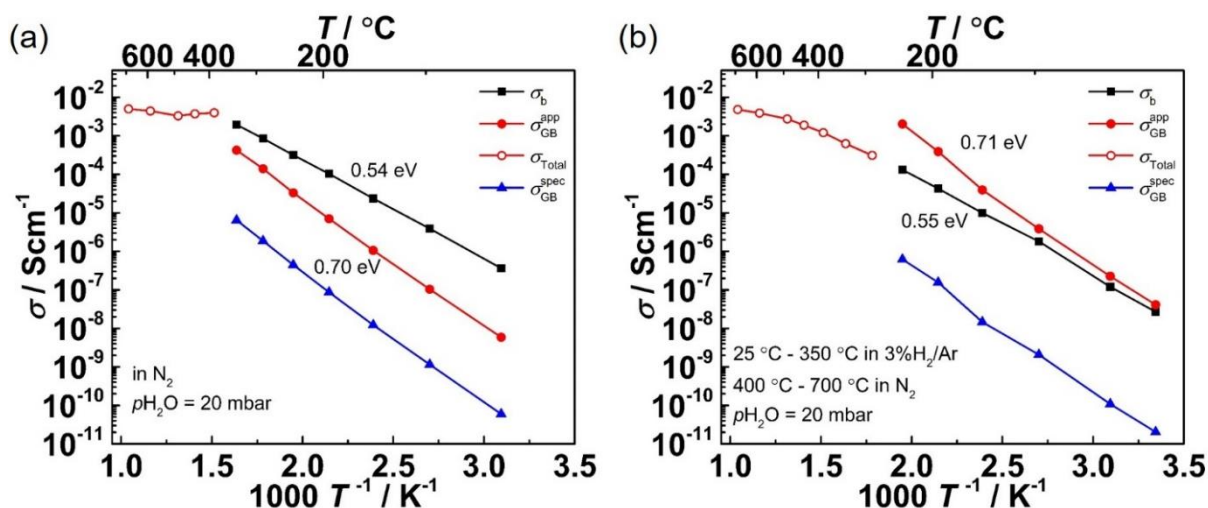


Figure 68: Arrhenius plots of (a) BZC20Y13.6-SPS sintered at 1400 °C 5 min and post-annealed at 1500 °C 4 h, and (b) BZC20Y13.6-1.0Ni sintered at 1550 °C 16 h in wet atmosphere ($p_{H_2O} = 20$ mbar).

Arrhenius plots of BZC20Y13.6-SPS and BZC20Y13.6-1.0Ni are summarized in **Figure 68**. The bulk, apparent GB, and specific GB conductivities were calculated from **Eq. (22)**, **Eq. (23)**, and **Eq. (24)**, respectively. At low temperature, the bulk and GB semicircles can be distinguished from the impedance spectra. The apparent GB conductivity of the SSRS sample is higher than for the Ni-free sample. Considering the comparable specific GB conductivity, the largely improved GB conductivity arises mainly from the much larger grain size of BZC20Y13.6-1.0Ni (see **Figure 35-(a)** and **Figure 35-(d)**). The bulk conductivity of BZC20Y13.6-1.0Ni is slightly lower than BZC20Y13.6-SPS due to its lower proton uptake (**Figure 60-(a)**) and lower proton mobility (see **Figure 69-(b)**). The bulk and GB semicircles cannot be separated anymore at high temperature (this temperature is lower for SSRS samples because of their higher GB conductivity) and only the total conductivity is obtained. At high temperature, the total conductivity is mainly determined by the bulk conductivity, and it is higher for the Ni-free sample. The activation energy was calculated from the log (σT) vs. $1/T$

plot. Both bulk and GB activation energies are comparable for BZC20Y13.6-SPS and BZC20Y13.6-1.0Ni.

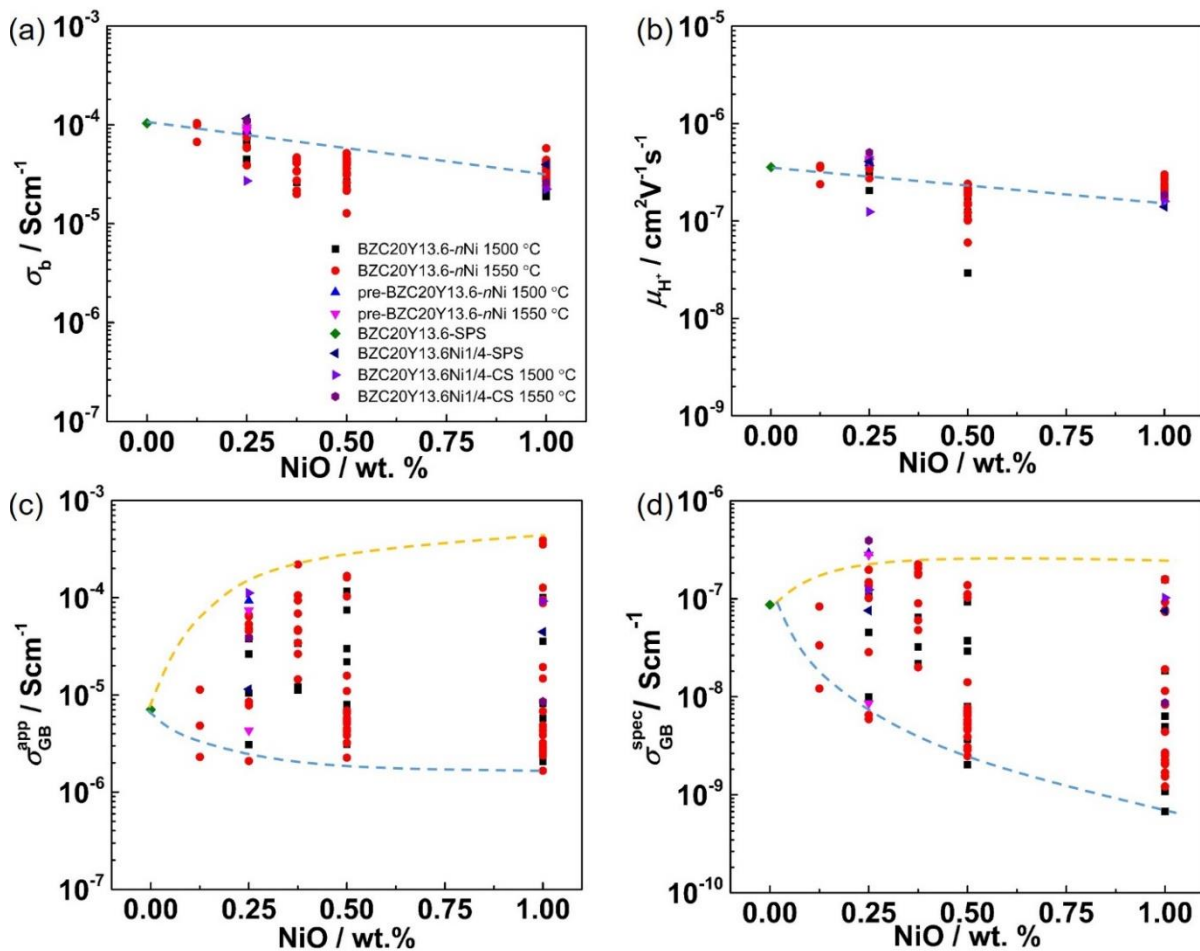


Figure 69: (a) bulk conductivity, (b) proton mobility, (c) apparent GB conductivity and (d) specific GB conductivity measured at 200 °C in wet H_2/Ar ($p_{\text{H}_2\text{O}} = 20$ mbar) versus NiO content. The dashed lines are only a guide for the eye.

Figure 69 shows the summary of the bulk, apparent GB, specific GB conductivity, and proton mobility of samples from different processing: Ni-free SPS, SSRS, SSRS with pre-calcined powder, Ni on B site. Regardless of the sintering method, the bulk proton conductivity at 200 °C decreases systematically with the NiO content, as shown in **Figure 69-(a)**, which comes from both decreased proton concentration (**Figure 60**) and proton mobility (**Figure 69-(b)**). The proton mobility was calculated based on

$$\sigma_b = e c_{\text{H}^+} \mu_{\text{H}^+} \quad (31)$$

where c_{H^+} is the proton uptake, which is obtained from TG measurement for each composition, and μ_{H^+} is the proton mobility. The proton mobility decreases with increasing NiO content may be because V_{Ba}'' and Ni_{Zr}'' formed during liquid phase formation and decomposition act as proton traps.

The apparent GB conductivity increases ~ 1.5 orders of magnitude when the NiO content increases from 0 – 1.0 wt.% with scatters (**Figure 69-(c)**). The scatter increases with the NiO content, indicating that the liquid phase sintering causes some inhomogeneity and decreases reproducibility, especially at GBs (cf. also **Figure 57**). For 1.0 wt.% NiO, the scatter of apparent GB conductivity at 200 °C is ~ 2.5 orders of magnitude, so some of the samples with NiO addition show lower apparent GB conductivity than the Ni-free SPS sample. The GB conductivity scattering will be discussed in more detail in the section 3.3.5. The specific GB conductivity calculated from C_b/C_{GB} (**Eq. (24)**) shows a similar range of scatter, with a slight increase with NiO content as shown in **Figure 69-(d)**. So the improved GB conductivity with NiO content results mainly from the strongly improved grain growth (**Figure 33**, **Figure 35**, **Figure 37**) in SSRS enabled by sufficient (Ba,Y,Ni) O_x transient liquid phase.

The effects of soaking time on GB conductivity are plotted in **Figure 70**. The grain size increases with soaking time as shown in **Figure 33** but does not show significant difference between nominally identical samples (see also section 3.3.5.5 **Figure 84**). As shown in **Figure 70-(a)**, the apparent GB conductivity for 0.5 wt.% NiO addition shows a scatter of 2 orders of magnitude regardless of the soaking time. The specific GB conductivity (**Figure 70-(b)**) indicates that prolonged soaking time does not necessarily result in better GB transport properties. Same phenomena also apply for 1.0 wt.% NiO addition. These also imply the complex nature of the transient liquid phase as discussed in section 3.2.3.

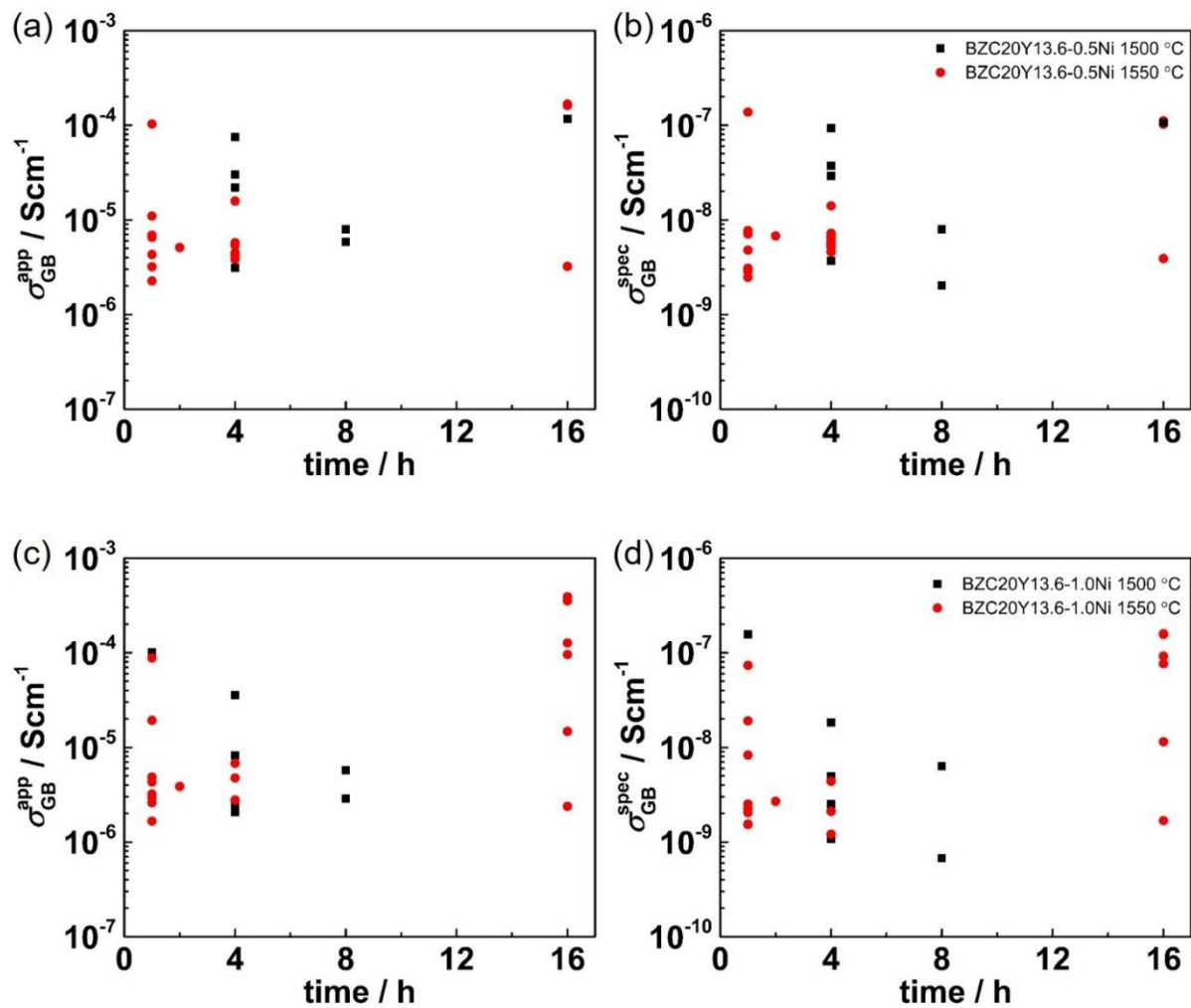


Figure 70: (a) and (c) apparent, and (b) and (d) specific GB conductivity measured at 200 °C in wet H_2/Ar ($p_{H_2O} = 20$ mbar) versus soaking time from BZC20Y13.6-0.5Ni (upper row) and BZC20Y13.6-1.0Ni (lower row) samples sintered at 1500/1550 °C.

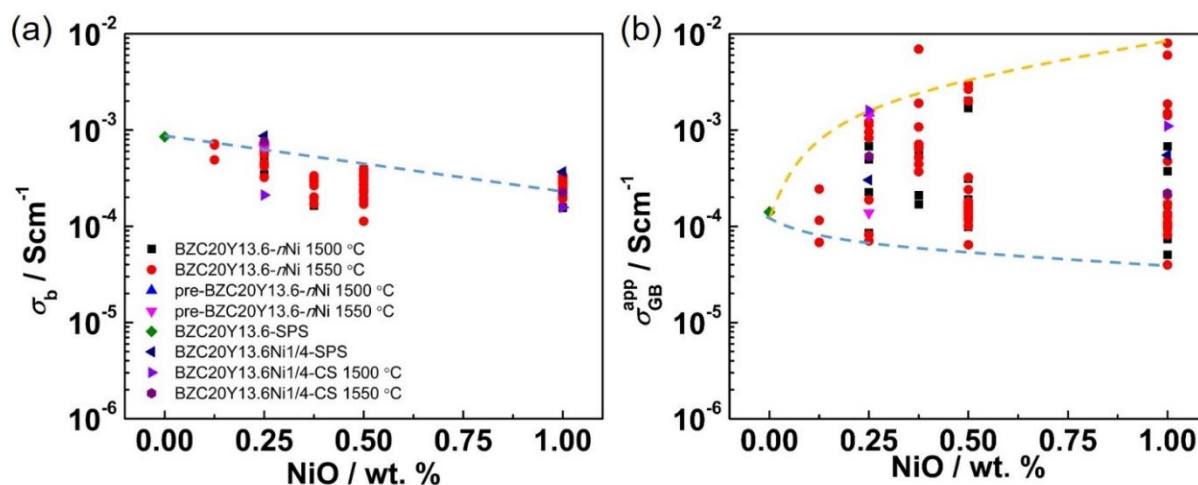


Figure 71: (a) bulk and (b) apparent GB conductivity measured at 300 °C in wet H₂/Ar (pH₂O = 20 mbar) versus NiO content. The dashed lines are only a guide for the eye.

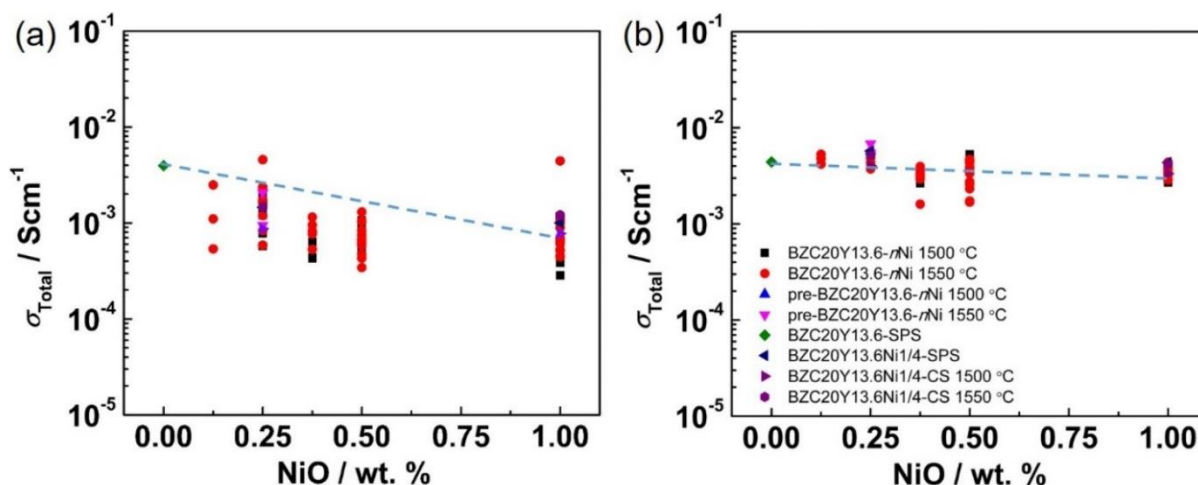


Figure 72: Total conductivity measured at (a) 400 °C and (b) 600 °C in wet N₂ (pH₂O = 20 mbar) versus NiO content. The dashed lines are only a guide for the eye.

The effects of varying NiO content are most pronounced at lowest temperatures. For comparison, **Figure 71** and **Figure 72** show conditions which are closer to actual PCFC operating conditions. The bulk conductivity at 300 °C shows the same decreasing tendency with NiO content (**Figure 71-(a)**), whereas the scatter of apparent GB conductivity decreases with increasing temperature, as shown in **Figure 71-(b)**. The apparent GB conductivity of BZC20Y13.6-1.0Ni increases by ~ 2 orders of magnitude compared to BZC20Y13.6-SPS.

With further increasing temperature to 400 °C, the scatter decreases further. Because the GB activation energy is higher than in the bulk, the total conductivity is mainly contributed from the bulk conductivity which decreases with the NiO content. At 600 °C, the scatter almost disappears, and all samples have a conductivity higher than $1 \times 10^{-3} \text{ Scm}^{-1}$. It is promising for membrane fabrication that the scatter at PCFC operation temperatures (400 – 700 °C) is decreased.

As shown in **Figure 73-(a)**, the bulk activation energy does not vary too much with the NiO content, so the decrease of the bulk conductivity arises mainly from the decreased proton uptake (**Figure 60-(a)**) and proton mobility (**Figure 69-(b)**). The GB activation energy decreases slightly, with a scatter of $\sim 0.2 \text{ eV}$.

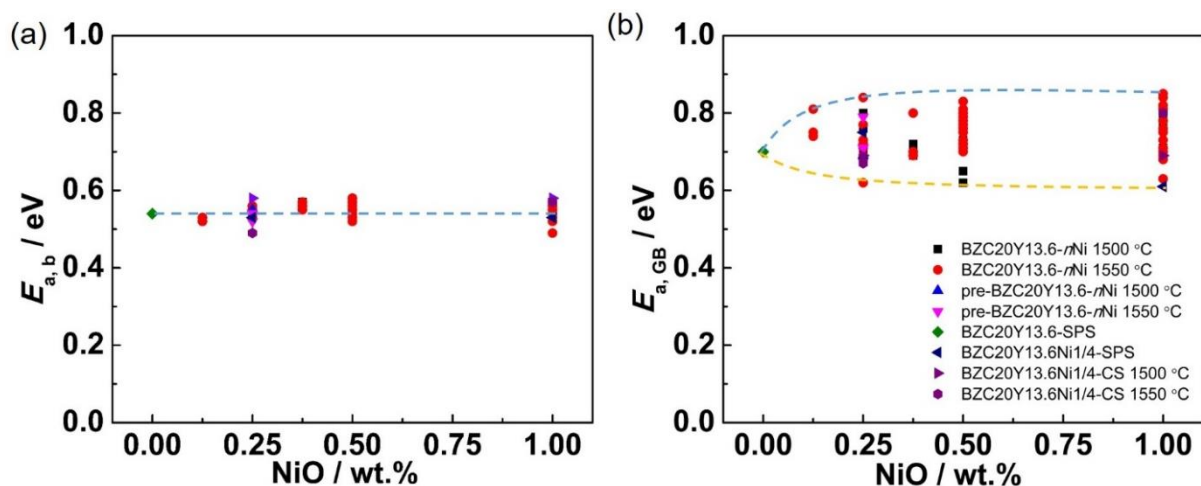


Figure 73: Bulk and GB activation energy (fitted from 100 °C to 350 °C) versus NiO content. The dashed lines are only a guide for the eye.

The results of sections 3.2 – 3.3 can be summarized as follows:

High NiO content improves sinterability and facilitates grain growth of the pellet, which results in largely improved apparent GB conductivity, while the proton uptake is decreased due to lower effective dopant concentration, leading to decreased bulk conductivity. Therefore, one must find the best compromise between the conflict of increased apparent GB and decreased bulk conductivity. Taking both into account, 0.5 wt.% NiO is suggested and used in this work for anode-supported electrolyte membrane preparation. More details about the membrane properties will be shown in section 3.4.

3.3.2 Comparison to literature

Bulk and apparent GB conductivity at 200 °C and total conductivity at 600 °C data from literature are summarized and compared with the results from the work in **Table 7**, **Figure 74**, and **Figure 75**. The present data are comparable with literature. The grain size obtained from literature agrees with the present work. It is important to note that most literature data use a higher acceptor concentration of 20 at.% (which leads to a more than proportional increase of bulk conductivity, cf. ^[164]). Also, several studies used a very high Ce content (open symbols in **Figure 74** and **Figure 75**) which is beneficial for sintering and high degrees of hydration at high temperature, but for which long-time stability versus H₂O, CO₂ is questionable. Not surprisingly, the bulk conductivity at 200 °C from literature decreases with NiO content, by about 1 order of magnitude with 2.0 wt.% NiO addition. Also, at 200 °C, the apparent GB conductivity from literature increases with NiO content with large scatter. The scatter for 0.25 wt.% NiO is as large as ~ 3 orders of magnitude (the corresponding scatter from the present work is ~ 1.5 orders), confirming the difficulty to achieve well-defined proton transport properties at GBs from SSRS. At 600 °C, the total conductivity still shows a scatter of ~ 1.5 orders of magnitude for 2.0 wt.% NiO addition, which is more than in the present work. This may originate from the very different sintering conditions used in the literature.

Table 7: Conductivity of BZCY sintered by SSRS or Ni on the B site results from literature. Bulk and GB conductivity are extracted at 200 °C and total conductivity are data from 600 °C.

Author	Composition	Sintering Conditions	Grain Size / μm	Conductivity / Scm^{-1}			Measurement Conditions
				σ_b	$\sigma_{\text{GB}}^{\text{app}}$	σ_{Total}	
D. Yun <i>et al.</i> [165]	BaZr _{0.8} Y _{0.2} O _{3-δ} + 2.0 wt.% NiO	1435 °C 15 h	0.82	$\sim 9 \cdot 10^{-5}$	$\sim 3 \cdot 10^{-6}$	$3 \cdot 10^{-3}$	Wet H ₂
		1485 °C 15 h	0.96	$\sim 1.2 \cdot 10^{-4}$	$\sim 9 \cdot 10^{-6}$	$3 \cdot 10^{-3}$	
		1535 °C 15 h	1.39			$1.24 \cdot 10^{-3}$	
S. Ricote <i>et al.</i> [100]	BaZr _{0.9} Y _{0.1} O _{3-δ} + 1.0 wt.% NiO	1535 °C 8 h	~ 3	$\sim 1.2 \cdot 10^{-4}$	$\sim 1.2 \cdot 10^{-4}$	$\sim 5 \cdot 10^{-3}$	Wet H ₂
	BaZr _{0.9} Y _{0.1} O _{3-δ} + 1.0 wt.% NiO	Pre-calcine: 1585 °C 6 h Sintering: 1600 °C 12 h	~ 3	$\sim 3 \cdot 10^{-5}$	$\sim 2 \cdot 10^{-6}$	$\sim 5 \cdot 10^{-3}$	
S. Ricote <i>et al.</i> [166]	BaZr _{0.9} Y _{0.1} O _{3-δ} + 1.0 wt.% NiO	1500 °C	1.3			$\sim 2 \cdot 10^{-3}$	Wet H ₂ /N ₂
	BaZr _{0.8} Ce _{0.1} Y _{0.1} O _{3-δ} + 1.0 wt.% NiO		3.1			$\sim 2.5 \cdot 10^{-3}$	
	BaZr _{0.7} Ce _{0.2} Y _{0.1} O _{3-δ} + 1.0 wt.% NiO		3.3			$\sim 3 \cdot 10^{-3}$	
	BaZr _{0.6} Ce _{0.3} Y _{0.1} O _{3-δ} + 1.0 wt.% NiO		3.4			$\sim 6 \cdot 10^{-3}$	
	BaZr _{0.5} Ce _{0.4} Y _{0.1} O _{3-δ} + 1.0 wt.% NiO		3.3			$\sim 8 \cdot 10^{-3}$	
J. Tong <i>et al.</i> [145]	BaCe _{0.8} Y _{0.2} O _{3-δ} + 0.72 wt.% NiO	1400 °C 12 h	~ 1.5	$\sim 1.3 \cdot 10^{-3}$	$\sim 1 \cdot 10^{-4}$	$5 \cdot 10^{-2}$	Wet Ar
		1400 °C 12 h		$\sim 2 \cdot 10^{-3}$	$\sim 1.6 \cdot 10^{-4}$	$2 \cdot 10^{-1}$	Wet H ₂ /Ar
		1000 °C 24 h in H ₂					
J. Tong <i>et al.</i> [108]	BaZr _{0.8} Y _{0.2} O _{3-δ} + 2.0 wt.% NiO	1500 °C 24 h	5			$3.3 \cdot 10^{-2}$	Wet Ar

Continued Table 7: Conductivity of BZCY sintered by SSRS or Ni on the B site results from literature. Bulk and GB conductivity are extracted at 200 °C and total conductivity are data from 600 °C.

D. Han <i>et al.</i> [162]	BaZr _{0.8} Y _{0.2} O _{3-δ} + 0.25 wt.% NiO	1400 °C 24 h	~1	~9·10 ⁻⁴	~1·10 ⁻⁵	Wet O ₂	
		1600 °C 24 h	~2.5	~9·10 ⁻⁴	~2·10 ⁻⁴		
	BaZr _{0.8} Y _{0.2} O _{3-δ} + 1.25 wt.% NiO	1400 °C 24 h	~2	~8·10 ⁻⁵	~2·10 ⁻⁵		
		1600 °C 24 h	~3	~8·10 ⁻⁵	~9·10 ⁻⁵		
D. Han <i>et al.</i> [106]	BaZr _{0.8} Y _{0.2} O _{3-δ} + 0.2 wt.% NiO	1300 °C 10 h 1500 °C 10 h in O ₂			~7.5·10 ⁻³	Wet H ₂	
	BaZr _{0.8} Y _{0.2} O _{3-δ} + 0.5 wt.% NiO				~9·10 ⁻³		
	BaZr _{0.8} Y _{0.2} O _{3-δ} + 1.0 wt.% NiO				~3·10 ⁻³		
	BaZr _{0.8} Y _{0.2} O _{3-δ} + 2.0 wt.% NiO				~4·10 ⁻³		
C. Y. Yoo <i>et al.</i> [167]	BaZr _{0.8} Y _{0.2} O _{3-δ} + 1.4 wt.% NiO	Pre-calcine: 1200 °C 10 h Sintering: 1450 °C 5 h	~5		~3·10 ⁻³	Wet Ar	
R. Costa <i>et al.</i> [168]	BaCe _{0.9} Y _{0.1} O _{3-δ} + 1.0 wt.% NiO	Pre-calcine: 1100 °C 1 h Sintering: 1450 °C 24 h	3	~2.5·10 ⁻⁴	~2·10 ⁻⁴	~8·10 ⁻³	Wet H ₂
S. Ricote <i>et al.</i> [105]	BaZr _{0.7} Ce _{0.2} Y _{0.09} Ni _{0.01} O _{3-δ}	1450 °C 6 h	~0.5	~1.3·10 ⁻³	~8.0·10 ⁻⁵	~2.5·10 ⁻³	Wet H ₂ /N ₂
	BaZr _{0.7} Ce _{0.2} Y _{0.08} Ni _{0.02} O _{3-δ}		~0.7	~6.3·10 ⁻⁴	~1.6·10 ⁻⁵	~1.5·10 ⁻³	
F. Bozza <i>et al.</i> [169]	BaZr _{0.8} Y _{0.19} Ni _{0.01} O _{3-δ}	1400 °C 24 h	0.45	~4·10 ⁻⁵	~2·10 ⁻⁷	Wet H ₂ /N ₂	
		1500 °C 24 h	1.54	~1.8·10 ⁻⁵	~2.2·10 ⁻⁶		
	BaZr _{0.8} Y _{0.18} Ni _{0.02} O _{3-δ}	1400 °C 24 h	0.86	~1.8·10 ⁻⁵	~2.2·10 ⁻⁶		
		1500 °C 24 h	2.26	~3.2·10 ⁻⁵	~1·10 ⁻⁶		
M. Caldes <i>et al.</i> [170]	BaCe _{0.88} Y _{0.1} Ni _{0.02} O _{3-δ}				~1·10 ⁻²	Wet H ₂ /Ar	
	BaCe _{0.85} Y _{0.1} Ni _{0.05} O _{3-δ}				~2·10 ⁻²		
	BaCe _{0.8} Y _{0.1} Ni _{0.1} O _{3-δ}				~1.2·10 ⁻²		
	BaCe _{0.7} Y _{0.1} Ni _{0.2} O _{3-δ}				~1.2·10 ⁻²		

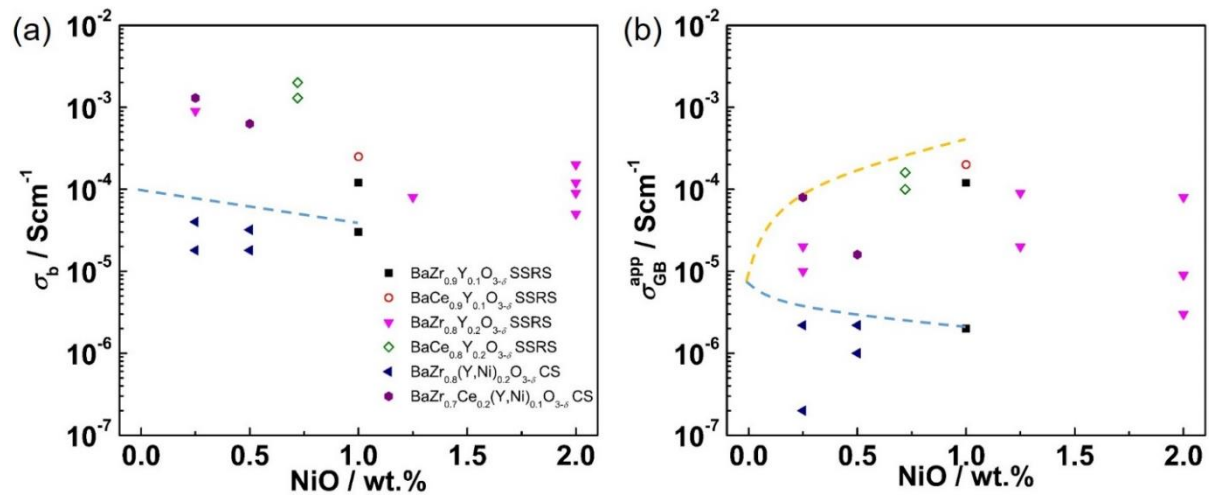


Figure 74: (a) bulk and (b) apparent GB conductivity data at 200 °C from literature [100,105,114,145,162,165,168,169]. The dashed lines are from this work for $\text{Ba}_{1.015}\text{Zr}_{0.664}\text{Ce}_{0.20}\text{Y}_{0.136}\text{O}_{3-\delta}$, cf. **Figure 69-(a)** and **Figure 69-(c)**. Open symbols indicate high Ce content samples.

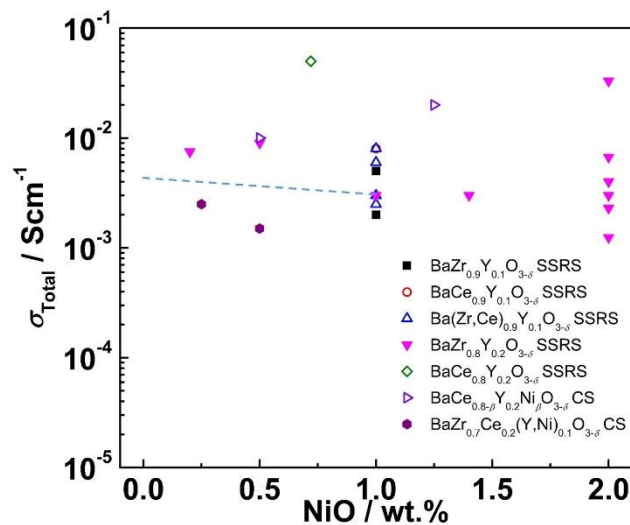


Figure 75: Total conductivity data at 600 °C from literature [100,105,106,108,114,145,162,165–168,170]. The dashed line is from this work for $\text{Ba}_{1.015}\text{Zr}_{0.664}\text{Ce}_{0.20}\text{Y}_{0.136}\text{O}_{3-\delta}$, cf. **Figure 72-(b)**. Open symbols indicate high Ce content samples.

3.3.3 Discussion in terms of space charge

The Debye length is determined by the acceptor dopant concentration, cf. **Eq. (6)**, and summarized in **Figure 76-(a)**. The increase of the experimentally extracted Debye length for SSRS samples with NiO content (~ 0.1 nm from Ni-free to 1.0 wt.% NiO) is primarily induced

by the decreased proton uptake as discussed in section 3.2.4 (**Figure 60**). **Figure 76-(b)** shows the space charge potential which is $\sim 0.45 \pm 0.08$ V for all BZC20Y13.6 with or without NiO addition. The space charge potential was extracted from the peak frequency ratio of ω_b/ω_{GB} from the impedance spectra. The thickness of the space charge depletion zone λ^* determined by the Mott-Schottky model (depending on space charge potential and proton concentration, **Eq. (7)**) therefore slightly increases with the NiO content, whereas the λ^* value deduced by assuming the brick layer model (determined by the capacitance ratio of C_b/C_{GB} and grain size, **Eq. (21)**) decreases with the NiO content due to decreased capacitance ratio. Also, the space charge zone thickness from the brick layer model exhibits a larger scatter.

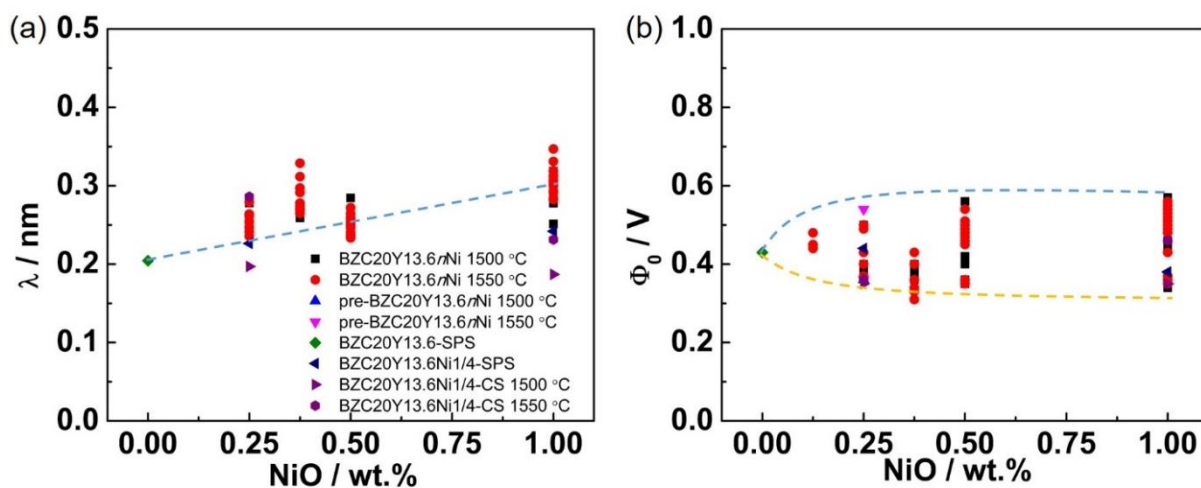


Figure 76: (a) Debye length and (b) space charge potential at 200 °C in wet H₂ versus NiO content. The space charge potential increases only slightly with temperature (~ 0.1 V from 50 – 350 °C.). The dashed lines are only a guide for the eye.

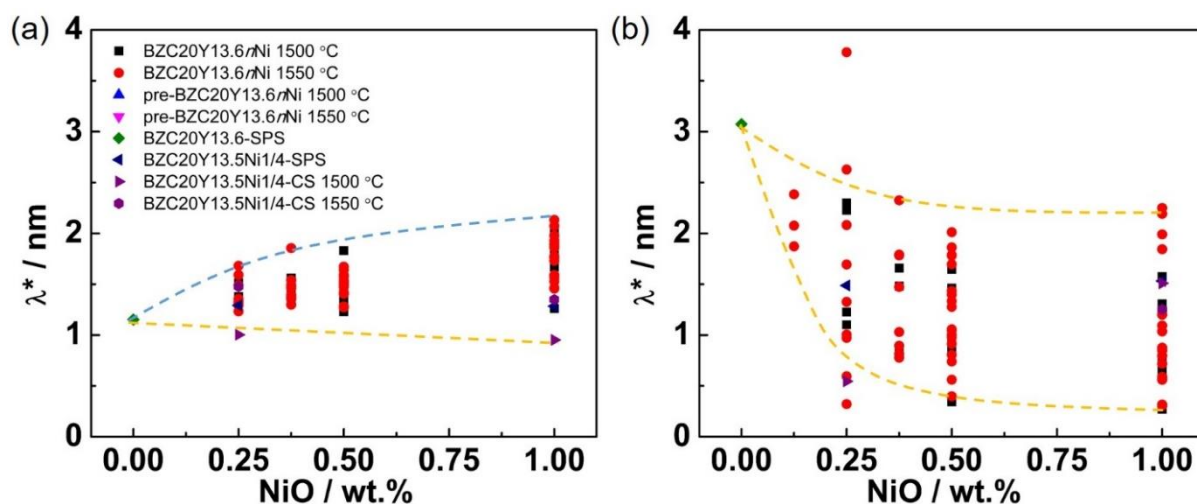


Figure 77: Space charge zone thickness at 200 °C calculated from (a) Mott-Schottky model and (b) brick layer model. The dashed lines are only a guide for the eye.

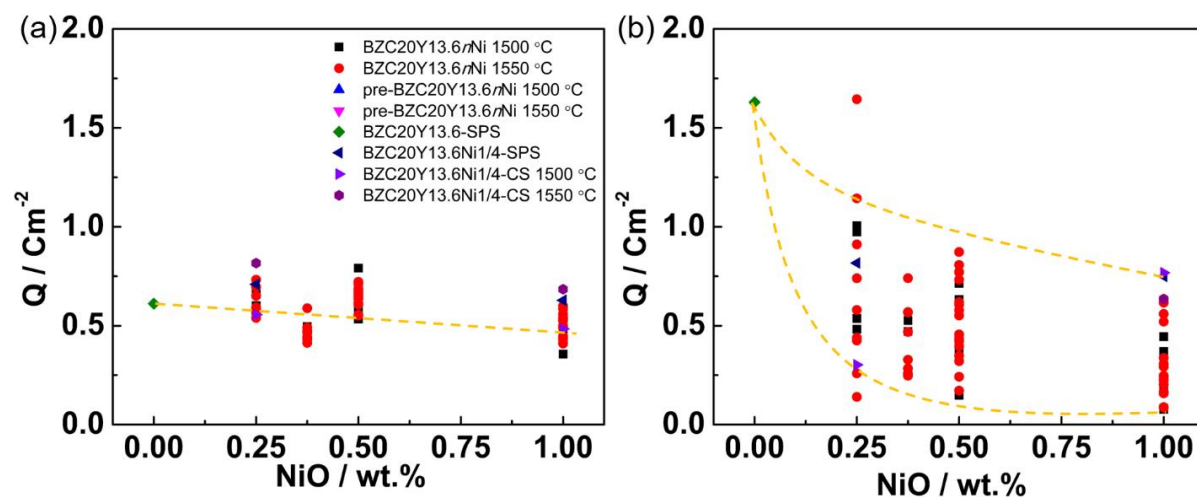


Figure 78: Core charge density at 200 °C calculated from (a) Mott-Schottky model and (b) brick layer model. The dashed lines are only a guide for the eye.

The charge densities of the GB core calculated from the Mott-Schottky model and the brick layer model are summarized in **Figure 78**. Both models result in a decreased core charge density with increasing NiO content, and the brick layer model shows a larger scatter caused by the variation of λ^* . Within the scattering range both analysis models agree, yielding $\lambda^* \approx 1.5$ nm and $Q \approx 0.5 \text{ Cm}^{-2}$. This core charge density corresponds to about 0.28 excess V_{O}^{\bullet} per perovskite formula unit if the core is assumed one unit cell thick (lattice constant of 4.256 Å is used). The slight decrease of Q with increasing NiO content might be related to less “structural

conflicts” in the GB core (leading to less V_O^{\bullet} segregation) when the GBs are formed in presence of sufficient $(Ba,Ni,Y)O_x$ liquid phase. A decreased positive core charge then also decreases the proton depletion in the space charge zone.

3.3.4 Long time stability

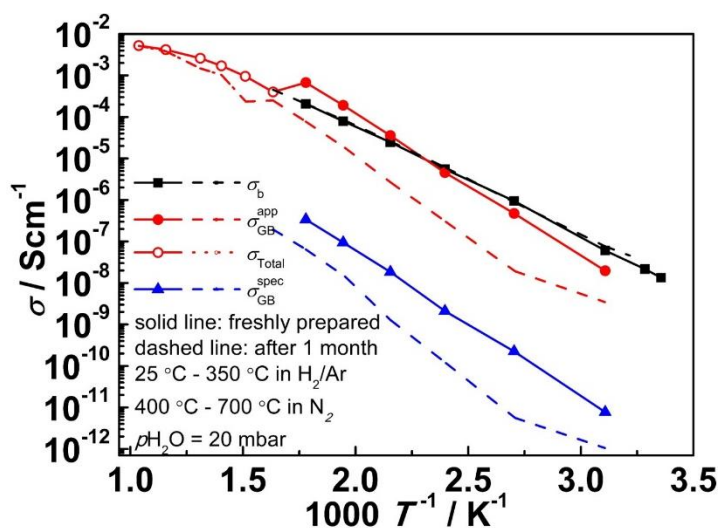


Figure 79: Conductivity comparison for BZC20Y13.6-1.0Ni sintered at 1500 °C 4 h freshly prepared samples (solid lines) and remeasured after 1 month (dashed lines).

In order to test the stability of the sample, second round measurements were conducted for several SSRS samples. **Figure 79** shows the comparison of sample BZC20Y13.6-1.0Ni sintered at 1500 °C 4 h. After 1 month, the bulk conductivity does not change whereas the apparent GB conductivity and specific GB conductivity degrade by ~ 1 order of magnitude, which might be related to the excess Ba accumulated at GBs (see **Figure 57-(a)**) reacting with H_2O and CO_2 in air. But fortunately, the total conductivity at 600 – 700 °C does not decrease. It indicates that for membrane fabrication, the amount of Ba needs to be further fine tuned.

3.3.5 Discussion on GB conductivity scattering

As shown in **Figure 69-(b)**, the scatter of the apparent GB conductivity at 200 °C is as high as ~ 2.5 orders of magnitude for 1.0 wt.% NiO addition. The scatter still exists when the same

NiO addition, same powder batch, and same sintering parameters are applied. Several attempts were tried to identify and eliminate the reasons of the scatter.

3.3.5.1 Insufficient hydration and/or current constriction

In order to check if the scatter is caused by insufficient hydration of the samples, the apparent GB conductivity was plotted versus the bulk conductivity at 200 °C (**Figure 80-(a)**). As there is no obvious relationship between the apparent GB and bulk conductivity, the assumption of incomplete equilibration can be excluded (otherwise the apparent GB conductivity should increase with the bulk conductivity). Also, as shown in **Figure 80-(b)**, the apparent GB conductivity decreases with increasing GB activation energy, which implies that current constriction from bad GB contact ^[171] does not play an important role for the scatter.

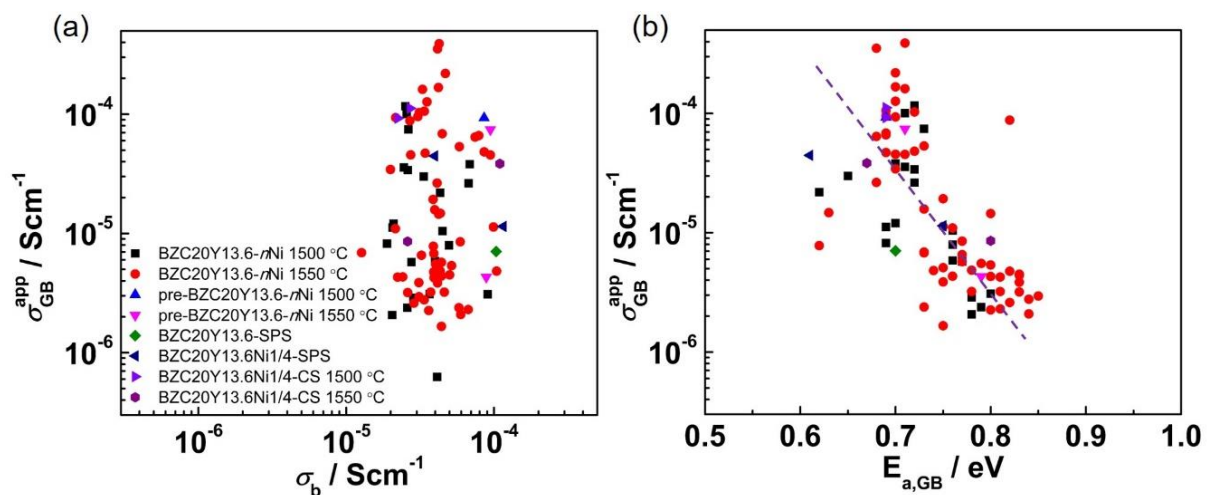


Figure 80: The apparent GB conductivity at 200 °C versus (a) bulk conductivity and (b) GB activation energy. The measurement was done in wet H_2 ($p_{\text{H}_2\text{O}} = 20$ mbar). The dashed line is only a guide for the eye.

3.3.5.2 Inhomogeneity within the sample pellet

During sintering, the formed transient liquid phase might drop to the lower part of the sample due to gravity, resulting in element inhomogeneity and unevenly distributed grain size for different parts of the sample. Therefore, several samples were deliberately sintered and then

cut distinguishing upper, middle and lower parts and measured by EIS. As shown in **Figure 81-(a)**, the bulk conductivity decreases with the NiO content as shown in **Figure 69-(a)**. The apparent GB conductivity (**Figure 81-(b)**) shows comparable scatter scale as all other measured samples. But the scatter happens only among different pellets, not from pieces from one pellet. The apparent GB conductivity is equal in the range of error for both upper and lower parts in one sample.

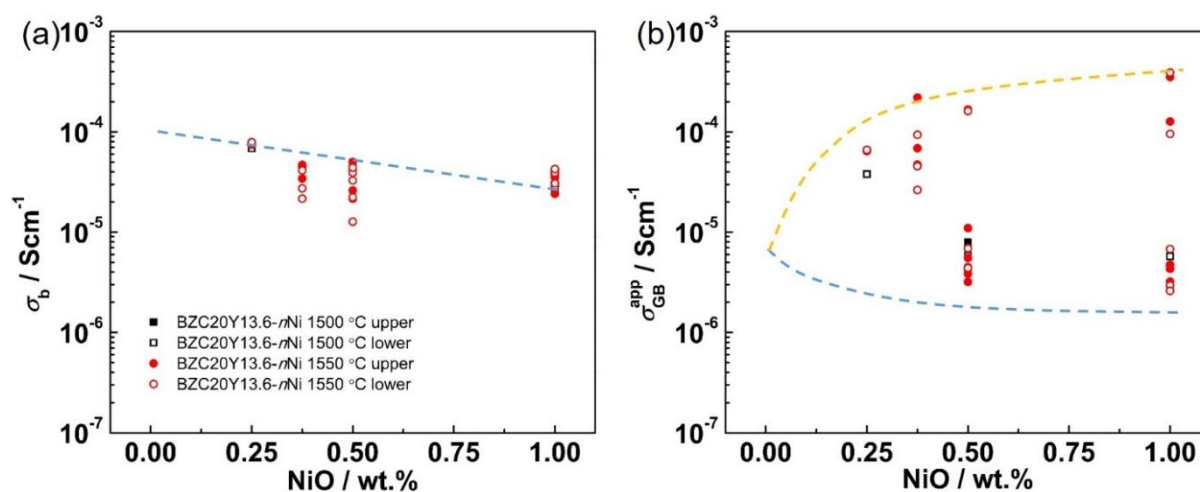


Figure 81: (a) bulk and (b) apparent GB conductivity at 200 °C measured in wet H₂ ($p_{\text{H}_2\text{O}} = 20$ mbar) from samples cut into upper and lower parts. The dashed lines are from **Figure 69-(a)** and **Figure 69-(c)**.

The other possibility resulting in inhomogeneity is that the edge slices of the sample may suffer more from BaO evaporation problem and Ni diffusion to the sacrificial powder than the inner part of a pellet. Accordingly, samples were cut into 3 parts separating the middle and edge parts. As shown in **Figure 82**, for the same pellet, the middle part has a slightly higher bulk conductivity and ~ 1.5 times higher apparent GB conductivity, except one sample has a middle part which has 8 times higher apparent GB conductivity than edge parts. The four measured samples were sintered in groups of two. The difference of apparent GB conductivity is > 1 order of magnitude. And samples sintered at the same time do not show too much variation. Therefore, both measurements taking the edge part into account, and some apparent difference between nominally identical sintering runs can lead to apparent GB conductivity scatter to some extent, which, however, is not enough to explain the large scatter from **Figure 69-(c)**.

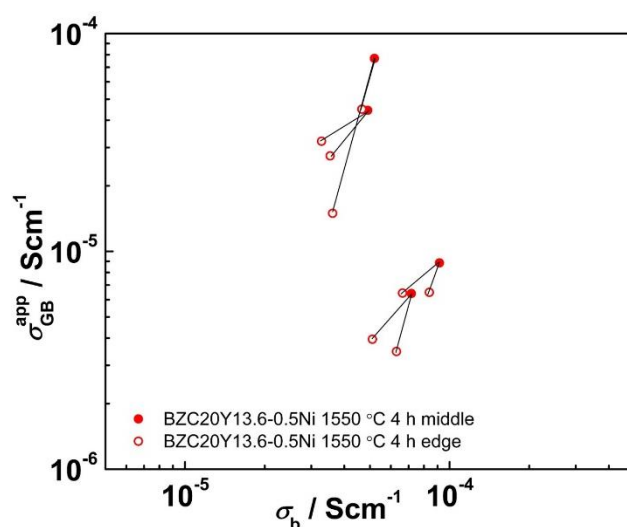


Figure 82: The apparent GB conductivity versus bulk conductivity at 200 °C in wet H₂ ($p_{\text{H}_2\text{O}} = 20$ mbar) from middle and edge parts. Thickness of samples are comparable to 1 mm. The pellets have same nominal composition of BZC20Y13.6-0.5 Ni and were sintered at 1550 °C 4 h. The results from the same pellet are linked by solid line.

3.3.5.3 Ni diffusion and effect of different crucible material

The scatter could also originate from Ni diffusion from samples with high Ni addition to low Ni samples when they were sintered together in the same crucible. The effect of zirconia (Y-doped ZrO₂, YSZ) and MgO crucibles was also investigated because YSZ crucibles might extract BaO from the samples (forming a BaZrO₃ layer) which does not occur for MgO.

BZC20Y13.6-0.25Ni and BZC20Y13.6-1.0Ni were sintered in two ways, (i) alone and (ii) deliberately put together (one BZC20Y13.6-0.25Ni and one BZC20Y13.6-1.0Ni pellets) in both YSZ and MgO crucibles. All the samples were sintered at the same time and in the same oven to exclude the effect from the potential instability of the oven. First, the conductivity does not show much difference for the different crucible materials. Samples sintered separately still have a scatter of ~ 1.5 orders of magnitude (**Figure 83**). Thus, the hypothesis that Ni diffuses from high Ni content to low Ni content samples cannot explain the scatter of the apparent GB conductivity at 200 °C. To exclude that this is caused by incomplete hydration of the less conducting samples, steam hydration was applied but all of them broke into small pieces. It might be because of the brittleness induced by high nominal Ba content.

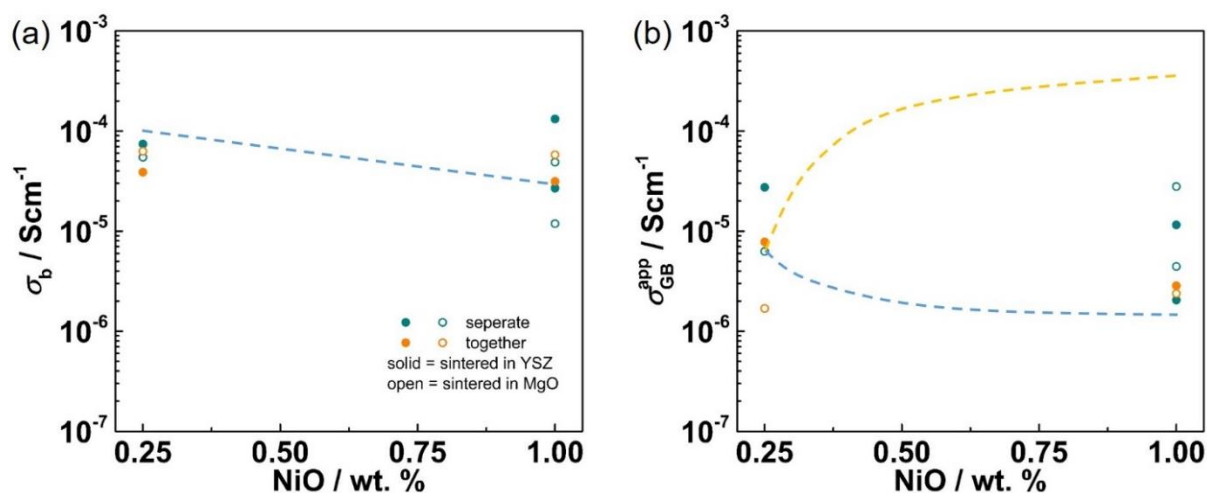


Figure 83: (a) bulk and (b) apparent GB conductivity measured at 200 °C in wet H₂ ($p_{\text{H}_2\text{O}} = 20$ mbar) versus NiO content. The samples were sintered either alone or together with another NiO content. The dashed lines are from **Figure 69-(a)** and **Figure 69-(c)**.

3.3.5.4 Difficulties in EIS

For some samples, typically with “bad” GB conductivity, it was difficult to separate the GB and electrode semicircles at low frequency. This can result in an overestimation of the fitted GB resistance. This phenomenon may result from an incomplete decomposition of the liquid phase at GBs for “bad” samples. It also indicates that the complexity of the SSRS process induces some uncertainty which can lead to inconsistencies between similarly prepared samples.

3.3.5.5 Grain sizes for nominally identical samples

Due to its significant impact on the apparent GB conductivity, the grain size from different BZC20Y13.6 samples with nominally identical NiO addition and sintering parameters was determined from SEM images. Here, chemical etching was used because it provides a faster way to measure the grain size than thermal etching. However, it is difficult to control the amount of etching material, which gives the impression of voids at the GB although in reality the samples have a high density. **Figure 84-(a)** and **Figure 84-(b)** show that for two separate pellets with 0.5 wt.% NiO addition sintered at 1550 °C for 16 h, the averaged grain size is

comparable with each other (3.08 and 3.16 μm , respectively), while the apparent GB conductivity shows a difference of about two orders of magnitude. The same phenomenon was observed also for 1.0 wt.% NiO addition. The grain size is 2.10 and 2.02 μm for samples with “good” (**Figure 84-(c)**) and “bad” (**Figure 84-d**) GB conductivity. There is no significant grain size difference for nominally identical samples.

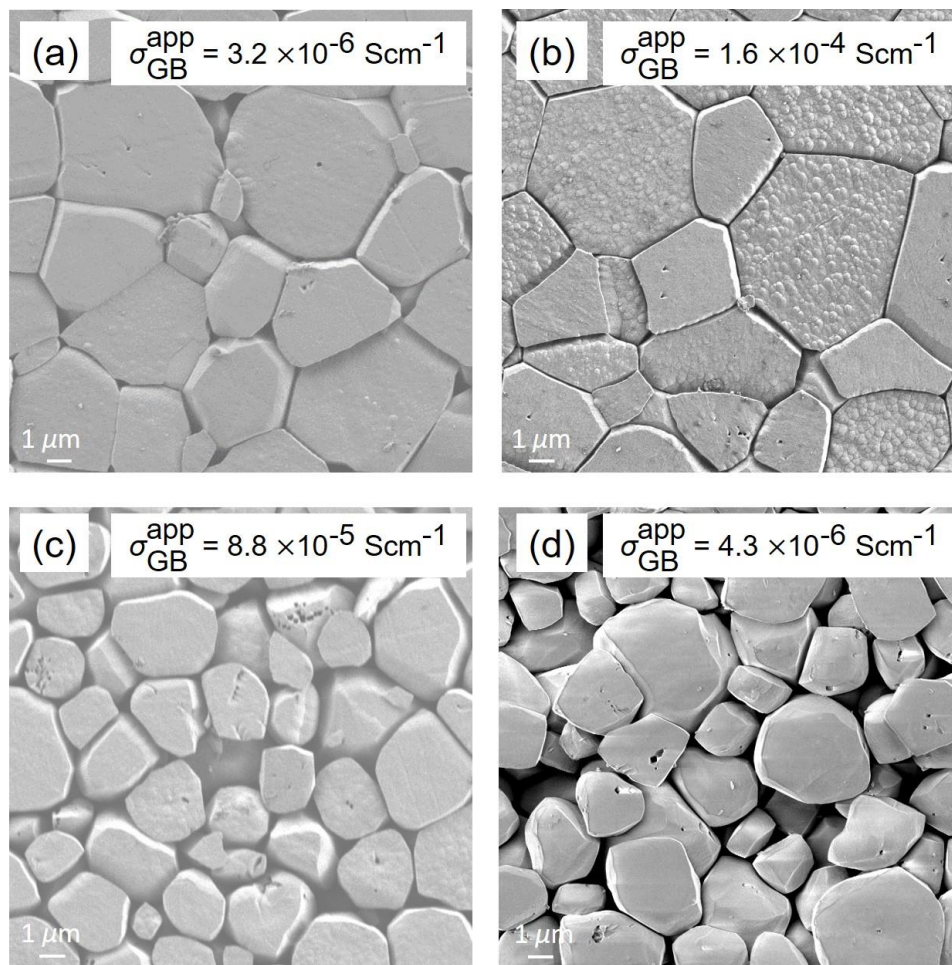


Figure 84: SEM images from chemically etched samples. (a) and (b) are from two BZC20Y13.6-0.5Ni samples sintered at 1550 °C 16 h. (c) and (d) are from two BZC20Y13.6-1.0 Ni samples sintered at 1550 °C 1 h. The apparent GB conductivities measured at 200 °C in wet H_2 ($p_{\text{H}_2\text{O}} = 20 \text{ mbar}$) are indicated for each sample.

3.3.5.6 Element distributions at GBs from TEM-EDX

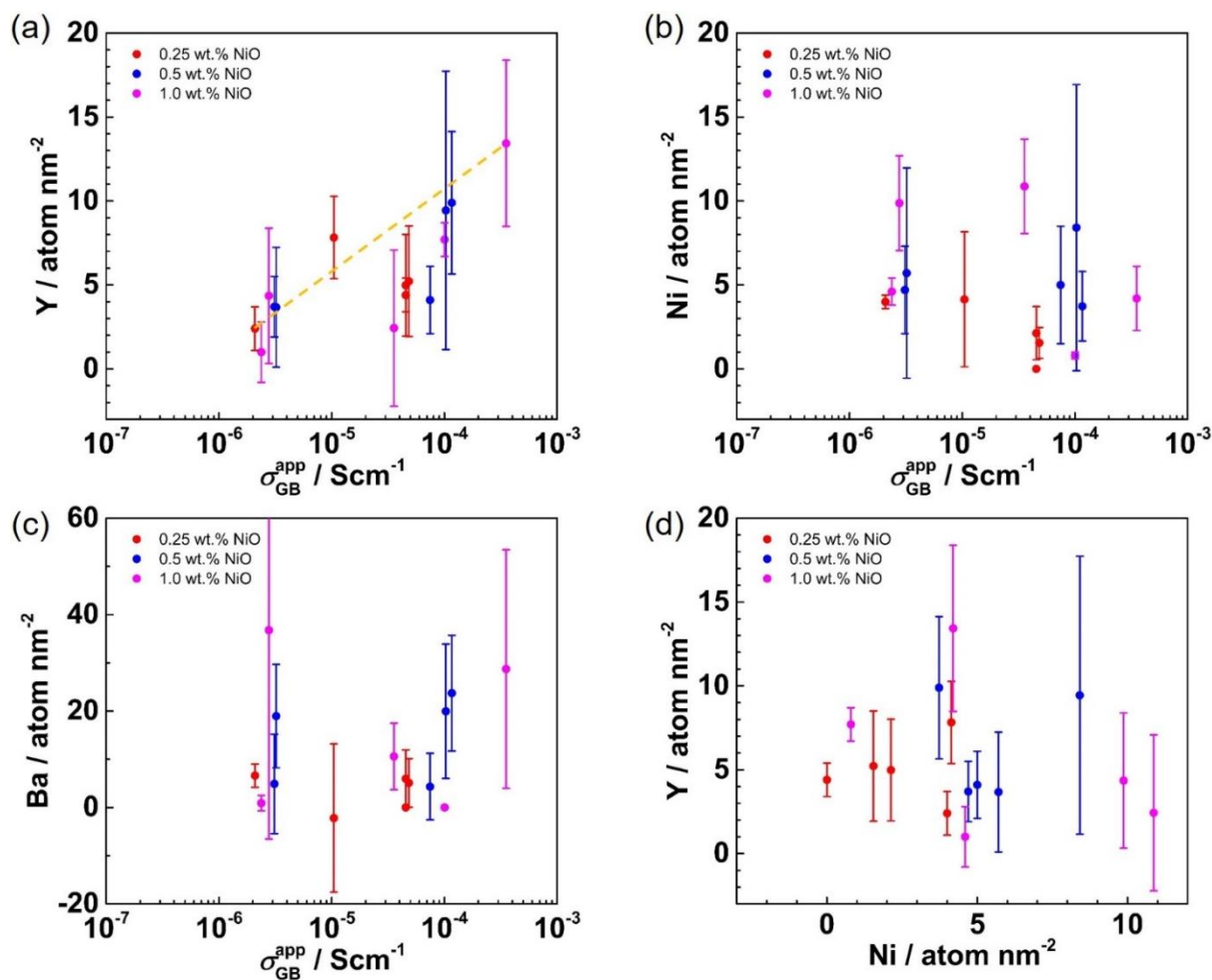


Figure 85: (a) Y, (b) Ni and (c) Ba excess concentration at GBs versus apparent GB conductivity at 200 °C. (d) correlation between Y and Ni excess concentration at GBs. The dashed line in (a) is only a guide for the eye. The measurement comprises a zone of 4 – 5 nm width around the GB, i.e. covers the GB core and the space charge zone. For each sample, at least 10 GBs were measured and the error bar indicates the range of concentrations within the sample.

Element distributions at GBs were investigated by TEM-EDX measurements in order to search for correlations with the large variation of the apparent GB conductivity. Not surprisingly, Y accumulation leads to higher apparent GB conductivity, as shown in **Figure 85-(a)**. Excess Y in the core decreases the core charge, and Y accumulation in the space charge zone represents a partial transition towards the Gouy-Chapman case (cf. also ref. ^[90]). Both effects decrease the blocking for proton transport. Assuming all Y occupies the B site in the form of Y'_{Zr} , an excess of 1 atom nm^{-2} of Y corresponds to a negative charge density of 0.16 Cm^{-2} , which is comparable to the core charge value of 0.5 Cm^{-2} (see also **Figure 78**). The pronounced variation of the local

Y concentration at the GBs within a given sample and between different samples (the bulk concentration is 13.6 at.% for all samples) is probably related to the decomposition of the liquid phase at the end of the sintering process. Ni (**Figure 85-(b)**) and Ba (**Figure 85-(c)**) do not show a strong correlation with the apparent GB conductivity. The Ni content at GBs does not have an obvious influence on Y accumulation, as shown in **Figure 85-(d)**.

3.3.5.7 Annealing treatment

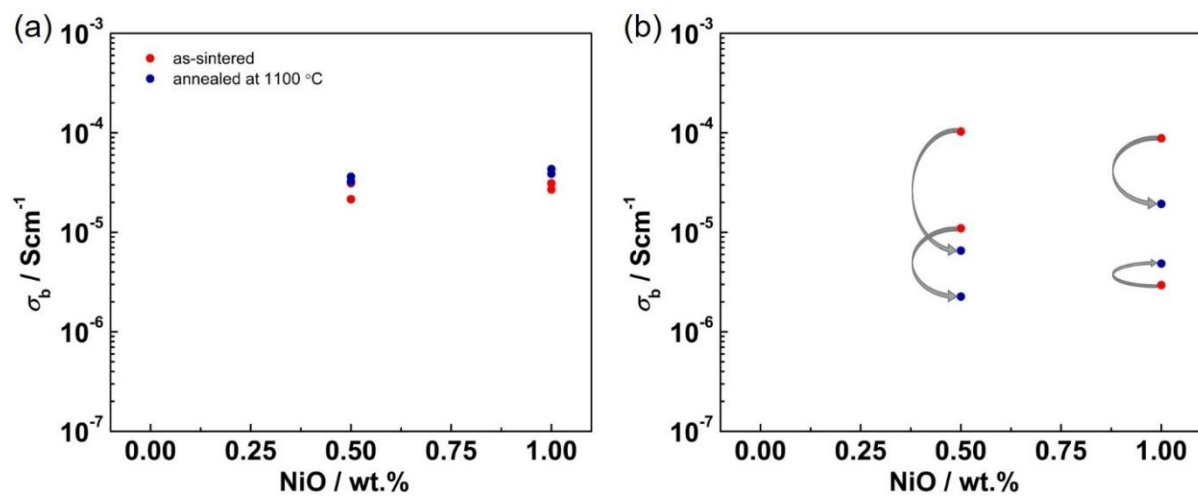


Figure 86: (a) bulk and (b) apparent GB conductivity measured at 200 °C in wet H_2 ($p_{\text{H}_2\text{O}} = 20$ mbar) versus NiO content. The samples were sintered at 1550 °C 1 h and annealed at 1100 °C for 100 h. The arrows in (b) indicate the change of conductivity for each sample.

H. S. Kim *et al.* ^[172] claimed that in sintered BaCeO_3 amorphous phases formed at GBs due to Ba excess, which induce degradation of GB conductivity and chemical instability. According to the phase diagram of BaO-CeO_2 ^[173], they proposed two possible solutions. (i) applying a nominal Ba deficient. This can move the composition from the two phase region (liquid + BaCeO_3) to single phase BaCeO_3 . The GB conductivity from their study was improved, nonetheless, Ba deficiency is known to be detrimental for proton uptake ^[94,147]. Therefore, the second method (ii) annealing treatment was tried in the present work. By post-annealing at a lower temperature than sintering (1100 °C 100 h), the composition can also be moved out from region containing the amorphous phase.

As shown in **Figure 86-(a)**, the bulk conductivity does not change after annealing treatment. However, the apparent GB conductivity degrades, especially for “good” samples. Although the scatter decreases as the “good” samples decrease more than “bad” samples, this result is not desired. The failure of this approach is possibly related to the fact that the BZC20Y13.6 composition is quite far from BaCeO_3 .

3.3.5.8 Higher Y content

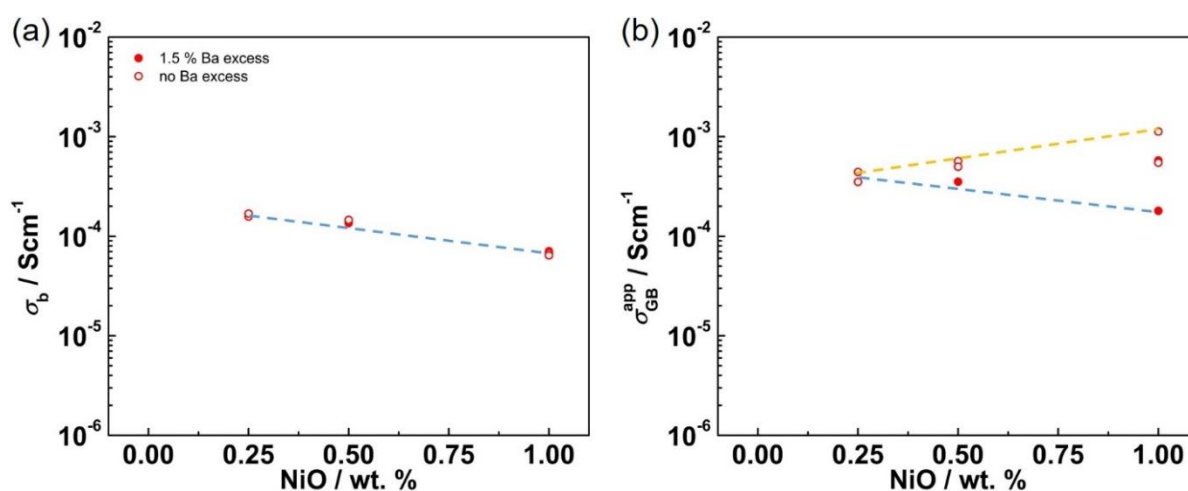


Figure 87: (a) bulk and (b) apparent GB conductivity measured at 200 °C in wet H_2 ($p_{\text{H}_2\text{O}} = 20$ mbar) from sample BZC20Y24- n Ni versus NiO content. The dashed lines are only a guide for the eye.

Since NiO addition decreases the effective acceptor concentration, and this in turn strongly decreases the GB conductivity^[64,90] another approach is using a higher Y content to make the GBs less blocking. Here 24 at.% Y was used (because the samples are stable for Y content < 28 at.%) with 0.25, 0.5 and 1.0 wt.% NiO addition. In **Figure 87**, the bulk conductivity of BZC20Y24- n Ni decreases linearly with NiO content same as for BZC20Y13.6- n Ni (**Figure 69-(a)**), at the meantime, the apparent GB conductivity increases with increasing NiO addition. The scatter also increases with NiO content but much less than BZC20Y13.6- n Ni (**Figure 69-(c)**). For 1.0 wt.% NiO addition, the scatter of BZC20Y13.6 is ~ 3 orders of magnitude, whereas for BZC20Y24 is less than 1 order of magnitude. Because of higher proton uptake, (**Figure 64-(a)**), the bulk conductivity increases from $\sim 5 \times 10^{-5} \text{ Scm}^{-1}$ for BZC20Y13.6-0.5Ni (**Figure 69-(a)**) to $\sim 1.5 \times 10^{-4} \text{ Scm}^{-1}$ for BZC20Y24-0.5Ni (**Figure 87-(a)**). The apparent GB conductivity

of “good” samples increases even stronger from $\sim 2 \times 10^{-4} \text{ Scm}^{-1}$ (**Figure 69-(c)**) to $\sim 1 \times 10^{-3} \text{ Scm}^{-1}$ (**Figure 87-(b)**) at 200 °C.

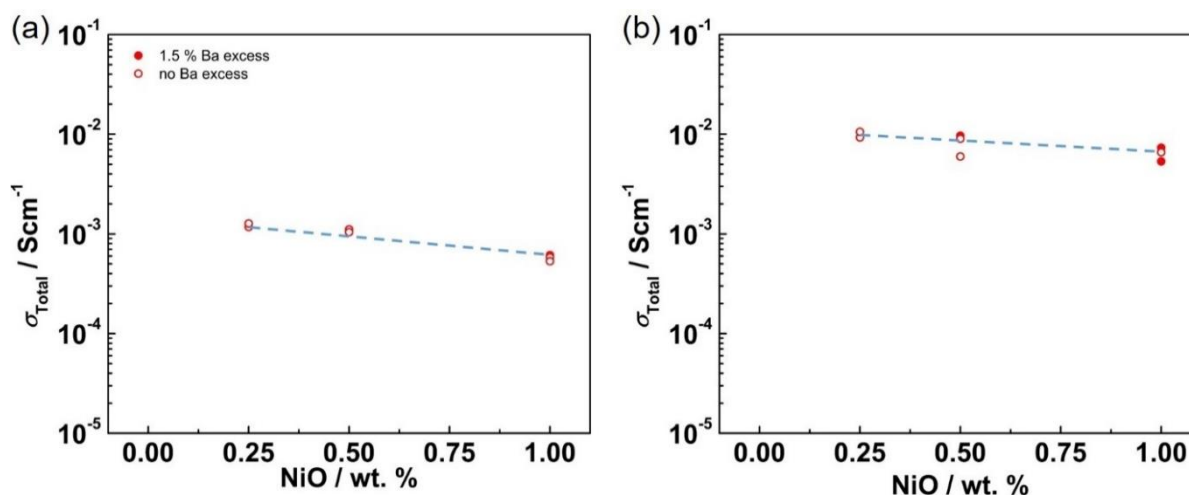


Figure 88: Total conductivity of BZC20Y24-*n*Ni measured at (a) 300 °C in wet H₂ ($p_{\text{H}_2\text{O}} = 20 \text{ mbar}$) and (b) 600 °C in wet N₂ ($p_{\text{H}_2\text{O}} = 20 \text{ mbar}$) versus NiO content. The dashed lines are only a guide for the eye.

At 300 °C, only the total conductivity can be read from the impedance spectra for BZC20Y24-*n*Ni, and it decreases with the NiO content (**Figure 88-(a)**). At 600 °C, the total conductivity of BZC20Y24-0.5Ni is $\sim 1 \times 10^{-2} \text{ Scm}^{-1}$ (**Figure 88-(b)**), ~ 3 times higher than BZC20Y13.6-0.5Ni ($\sim 3.5 \times 10^{-3} \text{ Scm}^{-1}$, **Figure 72-(b)**).

The results above show that, BZCY-*n*Ni with 24 at.% Y has high bulk and apparent GB conductivity at low temperature with much smaller scatter of apparent GB conductivity compared to lower Y content. At 600 °C, the total conductivity fulfills the requirement for PCFC membranes. Nevertheless, the stability for long time and in higher $p_{\text{H}_2\text{O}}$ should further be investigated. Thus, 24 at.% Y in SSRS electrolyte layer is recommended for future membrane fabrication.

3.3.6 Relation to TEM-EELS results on Ce valence

The EELS signal of cerium is sensitive to its oxidation state, the energies of the Ce M₅ absorption edge are $\sim 882 \text{ eV}$ and $\sim 884 \text{ eV}$ for Ce³⁺ and Ce⁴⁺, respectively^[174]. As shown in

Figure 89-(a) in the ADF image, EELS measurement was done across a GB. The decreased ADF signal in **Figure 89-(b)** marks the position of a 4 – 5 nm wide GB, whose length is comparable to the space charge zone thickness calculated in **Figure 77**. Inside of the GB area, a decrease of Ce M_5 edge from 884 eV to about 882.5 eV is observed, implying that Ce^{4+} is partially reduced to Ce^{3+} at the GB. In this scenario, the space charge model changes from the Mott-Schottky situation partially to the Gouy-Chapman. In the Mott-Schottky model, the dopant cations are immobile and the space charge zone is widened compared to the Gouy-Chapman case in which the acceptor concentration increases towards the GB core (either by mobile dopants, or –as here- by valence change). The specific GB conductivity is improved because the decreased Ce valence partially compensates the core charge and decreases the width of the space charge zone.

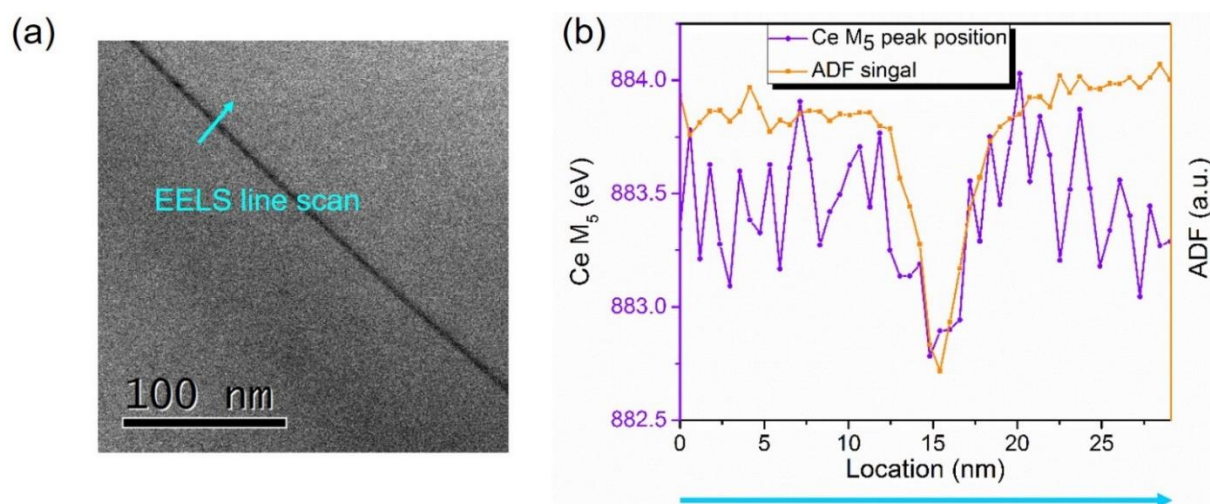


Figure 89: (a) ADF image and (b) corresponding EELS result. The arrow in (a) indicates the direction and position of the measurement. The sample is BZC20Y13.5-0.5Ni sintered at 1500 °C 4 h. The measurement was done by D. Zhou.

3.4 Transport properties of SSRS tape-cast membranes

Tape-casting is the standard method for fabrication of large-area ceramic membranes, e.g. for conventional SOFCs. However, microstructure and transport properties (in particular GB conductivity) may be sensitive to changes in the processing. Thus, it is important to investigate also the SSRS process and resulting conductivities for tape-cast BZCY membranes.

3.4.1 Sequential tape-casting, choice of anode composition

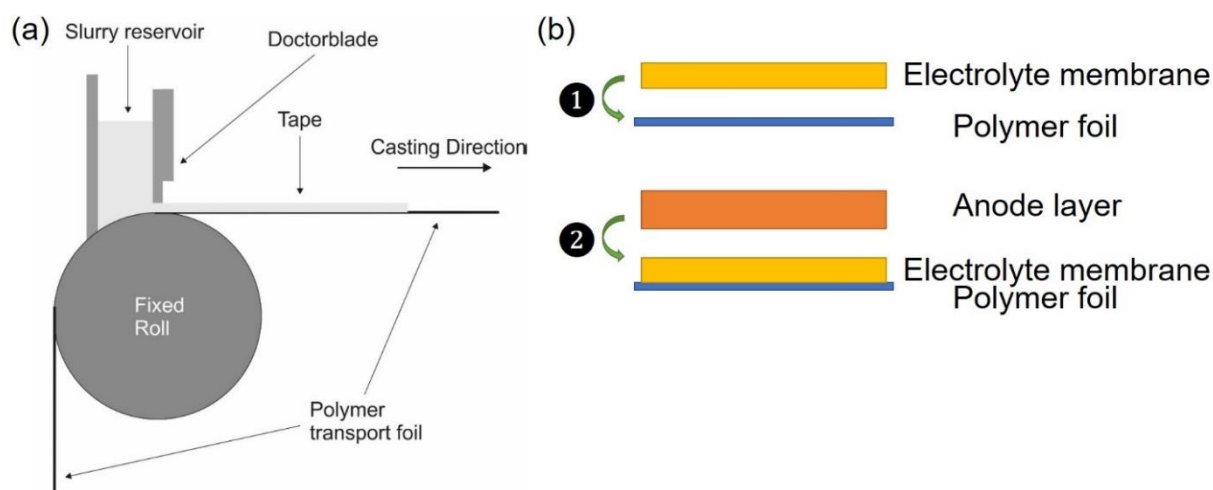


Figure 90: Schematic diagrams of (a) tape-casting and (b) sequential tape-casting used in this work.

Tape-casting is a suitable method for preparing large-area ceramic membranes. M. Marrony *et al.* ^[175] prepared the supporting anode layer for PCFCs (60 wt.% NiO + 40 wt.% BaZr_{0.1}Ce_{0.8}Y_{0.1}O_{3- δ}) by tape casting, but the electrolyte layer was applied by screen printing. Several other reports also used tape-casting for the NiO/BZCY (or BZY) anode and suspension spraying ^[176,177] for the electrolyte layer. Huang *et al.* ^[178] reported anode/BZY electrolyte assemblies prepared by tape-casting. However, the electrolyte layer using SSRS has a high NiO addition of 4 wt.%, which is detrimental for proton uptake ^[106] (see section 3.2.4), and the sample size was limited to a diameter of 2 cm.

In the present work, tape-casting was adopted for both electrolyte and anode layers. The final thickness of the electrolyte layer is about 10 μm , which suffices to obtain gas-tightness. The anode layer is much thicker because it has to supply the mechanical stability.

As shown in **Figure 90-(a)**, the slurry consisting of the ceramic powder with binders (PVB-98) and solvent (EtOH/MEK) flows in the casting direction on a polymer carrier foil. The thickness of each casted layer is controlled by the doctor blade. In the present work, sequential tape-casting was used. The $\sim 10 \mu\text{m}$ thick electrolyte layer was first casted onto the polymer foil, followed by the thicker anode layer, as shown in **Figure 90-(b)**. By the sequential tape-casting a uniform electrolyte layer having good contact with the anode layer can be obtained. The tape-casting was performed using a KAROcast 300-7 (KMS Automation GmbH, Dresden, Germany) tape caster. The casted tapes are dried at room temperature over 5 h for the electrolyte layer and 12 h for the anode layer, respectively, and then cut into the desired sizes. The tape-casting and sintering of membranes were done by W. Deibert from Forschungszentrum Jülich GmbH, IEK-1.

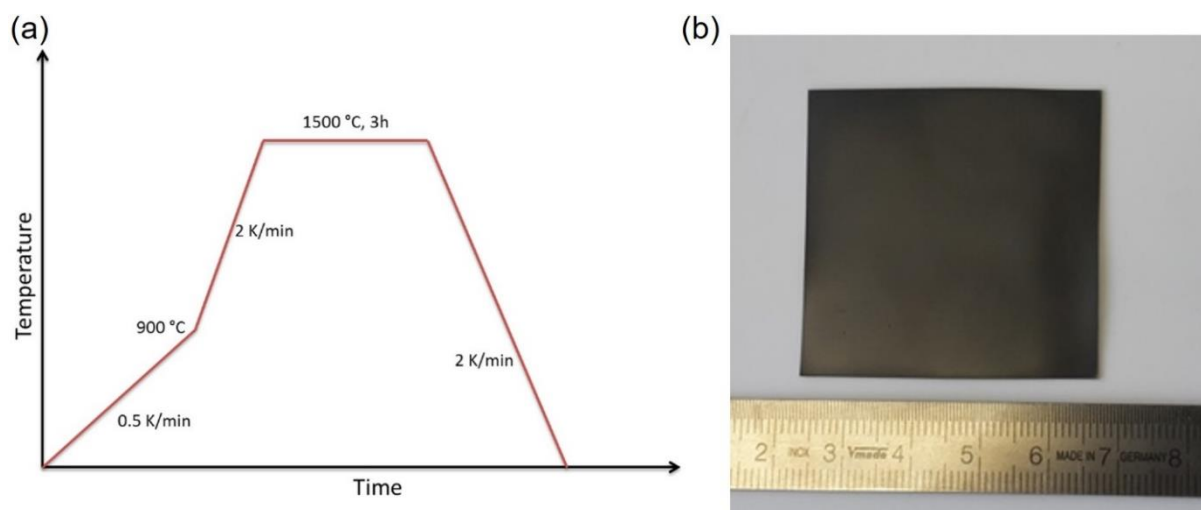


Figure 91: (a) sintering protocol and (b) as-sintered membrane sample.

Based on the discussion from the previous sections, 0.5 wt.% NiO was chosen as sintering aid and 17.5 at.% Y was used for the electrolyte layer in this thesis. The electrolyte powder was pre-calcined at 1100 °C for 4 h to reduce the volume shrinkage during sintering. The anode side is 40 wt.% BZCY perovskite powder having the same composition as the electrolyte ($\text{Ba}_{1.015}\text{Zr}_{0.625}\text{Ce}_{0.20}\text{Y}_{0.175}\text{O}_{3-\delta}$) plus 60 wt.% NiO. As shown in **Figure 91-(a)**, the organics in the slurry has to be burned out, and the heating rate is very slow to prevent pinhole and crack formation. The sample can be fully densified at 1450 °C. The membrane size reaches 5 cm \times 5

cm (**Figure 91-(b)**) and further upscaling is in progress. More details about membrane tape-casting and preparation can be found in ref. ^[179].

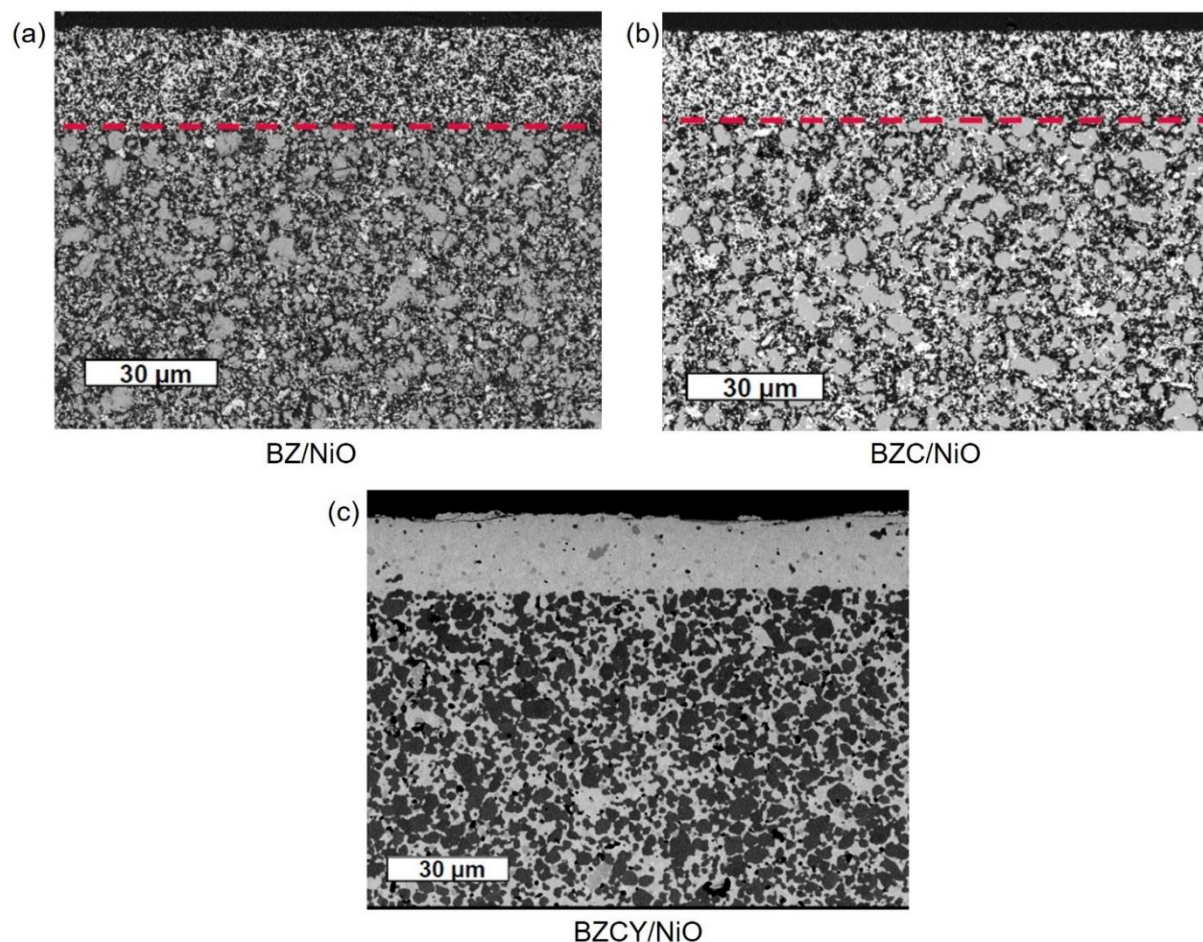


Figure 92: cross-section SEM images of BZCY electrolyte membranes with different anode material compositions after sintering. Images were recorded at IEK-1.

Although using BZCY in the anode with the same composition as the electrolyte layer yield best compatibility, the volume change of the anode layer during hydration/dehydration can result in mechanical problems. Therefore, two other possible anode materials, BaZrO_3 and $\text{Ba}(\text{Zr,Ce})\text{O}_3$ were tried, but in both cases the anode layers and thus also the electrolyte membrane cannot be fully densified (**Figure 92-(a)** and **Figure 92-(b)**). Only BZCY/NiO shows good densification. In order to suppress the expansion during hydration, a lower Y content (3 at.%) will be tried in future work with the expectation that this combination has low volume change and good sinterability.

3.4.2 Phases and morphology of the membranes

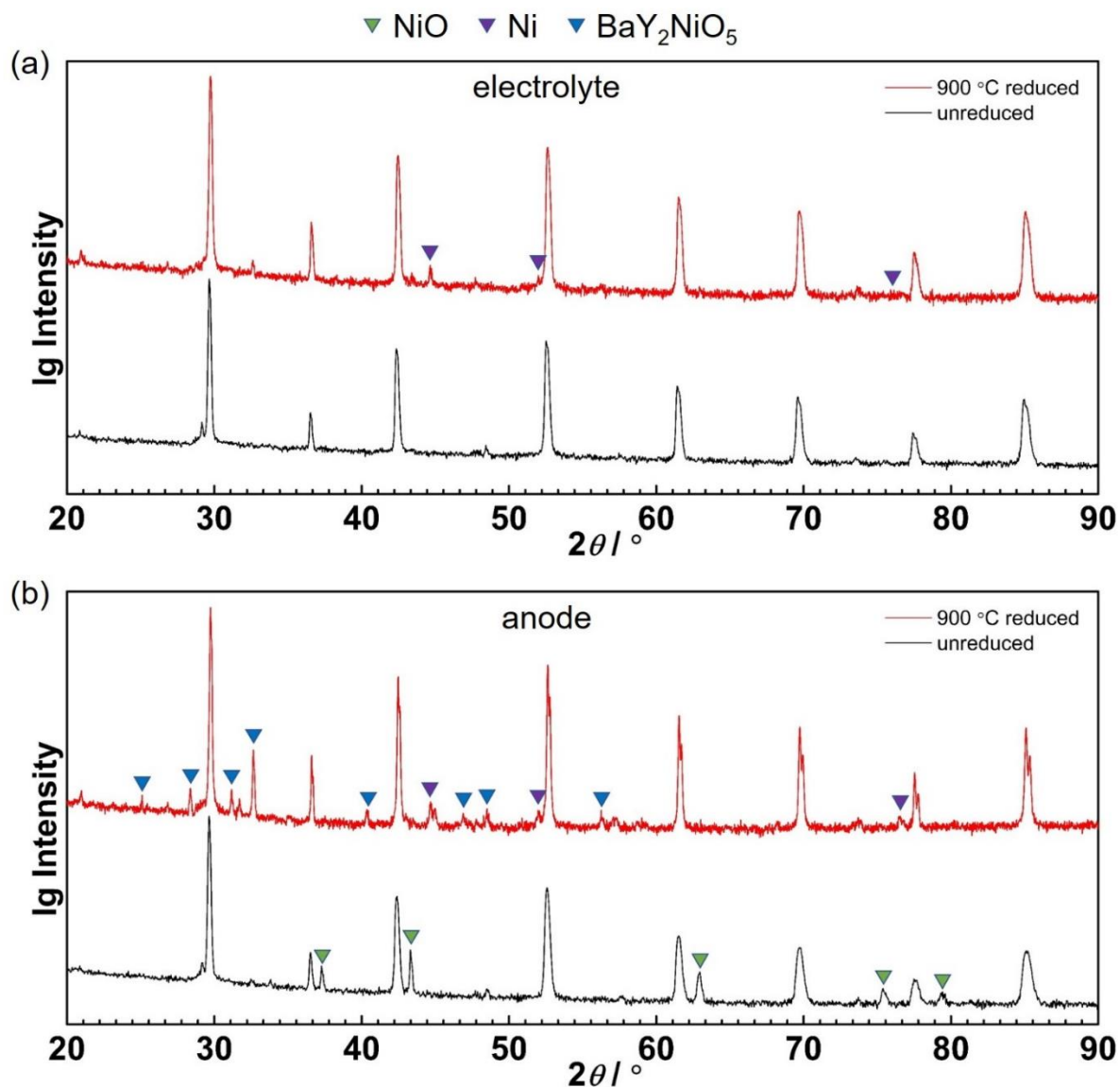


Figure 93: XRD pattern for (a) electrolyte and (b) anode side of the membrane sintered at 1450 °C for 6 h before and after reduced at 900 °C.

In order to have electronic conduction in the anode layer, the membranes were reduced in 3 vol.% H₂ at 900 °C for 3 h. **Figure 93** shows the XRD pattern for the membrane sintered at 1450 °C for 6 h before and after reduction. For the anode, in the reduction the NiO is transformed to Ni. Also some BaY₂NiO₅ is present as a residue from the transient liquid phase (the reducing conditions are so mild that BaY₂NiO₅ is not decomposed to BaYO_x and Ni metal).

The lattice constants of the electrolyte and anode layers (BZCY) are 4.272 and 4.266 Å before reduction, respectively. The corresponding lattice constant from the pellet sample BZC20Y17.5-0.5Ni is 4.259 Å, lower than for the membrane. The electrolyte side shows also weak peaks of metallic Ni for some samples. The appearance of Ni on the electrolyte side indicates potential problems, which have to be resolved in the future process optimization at IEK-1. It either originates from pinholes/cracks in the 10 μm thick electrolyte layer, through which Ni from the anode side becomes visible for XRD. Or the metallic Ni could be formed from Ni-rich residues of the transient liquid phase, which upon reduction forms metallic Ni. If Ni particles form a percolating path, this could lead to electronic short-circuit. Such pinholes/cracks are undesirable because the corresponding gas leakage will decrease the open cell voltage of the fuel cell.

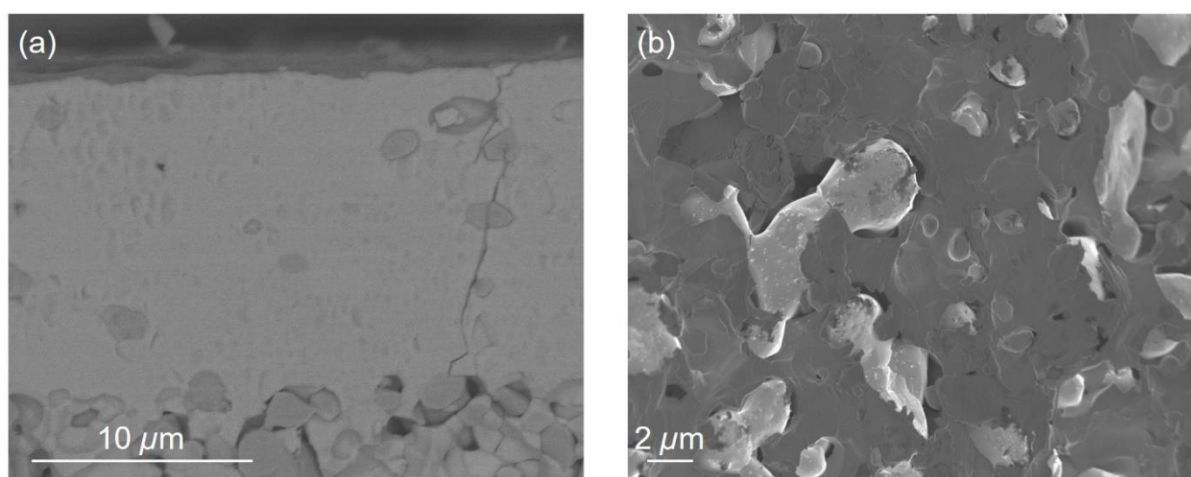


Figure 94: Cross-section SEM images of the BZC20Y17.5-0.5Ni membrane sample sintered at 1450 °C 6 h after reduction. (a) electrolyte side and (b) anode side after reduction. The sample was prepared by FIB. The measurement was done by J. Deuschle.

Figure 94 shows the cross-section SEM images from the BZC20Y17.5-0.5Ni membrane sample sintered at 1450 °C for 6 h after reduction. The electrolyte (**Figure 94-(a)**) has a thickness of ~ 10 μm and a grain size of ~ 1 μm. A few large dark particles are visible, which, based on SEM-EDX, are assigned to the BaY₂NiO₅ phase (not observed in XRD due to its low content and/or being located deeper in the electrolyte layer). A crack extending from the electrolyte to the anode can be clearly seen. It may be related to the short-circuit problem in

EIS measurements discussed later. The anode side, as shown in **Figure 94-(b)**, is composed of uniformly distributed Ni and BZCY particles, with reasonable porosity formed by the reduction of NiO to Ni.

In literature, Ni diffusion at the sintering temperature was detected from the anode to the electrolyte side ^[49,106,163]. Therefore, a SEM-EDX line scan was performed for the reduced sample. As shown in **Figure 95**, Ni shows a concentration profile at the interface of electrolyte/anode, and the diffusion length is 2 – 3 μm . For electrolyte layer composition without NiO addition, such a Ni in-diffusion might also lead to improved sintering. However, the whole process is more well-defined if some NiO is directly added into the electrolyte layer (as in the present thesis). Extensive Ni in-diffusion into the electrolyte layer is regarded detrimental, because it could lead to electronic short-circuit, or crack formation under reducing conditions. This also suggests that too long dwell time of the sintering temperature should be avoided.

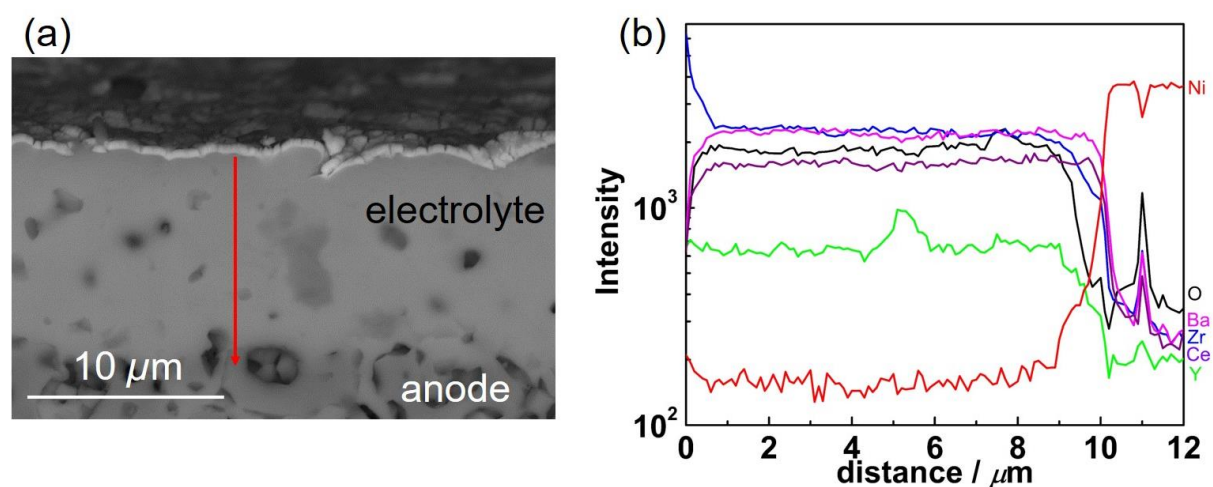


Figure 95: (a) cross-section SEM image of the the BZC20Y17.5-0.5Ni membrane sample sintered at 1500 $^{\circ}\text{C}$ 3 h after reduction and (b) corresponding SEM-EDX line scan measured at 15 kV. The red arrow in (a) indicates the line scan position and direction. The sample was prepared by FIB. The measurement was done by J. Deuschle.

Occasionally, XRD and/or TEM of the electrolyte layer also indicate some Y_2O_3 . This phase might either form by decomposition of BaY_2NiO_5 , or by BaO loss from BZCY. The latter issue is more pronounced for the membranes than for pellets, because they have a much larger surface to volume ratio, and cannot be covered by sacrificial BaZrO_3 powder.

3.4.3 Electrochemical properties of the membranes

Pseudo-four-wire impedance measurement was applied to obtain accurate conductivity of membranes. Exemplary impedance spectra measured at 200 °C and 600 °C in wet H₂ of the membrane sintered at 1500 °C for 3 h are shown in **Figure 96**. At 200 °C, the bulk semicircle is only partially visible. The bulk, GB and electrode semicircles have typical capacitances of 10⁻⁹, 10⁻⁶ and 10⁻³ F. At 600 °C, both bulk and GB semicircles disappear, and the total conductivity is extracted from the intersection of the spectra with the real axis at the high frequency side of the electrode semicircle, which can be ascribed to the Pt and Ag electrode. The very low resistance at high temperature is comparable to the resistance from the wires, confirming the necessity of pseudo-four-wire measurement.

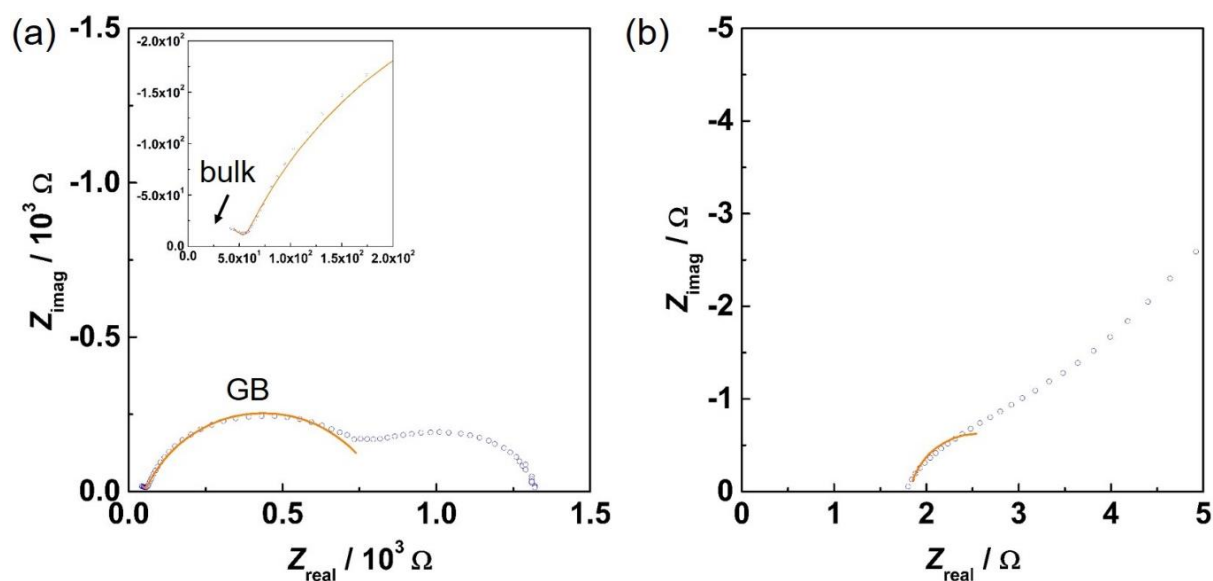


Figure 96: Impedance spectra of BZC20Y17.5-0.5Ni membrane sintered at 1500 °C 3 h after reduction. The measurement was done at (a) 200 °C and (b) 600 °C in wet H₂ ($p_{\text{H}_2\text{O}} = 20$ mbar).

Figure 97 shows two successfully measured membranes sintered at 1450 °C for 6 h (**Figure 97-(a)**) and 1500 °C for 3 h (**Figure 97-(b)**) compared to the comparable pellet sample. The membrane sintered at 1500 °C exhibits higher conductivity than 1450 °C 6 h. The bulk conductivity is almost equal to the pellet sample. The apparent GB conductivity is one order of magnitude lower. The total conductivity at 600 °C reaches $2.3 \times 10^{-3} \text{ Scm}^{-1}$, comparable to the pellet. Also, when comparing with the data from literature (**Table 8**), the conductivity from

this work falls in the upper range. Together with the large area and thin electrolyte layer this is promising. The conductivity results from the membranes certifies that the sequential tape-casting used in this work is good for large-scale fabrication. Nevertheless, further improvements of the sintering process are necessary to avoid short circuit and to improve the apparent GB conductivity.

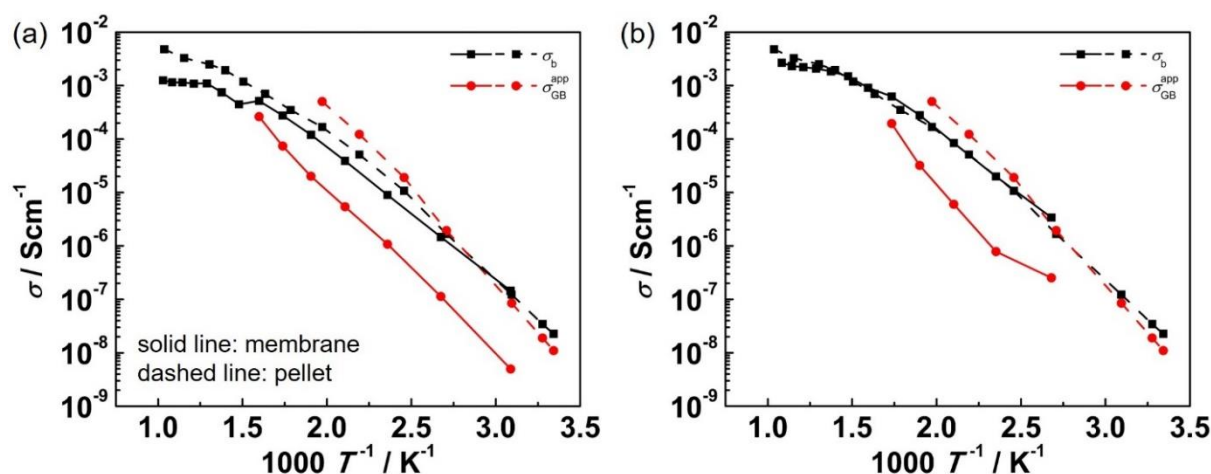


Figure 97: Arrhenius plot comparison of membranes sintered at (a) 1450 °C 6 h and (b) 1500 °C 3 h after reduction with corresponding pellet sample BZC20Y17.5-0.5Ni sintered at 1550 °C 4 h. The measurement of membranes was done in wet H₂ ($p_{\text{H}_2\text{O}} = 20$ mbar), and in wet H₂ ($p_{\text{H}_2\text{O}} = 20$ mbar) from room temperature to 350 °C and in wet N₂ ($p_{\text{H}_2\text{O}} = 20$ mbar) from 400 °C to 700 °C for the pellet.

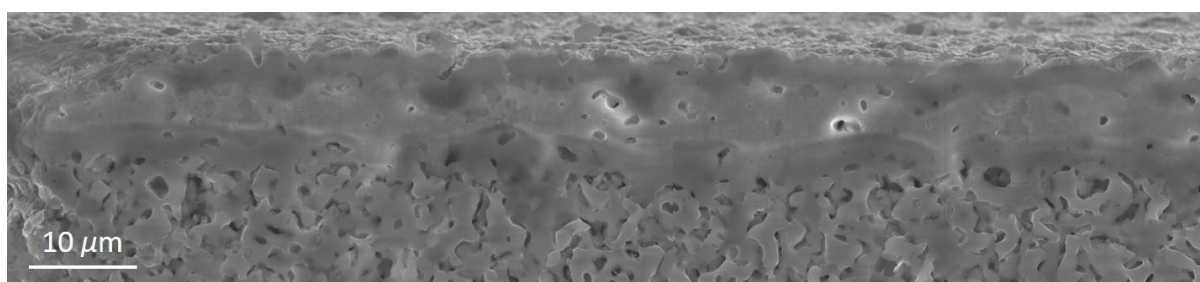


Figure 98: Cross-section SEM image of membrane sintered at 1500 °C 6 h after reduction. The sample was prepared by FIB.

Up to now, 80% of membranes have problems of short circuit. A few pinholes in a large-area membrane (**Figure 98**) should not be problematic for practical use as the oxide cathode will be on top of the electrolyte and not directly penetrate into the pinhole to create a short circuit. It

is difficult to measure the conductivity by EIS for a half cell because Pt/Ag was applied on the electrolyte which may diffuse through the pinholes and form an electronic conducting way at elevated temperatures.

Table 8: Total conductivity of electrolyte layer of anode-supported membranes measured at 600 °C from literature. All the cells measured with wet H₂ fed in anode side.

Author	Electrolyte		Anode	Cathode	Preparation	Co-Sinter. T	$\sigma_{\text{Total}} / \text{Scm}^{-1}$
	Composition	Thickness / μm					
W. Sun <i>et al.</i> [180]	BaZr _{0.8} Y _{0.2} O _{3-δ}	20	BaZr _{0.1} Ce _{0.7} Y _{0.2} O _{3-δ} + 60 wt.% NiO	Sm _{0.5} Sr _{0.5} CoO _{3-δ} + 40 wt.% Ce _{0.8} Sm _{0.2} O _{3-δ}	Co-pressing	1400 °C 10 h	1.43 · 10 ⁻³
E. Fabbri <i>et al.</i> [181]	BaZr _{0.7} Pr _{0.1} Y _{0.2} O _{3-δ}	20	BaZr _{0.8} Y _{0.2} O _{3-δ} + 70 wt.% NiO	BaZr _{0.7} Pr _{0.1} Y _{0.2} O _{3-δ} + 50 wt.% La _{0.6} Sr _{0.4} Co _{0.2} Fe _{0.8} O _{3-δ}	Co-pressing	1400 °C 6 h	~1.5 · 10 ⁻³
L. Bi <i>et al.</i> [182]	BaZr _{0.8} Y _{0.2} O _{3-δ}	30	BaZr _{0.8} Y _{0.2} O _{3-δ} + 50 wt.% NiO	BaZr _{0.7} Pr _{0.1} Y _{0.2} O _{3-δ} + 50 wt.% La _{0.6} Sr _{0.4} Co _{0.2} Fe _{0.8} O _{3-δ}	Co-pressing	1400 °C	~2.7 · 10 ⁻³
J. Xiao <i>et al.</i> [183]	BaZr _{0.8} Y _{0.2} O _{3-δ}	25	BaZr _{0.1} Ce _{0.7} Y _{0.2} O _{3-δ} + 40 wt.% NiO	Sm _{0.5} Sr _{0.5} CoO _{3-δ} + 30 wt.% Ce _{0.8} Sm _{0.2} O _{3-δ}	Dip-coating	1450 °C 6 h	~7.7 · 10 ⁻⁴
K. Bae <i>et al.</i> [184]	BaZr _{0.85} Y _{0.15} O _{3-δ}	2.5	BaZr _{0.85} Y _{0.15} O _{3-δ} + 56 wt.% NiO	La _{0.6} Sr _{0.4} CoO _{3-δ}	PLD		~2.8 · 10 ⁻³
L. Bi <i>et al.</i> [185]	BaZr _{0.8} Y _{0.2} O _{3-δ}	20	BaZr _{0.76} Y _{0.2} Ni _{0.04} O _{3-δ} + 60 wt.% NiO	BaZr _{0.8} Y _{0.2} O _{3-δ} + 50 wt.% PrBaCo ₂ O _{5-δ}	Spin-coating	1400 °C 6 h	~4.5 · 10 ⁻³
H. Bae <i>et al.</i> [186]	BaZr _{0.8} Y _{0.2} O _{3-δ}	5	Zr _{0.84} Y _{0.16} O _{2-δ} + 65 wt.% NiO	Gd _{0.1} Ce _{0.9} O _{2-δ} + La _{0.6} Sr _{0.4} Co _{0.2} Fe _{0.8} O _{3-δ}	Aerosol deposition	1200 °C 5 h	~5.7 · 10 ⁻⁴
H. Bae <i>et al.</i> [187]	BaZr _{0.8} Y _{0.2} O _{3-δ}	6.6	Zr _{0.84} Y _{0.16} O _{2-δ} + 65 wt.% NiO	Gd _{0.1} Ce _{0.9} O _{2-δ} + La _{0.6} Sr _{0.4} Co _{0.2} Fe _{0.8} O _{3-δ}	Aerosol deposition	1200 °C 5 h	~9.4 · 10 ⁻⁴
D. Pergolesi <i>et al.</i> [188]	BaZr _{0.8} Y _{0.2} O _{3-δ}	4	BaZr _{0.8} Y _{0.2} O _{3-δ} + 26 wt.% NiO	BaCe _{0.9} Yb _{0.1} O _{3-δ} + 50 wt.% La _{0.6} Sr _{0.4} Co _{0.2} Fe _{0.8} O _{3-δ}	PLD		1.43 · 10 ⁻⁴

Continued Table 8: Total conductivity of electrolyte layer of anode-supported membranes measured at 600 °C from literature. All the cells measured with wet H₂ fed in anode side.

Z. Sun <i>et al.</i> [189]	BaZr _{0.8} Y _{0.2} O _{3-δ} + 4 mol% CaO	25	BaZr _{0.8} Y _{0.2} O _{3-δ} + 60 wt.% NiO	BaZr _{0.8} Y _{0.2} O _{3-δ} + 61 wt.% La _{0.6} Sr _{0.4} Co _{0.2} Fe _{0.8} O _{3-δ}	Co-pressing	1400 °C 6 h	~1.7·10 ⁻³
C. Duan <i>et al.</i> [50]	BaZr _{0.8} Y _{0.2} O _{3-δ} + 1.0 wt.% NiO	20 – 30	BaZr _{0.8} Y _{0.2} O _{3-δ} + 55 wt.% NiO	BaCo _{0.4} Fe _{0.4} Zr _{0.1} Y _{0.1} O _{3-δ}	Direct SSRS	1450 °C	~9·10 ⁻⁴
C. Duan <i>et al.</i> [18]	BaZr _{0.8} Y _{0.2} O _{3-δ} + 1.0 wt.% NiO	25	BaZr _{0.8} Y _{0.2} O _{3-δ} + 60 wt.% NiO	BaCo _{0.4} Fe _{0.4} Zr _{0.1} Y _{0.1} O _{3-δ}	Screen- printing	1450 °C 18 h	~8·10 ⁻⁴
I. Luisetto <i>et al.</i> [190]	BaZr _{0.8} Y _{0.16} Zn _{0.04} O _{3-δ}	20	BaZr _{0.8} Y _{0.2} O _{3-δ} + 60 wt.% NiO	Pt	Slurry spin coating	1450 °C 5 h	~1.7·10 ⁻³
Y. Liu <i>et al.</i> [191]	BaZr _{0.7} Nd _{0.1} Y _{0.2} O _{3-δ}	30	BaZr _{0.7} Nd _{0.1} Y _{0.2} O _{3-δ} + 60 wt.% NiO	Ba _{0.5} Sr _{0.5} Co _{0.8} Fe _{0.2} O _{3-δ}	Dual dry pressing	1450 °C 5 h	~2.0·10 ⁻³
W. Sun <i>et al.</i> [192]	BaZr _{0.8} Y _{0.15} In _{0.05} O _{3-δ}	12	BaZr _{0.8} Y _{0.15} In _{0.05} O _{3-δ} + 65 wt.% NiO	Sm _{0.5} Sr _{0.5} CoO _{3-δ} + 40 wt.% Ce _{0.8} Sm _{0.2} O _{3-δ}	Drop-coating	1400 °C 5 h	~2.4·10 ⁻³
H. Dai <i>et al.</i> [193]	BaZr _{0.75} Y _{0.2} Pr _{0.05} O _{3-δ}	20	BaZr _{0.75} Y _{0.2} Pr _{0.05} O _{3-δ} + 60 wt.% NiO	BaZr _{0.75} Y _{0.2} Pr _{0.05} O _{3-δ} + La _{0.6} Sr _{0.4} Co _{0.2} Fe _{0.8} O _{3-δ}	Co-pressing	1400 °C 5 h	~2·10 ⁻³
S. Shafi <i>et al.</i> [194]	BaZr _{0.76} Y _{0.2} Ni _{0.04} O _{3-δ}	12	BaZr _{0.8} Y _{0.2} O _{3-δ} + 60 wt.% NiO	BaZr _{0.8} Y _{0.2} O _{3-δ} + 70 wt.% PrBaCo ₂ O _{5-δ}	Co-pressing	1450 °C 6 h	2.1·10 ⁻³

3.5 GB-decoration Method, amorphous phosphate at GB

Apart from SSRS, two other modifications of the sintering process were also tried to improve the GB transport properties. The first one is to decorate the GB core with alkali ions to mitigate the positive charges in the GB core caused by V_{O}^{\bullet} accumulation. The alkali ions are expected to substitute for Ba^{2+} and therefore act as acceptor dopant. The phase pure BZC20Y13.6 powder was decorated with K^+ or Rb^+ by impregnation with aqueous nitrate solutions. K^+ or Rb^+ substitutes Ba^{2+} on the A site as acceptor dopants and form negative $(\text{K,Rb})'_{\text{Ba}}$ defect which can partially compensate the positive charge at the GB core. Taking the grain size of BZCY-SPS = $0.5 \mu\text{m}$ (**Figure 35-(a)**) and BET result of $2.42 \text{ m}^2\text{g}^{-1}$) and assuming one K^+/Rb^+ ion covers an area of 2 \AA^2 , $\sim 0.1 \text{ at.}\%$ K^+/Rb^+ ion forms a monolayer at GBs.

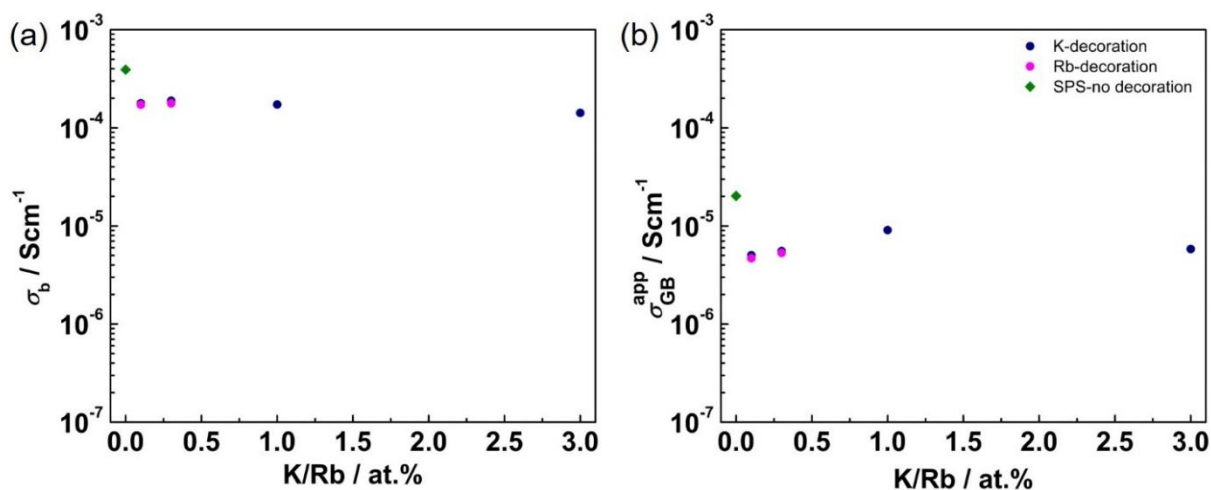


Figure 99: (a) bulk and (b) apparent GB conductivity measured at $200 \text{ }^\circ\text{C}$ in wet N_2 ($p_{\text{H}_2\text{O}} = 20 \text{ mbar}$) versus K^+/Rb^+ content. Samples were sintered by SPS at $1400 \text{ }^\circ\text{C}$ for 5 min and post-annealed at $1500 \text{ }^\circ\text{C}$ for 4 h.

As shown in **Figure 99**, all the decorated samples show lower bulk and apparent GB conductivity than BZC20Y13.6-SPS at $200 \text{ }^\circ\text{C}$. By using $1.0 \text{ at.}\%$ K^+ decoration, the apparent GB conductivity increases by about 5 times compared to $0.1 \text{ at.}\%$ K^+ . Pellets are not stable if more than $3.0 \text{ at.}\%$ Rb^+ is used, which can possibly be ascribed to the incomparable Rb^+ ion radius (1.72 \AA) to Ba^{2+} ions (1.61 \AA) on the A-site. The resulting structural distortions at GBs could make the pellet too brittle to be prepared or Rb-oxide phase is formed at GB, which reacts

with H₂O, CO₂ from air. Although K⁺ (1.64 Å) has a similar ionic radius as Ba²⁺, the pellets breaks into pieces upon storage for 3 months. An overall excess of A cations might lead to carbonate and hydroxide formation at GBs and therefore to cracks. Thus, the alkali ion decoration method was not further explored for membrane fabrications.

Another possibility is to decorate GBs with an amorphous layer, e.g. a proton conducting phosphate which may help to modify the GB structure such that V_O^{••} segregation to the GB core is decreased. 1 – 2 monolayers of phosphates forming amorphous phases at the sintering temperature for BZCY, for example La-phosphate ^[195], could potentially “soften” the GB structure. The chosen decoration species possesses a lower bulk conductivity than BZC20Y13.6 but higher than or comparable with the specific GB conductivity of BZC20Y13.6 (~ 10⁻⁵ Scm⁻¹ at 400 °C) (**Table 9**). The amount of phosphate is equivalent to a decoration layer with 10 Å thickness. After impregnation, the samples were sintered by SPS at 1400 °C 5 min and post-annealed at 1500 °C 4 h. Except for LPO, the pellets decorated with BLPO and ZPO have rather low relative densities, and the pellet with LWO immediately broke after sintering.

Table 9: Properties of phosphates and tungstate used for decorating BZC20Y13.6.

Decoration species	Bulk conductivity / Scm ⁻¹	Melting point / °C	Relative density / %
LaP ₃ O ₉	~10 ⁻⁴ (400 °C) ^[196]	1050	95.1
Ba _{0.75} La _{0.25} (PO ₄) _{0.75}	~10 ⁻⁵ (400 °C) ^[197]	1000	82.0
Zn(PO ₄) _{0.67}	~10 ⁻² (400 °C) ^[198]	900	86.2
La _{5.5} WO _x	~5 × 10 ⁻⁵ (500 °C) ^[199]		Difficult to sinter

The electrical conductivity of decorated samples (except BZC20Y13.6-LWO which broke immediately after sintering) were measured by EIS in wet N₂. For all phosphate decorated samples the bulk conductivity is slightly lower than for the undecorated sample (**Figure 100-(a)**). The apparent GB conductivity is almost 2 orders of magnitude lower (**Figure 100-(b)**). Also, the GB activation energies are higher for decorated samples (~ 0.9 eV) than for undecorated BZC20Y13.6-SPS (~ 0.7 eV). This indicates that instead of softening the GB

structure, the amorphous phosphate phase makes it more difficult for protons to migrate through the blocking GBs. Therefore, this method is also excluded for membrane fabrication.

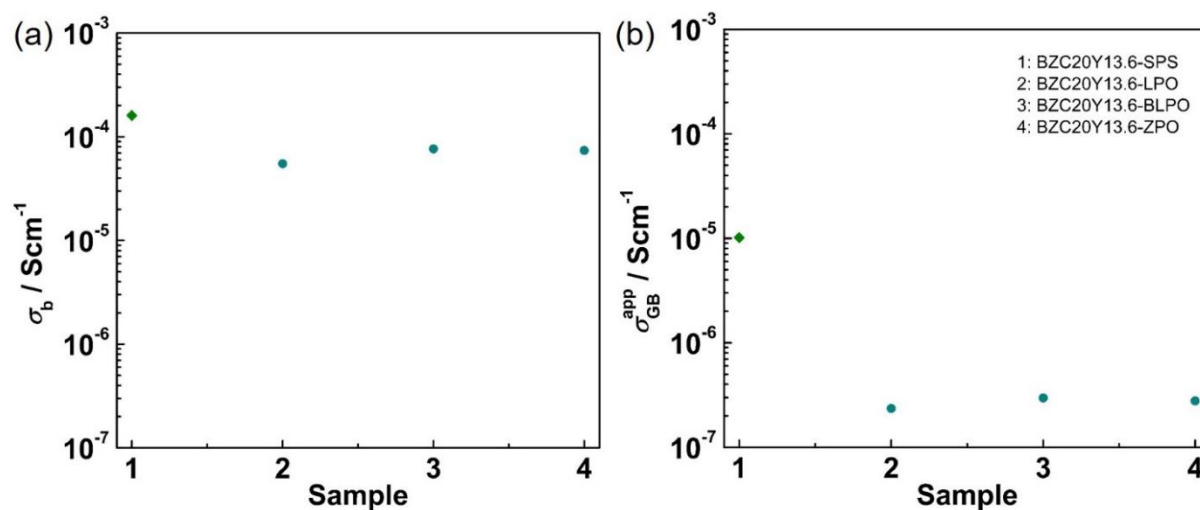


Figure 100: (a) bulk and (b) apparent GB conductivity measured at 200 °C in wet N_2 ($p_{\text{H}_2\text{O}} = 20$ mbar). Samples decorated with different decoration species were sintered by SPS at 1400 °C 5 min and post-annealed at 1500 °C 4 h.

Chapter 4 Conclusions

The present thesis is about improvement of sinterability, stability and conductivity of the proton-conducting electrolyte $\text{Ba}(\text{Zr,Ce,Y})\text{O}_{3-\delta}$ (BZCY) for protonic ceramic fuel cells (PCFCs). Improved sintering behavior including a decreased temperature (to minimize BaO loss) and increased grain size (to minimize the proton-blocking behavior of grain boundaries) is the key for manufacturing large-area ceramic membranes by processes such as tape-casting. It is known that Ce addition increases sinterability as well as grain boundary (GB) conductivity of $\text{Ba}(\text{Zr,Ce,Y})\text{O}_{3-\delta}$ ceramics, however, too high Ce contents decrease their stabilities versus H_2O and CO_2 . Thus, in the present thesis the Ce content is typically limited to 20 at.%. The bulk conductivity and even more the GB conductivity of $\text{Ba}(\text{Zr,Ce,Y})\text{O}_{3-\delta}$ increases strongly with Y content. In the first part of this thesis it is shown that the lattice expansion by Ce addition is also helpful to extend the solubility range of oversized Y dopants in BaZrO_3 .

The main focus of the present work is the detailed understanding of the “solid state reactive sintering” (SSRS) process utilizing NiO addition. SSRS combines perovskite phase formation from binary oxides/carbonates, ceramic densification and grain growth in a single step which occurs at lower temperature than conventional sintering of the pre-formed perovskite powder. For BZCY, the exact role and effects of NiO in the SSRS process were not clear from the literature. In the present work, the complex SSRS process is investigated combining XRD, density and grain size measurements, thermogravimetry, TEM-EDX investigations and electrochemical impedance spectroscopy (EIS). The following conclusions can be drawn:

(i) above 0.4 wt.% NiO addition, densification and grain growth are strongly enhanced already at 1450 – 1550 °C, and internal strain deduced from Williamson-Hall analysis vanishes. This indicates that NiO leads to the formation of a transient (Ba,Ni,Y)O_x liquid phase which allows for liquid-phase sintering. The estimated volume fraction of this liquid phase is small and even for quenched samples, the (Ba,Ni,Y)O_x phase is hardly seen directly.

(ii) TEM and TEM/EDX investigations show that at the end of the sintering, the cations from transient liquid phase are largely re-incorporated into the perovskite grains. Ni is mainly found in the GB region. The observed increased Y concentration in the GB region is assigned to either remnants of the (Ba,Ni,Y)O_x liquid phase and/or acceptor accumulation as a consequence of the positively charged GB core.

(iii) Thermogravimetry demonstrates a decrease of the maximum proton uptake with increasing NiO addition, and XRD shows decreasing lattice parameters. This indicates that the BaO required for (Ba,Ni,Y)O_x liquid phase formation is extracted from the perovskite lattice and only partly re-inserted at the end of the SSRS process. Since cation vacancies are energetically unfavorable, the BaO deficiency leads to a partial change of Y³⁺ from being an acceptor dopant on the (Zr,Ce)⁴⁺ site to being a donor on the Ba²⁺ site. This decreases the effective acceptor concentration and thus proton uptake. The Y concentration can be increased to 24 % without secondary phase formation to compensate the decreased effective acceptor concentration.

(iv) Impedance spectroscopy shows that the bulk proton conductivity decreases moderately with increasing NiO addition as a consequence of decreased proton concentration and also slightly decreased proton mobility. On the other hand, the apparent GB conductivity is increased for SSRS samples with NiO addition, which mainly results from the increasing grain sizes. The GB conductivities show pronounced scatter even for nominally identical samples. This scattering is assigned to the complexity of the SSRS process, but the detailed origin could not be fully resolved. At conditions relevant for PCFC operation (elevated temperature and higher Y content) the scattering decreases strongly.

(v) As a result of sintering, proton uptake and conductivity measurements, a NiO content of 0.5 wt.% is recommended as a good compromise. The liquid phase formed is then sufficient for good sintering and grain growth kinetics but not so extensive as to lead to excessive decrease of effective acceptor concentration (by BaO loss to the liquid phase). For ceramic Ba_{1.015}(Zr_{0.664}Ce_{0.20}Y_{0.136})O_{3-δ} samples this yields a total proton conductivity above 1 × 10⁻³ S/cm at 600 °C.

Based on these results, SSRS powders were supplied to IEK-1 (Research Center Jülich) for the tape-casting of large-area BZCY electrolyte membranes supported on a BZCY/NiO composite anode layer. Different cation compositions for the anode layer were explored. Y-free Ba(Zr,Ce)O₃ compositions lead to insufficient densification, indicating that Y is important for liquid phase formation. Membranes with a size of 5 × 5 cm² with a dense Ba_{1.015}(Zr_{0.625}Ce_{0.20}Y_{0.175})O_{3-δ} electrolyte layer thickness of about 10 μm could be prepared. However, optical microscopy, SEM-EDX and XRD measurements showed that occasionally secondary phases appear at the electrolyte layer surface, indicating that the membrane sintering process required further optimization. After reduction of the membranes converting NiO in the anode layer to Ni, some samples experienced electronic short-circuits owing to Ni-formation in the electrolyte. The membranes which were successfully measured have a total conductivity of 2.3 × 10⁻³ Scm⁻¹ at 600 °C, which is comparable to pellet samples with the same cation composition.

Thus, in the present thesis it could be demonstrated that despite its large volume shrinkage and chemical complexity, the SSRS process is also applicable for tape-casting of large electrolyte membranes. This is an important step towards actual PCFC manufacturing beyond lab-scale cells. The present thesis demonstrates that a detailed understanding of the underlying defect chemical processes is important for the improvement of the sintering process. While in general a liquid phase is helpful for sintering and grain growth of refractory oxides, the actual choice of its composition is challenging for functional ceramics such as proton conducting ceramic membranes. Although the volume fraction of the transient melt is low, it may severely affect the point defect concentrations and ionic carrier mobilities in bulk and at grain boundaries, which are sensitive even to small changes in cation stoichiometry. They can at least partially be compensated by adjusting the overall materials composition (e.g., increasing the nominal acceptor concentration). Modifying the temperature program with deliberate steps for transient melt formation and decomposition is another degree of freedom in such a complex process.

References

- [1] L. Yang, Y. Choi, W. Qin, H. Chen, K. Blinn, M. Liu, P. Liu, J. Bai, T. A. Tyson, M. Liu, *Nat. Commun.* **2011**, *2*, 357.
- [2] S. Singhal, *Solid State Ionics* **2000**, *135*, 305–313.
- [3] A. Atkinson, S. Barnett, R. J. Gorte, J. T. S. Irvine, A. J. McEvoy, M. Mogensen, S. C. Singhal, J. Vohs, *Nat. Mater.* **2004**, *3*, 17–27.
- [4] E. D. Wachsman, K. T. Lee, *Science*. **2011**, *334*, 935–939.
- [5] W. Wang, C. Su, Y. Wu, R. Ran, Z. Shao, *Chem. Soc. Rev.* **2013**, *113*, 8104–8151.
- [6] T. Suzuki, T. Yamaguchi, K. Hamamoto, Y. Fujishiro, M. Awano, N. Sammes, *Energy Environ. Sci.* **2011**, *4*, 940–943.
- [7] T. R. Smith, A. Wood, V. I. Birss, *Appl. Catal. A Gen.* **2009**, *354*, 1–7.
- [8] D. Yoon, A. Manthiram, *J. Mater. Chem. A* **2014**, *2*, 17041–17046.
- [9] Y.-H. Huang, R. I. Dass, Z.-L. Xing, J. B. Goodenough, *Science*. **2006**, *2*, 254–258.
- [10] Z. Shao, M. O. Tadé, in *Intermed. Solid Oxide Fuel Cells Mater. Appl.*, **2016**, pp. 247–266.
- [11] Y. Ando, H. Oozawa, M. Mihara, H. Irie, Y. Urashita, T. Ikegami, *Mitsubishi Heavy Ind. Tech. Rev.* **2015**, *52*, 47–52.
- [12] K. Hayashi, A. Miyasaka, N. Katou, Y. Yoshida, H. Arai, M. Hirakawa, H. Uwani, S. Kashima, H. Orisima, S. Kurachi, A. Matsui, K. Katsurayama, E. Tohma, *ECS Trans.* **2011**, *35*, 121–126.

- [13] M. Yoda, S. Inoue, Y. Takuwa, K. Yasuhara, M. Suzuki, *ECS Trans.* **2017**, 78, 125–132.
- [14] K. D. Kreuer, *Chem. Mater.* **1996**, 8, 610–641.
- [15] K.-D. Kreuer, S. J. Paddison, E. Spohr, M. Schuster, *Chem. Rev.* **2004**, 104, 4637–4678.
- [16] H. Iwahara, T. Esaka, H. Uchida, N. Maeda, *Solid State Ionics* **1981**, 3–4, 359–363.
- [17] H. Iwahara, T. Yajima, U. H., *Solid State Ionics* **1994**, 70–71, 267–271.
- [18] C. Duan, R. J. Kee, H. Zhu, C. Karakaya, Y. Chen, S. Ricote, A. Jarry, E. J. Crumlin, D. Hook, R. Braun, N. P. Sullivan, R. O'Hayre, *Nature* **2018**, 557, 217–222.
- [19] W. G. Coors, *J. Power Sources* **2003**, 118, 150–156.
- [20] B. Hua, N. Yan, M. Li, Y. F. Sun, Y. Q. Zhang, J. Li, T. Etsell, P. Sarkar, J. L. Luo, *Adv. Mater.* **2016**, 28, 8922–8926.
- [21] Z. Shi, J. L. Luo, S. Wang, A. R. Sanger, K. T. Chuang, *J. Power Sources* **2008**, 176, 122–127.
- [22] H. Iwahara, H. Uchida, K. Ono, K. Ogaki, *J. Electrochem. Soc.* **1988**, 135, 529.
- [23] T. Yajima, H. Suzuki, T. Yogo, H. Iwahara, *Solid State Ionics* **1992**, 51, 101–107.
- [24] H. S. Iwahara, T. Yajima, T. Hibino, K. Ozaki, **1993**, 61, 65–69.
- [25] T. Hibino, K. Mizutani, T. Yajima, H. Iwahara, *Solid State Ionics* **1992**, 57, 303–306.
- [26] T. Fukui, S. Ohara, S. Kawatsu, *J. Power Sources* **1998**, 71, 164–168.
- [27] R. L. Cook, J. J. Osborne, J. H. White, R. C. MacDuff, A. F. Sammells, *J. Electrochem. Soc.* **1992**, 139, L19.
- [28] Y. Larring, T. Norby, *Solid State Ionics* **1994**, 70–71, 305–310.
- [29] H. Fujii, Y. Katayama, T. Shimura, H. Iwahara, *J. Electroceramics* **1998**, 2, 119–125.
- [30] K. C. Liang, A. S. Nowick, *Solid State Ionics* **1993**, 61, 77–81.
- [31] K. C. Liang, Y. Du, A. S. Nowick, *Solid State Ionics* **1994**, 69, 117–120.
- [32] A. S. Nowick, Y. Du, *Solid State Ionics* **1995**, 77, 137–146.
- [33] H. G. Bohn, T. Schober, T. Mono, W. Schilling, *Solid State Ionics* **1999**, 117, 219–228.
- [34] S. Li, F. Schönberger, P. Slater, *Chem. Commun.* **2003**, 21, 2694–2695.
- [35] T. Shimura, Y. Tokiwa, H. Iwahara, *Solid State Ionics* **2002**, 154–155, 653–658.
- [36] M. S. Islam, R. A. Davies, C. A. J. Fisher, A. V. Chadwick, *Solid State Ionics* **2001**, 145, 333–338.
- [37] J. Bielecki, S. F. Parker, D. Ekanayake, S. M. H. Rahman, L. Börjesson, M. Karlsson, *J. Mater. Chem. A* **2014**, 2, 16915–16924.
- [38] J. Jankovic, D. P. Wilkinson, R. Hui, *J. Power Sources* **2012**, 201, 49–58.

- [39] M. Karlsson, A. Matic, C. S. Knee, I. Ahmed, S. G. Eriksson, L. Börjesson, *Chem. Mater.* **2008**, *20*, 3480–3486.
- [40] I. E. Animitsa, N. A. Tarasova, T. A. Denisova, Y. V. Baklanova, *J. Struct. Chem.* **2016**, *57*, 910–916.
- [41] P. Murugaraj, K. D. Kreuer, T. He, T. Schober, J. Maier, *Solid State Ionics* **1997**, *98*, 1–6.
- [42] M. H. D. Othman, A. F. Ismail, A. Mustafa, *J. Memb. Sci.* **2007**, *299*, 156–165.
- [43] R. S. Hay, P. Mogilevsky, E. Boakye, *Acta Mater.* **2013**, *61*, 6933–6947.
- [44] K. Toyoura, N. Hatada, Y. Nose, I. Tanaka, K. Matsunaga, T. Uda, *J. Phys. Chem. C* **2012**, *116*, 19117–19124.
- [45] R. Haugrud, T. Norby, *Nat. Mater.* **2006**, *5*, 193–196.
- [46] S. Choi, C. J. Kucharczyk, Y. Liang, X. Zhang, I. Takeuchi, H.-I. Ji, S. M. Haile, *Nat. Energy* **2018**, *3*, 202–210.
- [47] L. Yang, S. Wang, K. Blinn, M. Liu, Z. Liu, Z. Cheng, M. Liu, *Science*. **2009**, *326*, 126–129.
- [48] R. J. Braun, A. Dubois, K. Ferguson, C. Duan, C. Karakaya, R. J. Kee, H. Zhu, N. P. Sullivan, E. Tang, M. Pastula, A. Wood, T. Joia, R. O'Hayre, *ECS Trans.* **2019**, *91*, 997–1008.
- [49] H. An, H.-W. Lee, B.-K. Kim, J.-W. Son, K. J. Yoon, H. Kim, D. Shin, H.-I. Ji, J.-H. Lee, *Nat. Energy* **2018**, *3*, 870–875.
- [50] C. Duan, J. Tong, M. Shang, S. Nikodemski, M. Sanders, S. Ricote, A. Almansoori, R. O'Hayre, *Science (80-.)*. **2015**, *349*, 1321–1326.
- [51] E. Fabbri, L. Bi, D. Pergolesi, E. Traversa, *Adv. Mater.* **2012**, *24*, 195–208.
- [52] E. Vøllestad, R. Strandbakke, M. Tarach, D. Catalán-Martínez, M.-L. Fontaine, D. Beeaff, D. R. Clark, J. M. Serra, T. Norby, *Nat. Mater.* **2019**, *18*, 752–759.
- [53] H. Malerød-Fjeld, D. Clark, I. Yuste-Tirados, R. Zanón, D. Catalán-Martínez, D. Beeaff, S. H. Morejudo, P. K. Vestre, T. Norby, R. Haugrud, J. M. Serra, C. Kjøseth, *Nat. Energy* **2017**, *2*, 923–931.
- [54] S. Choi, T. C. Davenport, S. M. Haile, *Energy Environ. Sci.* **2019**, *12*, 206–215.
- [55] C. Duan, R. Kee, H. Zhu, N. Sullivan, L. Zhu, L. Bian, D. Jennings, R. O'Hayre, *Nat. Energy* **2019**, *4*, 230–240.
- [56] S. H. Morejudo, R. Zanón, S. Escolástico, I. Yuste-Tirados, H. Malerød-Fjeld, P. K.

- Vestre, W. G. Coors, A. Martínez, T. Norby, J. M. Serra, C. Kjøseth, *Science*. **2016**, 353, 563–566.
- [57] C. Duan, J. Huang, N. Sullivan, R. O’Hayre, *Appl. Phys. Rev.* **2020**, 7, 011314.
- [58] F. A. Kröger, *The Chemistry of Imperfect Crystals*, North-Holland Pub. Co., Amsterdam, **1964**.
- [59] K. D. Kreuer, S. Adams, W. Münch, A. Fuchs, U. Klock, J. Maier, *Solid State Ionics* **2001**, 145, 295–306.
- [60] K. D. Kreuer, *Annu. Rev. Mater. Res* **2003**, 33, 333–59.
- [61] W. Münch, G. Seifert, K. D. Kreuer, J. Maier, *Solid State Ionics* **1996**, 86–88, 647–652.
- [62] F. Shimojo, K. Hoshino, H. Okazaki, *J. Phys. Condens. Matter* **1998**, 10, 285–294.
- [63] W. Münch, K. D. Kreuer, G. Seifertli, J. Majer, *Solid State Ionics* **1999**, 125, 39–45.
- [64] G. Gregori, R. Merkle, J. Maier, *Prog. Mater. Sci.* **2017**, 89, 252–305.
- [65] H. G. Bohn, T. Schober, *J. Am. Ceram. Soc.* **2004**, 83, 768–772.
- [66] F. Iguchi, T. Yamada, N. Sata, T. Tsurui, H. Yugami, *Solid State Ionics* **2006**, 177, 2381–2384.
- [67] S. M. Haile, D. L. West, J. Campbell, *J. Mater. Res.* **1998**, 13, 1576–1595.
- [68] A. K. Azad, J. T. S. Irvine, *Solid State Ionics* **2007**, 178, 635–640.
- [69] F. Iguchi, N. Sata, T. Tsurui, H. Yugami, *Solid State Ionics* **2007**, 178, 691–695.
- [70] B. Joakim Nyman, E. E. Helgee, G. Wahnström, *Appl. Phys. Lett.* **2012**, 100, 061903.
- [71] E. E. Helgee, A. Lindman, G. Wahnström, *Fuel Cells* **2013**, 13, 19–28.
- [72] C. T. Chen, C. E. Danel, S. Kim, *J. Mater. Chem.* **2011**, 21, 5435–5442.
- [73] C. Kjøseth, H. Fjeld, Ø. Prytz, P. I. Dahl, C. Estournès, R. Haugsrud, T. Norby, *Solid State Ionics* **2010**, 181, 268–275.
- [74] X. Guo, W. Sigle, J. Maier, *J. Am. Ceram. Soc.* **2003**, 86, 77–87.
- [75] X. Guo, S. Mi, R. Waser, *Electrochem. Solid-State Lett.* **2005**, 8, J1–J3.
- [76] R. Meyer, X. Guo, R. Waser, *Electrochem. Solid-State Lett.* **2005**, 8, E67.
- [77] X. Guo, R. Waser, in *Solid State Ionics*, **2004**, pp. 63–67.
- [78] X. Guo, Y. Ding, *J. Electrochem. Soc.* **2004**, 151, J1.
- [79] J. S. Lee, U. Anselmi-Tamburini, Z. A. Munir, S. Kim, *Electrochem. Solid-State Lett.* **2006**, 9, J34–J36.
- [80] M. Vollmann, R. Waser, *J. Electroceramics* **1997**, 1.
- [81] S. Rodewald, J. Fleig, J. Maier, *J. Am. Ceram. Soc.* **2001**, 84, 521–530.

- [82] T. Hölbling, R. Waser, *J. Appl. Phys.* **2002**, *91*, 3037–3043.
- [83] M. Vollman, R. Waser, *J. Am. Ceram. Soc.* **1994**, *77*, 235–243.
- [84] F. Iguchi, C.-T. Chen, H. Yugami, S. Kim, *J. Mater. Chem.* **2011**, *21*, 16517.
- [85] M. Shirpour, R. Merkle, C. T. Lin, J. Maier, *Phys. Chem. Chem. Phys.* **2012**, *14*, 730–740.
- [86] M. Shirpour, R. Merkle, J. Maier, *Solid State Ionics* **2012**, *216*, 1–5.
- [87] M. Shirpour, B. Rahmati, W. Sigle, P. A. van Aken, R. Merkle, J. Maier, *J. Phys. Chem. C* **2012**, *116*, 2453–2461.
- [88] P. I. Dahl, H. L. Lein, Y. Yu, J. Tolchard, T. Grande, M. A. Einarsrud, C. Kjølseth, T. Norby, R. Haugrud, *Solid State Ionics* **2011**, *182*, 32–40.
- [89] F. Iguchi, T. Tsurui, N. Sata, Y. Nagao, H. Yugami, *Solid State Ionics* **2009**, *180*, 563–568.
- [90] M. Shirpour, G. Gregori, L. Houben, R. Merkle, J. Maier, *Solid State Ionics* **2014**, *262*, 860–864.
- [91] J. Maier, *Prog. Solid St. Chem.* **1995**, *23*, 171–263.
- [92] S. Imashuku, T. Uda, Y. Awakura, *Electrochem. Solid-State Lett.* **2007**, *10*, 175–178.
- [93] K. Katahira, Y. Kohchi, T. Shimura, H. Iwahara, *Solid State Ionics* **2000**, *138*, 91–98.
- [94] Y. Yamazaki, R. Hernandez-Sanchez, S. M. Haile, *J. Mater. Chem.* **2010**, *20*, 8158.
- [95] P. Babilo, T. Uda, S. M. Haile, *J. Mater. Res.* **2007**, *22*, 1322–1330.
- [96] Y. Guo, R. Ran, Z. Shao, S. Liu, *Int. J. Hydrogen Energy* **2011**, *36*, 8450–8460.
- [97] P. Babilo, S. M. Haile, *J. Am. Ceram. Soc.* **2005**, *88*, 2362–2368.
- [98] S. W. Tao, J. T. S. Irvine, *Adv. Mater.* **2006**, *18*, 1581–1584.
- [99] Z. A. Munir, U. Anselmi-Tamburini, M. Ohyanagi, *J. Mater. Sci.* **2006**, *41*, 763–777.
- [100] S. Ricote, N. Bonanos, A. Manerbino, N. P. Sullivan, W. G. Coors, *J. Mater. Chem. A* **2014**, *2*, 16107–16115.
- [101] S. Ricote, N. Bonanos, H. J. Wang, B. A. Boukamp, *Solid State Ionics* **2012**, *213*, 36–41.
- [102] S. Nikodemski, J. Tong, R. O’Hayre, *Solid State Ionics* **2013**, *253*, 201–210.
- [103] Y. Guo, Y. Lin, R. Ran, Z. Shao, *J. Power Sources* **2009**, *193*, 400–407.
- [104] N. Nasani, D. Pukazhselvan, A. V. Kovalevsky, A. L. Shaula, D. P. Fagg, *J. Power Sources* **2017**, *339*, 93–102.
- [105] S. Ricote, N. Bonanos, *Solid State Ionics* **2010**, *181*, 694–700.

- [106] D. Han, S. Uemura, C. Hiraiwa, M. Majima, T. Uda, *ChemSusChem* **2018**, *16*, 1–13.
- [107] J. Tong, D. Clark, L. Bernau, M. Sanders, R. O’Hayre, *J. Mater. Chem.* **2010**, *20*, 6333.
- [108] J. Tong, D. Clark, M. Hoban, R. O’Hayre, *Solid State Ionics* **2010**, *181*, 496–503.
- [109] D. Clark, J. Tong, A. Morrissey, A. Almansoori, I. Reimanis, R. O’Hayre, *Phys. Chem. Chem. Phys.* **2014**, *16*, 5076–5080.
- [110] Y. Liu, L. Yang, M. Liu, Z. Tang, M. Liu, *J. Power Sources* **2011**, *196*, 9980–9984.
- [111] S. Nikodemski, J. Tong, C. Duan, R. O’Hayre, *Solid State Ionics* **2016**, *294*, 37–42.
- [112] D. J. Buttrey, J. D. Sullivan, A. L. Rheingold, *J. Solid State Chem.* **1990**, *88*, 291–302.
- [113] D. Han, Y. Otani, Y. Noda, T. Onishi, M. Majima, T. Uda, *RSC Adv.* **2016**, *6*, 19288–19297.
- [114] D. Han, J. Iihara, S. Uemura, K. Kazumi, C. Hiraiwa, M. Majima, T. Uda, *J. Mater. Chem. A* **2016**, *4*, 10601–10608.
- [115] W. G. Coors, A. Manerbino, D. Martinefski, S. Ricote, in *Perovskite Mater. - Synth. Characterisation, Prop. Appl.*, InTech, **2016**.
- [116] K. D. Kreuer, *Solid State Ionics* **1999**, *125*, 285–302.
- [117] K. H. Ryu, S. M. Haile, *Solid State Ionics* **1999**, *125*, 355–367.
- [118] W. Atmospheres, S. V Bhide, A. V Virkar, *J. Electrochem. Soc.* **1999**, *146*, 2038–2044.
- [119] G. K. Williamson, W. H. Hall, *Acta Metall.* **1953**, *1*, 22–31.
- [120] R. D. Leapman, C. E. Fiori, C. R. Swyt, *J. Microsc.* **1981**, *63*, 229.
- [121] G. Cliff, G. W. Lorimer, *J. Microsc.* **1975**, *103*, 203.
- [122] K. D. Kreuer, E. Schönherr, J. Maier, *Solid State Ionics* **1994**, *70–71*, 278–284.
- [123] M. Shirpour, Grain Boundary Characterization of Electroceramics: Acceptor-Doped BaZrO₃, an Intermediate Temperature Proton Conductor, PhD thesis, University Stuttgart, **2011**.
- [124] J. E. Bauerle, *J. Phys. Chem. Solids* **1969**, *30*, 2657–2670.
- [125] T. Van Dijk, A. J. Burggraaf, *Phys. Status Solidi A-Applied Res.* **1981**, *63*, 229–240.
- [126] J. Fleig, J. Maier, *J. Eur. Ceram. Soc.* **1999**, *19*, 693–696.
- [127] J. Maier, *Berichte der Bunsengesellschaft für Phys. Chemie* **1986**, *90*, 26–33.
- [128] J. Fleig, *Solid State Ionics* **2002**, *150*, 181–193.
- [129] C. Hiraiwa, D. Han, A. Kuramitsu, A. Kuwabara, H. Takeuchi, M. Majima, T. Uda, *J. Am. Ceram. Soc.* **2013**, *96*, 879–884.
- [130] D.-K. Lim, T.-R. Lee, B. Singh, J.-Y. Park, S.-J. Song, *J. Electrochem. Soc.* **2014**, *161*,

- F991–F1001.
- [131] E. Fabbri, D. Pergolesi, S. Licoccia, E. Traversa, *Solid State Ionics* **2010**, *181*, 1043–1051.
- [132] D. Han, N. Hatada, T. Uda, *J. Am. Ceram. Soc.* **2016**, *99*, 3745–3753.
- [133] D. Gao, R. Guo, *J. Alloys Compd.* **2010**, *493*, 288–293.
- [134] K. Y. Park, Y. Seo, K. B. Kim, S. J. Song, B. Park, J. Y. Park, *J. Alloys Compd.* **2015**, *639*, 435–444.
- [135] S. Le, J. Zhang, X. Zhu, J. Zhai, K. Sun, *J. Power Sources* **2013**, *232*, 219–223.
- [136] G. S. Reddy, R. Bauri, *J. Alloys Compd.* **2016**, *688*, 1039–1046.
- [137] E. Fabbri, A. D’Epifanio, E. Di Bartolomeo, S. Licoccia, E. Traversa, *Solid State Ionics* **2008**, *179*, 558–564.
- [138] Y.-P. Fu, C.-S. Weng, *Ceram. Int.* **2014**, *40*, 10793–10802.
- [139] C. Zuo, S. Zha, M. Liu, M. Hatano, M. Uchiyama, *Adv. Mater.* **2006**, *18*, 3318–3320.
- [140] K. Leonard, Y. Lee, Y. Okuyama, K. Miyazaki, H. Matsumoto, *Int. J. Hydrogen Energy* **2017**, *42*, 3926–3937.
- [141] N. Nasani, P. A. N. Dias, J. A. Saraiva, D. P. Fagg, *Int. J. Hydrogen Energy* **2013**, *38*, 8461–8470.
- [142] M. Hakim, J. H. Joo, C. Y. Yoo, B. K. Kim, J. H. Yu, *J. Eur. Ceram. Soc.* **2015**, *35*, 1855–1863.
- [143] J. Bu, P. G. Jönsson, Z. Zhao, *J. Power Sources* **2014**, *272*, 786–793.
- [144] C. W. Tanner, A. V. Virkar, *J. Electrochem. Soc.* **1999**, *143*, 1386.
- [145] J. Tong, D. Clark, L. Bernau, A. Subramaniyan, R. O’Hayre, *Solid State Ionics* **2010**, *181*, 1486–1498.
- [146] Y. Huang, R. Merkle, J. Maier, *Solid State Ionics* **2020**, *347*, 11256.
- [147] K. D. Kreuer, T. Dippel, Y. M. Baikov, J. Maier, *Solid State Ionics* **1996**, *86–88*, 613–620.
- [148] P. Hartman, H. K. Chan, *Pharm. Res. An Off. J. Am. Assoc. Pharm. Sci.* **1993**, *10*, 1052–1058.
- [149] J. E. Burke, D. Turnbull, *Prog. Met. Phys.* **1952**, *3*, 220–292.
- [150] W. D. Kingery, H. K. Bowen, D. R. Uhlmann, *Introduction to Ceramics*, John Wiley & Sons, Inc., **1976**.
- [151] R. M. German, P. Suri, S. J. Park, *J. Mater. Sci.* **2009**, *44*, 1–39.

- [152] S. B. C. Duval, P. Holtappels, U. F. Vogt, U. Stimming, T. Graule, *Fuel Cells* **2009**, *9*, 613–621.
- [153] S. B. C. Duval, P. Holtappels, U. F. Vogt, E. Pomjakushina, K. Conder, U. Stimming, T. Graule, *Solid State Ionics* **2007**, *178*, 1437–1441.
- [154] Y. Yamazaki, R. Hernandez-Sanchez, S. M. Haile, *Chem. Mater.* **2009**, *21*, 2755–2762.
- [155] P. Babilo, Processing and Characterization of Proton Conducting Yttrium Doped Barium Zirconate for Solid Oxide Fuel Cell Applications, PhD Thesis, California Institute of Technology, **2007**.
- [156] R. Sažinas, I. Sakaguchi, M. A. Einarsrud, T. Grande, *Inorganics* **2018**, *6*, 14.
- [157] R. Sažinas, I. Sakaguchi, M. A. Einarsrud, T. Grande, *AIP Adv.* **2017**, *7*, 115024.
- [158] W. Gong, T. Chen, Z. Jin, *Trans. Nonferrous Met. Soc. China (English Ed.)* **2007**, *17*, 232–237.
- [159] S. Imashuku, T. Uda, Y. Nose, Y. Awakura, **2010**, *31*, 348–356.
- [160] J. J. Lander, *J. Am. Chem. Soc.* **1951**, *73*, 2450–2452.
- [161] J. M. Polfus, M.-L. Fontaine, A. Thøgersen, M. Riktor, T. Norby, R. Bredesen, *J. Mater. Chem. A* **2016**, *4*, 8105–8112.
- [162] D. Han, K. Shinoda, S. Tsukimoto, H. Takeuchi, C. Hiraiwa, M. Majima, T. Uda, *J. Mater. Chem. A* **2014**, *2*, 12552.
- [163] K. Xie, R. Yan, Y. Jiang, X. Liu, G. Meng, *J. Memb. Sci.* **2008**, *325*, 6–10.
- [164] M. Shirpour, R. Merkle, J. Maier, *Solid State Ionics* **2012**, *225*, 304–307.
- [165] D. Yun, J. Kim, S. J. Kim, J. H. Lee, J. N. Kim, H. Yoon, J. Yu, M. Kwak, H. Yoon, Y. Cho, C.-Y. Yoo, *Energies* **2018**, *11*, 3083.
- [166] S. Ricote, N. Bonanos, A. Manerbino, W. G. Coors, *Int. J. Hydrogen Energy* **2012**, *37*, 7954–7961.
- [167] C. Y. Yoo, D. S. Yun, J. H. Joo, J. H. Yu, *J. Alloys Compd.* **2015**, *621*, 263–267.
- [168] R. Costa, N. Grünbaum, M. H. Berger, L. Dessemond, A. Thorel, *Solid State Ionics* **2009**, *180*, 891–895.
- [169] F. Bozza, K. Bator, W. W. Kubiak, T. Graule, *J. Eur. Ceram. Soc.* **2016**, *36*, 101–107.
- [170] M. T. Caldes, K. V. Kravchyk, M. Benamira, N. Besnard, V. Gunes, O. Bohnke, O. Joubert, *Chem. Mater.* **2012**, *24*, 4641–4646.
- [171] J. Fleig, J. Maier, *J. Am. Ceram. Soc.* **2004**, *82*, 3485–3493.
- [172] H. S. Kim, H. Bin Bae, W. C. Jung, S. Y. Chung, *Nano Lett.* **2018**, *18*, 1110–1117.

- [173] J. P. Guha, D. Kolar, *J. Mater. Sci.* **1971**, *6*, 1174–1177.
- [174] S. O. Kucheyev, B. J. Clapsaddle, Y. M. Wang, T. Van Buuren, A. V. Hamza, *Phys. Rev. B - Condens. Matter Mater. Phys.* **2007**, *76*, 1–5.
- [175] M. Marrony, M. Ancelin, G. Lefevre, J. Dailly, *Solid State Ionics* **2015**, *275*, 97–100.
- [176] J. Dailly, G. Taillades, M. Ancelin, P. Pers, M. Marrony, *J. Power Sources* **2017**, *361*, 221–226.
- [177] J. Xiao, H. Yuan, L. Chen, C. Xiong, J. Ma, Y. Zhao, J. Chai, W. Du, X. Zhu, *Int. J. Mod. Phys. B* **2017**, *31*, 1744062.
- [178] J. Huang, Y. Ma, M. Cheng, S. Ruan, *Int. J. Hydrogen Energy* **2018**, *43*, 12835–12846.
- [179] W. Deibert, M. E. Ivanova, Y. Huang, R. Merkle, J. Maier, W. A. Meulenberg, *in preparation*.
- [180] W. Sun, L. Yan, Z. Shi, Z. Zhu, W. Liu, *J. Power Sources* **2010**, *195*, 4727–4730.
- [181] E. Fabbri, L. Bi, H. Tanaka, D. Pergolesi, E. Traversa, *Adv. Funct. Mater.* **2011**, *21*, 158–166.
- [182] L. Bi, E. Fabbri, Z. Sun, E. Traversa, *Energy Environ. Sci.* **2011**, *4*, 1352–1357.
- [183] J. Xiao, W. Sun, Z. Zhu, Z. Tao, W. Liu, *Mater. Lett.* **2012**, *73*, 198–201.
- [184] K. Bae, D. Y. Jang, H. J. Choi, D. Kim, J. Hong, B.-K. Kim, J.-H. Lee, J.-W. Son, J. H. Shim, *Nat. Commun.* **2017**, *8*, 14553.
- [185] L. Bi, E. H. Da'as, S. P. Shafi, *Electrochem. commun.* **2017**, *80*, 20–23.
- [186] H. Bae, J. Choi, K. J. Kim, D. Park, G. M. Choi, *Int. J. Hydrogen Energy* **2015**, *40*, 2775–2784.
- [187] H. Bae, G. M. Choi, *J. Power Sources* **2015**, *285*, 431–438.
- [188] D. Pergolesi, E. Fabbri, E. Traversa, *Electrochem. commun.* **2010**, *12*, 977–980.
- [189] Z. Sun, E. Fabbri, L. Bi, E. Traversa, *J. Am. Ceram. Soc.* **2012**, *95*, 627–635.
- [190] I. Luisetto, S. Licoccia, A. D'Epifanio, A. Sanson, E. Mercadelli, E. Di Bartolomeo, *J. Power* **2012**, *220*, 280–285.
- [191] Y. Liu, Y. Guo, R. Ran, Z. Shao, *J. Memb. Sci.* **2012**, *415–416*, 391–398.
- [192] W. Sun, Z. Shi, M. Liu, L. Bi, W. Liu, *Adv. Funct. Mater.* **2014**, *24*, 5695–5702.
- [193] H. Dai, *Ceram. Int.* **2017**, *43*, 7362–7365.
- [194] S. P. Shafi, L. Bi, S. Boulfrad, E. Traversa, *J. Electrochem. Soc.* **2015**, *162*, F1498–F1503.
- [195] G. Harley, R. Yu, L. C. De Jonghe, *Solid State Ionics* **2007**, *178*, 769–773.

-
- [196] N. Hatada, K. Toyoura, T. Onishi, Y. Adachi, T. Uda, *J. Phys. Chem. C* **2014**, *118*, 29629–29635.
- [197] N. Sharova, H. Fjellvåg, T. Norby, *Solid State Ionics* **2009**, *180*, 338–342.
- [198] H. Sumi, Y. Nakano, Y. Fujishiro, T. Kasuga, *Solid State Sci.* **2015**, *45*, 5–8.
- [199] G. S. Partin, D. V. Korona, A. Y. Neiman, K. G. Belova, *Russ. J. Electrochem.* **2015**, *51*, 381–390.

Acknowledgements

First of all, I would like to thank Prof. Dr. Joachim Maier for giving me such a great chance to study and to do research in his group. It has been four wonderful years, during which time I learned a lot from him. His profound knowledge, enthusiasm for science, and constructive advice for me encouraged me a lot. It is a great honor to be his student.

Then many thanks to Prof. Dr. Frank Gießelmann and Prof. Dr. Thomas Schleid for being my defense committee, reviewing my thesis and giving me valuable suggestion.

I would like to express my special thankfulness to Dr. Rotraut Merkle. Not only has she taught and guided me from the very beginning of my PhD study when I did not know too much about protonic conducting ceramics, but also her hard working attitude, deep knowledge about the research field, and logical and critical thinking have shown me a very good example of professional scientist. Even when she was busy, she could always spare time to discuss with me about my project in depth and gave me very useful and practical advice. She is a great teacher and advisor.

I am also thankful for Prof. Dr. Peter van Aken for his full support for TEM experiments. Many sincere thanks to Dr. Wilfried Sigle. Apart from being my external PhD advisor, he worked together with me in a project. His sight in depth and a lot of constructive advice helped me understand my topic and generated new thoughts. I would like to thank Dr. Dan Zhou and Rana Yekani for TEM measurements and useful discussion. I sincerely thank Ute Salzberger for

skillful TEM and FIB preparation. I would also like to thank Dr. Julia Deuschle for massive SEM-FIB and TEM sample preparation and Felicitas Predel for SEM-EDX measurements.

I genuinely thank Prof. Dr. Wilhelm Albert Meulenberg, Dr. Mariya Ivanova and Dr. Wendelin Deibert for the collaboration on ProtOMem. The useful discussions we had and the on-time update on our progress promote our project. It was a wonderful experience.

My warm thanks to Sofia Weiglein and Madeleine Burkhardt for their heartfelt administrative helps. Many thanks to Annette Fuchs, Udo Klock, Florian Kaiser for many technical supports in labs, to Dr. Helga Hoier for XRD measurements, to Uwe Traub for computer techniques, and to Armin Sorg for SPS preparation.

I thank Barbara Baum for cutting and polishing a large quantity of pellets. I thank Bernhard Fenk for teaching and helping me for SEM measurements. Thanks to Samir Hammoud for ICP-OES measurements and to Armin Schulz for Raman spectroscopy.

I would sincerely thank Dr. Hans-Georg Libuda, former coordinator of IMPRS-CMS (international Max Planck Research School for Condensed Matter Science). Since the first day I came to Max Planck Institute for interview, he gave me enormous helps. His clear instructions and useful information made the first days of me in Germany much easier.

In particular, I would like to thank my officemate Giulia Raimondi for many constructive discussions about research and casual talks about life. She organized many get-togethers for our group which made my PhD more colorful.

I would also like to express my many thanks to my other PhD and postdoc friends. The enjoyable lunches and events we had together, and all the helps they provided me made my PhD life whole.

At last but not least, I would like to thank my parents (Guijie Huang and Xiaoyue Liu) for their unconditional supports and encouragement. I appreciate a lot for my dear boyfriend Markus Joos, also a PhD candidate in our group, for the resonance not limited to research and life. His faithful encourage strengthens my confidence to tide over difficulties. Many sincere thanks to Markus' parents (Friewald Joos and Renate Joos) for so many warm helps and making Germany my second home.

Curriculum Vitae

Name Yuanye Huang

Date of Birth 18.06.1992

Place of Birth Beijing, China

Since Sep. 2016

PhD

Max Planck Institute for Solid State Research,

Department of Prof. Dr. Joachim Maier

And Chemistry Department, University of Stuttgart, Germany

Title of thesis: Proton conducting electrolytes for ceramic fuel cells

Sep. 2014 – Feb. 2016

M.Sc. in Materials Science and Engineering

Columbia University, New York City, New York, America

Sep. 2010 – Jul. 2014

B. Eng. in Materials Science and Engineering

Beijing University of Technology, Beijing, China

Title of thesis: Topological synthesis and mechanism of 1-D
ferroelectric nanorods

Sep. 2007 – Jul. 2010

High School

Beijing National Day School, Beijing, China